Investigation of Free-surface Flow Associated with Drop Impact: Numerical Simulations and Theoretical Modeling

Vom Fachbereich Maschinenbau an der
Technischen Universität Darmstadt zur
Erlangung des Grades eines Doktor-Ingenieurs
(Dr.-Ing.) genehmigte

D i s s e r t a t i o n

vorgelegt von

Dipl.-Ing. Edin Berberović, M.Sc.

aus Zenica, Bosnien und Herzegowina

Berichterstatter:	Prof. Dr.-Ing. C. Tropea
Mitberichterstatter:	Prof. Dr.-Ing. B. Weigand
	Priv.-Doz. Dr.-Ing. I.V. Roisman
Tag der Einreichung:	09.08.2010
Tag der mündlichen Prüfung:	02.11.2010

Darmstadt 2010
D17

Hiermit versichere ich, die vorliegende Doktorarbeit unter der Betreuung von Prof. Dr.-Ing. C. Tropea nur mit den angegebenen Hilfsmitteln selbständig angefertigt zu haben.

Darmstadt, August 2010

...dedicated to my family, with love and gratitude...

Acknowledgments

I wish to express my gratitude to Prof. Dr.-Ing. Cameron Tropea for accepting me as an external Ph.D student and giving me the opportunity to conduct the research at the Institute for Fluid Dynamics and Aerodynamics (FG SLA) at the Technische Universität Darmstadt. Special thanks to my supervisors: Dr.-Ing. Suad Jakirlić for his advice, guidance and continuous support before as well as throughout this work, and to Dr.-Ing. Ilia V. Roisman for his encouragement and fruitful discussions with always positive criticism.

My thanks goes also to Prof. Dr.-Ing. Bernhard Weigand from the Institute of Aerospace Thermodynamics at the Universität Stuttgart for kindly accepting to be the co-referee and external examiner.

Helpful suggestions from the colleagues from FG SLA are greatly appreciated. I also wish to express my gratitude to the administrative staff at FG SLA for taking over the bureaucratic matters.

Help and support of my friends in Darmstadt, especially Sanjin and his wife Aida, Ladislav and Emir, in solving many everyday problems is gratefully acknowledged.

I am thankful to Prof. Dr. Aleksandar Karač from my home university (University of Zenica, Bosnia and Herzegovina) for helping me clarify many tricky numerical issues. Valuable suggestions of Dr. Hrvoje Jasak are gratefully acknowledged.

This work could not be conducted without the financial support of the German Academic Exchange Service (Deutscher Akademischer Austauschdienst - DAAD) through the Research grants for doctoral candidates and young academics and scientists (Forschungsstipendien für Doktoranden und Nachwuchswissenschaftler) which is expressly acknowledged.

I owe my gratitude to the families Glowatz and Wallutis from Gelsenkirchen who helped me in making my first steps in Germany long time before.

Finally, I wish to express my cordial thanks to my family back home, my parents Mirsada and Hasib, brother Kenan, aunt Azra and her family, and especially to my wife Belma and our son Imran without whose support and great love I could probably not have finished this work.

Darmstadt, August 2010

Dipl.-Ing. Edin Berberović, M.Sc.

Abstract

This work is devoted to investigation of free-surface flow associated with drop impact. The main goal of the work is the computational and the theoretical study of the flow generated by drop collisions and drop impact onto different surfaces, with relevance for spray impingement.

The considered flow configurations include drop impact onto a shallow liquid layer, binary drop collision, drop impact onto a dry wall, nonisothermal drop impact onto a heated wall with the accompanying simultaneous heat transfer within the wall, and drop impact onto a porous substrate.

The potential of the new interface capturing methodology developed by OpenCFD Ltd and based on the volume-of-fluid (VOF) model within the framework of Computational Fluid Dynamics (CFD) is evaluated by contrasting the results of numerical simulations to the in-house experimental results and the existing experimental and numerical result databases. The novelty in the numerical approach is the introduction of an additional convective term into the equation for the indicator function, which acts as an artificial compressive contribution in the integrated equation and enables suppression of the numerical diffusion thereby providing a sharp definition of free surfaces. The flows studied are treated as being laminar and computed in the framework of the finite-volume numerical method.

In general, the numerical model and the computational procedure demonstrate good predictive capabilities by reproducing correctly the studied flows mentioned above, both qualitatively and quantitatively. All important effects observed in the experiments are reproduced and particularly some distinctive features of the flow are properly captured.

The numerical simulations of the different flow configurations pertinent to spray impact provide a detailed insight into the dynamics of the flow and enable analytical modeling using simplified theoretical approaches. In particular the computational results provide all the flow details which are inaccessible by present experimental techniques, they are used to prove the theoretical assumptions and yield the required database for defining new flow patterns and their analytical modeling.

Zusammenfassung

Untersuchung der Strömung mit freien Oberflächen verbunden mit Tropfenaufprall: numerische Simulationen und theoretische Modellierung

Die vorliegende Arbeit beschäftigt sich mit Untersuchung von Strömungen mit freien Oberflächen verbunden mit Tropfenaufprall. Das Hauptziel der Arbeit ist die numerische und die theoretische Untersuchung der Strömungen erzeugt durch Tropfenkollisionen und Tropfenaufprall auf verschiedene Oberflächen, die von Bedeutung in Sprayaufprall sind.

Die in Betracht gezogenen Strömungskonfigurationen beziehen Tropfenaufprall auf eine flache Flüssigkeitsschicht, binäre Tropfenkollisionen, Tropfenaufprall auf eine trockene Wand, nicht isothermen Tropfenaufprall auf eine beheizte Wand mit der gleichzeitigen Wärmeübertragung innerhalb der Wand und Tropfenaufprall auf eine poröse Schicht ein.

Das Vermögen der neuen auf dem volume-of-fluid (VOF) Model basierenden und von OpenCFD Ltd vorgeschlagenen Methodologie zur Erfassung der freien Oberflächen im Rahmen von Computational Fluid Dynamics (CFD) wird beurteilt durch Gegenüberstellung der numerischen Ergebnisse den vor Ort gewonnenen experimentellen Ergebnissen und der existierenden experimentellen und numerischen Datenbank von Ergebnissen. Die Neuigkeit in dem numerischen Verfahren ist die Einführung eines zusätzlichen Konvektionsterms in die Transportgleichung für die Indikatorfunktion, welches eine künstliche kompressive Auswirkung in der integrierten Gleichung erzeugt und zur Unterdrückung der numerisch erzeugten Diffusion führt und dabei eine scharfe Definition der freien Oberflächen ermöglicht. Die untersuchten Strömungen werden als laminar betrachtet und im Rahmen des numerischen Finite-Volumen Verfahrens berechnet.

Generell, das numerische Model und die Rechenprozedur demonstrieren eine gute prädiktive Kapazität indem sie die untersuchten oben genannten Strömungen korrekt reproduzieren, sowohl im qualitativen als auch in quantitativen Sinne. Alle wichtigen Effekte aus den Experimenten werden reproduziert, wobei speziell einige kennzeichnenden Merkmale genau erfasst werden.

Numerische Simulationen der verschiedenen Strömungskonfigurationen bezogen auf Sprayaufprall liefern einen detaillierten Einblick in das dynamische Verhalten der Strömung und ermöglichen analytische Modellierung unter Einsatz von vereinfachten theoretischen Ansätzen. Die Rechenergebnisse stellen insbesondere alle derzeit mit experimentellen Methoden unzugänglichen Details der Strömung zur Verfügung, sie bestätigen die theoretisch getroffenen Annahmen und bringen die erforderliche Datenbank der Ergebnisse zum Definieren neuer Strömungsstrukturen und deren analytischen Modellierung hervor.

Contents

List of Figures

List of Tables

Nomenclature

Latin characters

Symbol	Description	Unit
a_P	diagonal matrix coefficient	variable dependent
a_N	neighbor-cell matrix coefficient	variable dependent
A	coefficient	variable dependent
$\mathbf{A}$	coefficient matrix	variable dependent
b	source term coefficient	variable dependent
$\mathbf{b}$	source array	variable dependent
B	coefficient	-
Ca	capillary number	-
Co	Courant number	-
c_p	specific heat at constant pressure	J/(kgK)
C_γ	compression coefficient	-
$\mathbf{d}$	distance vector	m
D	diameter	m
e	effusivity	$\mathrm{J/(m^2Ks^{1/2})}$
Eck	Eckert number	-
$\mathbf{f}$	body force	$\mathrm{N/m^3}$
f_d	geometric weighting factor	-
Fr	Froude number	-
g	acceleration due to gravity	$\mathrm{m/s^2}$
$\mathbf{g}$	acceleration vector due to gravity	$\mathrm{m/s^2}$
h	heat transfer coefficient	$\mathrm{W/(m^2K)}$
	or height	m
H	height	m
$\mathbf{I}$	identity tensor	-
$\mathcal{I}$	function of the Prandtl number	-
k	differencing scheme parameter	-
	or thermal conductivity	W/(mK)
K	K-parameter	-
K_p	dimensionless parasitic velocity	-
K	porous medium permeability	$\mathrm{m^2}$
$\mathcal{L}$	general spatial derivative term	variable dependent
$\mathcal{L}^*$	discretized general spatial derivative term	variable dependent
$\mathbf{n}$	unit normal vector	-
n_f	unit normal flux	$\mathrm{m^2}$
N	number of cells or cell-faces	-
Nu	Nusselt number	-

Oh	Ohnesorge number	-
p, p_d	pressure, modified pressure	$\mathrm{N/m^2}$
Pr	Prandtl number	-
$\dot{q}$	heat flux	$\mathrm{W/m^2}$
Q	heat transfer	J
r	gradient ratio	-
	or radial coordinate	m
R	radius	m
Re	Reynolds number	-
S	source term	variable dependent
$\mathbf{S}_f$	cell-face surface-normal vector	$\mathrm{m^2}$
t	time	s
T	temperature	K
$\mathbf{T}$	viscous stress tensor	$\mathrm{N/m^2}$
U	velocity component (magnitude)	m/s
$\mathbf{U}$	velocity vector	m/s
V	volume	$\mathrm{m^3}$
We	Weber number	-
x, y, z	Cartesian coordinates	m
$\mathbf{x}$	position vector	m

Greek characters

Symbol	Description	Unit
α	thermal diffusivity	m^2/s
β	empirical parameter	-
γ	indicator function (volume fraction)	-
Γ	diffusivity	m^2/s
δ_{ij}	Kronecker delta	-
δ	stabilization factor	1/m
	or small value	-
ε	porous medium porosity	-
	or small value	-
η	empirical parameter (function)	-
θ	angle	rad
κ	mean surface curvature	1/m
λ	weighting factor, damping factor	-
μ	dynamic viscosity	Ns/m^2
ν	kinematic viscosity	m^2/s
ξ	self-similar variable	-
ρ	density	kg/m^3
σ	surface tension coefficient	N/m
τ	empirical parameter, time shift	-
ϕ	general tensorial variable	variable dependent
Φ	solution array	variable dependent
φ	angle	rad
ψ	blending factor	-
Ψ	velocity potential	m^2/s
ω	vorticity	1/s
Ω	vorticity scale	1/s

Superscripts and subscripts

Symbols	Description
b	boundary, bottom
bl	boundary layer
c	compression, center, contact
cl	contact line
cr	crater
cyl	cylinder
d	droplet
dyn	dynamic
e	equatorial
eq	equilibrium
f	cell-face value
g	gas
$Hoff$	Hoffman's function
$init, 0$	initial value
inv	inviscid
l	liquid
L	lamella
max	maximum
$mean$	mean value
n	normal
o	previous (old) time step
p	parasitic, polar, pore
por	porous
ref	reference value
r	relative, radial
res	residual
s	solid
sph	sphere
t	tangential
T	transpose
$theor$	theoretical
$visc$	viscous
w	wall

Special symbols

Symbol	Description
$\perp$	normal component
—	normalized (dimensionless) value
$\langle \quad \rangle$	averaged value

Abbreviations

Symbols	Description
CBC	Convection Boundedness Criterion
CCM	Computational Continuum Mechanics
CD	Central Differencing
CFD	Computational Fluid Dynamics
CICSAM	Compressive Interface Capturing Scheme for Arbitrary Meshes
CLSVOF	Combined Level Set Volume Of Fluid
CSF	Continuum Surface Force
CSS	Continuum Surface Stress
DD	Downwind Differencing
DIC	Diagonal-based Incomplete Cholesky
DILU	Diagonal-based Incomplete Lower-Upper
DNS	Direct Numerical Simulation
GD	Gamma Differencing
HRIC	High Resolution Interface Capturing
LES	Large Eddy Simulation
LL	Limited Linear
LS	Level Set
LVIRA	Least-square Volume-of-fluid Interface Reconstruction Algorithm
MAC	Marker And Cell
MD	Molecular Dynamics
MPI	Message Passing Interface
MULES	Multidimensional Universal Limiter for Explicit Solutions
NVD	Normalized Variable Diagram
OpenFOAM	Open Field Operation And Manipulation
PBiCG	Preconditioned Bi-Conjugate Gradient
PCG	Preconditioned Conjugate Gradient
PISO	Pressure Implicit with Splitting of Operators
PLIC	Piecewise Linear Interface Calculation
PROST	Parabolic Reconstruction Of Surface Tension
SLIC	Simple Line Interface Calculation
TVD	Total Variation Diminishing
UD	Upwind Differencing
UQ	Ultimate Quickest
VOF	Volume Of Fluid

1 Introduction

1.1 Background and Motivation

Collision of a drop with a surface can be observed in everyday life and also builds the basis of spray impact. The phenomenon of a drop impact is not only aesthetically beautiful, but also is a challenging physical problem, very rich in fluid dynamics, requiring insight which may enable improvements in many technical, environmental and industrial fields to be achieved. The impact of a single drop on a surface has attracted the attention of scientists for over one century, though detailed studies of its dynamics were not possible before high-speed digital cameras could be used for photography and powerful computers for calculations.

The imposing phenomena occurring when liquid drops splash on various surfaces is of great relevance to various applications, ranging from sprinkler systems for fire suppression, soil erosion, dispersal of seed and microorganisms and pesticide spraying in agriculture, steam turbines, spray cooling to enable high heat fluxes in microelectronics where even small temperature gradients across the chip may cause component failure, high-quality ink-jet printing and coverage of surfaces in paint spraying, to internal combustion engines with direct fuel injection, where the fuel is sprayed into engine cylinders in a form of small droplets which splash on the inner walls of cylinders and applications involving liquid deposition, where it is desirable to deposit a droplet without trapping air bubbles. Splashing of drops on liquid layers is of importance in atmospheric sciences for separation of electrical charges by the liquid disintegration during splashing. Rainwater separation in water boxes in air-conditioning systems in automobiles also requires knowledge and control over this process. In medical science cryogenic spray cooling is used to pre-cool the outer layer of the human skin during dermatological laser treatments such as hair removal.

Deposition of a liquid onto a solid surface is often performed with the use of liquid droplets. Forced wetting is an important mechanism in coating processes, where a thin liquid layer is continually deposited onto a moving solid surface, and plays an important role in composite manufacture and designing molding processes which require a knowledge of the filling front evolution in order to avoid defects such as dry spots. Microfabrication of electronic circuits produced by precision solder-drop dispensing requires knowledge in drop impact.

Investigations of heat transfer during impingement of small drops are of particular interest since the thin liquid layer formed by a number of small-size droplets enhances heat transfer rates compared to thicker liquid layers. In the process industry equipment is used that often requires rapid heat removal from solid surfaces to a

liquid. The heat rate depends to a great extent on the manner in which heat is transferred from or to the surface. Heat removal from a hot surface by spraying it with liquid represents an enhanced way of cooling. In such technologies the nonisothermal flow generated by impacts of drops and their interactions represents a core of the physical process. The liquid-vapor phase change process, such as evaporation of liquid drops, plays a major role in air-conditioning or refrigeration systems and combustion engines. Another example is the solidification of rain droplets falling onto airplane wings, which may lead to accumulation of ice structures within the boundary layer and may significantly influence the aerodynamics of flight.

The development of fuel cell systems as an alternative power source in automotive industry has become very attractive. Such systems consume either hydrogen or hydrocarbon fuels to enable electrochemical reaction within the fuel cell membrane. The water produced in the cell ensures the ion conductivity of the membrane, but too large amounts of water may degrade the fuel cell performance. The water within the cell forms droplets rather than a liquid film, which are swept away by the air flowing with the velocity determined by the droplet size.

A distinct area of investigation in fluid mechanics deals with the process of spray impact. When a spray impacts on a target, single droplet collisions occur at time scales determined by the spray impact parameters, such as distributions of drop sizes and velocities and flux densities. During the process several interacting occurrences take place. Single drops penetrate into the wall film and cause cavities or craters to be formed in the underlying liquid film, the sides of which may rise and build thin circumferential liquid sheets known as a crowns or coronas. The uprising crowns collide with the incoming drops and influence their motion. The collisions between drops occur also already before reaching the surface, thereby exchanging mass, momentum and energy with each other. Due to continuously impacting droplets, the surface of the wall film covering the substrate is highly irregular and deformed, leading to a strong interaction between the falling droplets and the film. In this manner the continuous process of spray impact consists of a number of subsequent single drop impacts and interactions, all having in general different impact conditions and producing different outcomes. Tropea and Roisman [114] have shown that the single droplet impingement models can be extrapolated to the spray impingement in the case of sparse sprays, however this approximation is questionable for very dense sprays.

The small scales and high velocities involved inhibit direct experimental access to these phenomena where high-speed photography is a primary source of information, which is the reason why numerical simulations are receiving more and more attention. For practical reasons, direct numerical simulation (DNS) of spray impingement is far beyond the capacity of the present computer power. This is because spray impact involves a large range of different time and length scales. Sprays consist of a large number of drops of different sizes and velocities impinging on a surface. The length scale of the wall film fluctuation may be much larger than the diameter of a single drop and the time scale determining these fluctuations may be much larger than the time scale of a single-drop impact. The two-phase flow of the underlying gas and the falling droplets is rather complex and difficult to model by the existing

turbulence models. Thus, a deterministic approach for spray impingement including individual treatment of all droplets is still practically impossible.

Investigations of spray impact may be conducted twofold. For engineering applications the representative statistical values are of importance. These include statistically averaged values using probability density functions to represent distributions of droplet sizes, their velocities as well as other data enabling integral engineering analysis, such as average heat transfer from the surface to the spray in cooling applications. Obtaining such values is rather difficult, both experimentally and numerically. Therefore mathematical models resulting from simplified analysis are commonly used in industry for optimization or parameter studies. On the other hand, in order to gain insight into the fundamental underlaying physics of spray impact, studying flows induced by single-drop impacts presents a reasonable alternative. The key is the possibility to reproduce identical initial and boundary conditions to a great extent in single-drop impacts. Thus, single-drop impact studies may be conducted by isolating effects of one or several parameters, which represents a great difficulty in experiments with sprays. Clearly, such investigations cannot be conducted by observing impacts of single drops during the impingement of a spray. Impingement of an isolated single drop can be modeled relatively accurately, whereas the impingement of a spray is much more complicated due to the complex drop-to-drop and drop-to-wall film interactions and vice versa. In simulations of spray impingement such complicated effects are commonly neglected (Mundo et al. [61]) and the modeling is based solely on the splashing criterion which determines the number and the sizes of the secondary droplets.

On the other hand a single-drop impact onto a surface also imposes challenges for development of numerical models but it represents an excellent model system which enables assessment of their capabilities. Rapid advances in computer hardware and developments of numerical algorithms have enabled a broader use of computational methods for investigating the drop impact phenomena. Numerical simulations provide a detailed database comprising not only the dynamics of the drop surface with respect to its position and form but also the temporal behavior of entire velocity, pressure and temperature fields, being beyond the reach of the existing experimental methods.

A complete understanding of the drop impact phenomenon still remains non-trivial and challenging. For many applications of practical interest, the hydrodynamics and heat transfer, as well as physical and chemical mechanisms governing the process of liquid displacing a fluid from a solid surface are still unresolved. The main reason is the difference between the molecular or submicroscopic length scales at which the process in reality takes place and the macroscopic scales accessible by experimental equipment.

1.2 Flows Generated by Impacts of Drops

The final outcome of drop impact depends on various parameters, such as the magnitude and direction of the impact velocity, physical properties of the liquid including

surface tension, roughness and wettability of the impacting surface and optionally nonisothermal effects including wall and ambient temperature and phase change. Numerous additional influencing factors may affect the outcome: the drop may not be of a perfect spherical shape at the instant of impact, the impacting target may be a perturbed surface of an underlying deep pool or a shallow film of same or different liquid, a dry or partially wetted hard, deformable or porous substrate, which may further be flat or curved, normal or inclined to the incoming drop, the liquids may be non-Newtonian, miscible, etc.

1.2.1 Dimensionless Parameters Characterizing the Flow

In order to establish general parameters describing the impact conditions and to enable the direct comparison between different cases, several dimensionless parameters can be used. These parameters are used to characterize the flow and heat transfer using dimensional length and time scales and combining with them the thermophysical properties of fluids.

As a scale for the time, the time required for a drop to cover a distance of one diameter, i.e. D_0/U_0 is commonly used. Thus, the time is made dimensionless as

$$\bar{t} = t\frac{U_0}{D_0}. \tag{1.1}$$

Normalization of lengths expressing dimensionless heights of spreading drops or spreading diameters (termed spreading ratios), dimensionless boundary layer thicknesses or dimensionless penetration depths in cases of drop impact on a liquid film, is performed using drop diameter D_0 and liquid film height H_0, or some equivalent, as length scales

$$\overline{D} = \frac{D}{D_0}, \tag{1.2}$$

$$\overline{H} = \frac{H}{H_0} \quad \text{or} \quad \overline{H} = \frac{H}{D_0}. \tag{1.3}$$

Reynolds number represents a measure of relative importance of inertial and viscous effects

$$\mathrm{Re} = \frac{D_0 U_0}{\nu}. \tag{1.4}$$

Weber number presents a ratio between inertial and surface tension forces

$$\mathrm{We} = \frac{\rho U_0^2 D_0}{\sigma}. \tag{1.5}$$

Ohnesorge number provides an estimate of the strength of the viscous forces relative to inertial and surface tension forces

$$\mathrm{Oh} = \frac{\sqrt{\mathrm{We}}}{\mathrm{Re}} = \frac{\mu}{\sqrt{\rho D_0 \sigma}}. \tag{1.6}$$

Capillary number represents the inertial and viscous effects relative to the surface tension

$$\mathrm{Ca} = \frac{U_0 \mu}{\sigma}. \tag{1.7}$$

In cases involving heat transfer, dimensionless parameters relating the flow to the heat transfer are the Prandtl number

$$\mathrm{Pr} = \frac{\nu}{\alpha}, \tag{1.8}$$

representing the ratio between momentum and thermal diffusivities, then the Peclet number

$$\mathrm{Pe} = \mathrm{Re}\,\mathrm{Pr} = \frac{D_0 U_0}{\alpha}, \tag{1.9}$$

relating the rate of advection of a flow to its rate of thermal diffusion, and the Eckert number

$$\mathrm{Eck} = \frac{U_0^2}{c_p \Delta T}, \tag{1.10}$$

providing the ratio of the kinetic energy and enthalpy and commonly used in estimating the importance of viscous energy dissipation.

Froude number, comparing the effects of inertial and gravitational forces is used in cases with significant influence of gravity

$$\mathrm{Fr} = \frac{U_0^2}{g D_0}. \tag{1.11}$$

If the flow includes more than one drop the characteristic dimensionless numbers are commonly expressed using the relative drop velocity. For example, in the case of binary drop collision the impact velocity of one drop is half of the relative drop velocity and therefore $\mathrm{We}_r = 4\mathrm{We}$, $\mathrm{Re}_r = 2\mathrm{Re}$. Here We_r and Re_r are the impact Weber and Reynolds numbers based on the relative velocity of the drops as often used in the studies of binary drop collisions.

1.2.2 Flow Patterns

Drop impact onto a thin pre-existing liquid layer on the wall may lead to different flow patterns depending on the drop impacting velocity. An experimental study on the impact of a train of drops onto a solid surface conducted by Yarin and Weiss [135] revealed two different outcomes. At lower impact velocities the drops deform into a thin lamella spreading over the wall with a rim formed at its edge, whereas if the impact velocities are higher and the surface is wetted the lamella deforms into an uprising crown-like thin liquid sheet with a rim at its top edge ejecting a number of secondary droplets. The crown formation is a consequence of the momentum jump in the region where the fast-moving liquid in the lamella meets the liquid in the stationary layer. It is referred to as splashing and this scenario is shown on the photograph in Fig. 1.1 from Cossali et al. [17], which clearly resolves the unstable

free rim where small finger-like jets are generated from bending perturbations of the rim before braking up by surface tension and enabling secondary droplets of different sizes to be detached from their tips. The free rim on the top of the crown propagates with the velocity determined by the surface tension, the liquid density and the thickness of the crown wall (Taylor [111]).

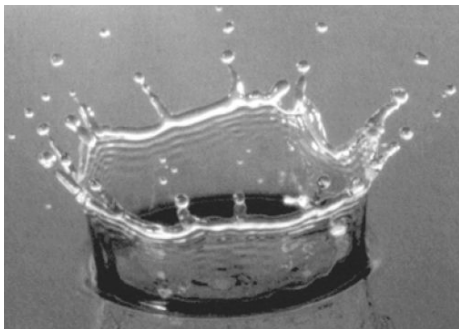

Figure 1.1: Drop splashing, from Cossali et al. [17]

Neglecting viscous losses at the instance of the impact Yarin and Weiss [135] found an asymptotic solution to the flow in a thin liquid layer and derived an analytical model for the dimensionless crown radius in the following form

$$\overline{R}_{cr} = \beta\sqrt{(\overline{t} - \tau)}, \tag{1.12}$$

applicable to single-drop impacts, where β depends on the impact velocity, the initial drop diameter and the thickness of the pre-existing liquid film and τ is the time shift.

The critical conditions at which splashing occurs is termed the splashing threshold. The threshold velocity for splashing is found by Yarin and Weiss [135] to be a function only of physical properties, indicating the fact that the crown ejection has its origin in the spreading lamella long after the actual time instance of the impact. In single-drop impacts onto a thin liquid film an equivalent parameter characterizing the splashing threshold is the so-called K-parameter introduced by Cossali et al. [17]

$$\mathrm{K} = \frac{\mathrm{We}}{\mathrm{Oh}^{0.4}}, \tag{1.13}$$

which depends on the relative film thickness and on surface roughness for very thin liquid films. A higher roughness affects the flow in the thin region in the vicinity of the surface, triggering the splash at lower impact velocities and therefore the splashing threshold decreases with increasing surface roughness.

In the initial moments of the impact at higher velocities the formation of a small-scale radial jet in the region of the neck between the drop and the liquid layer may be observed. This jetting results from squeezing the liquid of the oncoming drop and pushing it outward with the speed that can be an order of magnitude higher than the drop impact velocity. Another phenomenon observed in the initial moments of impact is the air encapsulation, pertinent also to drop collisions with

the dry substrate or in binary drop collisions. An air lens may be entrapped between the oncoming drop and the impacting target which evolves into a toroidal shape and finally leads to formation of one or several small air bubbles.

In impacts onto a dry surface the possible flow patterns are much more diverse. In experiments done by Rioboo et al. [91] several different outcomes were observed. In Fig. 1.2 six horizontal lines represent time sequences of the flow regimes after drop impact termed as deposition, prompt splash, corona splash, receding break-up, partial rebound and complete rebound, respectively.

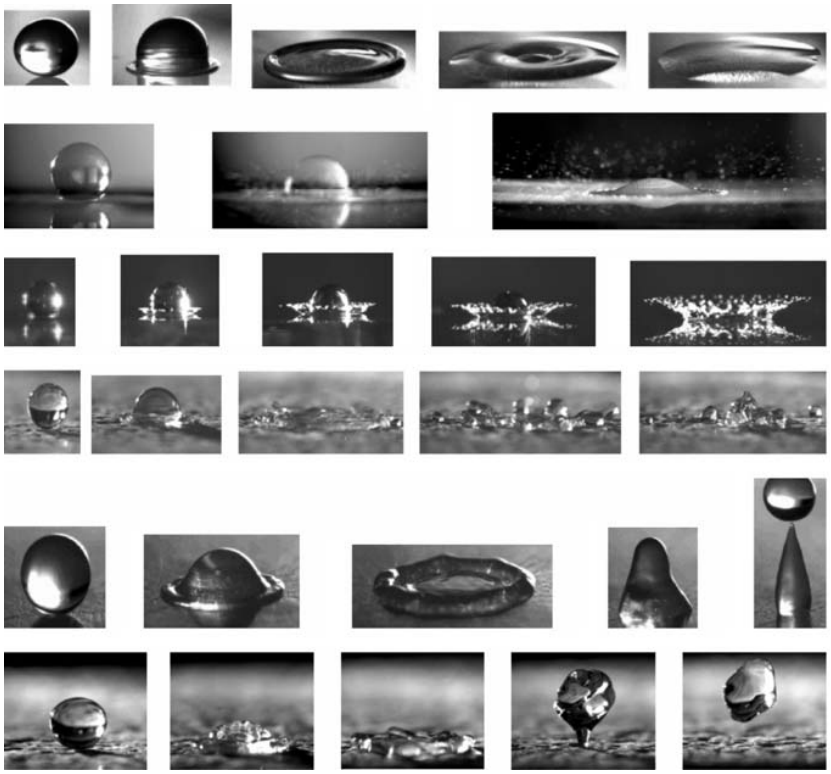

Figure 1.2: Drop impact onto a dry wall, from Rioboo et al. [91]

In the deposition regime the lamella stays spread over the surface. The spreading ratio is proportional to the square root of time in the initial phase, whereas the dependence on the liquid properties becomes pronounced only at later stages of the spreading. Prompt splash is characterized by higher impact velocities and increased surface roughness resulting in detachment of small-sized droplets from the edge of the spreading lamella. The lamella stays spread over the surface as in the previous case. If the surface tension is decreased, the lamella may detach from the wall and crown is formed similar to the drop impact onto a liquid layer. The resulting flow pattern is the corona splash and the formation of the crown is triggered by surface roughness.

An important issue in drop impact on a surface is the surface capillarity, represented by the contact angle which develops between the impacting dry surface and

the drop surface. In many industrial processes, speed and uniformity of wetting must be controlled in such manner that overrunning and entrainment of the fluid, commonly gas, being displaced by the advancing liquid must be avoided. In impacts at higher velocities, after the lamella has reached the maximum spreading ratio it begins to recede driven mainly by the surface tension and the surface wettability. According to the capability of a given surface to *hold* the drop, the surface is said to be hydrophilic (with a contact angle lower than 90°), or hydrophobic (with a contact angle higher than 90°). If the surface is hydrophobic with higher values of the contact angle, the receding break-up flow pattern develops. The value of the contact angle depends on numerous parameters, some of which are the capillary and Weber numbers, ratios of densities and viscosities of lighter and heavier fluids (gas and liquid), the speed of the contact line, the material and the state of the target surface (Šikalo et al. [107]). Moreover, the static contact angle is not single valued and depends on the history of the system. The value of the contact angle may differ according to whether the contact line was brought to rest by wetting or de-wetting, i.e. by advancing or receding of the liquid. This behavior is known as the contact angle hysteresis. Since even at very small distances from the contact line, the free surface may be sharply curved and measured contact angles depend on the length scales resolvable by experimental equipment, the measured contact angle is called the apparent contact angle.

During the spreading motion of the lamella, the initial kinetic energy of the impacting drop is partly dissipated due to viscosity and partly converted into the surface energy due to the increased free-surface area. The surface energy of the lamella at the beginning of the receding motion may be sufficiently large to produce the receding velocity of the lamella high enough to result in its collapse around the impact point and push the liquid upward in the form of a rising liquid column similar to the Worthington jet. The uprising jet may stay connected to the surface and eject one or more droplets, which is the partial rebound, or completely detach from the surface as in the complete rebound. Rioboo et al. [91] have found that the onset of the different flow regimes cannot be characterized solely with the dimensionless groups outlined in Section 1.2.1, indicating the importance of the wettability and surface roughness in drop impacts onto a dry wall.

In binary drop collisions the flow patterns are rather similar to those encountered in drop impact onto a dry wall. The experimental study of Willis and Orme [130] performed with binary drop collisions in vacuum revealed two characteristic flow regimes occurring after the collision, the sequence of which is depicted in Fig. 1.3. Those were termed the oblate (the left column in Fig. 1.3) and the prolate flow regime (the right column in Fig. 1.3).

The deformation of the drops after the collision in the oblate regime is characterized by stretching and formation of an extremely thin liquid sheet bounded by a rim at its edge. Similar to the drop impact onto a dry wall the kinetic energy of the colliding drops is lost into heat by viscous actions and simultaneously converted into the surface energy. After reaching the maximum spreading, the receding prolate motion begins driven by surface tension, in which the liquid sheet collapses forming

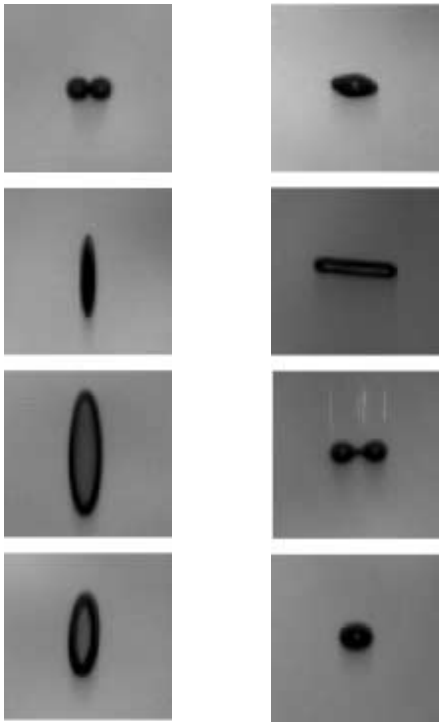

Figure 1.3: Normal binary drop collision, from Willis and Orme [130]

an almost spherical shape followed by a prolate elongation. Depending on the impact parameters, the separation of the liquid may occur in either regimes, referred to as the shattering collision, if it occurs during the oblate regime and the reflexive separation, if occurred within the prolate regime. It is interesting to note that the normal axisymmetric collision of two drops may be represented as the impact of a single drop onto a plane of symmetry, which is similar to the initial phase of the impact onto a dry wall if the viscous effects near the wall can be neglected.

1.3 Overview of Related Studies

Because of their practical and industrial relevance a great amount of work has been invested in studying drop impacts experimentally, theoretically and numerically in the past decades. It is not possible to give a detailed overview of the entire available research and achievements made. Therefore only selected investigations are presented that are considered to be the most interesting and relevant in the light of the present work. Mainly computational and some theoretical studies are reviewed and more comprehensive general reviews are provided by Rein [85] and Yarin [132].

1.3.1 Numerical Methods for Free-surface Flows

Due to the rapidly growing computer power, numerical methods have become attractive for simulations of flows with free surfaces within the branch of the Compu-

tational Fluid Dynamics (CFD). Even after more than three decades of work, the numerical simulations of free-surface flows still remained a great challenge for CFD, the main difficulties being the accurate time and space tracking of the free surface, the existence of high density ratios within the flow field and the accurate calculation of the surface tension forces.

Based on the methodology used to track or capture the free surface, two main approaches are available for a free-surface flow simulation:

- interface tracking (also referred to as surface or front tracking) and
- interface capturing (also called volume tracking).

The interface tracking methods are Lagrangian, employing a computational mesh that moves with the free surface and identifies it with the cell faces of the moving mesh. These methods consider the free surface as a boundary on which the kinematic and dynamic boundary conditions are applied (Ferziger and Perić [25]): the kinematic condition implies that no fluid flow is allowed through the free surface in the absence of phase change, whereas the dynamic condition requires the normal stresses to be balanced and the tangential stresses to be continuous across the interface. Commonly only the liquid flow is solved and the gas pressure from the surroundings is set as a boundary condition along the interface. Although these methods allow a sharp interface definition they encounter serious problems in cases when the interface undergoes large deformations where the moving mesh may become severely distorted, as depicted in Fig. 1.4.

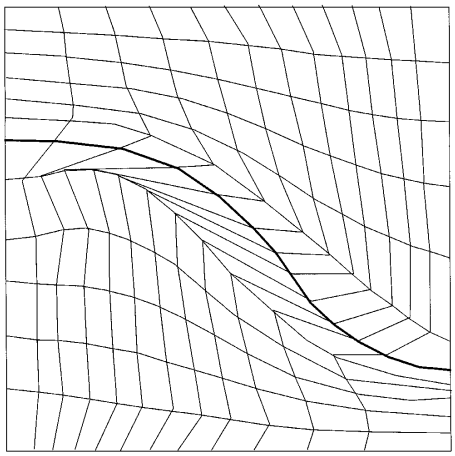

Figure 1.4: Mesh deformation in interface tracking, from Scardovelli and Zaleski [103].

Such situations are represented by breakup of thin liquid sheets or ejections of different-sized secondary droplets commonly observed in drop impacts. The numerical mesh has to respond correctly to the movement of the free surface and it is difficult to develop an algorithm that will be robust and general at the same

time, but it often requires a problem-specific procedure in cases with complicated geometries. The interface tracking methods are not considered in the present work.

The interface capturing methods, on the other hand, use an Eulerian mesh fixed in space, where the position and the movement of the free surface have to be captured by the solution algorithm itself. This can be achieved in three different ways:

- by tracking the seeded particles,
- by introducing a level-set function and
- by tracking fluid volumes using an indicator function.

The first approach is the Marker and Cell (MAC) method of Harlow and Welch [36], in which the space near the interface or the entire space of the mesh representing one phase is seeded with massless tracer particles which follow the local flow field, as shown in Fig. 1.5. Although this method allows a subgrid interface capturing, it is not suitable for flows with large density ratios since the subgrid velocity and pressure scales may not be resolved.

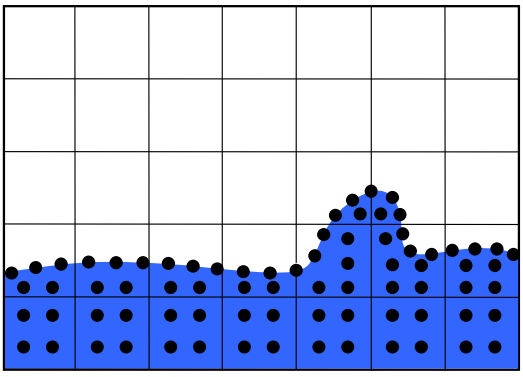

Figure 1.5: An illustration of the MAC method.

The second is the level-set (LS) method of Osher and Sethian [71], in which a continuous function is initialized throughout the computational domain as a signed distance from the interface, positive in one phase and negative in the other, with the contour of zero (zero level) representing the free surface, Fig. 1.6. The movement of the interface is captured by solving the transport equation for the level-set function. However, since this transport equation does not represent a conservation law (because the level-set function is not a physical quantity), the method is not mass conservative and requires re-initialization procedures in every time step to control the artificial mass sources or sinks.

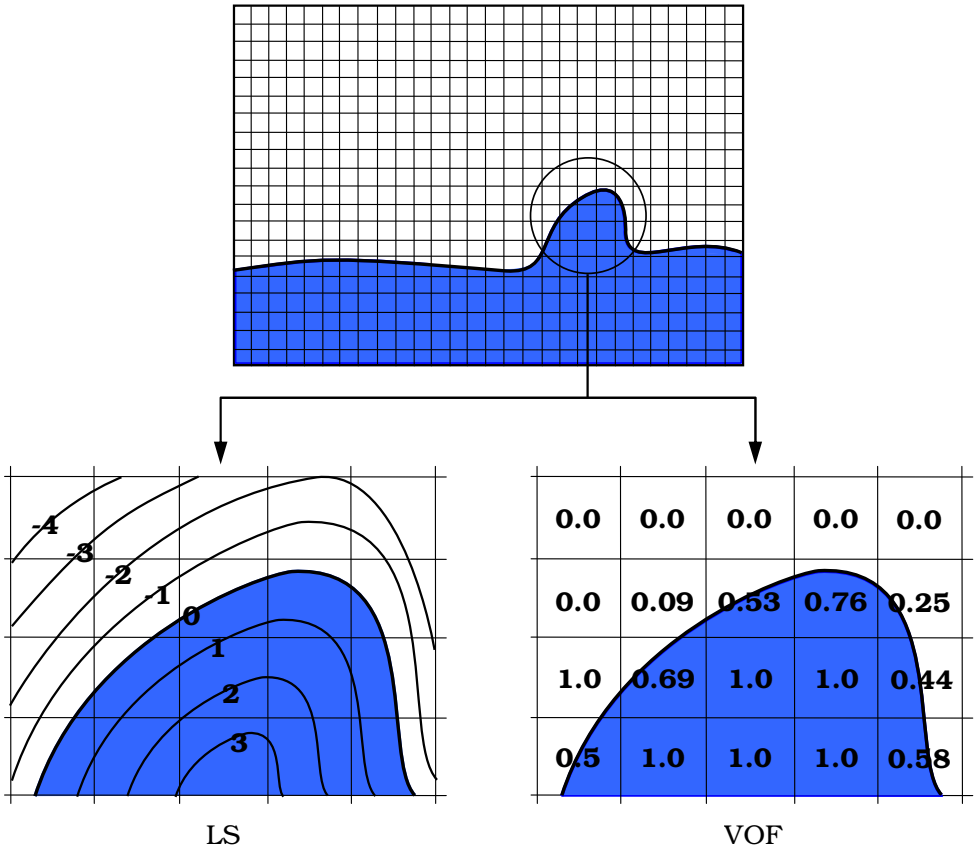

Figure 1.6: Illustrations of the LS and VOF methods.

The most widely used interface capturing algorithms belong to the third category, the volume-of-fluid (VOF) method, firstly proposed by Hirt and Nichols [40]. These methods introduce an indicator function to track the volumes of different fluids by solving a transport equation for the indicator function. The values for the indicator function are uniform and different, commonly zero and one, associated with a particular phase and varying discontinuously across the phase-interface, Fig. 1.6. The physical volume fraction or phase fraction of one phase is commonly used as the indicator function. In the early numerical studies, including Hirt and Nichols [40], the function is used to indicate cells filled with fluid and cells not containing any fluid (empty cells), whereby only one phase is captured (liquid) while the presence of the other phase (gas) is neglected. Only in recent years computational models were developed that include both phases, some of which are mentioned below.

From the point of view of the finite-volume numerical method to be used in the present work, one of the major difficulties in the VOF method is ensuring the transport of sharply defined interfaces without artificial numerical diffusion or dispersion. The distribution of the phase fraction is such that the contour of the free surface is not uniquely defined, but it is commonly smeared over a few mesh cells. Here one can distinguish between the geometrical interface-reconstructing methods

and methods based on algebraically formulated differencing schemes without interface reconstruction. The geometric methods consist of two basic steps in solving the phase fraction transport equation, namely the explicit interface reconstruction followed by the advection algorithm (Rider and Kothe [89]). These methods are developed mainly for two-dimensional geometries where the interface is represented as a series of piecewise straight line segments. The problem reduces to finding the corresponding normal vector to the interface using the known distribution of the phase fraction and reconstructing a straight line that exactly matches the computed phase fraction values in each interface-containing cell. Several such models were proposed, the most common being the Simple Line Interface Calculation (SLIC), where the interface is reconstructed as a series of lines aligned to the mesh, and the Piecewise Linear Interface Calculation (PLIC), which reconstructs the interface as a series of linear function segments passing either through the cells or through the cell-faces containing the interface, Fig. 1.7. A review of the geometric interface-reconstruction methods is given by Rider and Kothe [89]. Once the interface is reconstructed, it is advected by the underlying flow field using the operator split procedure, i.e. the phase fractions are advected along the coordinate directions in subsequent separate one-dimensional steps.

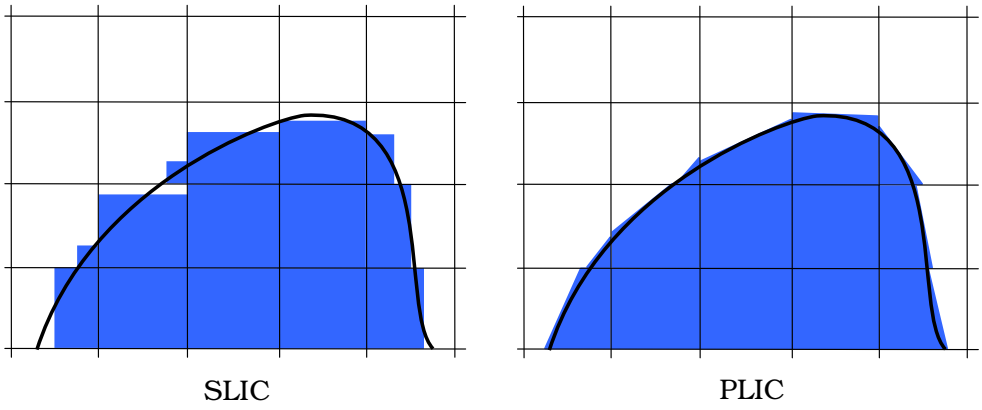

Figure 1.7: Representations of the free-surface in the SLIC and PLIC geometric reconstruction.

The SLIC and PLIC methods do not reconstruct the interface as a series of connected line segments. This leads to the formation of either isolated, subgrid-sized, separated fluid bodies or disconnected free surfaces. For this reason, in addition to the above mentioned reconstruction techniques, more recently a lot of efforts is devoted to developing more accurate interface calculation procedures. Rudman [99] presented a direction-split interface capturing algorithm based on the flux-corrected transport without explicit interface reconstruction. The idea is to determine intermediate values for the phase fraction by using a diffusive low-order scheme and correct them by applying higher-order anti-diffusive fluxes. Scardovelli and Zaleski [102] used quadratic least-square fit to approximate the interface as a portion of a circle

and proposed a mixed Eulerian implicit-Lagrangian explicit advection algorithm. The method was extended to three-dimensions by Aulisa et al. [3]. López et al. [56] introduced an interface reconstruction method based on spline interpolation. The orientation of the segments representing the interface is re-adjusted using a cubic spline interpolation through the segments' center points. Pilliod and Puckett [78] presented a least-squares interface reconstruction algorithm with multidimensional advection. The reconstruction algorithm is based on minimizing the error between the computed phase fractions and their linear-segment approximations.

Contrary to the geometric reconstruction algorithms, the VOF method has a notable feature that the volume fluxes can be formulated algebraically, without explicit interface reconstruction, by using the so-called High Resolution Differencing Schemes. This approach is rather beneficial since the schemes with geometric reconstruction use operator splitting (separate one-dimensional advection steps), thus making the advected volume fluxes dependent on which order of coordinate directions is used for the advection. Although the VOF method is generally conservative by definition, errors in mass conservation may arise in the direction-split geometric interface reconstruction methods, where the fluxes along one coordinate are computed first and the phase fraction values are updated to an intermediate level, followed by the same procedure for the other coordinate. The mass conservation errors come from adding these fluxes which may lead to inconsistent phase fraction field (Ubbink and Isa [115]). In addition, the implementation of such algorithms on arbitrary unstructured meshes is rather difficult. The problem in algebraically formulated schemes represents the proper convection flux evaluation at cell-faces, requiring a differencing scheme which preserves boundedness and prevents smearing of the sharp interfaces, but the computationally rather expensive explicit interface reconstruction can be avoided. The requirements to be satisfied are rather contradictory: while higher-order schemes result in unbounded solution, the first-order upwind differencing (UD) scheme is bounded but produces an unacceptable amount of numerical diffusion and the first-order downwind differencing (DD) scheme yields too much negative numerical diffusion and tends to artificially wrinkle and steepen the interface (Hirt and Nichols [40], Ubbink and Issa [115]). As discussed by Rudman [99] an algebraic interface capturing algorithm may be designed by a suitable combination of the UD and DD schemes. Such combined schemes are commonly refereed to as *compressive* schemes to indicate their ability to sharpen smeared profiles.

The firstly proposed VOF method of Hirt and Nichols [40] represents basically a compressive scheme with the donor-acceptor formulation for the approximation of fluxes to be advected through cell-faces and it reconstructs the interface as piecewise constant line segments aligned with the mesh. Switching between the UD (donor cell) and the DD (acceptor cell) is done according to the angle between the interface and the direction of motion, UD being used when the interface is more tangentially oriented to the flow and DD in the opposed case. It was indicated that the method does not preserve local boundedness and therefore local ad-hoc corrections of the computed phase fraction values are required.

The Compressive Interface Capturing Scheme for Arbitrary Meshes (CICSAM)

of Ubbink and Issa [115] is based on the concept of the Normalized Variable Diagram (NVD) and makes use of the Convection Boundedness Criterion (CBC) of Gaskell and Lau [29]. The scheme combines the Ultimate Quickest (UQ) scheme and the upper bound of the CBC (Leonard [54]). The non-linear weighting factor is determined based on the orientation of the interface relative to the mesh, such that CBC is applied where UQ fails to maintain the interface sharpness and vice versa. The operator splitting problem is overcome by advecting the phase fraction in one step in all directions using averages of separate sweeps and a predictor-corrector solution procedure to remove eventual non-physical values.

A similar approach was adopted by Muzaferija and Perić [62] in their High Resolution Interface Capturing (HRIC) scheme. The normalized cell-face value is calculated from a scheme combining the UD and DD schemes. Then the estimated normalized cell-face value is corrected according to the orientation of the free surface relative to the cell-face and the local Courant number. The final cell-face value is calculated as blended between the upstream and the downstream cell-center values with the normalized cell-face value used as the blending factor.

A comparison of the performance of CICSAM and HRIC schemes was made by Waclawczyk and Koronowicz [123] using the common test cases of rotation of a slotted body and sloshing in an oscillating tank. It was shown that CICSAM preserves a sharper defined interface with less smearing and produces more accurate results. However, the CICSAM scheme becomes problematic in cases with very low bulk velocity, such as stagnation points. The free surface receives not enough compression from the numerical scheme and deforms non-physically. This was shown by Ubbink [116] in the simulation of a rising bubble, where the free surface at the bottom of the bubble was severely deformed at some time instant.

As already mentioned, the calculation of the surface tension forces is one of the problems in simulations of flows with free surfaces. An ideal implementation would impose the surface tension force as a discontinuous local source acting across the free surface. However, this is not possible within the framework of the finite-volume method, since it would impose infinite gradients across the free surface. Several models were proposed to overcome this difficulty, but the most commonly used are the Continuum Surface Force (CSF) model of Brackbill et al. [10] and its subsequent variant called Continuum Surface Stress (CSS) model of Lafaurie et al. [52]. Both models include some smoothing of the theoretically ideally sharp interface to enable calculation of gradients and are suitable for the implementation as volumetric sources within the finite-volume framework, rather than discontinuities. In a recent study conducted by Gerlach et al. [31] the capabilities of three different interface capturing methods with differently implemented surface tension force were presented. Compared were the Least-square Volume-of-fluid Interface Reconstruction Algorithm (LVIRA) of Pucket et al. [81], the Parabolic Reconstruction Of Surface Tension (PROST) model of Renardy and Renardy [88] and a Combined Level-Set and Volume-Of-Fluid method (CLSVOF). The surface tension force in LVIRA is evaluated as smoothed over the interface using a radially symmetric smoothing kernel, PROST uses the interface normal to the reconstructed parabolic interface segments and CLSVOF a smoothed Heaviside step function to evaluate

the curvature needed in the evaluation of the surface tension force. As expected, the results showed the higher accuracy of the PROST method due to higher-order representation of the interface, but on the other hand, the geometric reconstruction here requires much more intensive computer efforts. The smoothed kernel method was shown to be the most weak of the compared methods.

One of the well-known problems associated with the implementation of the surface tension force as a continuous volumetric force is the occurrence of the so-called parasitic currents. These artificial velocities may lead to non-physical instabilities of the interface in conditions of flows with high density ratios and high surface tension effects (capillary driven flows). Such situation is highlighted in Fig. 1.8 from Harvie et al. [37], where the artificial velocities obtained in the simulation of a stationary two-dimensional drop are shown. In an ideal VOF model, in the absence of fluid motion the surface tension force would be exactly balanced by the pressure gradient across a curved surface, say of a stationary drop or a bubble. However, as discussed by Harvie et al. [37], this is not the case in a real VOF simulation, where numerical errors are introduced when the phase fraction equation is integrated over the finite dimensions of the computational mesh cells. The errors, although small in a case of a converging simulation, result in the normal vector not being determined as precisely perpendicular to the interface, which in turn leads to inaccuracies in the calculation of the surface curvature and the weighted physical properties at the interface.

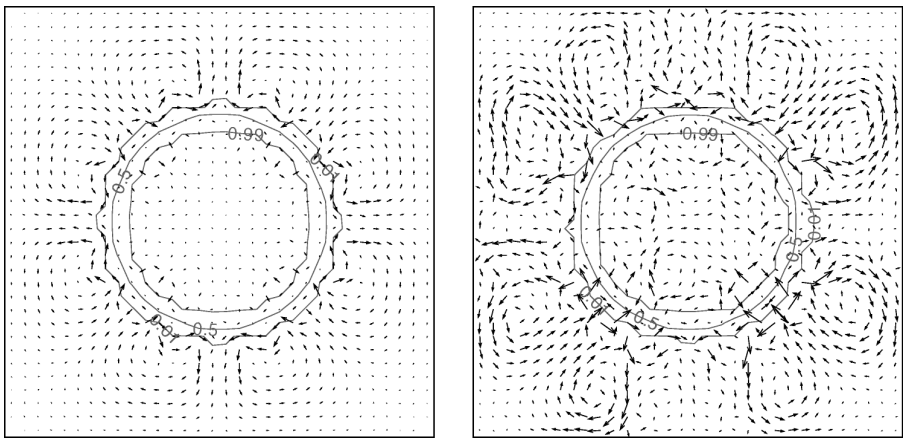

Figure 1.8: Parasitic currents at a stationary planar drop, Ca $\sim 10^{-4}$ (left) and Ca $\sim 10^{-5}$ (right), from Harvie et al. [37].

Thus, even for a stationary drop or a bubble, a small rotational component of the surface tension force is artificially generated, that cannot be balanced by the irrotational pressure gradient alone, but must instead be balanced by one or more of the velocity dependent terms in the momentum equation. Once generated, the parasitic currents will not disappear in a simulation. They will accordingly lead to inaccuracies in the calculation of the pressure and may even cause a failure of convergence on mesh refinement (Harvie et al. [37], Tong et al. [113]).

Based on dimensional analysis, Lafaurie et al. [52] suggested that the magnitude of these velocities scale as the inverse of the capillary number, i.e. $\overline{U}_p = K_p \mathrm{Ca}^{-1}$, where the numerical experiments have shown that the proportionality constant is $K_p \sim 10^{-2}$ for their implementation of the surface tension force. Tong at el. [113] presented an implementation algorithm for the surface tension force as a pressure gradient rather than a volumetric force in the CLSVOF scheme. The algorithm was tested in two-dimensional simulations where it produced lower parasitic currents compared to simulations with the CSF model. However this algorithm is more computationally demanding since it requires two iteration cycles for pressure in every time step. Harvie et al. [37] proposed a scaling for the estimation of the magnitude of the parasitic currents based on the order-of-magnitude analysis of the terms in the momentum equation. According to this scaling, the parasitic currents are limited by the viscous term in flows with low inertial effects where the scaling reduces to the same as the one of Lafaurie et al. [52], and they are limited by the convection term in flows with higher velocities, decreasing as the Weber number increases for a fine enough mesh. Francois et al. [26] reconstructed temporary distance functions from computed phase fractions as accumulated normal distances from the piecewise linear interface segments. The reconstructed distances were used to impose the surface tension-induced pressure jump. However, the procedure was tested and the results were compared with the CSF model only in a simple case of an equilibrium drop. As expected the CFS model yielded a somewhat smoother interfacial transition, but both methods produced the parasitic velocities of the same order of magnitude.

Finally, in addition to the interface tracking and capturing methods, worth mentioning are the lattice-Boltzmann models that recently gained attention in free-surface flow simulations (Mukherjee and Abraham [60]). In such models the fluid flow is modeled by movement of particles, each having mass and momentum corresponding to the fluid at given locations. The particles move along lattices and are allowed to collide according to predefined collision rules, thus providing a representation of the macroscopic fluid flow based on a microscopic molecular approach.

All the mentioned approaches are aimed at solving the transport equations describing the fluid flow directly, without turbulence modeling. The methods are commonly applied to simulate flow of a single, or at most two drops, due to the high required space and time resolutions in order to resolve all the small scales of the motion of the free surface. Therefore the flow is generally solved using two-dimensional axisymmetric geometries, although there are no limitations, at least conceptually, for incorporating turbulence models. Recently one such study was performed by Watanabe et al. [124] by coupling the large eddy simulation (LES) with the level-set method to simulate vortex rings forming in the underlying deep pool after normal and oblique drop impacts. However, the validity of such approaches is not within the scope of the present work and focus is given here to numerical simulations of laminar flows.

According to the above mentioned and despite of some of the addressed deficiencies, the VOF method is considered to be most suitable for simulation of free-surface flows. The advantages rendering the method more powerful compared to the others are:

- the method is conservative by its definition (as opposed to the level-set method),
- it is robust and relatively easy to implement using the algebraic formulation,
- it is capable of handling large interface deformations and small-scale interface topologies such as breakup and reconnection (as opposed to front tracking),
- it is local in the sense that only neighboring values are required to update the phase fraction in a computational cell,
- it may be used for flows with more than two fluids creating more than one fluid-fluid interface and
- it can be extended to there dimensions and applied to arbitrary unstructured meshes within the framework of the finite-volume numerical method (using the algebraic formulation instead of the explicit interface reconstruction).

Due to the aforementioned reasons the VOF methodology has in a certain way become a standard in the simulation of flow with free surfaces and is presently available in the widely used commercial CFD software. Therefore, the interface capturing procedure based on the VOF method is used in the present study.

1.3.2 Nonisothermal Drop Collisions

A computational study of drop impact on thin liquid film with an analysis of vorticity, velocity and pressure fields was reported by Gueyffier and Zaleski [35]. Calculations were performed on a MAC mesh using a VOF-based method with the PLIC method. Pressure fields obtained in simulations show a high-pressure region just after the impact at the contact line between the impacting drop and the liquid film. Computed fluid velocities at the beginning of the impact were several times larger than the drop impact velocity and high vorticities were resolved in the region of the rim formed on the top of the crown.

Oğuz and Prosperetti [67] performed numerical simulations of the interface dynamics using the boundary-integral method and treating the impact of drops on liquid surfaces as a potential flow. The obtained results suggested that in a certain range of impact parameters an air bubble is entrapped because the crater bottom has a larger downward momentum than its sides and the buoyancy may not reverse the motion of the crater bottom before the crater sidewalls collapse.

The evolution of the crown occurring during drop splashing on a shallow liquid film was numerically computed by Rieber and Frohn [90] using a VOF-based method on a MAC mesh. In the simulations disturbances on the liquid film surface were initialized using Gaussian distribution in order to initiate and resolve instabilities of the rim on top of the crown leading to creation and ejection of secondary droplets.

A theoretical and numerical investigation of droplet splashing on a thin liquid film was conducted by Josserand and Zaleski [46]. Numerical simulations based on the VOF model with the PLIC calculation of the free surface were used. They proposed a theory for prediction of the transition between splashing and deposition,

based on the assumption that the width of the ejected liquid jet upon the impact is controlled by an introduced viscous length scale.

Nikolopoulos et al. [64] computed drop impact onto a wall film using a VOF-based model with the adaptive mesh refinement. The numerical model was capable of predicting splash, crown dynamics and formation and detachment of secondary droplets. The artificial disturbances in the underlying liquid surface (as in Rieber and Frohn [90]) were not applied in order to numerically resolve the details of splash. Instead of it, the drop was initialized at a higher distance above the surface, thus allowing the shape of the drop to deviate from spherical and small perturbations of the liquid layer to be created by the interaction of the drop with the surrounding air before the impact.

Morton et al. [59] applied a model based on the VOF method in their numerical simulations of drop impact onto a deep pool. The model neglects the presence of air, tracking only the liquid, and the surface tension force is treated as continuous rather than as an imposed boundary condition. Although the mesh was rather fine in simulations and air flow was not accounted for, a small closed cavity free of fluid interpreted as an entrapped bubble was resolved at the symmetry axis when the crater was collapsing.

A theoretical analysis, supported by experimental investigation of single water and propanol drops impacting onto a liquid layer at high Reynolds numbers was conducted by Roisman et al. [98]. They derived an analytical solution for the crater propagation speed in the same form as the asymptotic solution of Yarin and Weiss [135] by applying a quasi-stationary Bernoulli equation to the propagation direction. The obtained solution is used to estimate the time to reach and the value of the maximum crater diameter.

Dai and Schmidt [18] simulated numerically a head-on collision of two equal-size droplets using a moving mesh algorithm without explicit interface reconstruction. The results of the simulations confirmed the observations and analysis of Willis and Orme [130] that the dissipated energy and the maximum deformation depends on Reynolds number, the dependency becoming negligible at high Reynolds numbers.

A level-set method was used by Pan and Suga [73] to simulate the binary drop collision. The bouncing regime and formation of satellite droplets were captured well in simulations, whereas the numerics was not able to correctly predict the secondary coalescence collision occurring at lower Weber numbers.

A head-on collision dynamics of two impinging droplets was investigated by Pan et al. [72]. Numerical computations were performed using a front tracking method on a stationary mesh with explicitly representing the interface by a separate, unstructured mesh that moves through the stationary mesh. The analysis of the estimated energy budgets showed a negligible energy dissipation in the gaseous phase.

Nikolopoulos et al. [63] simulated numerically a central collision of two equally sized hydrocarbon droplets at various Reynolds and Weber numbers using an extended VOF method with two indicator functions, one associated with each droplet, and utilizing adaptive local mesh refinement. They showed that the droplet kinetic energy is initially converted to surface energy upon collision, while at later stages

the opposite occurs, and that energy losses are mainly due to viscous dissipation in the liquid phase. In a subsequent study Nikolopoulos et al. [66] computed flow arising from the off-center binary collision of equally sized drops. The simulations were capable of predicting flow details such as air bubble entrapment and satellite droplet formation.

Gotaas et al. [34] investigated experimentally and numerically the effects of viscosity on droplet-droplet collision. Various liquids were used in experiments providing a wide range of viscosities and Weber numbers. Numerical computations were performed using a VOF-based model. The model for the onset of separation due to Qian and Law [82] implying a linear dependence between the Ohnesorge and Weber numbers was proved to be valid only for small Ohnesorge numbers.

Roisman [96] investigated theoretically the unsteady viscous flow in a spreading liquid film at high Weber and Reynolds numbers. He derived an analytical self-similar solution for the flow in the spreading drop which also satisfies full Navier-Stokes equations. The boundary layer thickness was shown to consist of the inviscid part, predicted by the remote asymptotic solution of Yarin and Weiss [135] and an increment resulting from viscous effects, the latter becoming significant at larger times of spreading and small lamella thicknesses.

Bussmann et al. [12] computed droplet impact on an inclined wall and on a sharp solid edge using the VOF model. Surface tension force was evaluated as a smoothed step profile. Dynamic contact angles obtained in experiments were set as boundary conditions and the model predicted accurately the fluid deformation during the impact. In a subsequent study Bussmann et al. [11] simulated numerically the fingering and splashing of molten tin, water and heptane droplets impacting a solid surface. They applied a perturbation in a combined exponential and trigonometric form to the radial component of the velocity near the solid surface at a small time after the moment of impact.

Afkhami and Bussmann [1] applied height functions for calculations of interface normals and curvatures in the framework of a VOF-based model with PLIC technique. The height functions are calculated by summing phase fractions in a stencil of cells around each cell containing the interface. The procedure was tested in the simple surface tension driven flow representing movement of a sessile drop exposed to a sudden change in the specified contact angle.

Šikalo et al. [107] performed numerical simulations of drop impact on a horizontal wall. The dynamic contact angle was accounted for in the simulations by applying the empirical correlation due to Kistler [49]. The experiments from the studies of the same authors were numerically simulated by Lunkad et al. [57] who applied a model based on the VOF method using both static and dynamic contact angles. They showed that the model with the constant contact angle predicts the flow well for less wettable horizontal surfaces, whereas it fails to correctly predict the liquid deformation and rebound in the case of inclined impacts.

Numerical investigation of the normal impact of a water/glycerin drop on solid dry flat and rough surfaces were conducted by Geldorp et al. [30]. The computational model utilized the VOF-based method with the HRIC scheme. A good agreement with the experimental results was obtained during the spreading phase, but the in

the receding phase the computed maximum values of the spreading ratio were lower. The simulation predicted a perturbation of the tip of the spreading lamella on the rough surface, an effect that enhances prompt splash.

Pasandideh-Fard et al. [75] studied experimentally and numerically the influence of surface tension and contact angle on the impact dynamics of water droplet falling onto a dry stainless steel surface. The free-surface flow was computed using the MAC technique neglecting the presence of air and the Laplace surface pressure was imposed as a boundary condition at the free surface. In their experiments a single bubble is observed in the drop at the point of impact that could not be resolved in the simulation. They extended the energy conservation model of Chandra and Avedisian [14] and estimated the viscous dissipation using the boundary layer thickness instead of the proposed lamella thickness.

Mehdi-Nejad et al. [58] computed impacts of drops of different liquids on a dry solid surface. Their simulations, based on the VOF model, resolved air bubbles entrapped at the solid surface under the impacting drop. The bubbles were created due to the increased air pressure beneath the falling drop which caused flattening of the drop surface and enabled a closed region filled with air to be formed. The bubble remained attached to the wall for liquids with higher contact angles, whereas they moved upward and escaped through the free surface for liquids with lower contact angles.

Fukai et al. [28] used a numerical model utilizing a deforming finite-element mesh to simulate deformation of molten tin and water droplets impinging upon a flat surface. Their study showed that the initial rate of change of the lamella height is proportional to the droplet impact velocity. As expected, the maximum radius of the lamella decreased with increasing the value of the dynamic contact angle in the spreading stage and the effects of the impact velocity on droplet spreading were more pronounced.

1.3.3 Drop Impact on a Heated Wall

Di Marco et al. [21] investigated thermal behavior of a water droplet gently deposited on a heated surface in a range of surface temperatures. They compared the performance of two models, namely the coupled model for fluid flow and simultaneous heat transfer in the droplet and the wall, and the decoupled model with a constant heat flux imposed as a boundary condition at the fluid-solid interface. The constant heat flux model failed to capture the transient behavior correctly even in the relatively slow flow with low inertia.

Chandra and Avedisian [14] studied collisions of n-heptane droplets with a dry stainless steel surface and with a liquid film created by deposition of prior droplets in a wide range of temperatures. At lower temperatures the creation of a single bubble was observed at the impact point, whereas at higher temperatures a population of bubbles was formed due to activation of nucleation sites on the surface. The droplet spreading and shape were shown to be unaffected by the presence of the bubbles.

Nikolopoulos et al. [65] computed flow and evaporation of n-heptane and water droplets during normal impingement onto a hot surface. An evaporation model

predicting the vapor creation during the impact was coupled with the VOF procedure for interface capturing utilizing an adaptive local mesh refinement and applied in simulations with different temperature ranges, below and above the Leidenfrost temperature.

Bhardwaj and Attinger [9] used a finite-element model with a Lagrangian free-surface tracking scheme to study dynamics of wetting during the impact of water drop on a silica substrate under isothermal and nonisothermal conditions. The main finding was that the drops at elevated temperatures spread more than cold drops due to reduction of viscosity and not because of the increase of wetting.

Selvam et al. [104] studied spray cooling by simulating vapor bubble growth within a thin liquid layer, followed by a subsequent impact of a liquid drop onto the layer. Level-set method was used to capture the movement of the free surface. The mechanism of enhanced spray cooling was explained by high heat fluxes obtained during a short period of transient heat conduction when the vapor bubble breaks due to drop impact and the liquid spreads over the dry hot surface.

Pasandideh-Fard et al. [74] investigated experimentally and numerically, based on the VOF model, the impact of a water drop on a heated steel surface in a temperature range avoiding boiling flow regime. Increasing the impact velocity did not enhance the heat flux from the substrate significantly. They developed a simplified theoretical model for heat transfer into the drop, based on one-dimensional conduction across the boundary layer and estimated the cooling effectiveness of the spreading drop, predicting the dependance of the cooling effectiveness on Weber number only, if Reynolds number is high enough.

Healy et al. [39] applied level-set method to compute the flow and heat transfer without boiling during spreading of a water droplet impacting on aluminium and glass surfaces. The results showed that even if the amount of heat transfer during the initial spreading period can be relatively low compared to heat transfer due to phase change, the temperature rise in the liquid may cause changes in thermophysical properties leading to a significant increase in spreading ratio. They indicated that neglecting heat transfer in the spreading stage of motion, as commonly done in modeling spray impact, may therefore lead to erroneous initial conditions for the subsequent analysis of the evaporation process.

Strotos et al. [109] used a VOF-based method in the numerical simulation of flow and heat transfer under same conditions as Pasandideh-Fard et al. [74], but allowing for phase change due to drop evaporation. The results of simulations indicated that during the initial spreading stage the impact velocity has only small influence on the cooling effectiveness and that the effects of the phase change process are more important not during the initial stages of the impact but during the receding phase.

More recently the results of investigations of heat transfer during water droplet impact onto a dry epoxy target and onto a shallow water pool were reported by Vu et al. [122]. They divided heat transfer from the dry surface into a convective phase in which the droplet is initially spreading or penetrating into the water pool and a conductive phase where the droplet becomes stagnant while still cooling the surface. The rate of heat transfer from the wall was significantly reduced in the presence of the shallow liquid pool.

1.3.4 Drop Impact on a Porous Substrate

A theoretical model describing the spreading and absorbtion of a liquid drop on porous surfaces was proposed by Clarke et al. [16]. The porous substrate was assumed to be filled vertically without radial flow within it and the filling at a particular radius started after the contact line reached that radius. The model was experimentally verified for a range of porous membranes relevant to drop impact in ink-jet printing.

Kumar and Deshpande [51] observed drops of silicon oil and alcohol-water solution spreading on heterogeneous and anisotropic fibrous porous media. The volume of the drop absorbed in the porous material was found to increase with square root of time for silicon oil, but it increased linearly with time for alcohol-water solution. They divided the spreading process into two distinguishable stages: the first stage, in which the contact radius on the surface increases to its maximum, and the second stage, where the contact radius shrinks and the drop disappears. For drops of alcohol-water solution an intermediate stage could also be observed, in which the contact radius remains relatively constant over a period of time.

Seveno et al. [105] developed a theoretical model for spreading in a single pore and validated it using a molecular dynamics (MD) simulation. The drop placed initially on a porous surface was assumed to retain the shape of an ideal spherical cap during time and the instantaneous configuration of the spreading drop was determined by the contact radius and the dynamic contact angle. Generalization to the case of multiple pores, based on the assumption that the number of pores is proportional to the contact area between the drop and the solid, enabled the time for the complete absorbtion and the maximum contact radius to be computed.

Hsu and Ashgriz [41] computed the impact and penetration of a droplet in a radial capillary modeled as a two-plate gap with an orifice in the upper plate to allow the liquid penetration. The numerical model, based on the VOF method was used for the simulation. The presence of air was neglected and the surface-tension-induced pressure jump was applied as a boundary condition across the free surface. The simulations were carried out using prescribed constant values for the contact angle. For the used configuration a limiting value for the contact angle was obtained above which the capillary penetration was impossible.

Golpayan et al. [33] recently used the numerical model of Hsu and Ashgriz [41] to study drop spreading and penetration in a porous medium. The porous substrate was utilized as a stack of perforated plates placed on top of each other in a staggered arrangement. These internal obstacles were numerically treated by introducing an additional phase fraction for the solid with the cells containing the solid characterized by infinite density and zero velocity. The general finding was that the liquid spreading within and the penetration into the porous medium is governed by Weber and Reynolds numbers, respectively.

Reis et al. [86] performed numerical simulations of drop impact onto a porous medium using a VOF-based computational model with MAC particles, coupling the external flow to the flow in the porous substrate. In solving the flow within the porous medium viscous and inertial drag resistances were included. The presence

of air was neglected, the pressure at the free surface outside the porous medium was calculated using the mean curvature and surface tension coefficient and inside the porous medium the pressure is set as the capillary pressure of a fully saturated medium. The impacting drops were considered to be perfectly wetting the impacting surface.

More recently Reis et al. [87] used their computational model and conducted a parametric study of drop impact on porous surfaces to obtain a detailed information about the dynamics of the flow during the impact and the absorption. As expected the main influence of the Weber number is related to the capillary action, but the effects of the Reynolds number were found to be important in both outside and inside the porous region. Interestingly, in the case of a hydrophilic surface neither the penetration depth nor the spreading ratio showed dependence on the contact angle for a range of values and the obtained results were almost identical as in the case of the completely wetting surface.

1.3.5 Summary

Following the current state-of-the-art there are definite gaps in understanding of flows related to drop impacts and in the existing numerical methods. The VOF-based methods lead to artificially smeared interfaces requiring special care in simulations. Strategies for suppressing numerical diffusion must be applied improving predictive capabilities of numerical codes, thus allowing to investigate drop impact. The existing experimental methods are not able to extract all features of a drop impact. For example, it is impossible to measure the thickness of the lamella obscured by a rim formed at its edge. It is also not possible to accurately measure the crown thickness upon a splash. It is very difficult to measure temperature distributions in a spreading drop or to observe the drop penetration into a porous medium. These are the reasons why, in order to better understand the physics of drop impacts, one cannot rely only upon experimental research and numerical simulations are required.

1.4 Objectives of the Study and Thesis Outline

The main subjects of the present study are the computational and the accompanying theoretical investigations of flow induced by single-drop impacts. The objective is to assess the capabilities of the computational procedure for interface capturing based on the VOF-method and to improve the overall understanding of the underlying physical mechanisms. The following characteristic flows pertinent to spray impingement are identified, computed and analyzed:

- drop collisions, comprising collision with a shallow liquid layer, binary drop collision, and collision with a dry wall,
- drop impact onto a heated wall with the simultaneous heat transfer in the wall and
- drop impact onto a porous substrate.

All the flows studied are treated as laminar, although this might eventually represent an approximation for some of the configurations. The numerical code used is appropriately extended to account for the advancing and receding contact angles, the nonisothermal free-surface flow and simultaneous heat transfer in the solid and for fluid penetration in the porous substrate.

The formation and evolution of the crater formed upon the drop impact on a liquid layer are investigated. Based on the results obtained by numerical simulations, the crater penetration and the formation of the residual liquid film on the substrate are theoretically described. The investigation of the flow generated by normal drop collision with a rigid substrate or by collision with another drop enables the dynamics of the expansion of the spreading lamella to be described. The existing results, commonly based on the energy balance approach, are examined. The early stages of the drop initial deformation and spreading are computed numerically providing the database of results required for the theoretical modeling which are presently not available in the literature. Modeling the complicated wall effects is avoided in the simulation of binary drop collision.

Drop impact onto a heated wall is examined with respect to the developing temperature distribution in the spreading lamella and simultaneously in the wall. Coupled numerical simulations of the nonisothermal free-surface flow above and the conjugate heat transfer in the wall are performed, utilizing temperature-dependent thermophysical properties. The numerical simulation enables the temporal distributions of the wall temperature and the removed heat flux to be determined.

Drop impact on a porous substrate is computed using two approaches. In the first approach, the computational model for interface capturing is extended and the combined model is formulated including both the external flow for the spreading and the flow of the absorbed fluid in the porous substrate. In the second approach, drop spreading on the porous surface is numerically simulated by computing only the external flow generated by the drop impact and the existence of the porous surface is accounted for by formulating an appropriate boundary condition for the permeable wall. The capabilities of both approaches are analyzed.

In the introductory part, Chapter 1, a short background in drop and spray impact is given outlining some of the important perspectives which were the basic motivation for this work. The main phenomenological aspects of the flow are delineated and main computational strategies for free-surface flows are revised. A brief overview of some of the previously published research related to the present study is given.

In Chapter 2 the numerical code and the computational procedure relying on the finite-volume method are described.

The subsequent chapters comprise the analysis and results of the studied flow configurations. The computational models are validated using the common test cases from the existing literature. The governing equations and the main considerations for the specific flow are given, followed by the presentation of the results obtained by the numerical simulations and the theoretical models. Chapter 3 presents the investigation of the flow generated by drop collisions, including collision with a shallow liquid layer, binary drop collision and collision with a dry wall. In Chapter 4

the results of the investigation of the nonisothermal drop impact onto a dry heated wall with the simultaneous heat transfer within the wall are presented. Chapter 5 deals with the investigation of drop spreading on and absorbtion in the porous substrate.

General conclusions are presented in Chapter 6 with the accompanying recommendations for future work.

2 Computational Procedure

In this Chapter the numerical code used for the simulation is briefly described and the basic discretization techniques applied in the framework of the finite-volume numerical method are outlined. The discretization practice and the solution technique are applied to the generic transport equation, which has the same general form taken by the transport equations governing the studied flows. These governing equations form equation systems describing the flows and consist of the equations for the conservation of mass, phase fraction (indicator function) and linear momentum, including the energy conservation equation in the nonisothermal flow. The governing equations pertinent to the specific flow are introduced in the corresponding subsequent Chapters where also some additional numerical features and the details of the implementation are presented.

2.1 Description of the Open Source CFD Toolbox OpenFOAM

All numerical simulations were performed using OpenFOAM (Open Field Operation And Manipulation), a free-source CFD-toolbox produced by OpenCFD Ltd. It is based on the finite-volume numerical method with the co-located variable arrangement for solving systems of transient transport equations on arbitrary unstructured meshes in three-dimensional space. The software consists of a number of pre-compiled libraries and solvers, accompanied by the corresponding open-source codes written in C++ programming language in an object-oriented manner suitable for solving problems in Computational Continuum Mechanics (CCM). Using the object-oriented programming approach creation of data types (fields) closely mimicking those of mathematical field theory is enabled, and the feature of operator overloading in C++ allows mathematical symbols to be applied on scalar, vector and tensor fields very similar to those in ordinary mathematics (vector and tensor products or differential operators). Contrary to numerical codes written in procedural languages (like FORTRAN) that require implementation of transport equations and models at a low programming level, this task is accomplished at the highest coding level (top user level) in OpenFOAM, resembling closely the standard tensor notation. It is utilized by the OpenFOAM programming language which is generic, making extensive use of C++ class and function templates and the principle of class inheritance (Weller et al. [129]).

For the finite-volume discretization, a variety of discretization practices are implemented for the temporal, convection, diffusion and source terms in the transport equations. All numerical schemes are run-time selectable and can be used indepen-

dently of the geometry of the cases studied. Coupling between equations is handled in a segregated fashion, by formulating and solving equations for each variable separately and iterating over the equations' system until the predefined convergence criteria are satisfied. From the implementation point of view boundary conditions are treated as an integral part of the overall tensor field, rather than being extra added. Available are basic conditions, including fixed value, zero gradient, fixed gradient, symmetry and cyclic, and a number of derived boundary conditions combining the basic ones. A number of iterative solvers for linear systems of equations is available and run-time selectable, including conjugate gradient, algebraic and geometric multigrid solvers.

For the code parallelization OpenFOAM uses the domain decomposition method, where the computational domain is split into a number of subdomains, one for each processor. At run-time each processor receives a separate copy of the compiled code to be run on each subdomain. For the communication between processors the Message Passing Interface (MPI) is used. The inter-processor communication is implemented at the level of field classes (representing scalar, vector or tensor fields), thereby enabling any new code written at the higher user level for solving partial differential transport equations to be automatically parallelized.

2.2 Finite-Volume Discretization

The finite-volume numerical discretization procedure consist of three basic steps applied to the considered system: transformation of the space, of the time and of the transport equations into discrete forms (Ferziger and Perić [25]). The solution domain is represented by the computational mesh covering the part of the space of interest subdivided into a number of control volumes or cells with computational points placed at cell-centroids. The time in transient flows is subdivided into a number of time steps covering the time from the beginning to the end of the period in which the flow is resolved. The governing transport equations are discretized and both space and time integrated over the volumes of the mesh cells.

2.2.1 Discretiation of the Solution Domain

The computational mesh consists of a number of cells, each two of which share exactly one cell-face, as shown in Fig. 2.1. The variables are computed at computational points stored at cell-centroids P and all cells are bounded by a finite number of flat faces f. The cell-centroids are commonly termed cell-centers.

For the discretization of spatial derivatives values at cell-faces are required. For the cell-face interpolation, the values of the variables at the neighboring computational points N are used, the shortest distances between the computational point of interest P and its neighbors N are defined with the vectors $\mathbf{d}$ and the cell-face surface normal vectors $\mathbf{S}_f$ are located at cell-face centroids. There are two groups of cell-faces: the internal faces connecting the cells within the domain and the boundary faces covering the domain boundaries. Each internal face has one cell defined

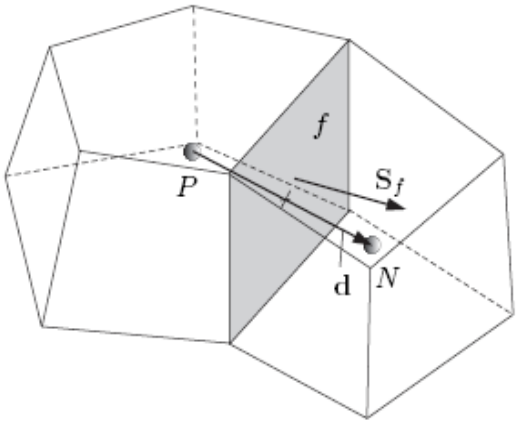

Figure 2.1: Discretization of the solution domain, from OpenCFD Ltd [69].

as its owner and one as its neighbor, determined by the lower and the higher labels in the list, respectively. The surface normal vectors point outward from the owner cells and have magnitudes equal to the areas of the cell-faces. The boundary faces are defined by having only owner cells and point out of the computational domain.

2.2.2 Discretiation of the Transport Equations

The partial differential equation representing a conservation law of a physical quantity ϕ expressed per unit volume may be written as a generic transport equation in the form

$$\frac{\partial(\rho\phi)}{\partial t} + \nabla \cdot (\rho \mathbf{U}\phi) = \nabla \cdot (\Gamma \nabla \phi) + S_\phi(\phi). \tag{2.1}$$

The generic transport equation states that the total rate of change of ϕ, consisting of the local transient change and convective change due to flux of ϕ (the terms on the l.h.s. of Eq. (2.1)), is balanced by diffusion transport characterized by diffusion coefficient Γ and either production or destruction of ϕ as sources $S_\phi(\phi)$ (the terms on the r.h.s. of Eq. (2.1)).

All terms in Eq. (2.1) are discretized using the finite-volume approximations. The transport equation is integrated over all cell-volumes around computational points and over time

$$\begin{aligned} &\int_t^{t+\Delta t} \left[\frac{\partial}{\partial t} \int_{V_P} \rho\phi \mathrm{d}V + \int_{V_P} \nabla \cdot (\rho \mathbf{U}\phi) \mathrm{d}V \right] \mathrm{d}t = \\ &= \int_t^{t+\Delta t} \left[\int_{V_P} \nabla \cdot (\Gamma \nabla \phi) \mathrm{d}V + \int_{V_P} S_\phi(\phi) \mathrm{d}V \right] \mathrm{d}t. \end{aligned} \tag{2.2}$$

2.2.2.1 Spatial Derivatives

For the discretization of terms containing spatial derivatives the volume integrals are converted into surface integrals using Gauss's theorem and summation over all

surfaces is performed. The terms containing gradients are discretized according to the expression

$$\int_{V_P} \nabla\phi \mathrm{d}V = \int_{S_P} \mathrm{d}\mathbf{S}\phi \approx \sum_f \mathbf{S}_f \phi_f, \tag{2.3}$$

where S_P is the total surface area of all cell-faces enclosing the control volume V_P and $\mathrm{d}\mathbf{S}$ is the differential of the cell-face surface normal vector. The summation is performed over all cell-faces bounding a cell. Accordingly the terms with divergences are approximated as

$$\int_{V_P} \nabla \cdot \phi \mathrm{d}V = \int_{S_P} \mathrm{d}\mathbf{S} \cdot \phi \approx \sum_f \mathbf{S}_f \cdot \phi_f. \tag{2.4}$$

Similarly, the terms involving second-order spatial derivatives are discretized as

$$\int_{V_P} \nabla \cdot (\Gamma\nabla\phi) \mathrm{d}V = \int_{S_P} \mathrm{d}\mathbf{S} \cdot (\Gamma\nabla\phi) \approx \sum_f \Gamma_f \mathbf{S}_f \cdot (\nabla\phi_f). \tag{2.5}$$

The gradient at the cell-face is the surface-normal gradient in orthogonal meshes evaluated as

$$(\nabla\phi)_f^{\perp} \approx \frac{\phi_N - \phi_P}{|\mathbf{d}|}. \tag{2.6}$$

For a non-orthogonal mesh, an additional correction term is introduced, evaluated by interpolating the gradient evaluated at computational points to the cell-faces (Jasak [45]).

2.2.2.2 Cell-face Interpolation

In the evaluation of surface integrals values of the unknown variables are interpolated to the centers of the cell-faces. While the estimation of the gradient-containing terms does not impose severe restrictions and commonly linear interpolation may be used, discretization of the term involving the divergence (in particular the convective term in the momentum equation) is more problematic. Successful approximation of the convective term is probably one of the most challenging problems in CFD. Since convection physically describes fluid transport from the upstream to the downstream region with respect to a point in space, the numerical approximation of convection should be upstream-biased. Many discretization practises are at hand for the cell-face interpolation, of which the most commonly used are the CD and UD schemes. The CD scheme is second-order accurate in space, but does not guarantee boundedness of the solution, whereas the UD scheme is first-order accurate in space and assures the boundedness of the solution, but it imposes an artificial numerical diffusion flux (Ferziger and Perić [25]).

In addition, the discretization of the convective term in the equation for the indicator function is crucial. First-order schemes, such as UD, tend to smear the interface too much producing an effect of artificially mixing the fluids, while on the other hand, second-order schemes, like CD, result in an unbounded solution.

The value of the phase fraction must be bounded and therefore such a discretization scheme must be used which avoids over- and undershoots. Although the only scheme that is unconditionally bounded is the UD scheme, it cannot be used because of the large amount of numerical diffusion which it produces.

With the notion in Fig. 2.1, the value at the cell-face in the UD scheme is obtained from the expression

$$\phi_{f,UD} = \text{pos}(\mathbf{U}_f \cdot \mathbf{S}_f)\phi_P + [1 - \text{pos}(\mathbf{U}_f \cdot \mathbf{S}_f)]\phi_N, \tag{2.7}$$

and in the CD scheme from the expression

$$\phi_{f,CD} = f_{\mathbf{d}}\phi_P + (1 - f_{\mathbf{d}})\phi_N, \tag{2.8}$$

with the weighting factor of the linear interpolation scheme $f_{\mathbf{d}} = \overline{fN}/\overline{PN}$. The operator $\text{pos}(\mathbf{U}_f \cdot \mathbf{S}_f)$ is a switch, which accounts for the flow direction defined as

$$\text{pos}(\mathbf{U}_f \cdot \mathbf{S}_f) = \begin{cases} 1, \text{ for } \mathbf{U}_f \cdot \mathbf{S}_f > 0 \\ \quad \text{(the flow is from P to N)} \\ 0, \text{ for } \mathbf{U}_f \cdot \mathbf{S}_f < 0 \\ \quad \text{(the flow is from N to P).} \end{cases} \tag{2.9}$$

In order to overcome the disadvantages of these two schemes and preserve boundedness with acceptable accuracy, a variety of discretization schemes are proposed utilized as combinations of the UD and the CD schemes

$$\phi_f = \psi\phi_{f,CD} + (1 - \psi)\phi_{f,UD}, \tag{2.10}$$

which can be rewritten, using Eqs. (2.7–2.8), as

$$\begin{aligned} \phi_f &= \{(1 - \psi)\text{pos}(\mathbf{U}_f \cdot \mathbf{S}_f) + \psi f_{\mathbf{d}}\}\phi_P \\ &+ \{(1 - \psi)[1 - \text{pos}(\mathbf{U}_f \cdot \mathbf{S}_f)] + \psi(1 - f_{\mathbf{d}})\}\phi_N. \end{aligned} \tag{2.11}$$

The amount of the numerical diffusion is controlled by the blending or weighting factor ψ with values between zero and one. It can be shown that the numerical diffusion contributed from the upwind differencing depends on the mesh spacing, the convection velocity and the mesh-to-flow alignment (Jasak [45]). Such blending discretization schemes use varying flux limiters and blending factors based on the concepts of the Total Variation Diminishing (TVD) of Sweby [110] and the Normalized Variable Diagram (NVD) of Leonard [53] with the Convection Boundedness Criterion (CBC) of Gaskell and Lau [29] for the cell-face interpolation of the convected variable. According to the CBC criterion the interpolated value is bounded below and above by first-order upwind and downwind differencing schemes, respectively, and the interpolation then requires a blending between the two.

In this study, for the discretization of the convective terms a cell-face interpolation based on limited, high resolution differencing schemes is used, with blending factors evaluated based on the ratios between flux gradients calculated at the adjacent cell-face and cell center, as formulated by Jasak [45]. The expression for the

interpolated cell-face value ϕ_f in Eq. (2.11) of a variable ϕ between the computational points P and N in Fig. 2.1 reduces to

$$\phi_f = \lambda(\phi_P - \phi_N) + \phi_N, \tag{2.12}$$

where λ is calculated using the weighting factor ψ from the limited scheme

$$\lambda = \psi f_{\mathbf{d}} + (1 - \psi) \cdot \mathrm{pos}(\mathbf{U}_f \cdot \mathbf{S}_f). \tag{2.13}$$

The NVD approach normalizes the variables by the difference between the values at the first downstream and the upstream nodes and the normalized cell-face value of the variable is a function of the normalized adjacent upstream value. Jasak [45] modified the NVD criterion for unstructured meshes and reformulated the normalized variable at the computational point of interest as

$$\overline{\phi}_P = 1 - \frac{\mathbf{d} \cdot (\nabla\phi)_f}{2\mathbf{d} \cdot (\nabla\phi)_P}. \tag{2.14}$$

In the TVD approach the flux limiter is a function of the ratio r of the consecutive gradients of the variable of interest between two adjacent computational points. By definition, there is a one-to-one correspondence between the normalized variables and the gradient ratios

$$\overline{\phi}_P = \frac{r}{1+r} \quad \text{and} \quad r = \frac{\overline{\phi}_P}{1 - \overline{\phi}_P}, \tag{2.15}$$

and the gradient ratio r may then be evaluated as

$$r = \frac{2\mathbf{d} \cdot (\nabla\phi)_P}{\mathbf{d} \cdot (\nabla\phi)_f} - 1. \tag{2.16}$$

In the above expressions the product between the cell-face gradient and the distance between cell-centers is calculated directly as the difference in values between the two neighboring computational points

$$\mathbf{d} \cdot (\nabla\phi)_f = \phi_N - \phi_P. \tag{2.17}$$

The weighting factor ψ is determined using either $\overline{\phi}_P$ or r in NVD- or TVD-based schemes, respectively. For the discretization of the convective term in the momentum equation in this study applied was the limiter referred to as limited-linear (LL) in OpenFOAM, which corresponds to the Chakravarthy-Osher limiter in Waterson and Deconink [125] with the appropriate definition for r

$$\psi = \max\left[\min\left(\frac{2}{k}r, 1\right), 0\right], \tag{2.18}$$

In some of the computed cases the weighting factor from the Gamma differencing (GD) scheme of Jasak [45] was utilized

$$\psi = \min\left[\max\left(\frac{2}{k}\overline{\phi}_P, 0\right), 1\right], \tag{2.19}$$

showing no noticeable difference in the results. In the above expressions $0 \leq k \leq 1$ is the parameter of the scheme and the recommended value of $k = 1$ was used. The convective term in the equation for the indicator function (phase fraction) is discretized similarly using the limiter of Van Leer [119]

$$\psi = \frac{r + |r|}{1 + |r|}, \tag{2.20}$$

due to its more pronounced effects of downwind differencing, which is desired for obtaining sharply resolved interfaces. It was found to be suitable for the discretization of the convection term, since it maintains the correct shape and the sharpness of the interface (Weller [128]). Additional computational details regarding the phase fraction equation are given in Chapter 3.

Using Eqs.(2.15), the normalized cell-face values $\overline{\phi}_f$ in the limited schemes can be represented in the NVD diagram, Fig.2.2.

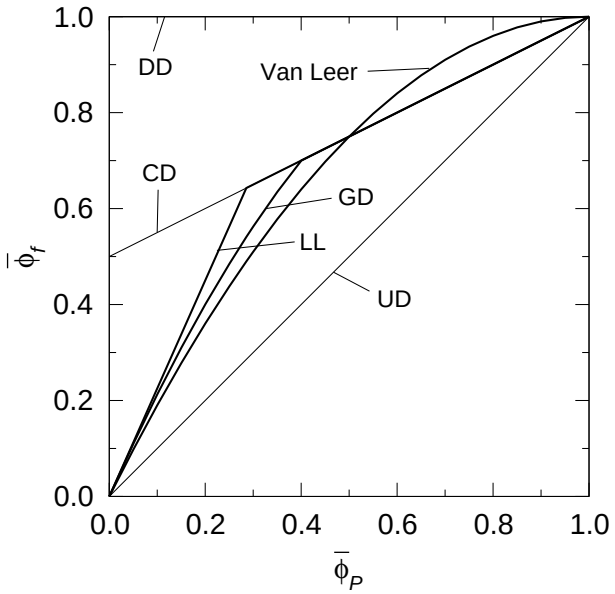

Figure 2.2: Differencing schemes in the NVD diagram.

2.2.2.3 Source Terms

The general source term may be an unknown function of ϕ which is linearized and integrated over the cell volume

$$\int_{V_P} S_\phi(\phi) \mathrm{d}V \approx S_{\phi_1} V_P + S_{\phi_2} \phi_P V_P. \tag{2.21}$$

In calculations of source terms involving surface integration, the corresponding values at cell-centers are reconstructed from the cell-faces, according to the expression

$$\phi_P = \left(\sum_f \frac{\mathbf{S}_f \mathbf{S}_f}{|\mathbf{S}_f|} \right)^{-1} \cdot \left(\sum_f \frac{\mathbf{S}_f}{|\mathbf{S}_f|} \cdot \phi_f |\mathbf{S}_f| \right). \tag{2.22}$$

The first sum on the r.h.s. of Eq. (2.22) is a second-order tensor with all non-diagonal values equal to zero and the diagonal values representing the sum of face areas for a given cell in the corresponding coordinate directions. The second sum is a vector, the components of which are sums of products of cell-face values of a given variable and cell-face surfaces in each coordinate direction. As a result of the inner product, the values at cell-centers are recovered as weighted averages of the (staggered) values at cell-faces. For example, a source containing gradients is calculated as

$$(\nabla\phi)_P = \left(\sum_f \frac{\mathbf{S}_f\mathbf{S}_f}{|\mathbf{S}_f|}\right)^{-1} \cdot \left(\sum_f \frac{\mathbf{S}_f}{|\mathbf{S}_f|} \cdot (\nabla\phi)_f^{\perp}|\mathbf{S}_f|\right). \tag{2.23}$$

2.2.3 Time Integration

For the integration of the terms in Eq. (2.2) over time, the Euler implicit time differencing scheme is used. The scheme is unconditionally stable, first-order accurate in time and guaranties boundedness of the solution. The volume integral in the transient term is evaluated as

$$\frac{\partial}{\partial t}\int_{V_P}(\rho\phi)\mathrm{d}V \approx \frac{(\rho_P\phi_P V_P)_{(t+\Delta t)} - (\rho_P\phi_P V_P)_t}{\Delta t}, \tag{2.24}$$

a linear variation in time of all unknown variables in Eq. (2.2) is assumed and all quantities are evaluated at the new time level in the time integration step yielding

$$\int_t^{t+\Delta t}\left[\frac{\partial}{\partial t}\int_{V_P}\rho\phi\mathrm{d}V\right]\mathrm{d}t \approx (\rho_P\phi_P V_P)_{(t+\Delta t)} - (\rho_P\phi_P V_P)_t, \tag{2.25}$$

$$\int_t^{t+\Delta t}\left[\int_{V_P}\mathcal{L}\phi\mathrm{d}V\right]\mathrm{d}t \approx \mathcal{L}^*(\phi_P)_{(t+\Delta t)}\Delta t, \tag{2.26}$$

$$\int_t^{t+\Delta t}\left[\int_{V_P}S_\phi(\phi)\mathrm{d}V\right]\mathrm{d}t \approx (S_{\phi_1}V_P + S_{\phi_2}\phi_P V_P)_{(t+\Delta t)}\Delta t, \tag{2.27}$$

as the final discretized forms for the transient, spatial derivative and source terms, respectively, where the general spatial derivative (convection-diffusion) terms are symbolically denoted as $\mathcal{L}\phi$ with $\mathcal{L}^*$ being the discretized form of the arbitrary differential operator $\mathcal{L}$, as defined in Eqs. (2.3–2.5).

2.2.3.1 Adaptive Time Step Control

Since the flow field is unknown at the beginning of the calculation, introducing some small but still fixed value for the time step may be difficult. On one hand, when the values of the time steps are not controlled during the calculation it may result in an unstable solution procedure or even in obtaining a solution which is correct only in the time interval where the values of the local Courant are small. On the other hand, simulations with extremely small time steps consume much more computational

effort. The use of adjustable time steps enables accurate calculations and in some cases huge reductions in calculation time, which is an important consideration in numerical simulations.

The time step is adjusted according to the prescribed maximum Courant number and maximum time step size. The new time step is firstly evaluated from the expression

$$\Delta t = \min\left\{\min\left[\min\left(\frac{\mathrm{Co}_{\max}}{\mathrm{Co}_o}\Delta t_o, (1+\lambda_1\frac{\mathrm{Co}_{\max}}{\mathrm{Co}_o})\Delta t_o\right), \lambda_2\Delta t_o\right], \Delta t_{\max}\right\}, \quad (2.28)$$

where the Courant number is determined from

$$\mathrm{Co} = \frac{|\mathbf{U}_f \cdot \mathbf{S}_f|}{\mathbf{d}\cdot\mathbf{S}_f}\Delta t. \quad (2.29)$$

The local Courant number Co_o is calculated using values from the previous (old) time step. In order to avoid time step oscillations the increase of the time step is damped using the factors λ_1 and λ_2.

For the solution to be stored at exactly specified time intervals, output is adjusted by calculating the number of time steps remaining to the next write, rounded to a first greater integer value, and the value for new time step is then accordingly re-evaluated. Since the re-evaluated value for the time step may differ from that determined in Eq. (2.28), to keep consistency and avoid instability an additional control of both the decrease and the increase of the time step is provided. If the re-evaluated time step size is greater a portion of it is used, and in the opposite case its multiple is chosen, limited by the value determined from Eq. (2.28).

At the beginning of the calculation the time step size is evaluated from

$$\Delta t_o = \min\left(\frac{\mathrm{Co}_{\max}\Delta t_{init}}{\mathrm{Co}_o}; \Delta t_{\max}\right) \quad (2.30)$$

and this intermediate value is then used in Eq. (2.28) in order to ensure that the value of Co_o at the initial time step be close to the prescribed limit value $\mathrm{Co}_{\max}$.

Depending on the specific case studied, the size of the time step may vary during the calculation between two or more orders of magnitude. It was found by experience that the limiting value for the Courant number should not exceed $\mathrm{Co}_{\max} \approx 0.2$, which is the value used in this study, and values for the damping factors are $\lambda_1 = 0.1$ and $\lambda_1 = 1.2$. Using the above prescription, the time step is adjusted smoothly, keeping the maximum local Courant number nearly equal to the prescribed limiting value.

2.2.3.2 Temporal Sub-cycling

It is commonly found in VOF-based methods that the convergence and stability of the solution procedure are very sensitive with respect to the equation for phase fraction. Bounded discretization schemes for convection terms and time step control are both used to overcome these difficulties but it is generally recommended to keep

the maximum local Courant number much below unity. It is beneficial to solve the phase fraction equation in several sub-cycles within a single time step. The time step to be used in a single time sub-cycle is set by dividing the global time step by the preset number of sub-cycles.

A drawback of this is that the fluxes must be accumulated during the sub-cycling and this is an additional reason for using the implicit time integration. After the phase fraction in each sub-cycle is updated the corresponding mass flux through cell-faces is calculated and the total mass flux corresponding to the global time step is obtained by summing the sub-cycle mass fluxes.

In this way the local Courant number is kept small providing a more accurate solution of the phase fraction equation, and the global time step size is allowed to be greater for the solution of other transport equations, thereby considerably speeding up the solution procedure.

2.3 Initialization and Boundary Conditions

At the initial time, the distribution of all variables is prescribed in all cells of the mesh. In the present study they include the scalar fields of the indicator function (phase fraction), pressure, temperature (in nonisothermal flow) and the vector field of velocity. The initial distributions should correspond to real conditions as determined in experiments.

At all cell-faces coinciding with the domain boundaries the values of the variables must either be set explicitly or be implicitly accounted for. The two basic boundary conditions, the Dirichlet and the von Neumann, prescribe fixed values ϕ_b and gradients $(\mathbf{S}_f/|\mathbf{S}_f|) \cdot (\nabla\phi)_b$ of the variables at the boundary cell-faces, respectively. Different physical boundary conditions derived from the basic ones are applied to fluid flow simulations.

At the impermeable solid wall the convection flux is zero and the velocity is set equal to that of the wall (no-slip condition). For stationary walls it reduces to zero velocity at cell-faces coinciding with the wall surface. Due to the zero flux through the wall, the pressure gradient is set to zero. The temperature distribution is prescribed either explicitly or implicitly through an applied wall heat flux.

At the plane of symmetry the surface-normal gradients of variables are zero and the components parallel to the plane are projected from the neighboring cells inside the domain.

At open boundaries either inlet or outlet flow conditions may exist. At the inlet the values for the velocities are prescribed and the pressure gradient is zero, the opposite being at the outlet, with the prescribed pressure distribution and zero gradient for velocity. If known, the temperature distribution is prescribed, otherwise the boundary condition can be zero gradient for temperature, indicating an adiabatic boundary.

Inlet and outlet conditions can also be combined on the same boundary, according to the flow direction, if the fluid is allowed to flow into and out of the domain. For a scalar variable the combination can be a switch between the fixed value and

the zero gradient at the open boundary, depending on the sign of the volumetric flux as shown in Fig. 2.3, according to the expression

$$\phi_b = [1 - \text{pos}(\mathbf{U}_f \cdot \mathbf{S}_f)]\phi_{b,ref} + \text{pos}(\mathbf{U}_f \cdot \mathbf{S}_f)\phi_P. \tag{2.31}$$

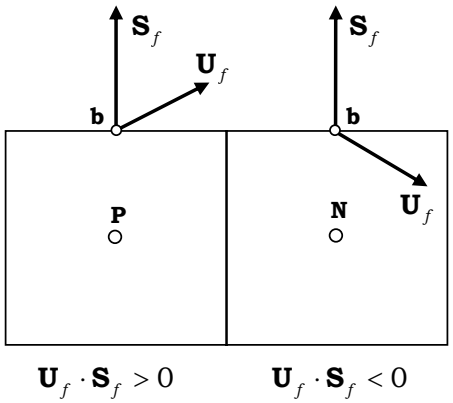

Figure 2.3: A combined inlet-outlet boundary condition.

Thus, the values at the boundary are obtained as

$$\phi_b = \begin{cases} \phi_P, \text{ for outflow} \\ \phi_{ref}, \text{ for inflow} \end{cases} \tag{2.32}$$

where *ref* denotes the prescribed referent value. For vector quantities, such as velocity, a corresponding expression similar to Eq. (2.31) is used.

The value for the pressure may be set also as a fixed value for the total pressure p_{tot}, consisting of the static and the dynamic parts. The static pressure is then adjusted at the boundary using the dynamic pressure calculated from the density and velocity. A combination is possible according to the sign of the volumetric flux

$$p_b = \begin{cases} p_{tot,ref} - p_{dyn}, \text{ for inflow} \\ p_{tot,ref}, \text{ for outflow.} \end{cases} \tag{2.33}$$

In axisymmetric cases, the mesh has the shape of a slice with only one cell in the azimuthal direction. The cells aligned with the axis of symmetry have faces with zero surfaces at the axis, which is accounted for by suppressing the discretization coefficients. At the front and back planes of the mesh the scalar variables are transferred and the vectors are rotated to the boundary faces from the computational points preserving same magnitudes.

The boundary condition for the moving contact line in drop impacts onto a dry wettable surface imposes serious problems in numerical simulations. As previously discussed this is due to the complex physical dependence of the dynamic contact

angle on different parameters, among which is the contact-line speed, that is not known in advance

$$\theta_{dyn} = f(\theta_{eq}, \mathrm{Ca}, \mathrm{We}, \mu_l/\mu_g, \rho_l/\rho_g, ...). \tag{2.34}$$

In the immediate vicinity of the wall the liquid flows very slowly due to the effects of the molecular viscosity, but near the contact line the wettability-driven propagation exists and the contact line should slip over the wall. However if the bulk velocity of the spreading is high enough, this slip is negligible and the movement of the contact line at the macroscopic level may be viewed as the rolling motion (Yarin [132]).

The effects of wall adhesion are accounted for by using the prescribed contact angle θ at the wall. The contact angle may be either static, having one value for the entire computation, or quasi-dynamic, with two different values prescribed for the advancing and the receding phases of drop spreading, or dynamic, applied using some empirical relationship. The capillarity at the wall enters the momentum equation as a force acting at the contact line. The unit normal to the interface required to calculate the mean surface curvature at the contact line is obtained from the following expression

$$\mathbf{n}_w = \left(\frac{\nabla\gamma}{|\nabla\gamma|}\right)_w = \mathbf{n}_n \cos\theta + \mathbf{n}_t \sin\theta, \tag{2.35}$$

with $\mathbf{n}_n$ and $\mathbf{n}_t$ being the unit normal vectors to the contact line directed into the wall and tangential to the wall, respectively, as depicted in Fig. 2.4.

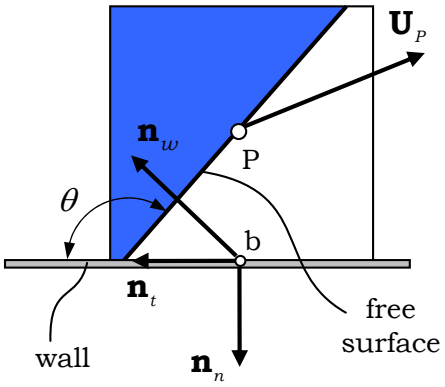

Figure 2.4: Contact-line boundary condition.

According to Brackbill et al. [10], before using Eq. (2.35) the unit normal $\mathbf{n}_t$ is obtained by assuming the zero gradient condition for the phase fraction at the wall yielding $\mathbf{n}_t = (\nabla\gamma/|\nabla\gamma|)_P$, while the unit normal $\mathbf{n}_n$ is given by $\mathbf{n}_n = \mathbf{S}_f/|\mathbf{S}_f|$.

2.4 Solution Procedure

The fluids in all computed flows in the present study are assumed to be Newtonian and incompressible. In such flows there exists no explicit equation for pressure

and therefore de-coupling of pressure from velocity must be avoided. This is done by deriving a discretized pressure equation from the semi-discretized momentum equation, using the continuity restriction of a divergence-free velocity field coming from the equation for mass conservation. The velocity and pressure are coupled through the Pressure Implicit with Splitting of Operators (PISO) algorithm for transient flows of Issa [43]. A summary of the algorithm presented by Jasak [45] with more details provided by Rusche [100] is shortly reproduced here.

2.4.1 The PISO Algorithm for Transient Flows

In the PISO algorithm the pressure-velocity coupling is applied in three basic steps:

- the momentum predictor step, where the last known solution for pressure is used in solving the momentum equation to obtain the first approximation for the velocity, which at this stage does not satisfy the continuity restriction,
- the pressure solution step, where the matrix for the pressure equation is assembled and solved to yield the new estimation for the pressure and
- the explicit velocity correction step, where the obtained pressure is used to calculate the new conservative volumetric fluxes and reconstruct the velocities consistent with the new pressure field.

Since the velocity does not depend only on the pressure field but also on the contributions from the updated velocities in the neighboring cells, the last two steps in the PISO loop are repeated until a pre-defined tolerance is met. Details of implementation for the co-located variable arrangement are provided by Kärrholm [47].

2.4.2 Solution of Linear Equation Systems

The discretization procedures outlined in this Chapter convert every partial differential equation into a corresponding system of linear algebraic equations, with one equation for each control volume (computational cell). The linear equation systems are different for each governing equation, but they all have the same general form

$$a_P \phi_{P(t+\Delta t)} + \sum_N a_N \phi_{N(t+\Delta t)} = b, \tag{2.36}$$

which is written in the matrix notation as

$$\mathbf{A} \cdot \Phi = \mathbf{b}. \tag{2.37}$$

The matrix $\mathbf{A}$ is sparse, containing the coefficients a_P on its diagonal and a_N off the diagonal, Φ is the array of unknowns ϕ and $\mathbf{b}$ is termed the source array.

The linear equation systems are inverted to obtain the numerical solutions of the governing equations. The system in Eq. (2.37) is solved using the iterative procedure, which starts from an initial guess and continually improves the solution in every iteration. The iteration loop is stopped when some prescribed condition is

fulfilled, e.g. when the difference between two consecutive solutions is smaller than some prescribed small tolerance, and the obtained values for ϕ are considered to be the approximate solutions. In order to improve the convergence rate the equations' system can be preconditioned, i.e. multiplied by a suitable preconditioning matrix. In this study, for symmetric matrices the Preconditioned Conjugate Gradient (PCG) solver with Diagonal-based Incomplete Cholesky (DIC) preconditioner is used, and for asymmetric matrices the Preconditioned Bi-Conjugate Gradient (PBiCG) with Diagonal-based Incomplete Lower-Upper (DILU) preconditioner is adopted. The description of the algorithms may be found in Saad [101].

The effects of turbulence are not modeled in the present study. The interface between two phases is in theory infinitesimally small and in reality it represents a region in space with a submicroscopic width. In order to sharply resolve the phase-interface commonly a fine mesh resolution is required, at least in regions of free-surface motion. In order to ensure boundedness of the phase fraction, independent of the numerical discretization schemes, the solution procedure utilizes the Multidimensional Universal Limiter for Explicit Solutions (MULES) of OpenCFD Ltd [70]. It is similar to the idea of the flux-corrected transport, where the antidiffusive flux (or the flux correction) is calculated as a difference between the higher-order flux obtained using the limited scheme and the first-order upwind flux. The flux correction is then limited in a manner such that the new obtained solution for the phase fraction will be limited by the extrema determined in all the neighboring cells to the cell of interest.

3 Isothermal Drop Collisions

3.1 Introduction

This Chapter deals with the hydrodynamics of isothermal flows induced by drop collisions. Three different scenarios are investigated: drop collision with a shallow liquid layer, symmetric drop collision with another drop (binary drop collision) and drop collision with a dry wall. The governing transport equations are introduced, followed by the computational details and simulations. The numerical and theoretical results with the appropriate discussions are presented.

3.2 Governing Equations and Computational Details

In the VOF method for incompressible two-phase flow with free-surfaces introduced by Hirt and Nichols [40], the transport equation for the indicator function, representing one phase, is solved simultaneously with the continuity and momentum equations

$$\nabla \cdot \mathbf{U} = 0, \tag{3.1}$$

$$\frac{\partial \gamma}{\partial t} + \nabla \cdot (\mathbf{U}\gamma) = 0, \tag{3.2}$$

$$\frac{\partial (\rho \mathbf{U})}{\partial t} + \nabla \cdot (\rho \mathbf{U}\mathbf{U}) = -\nabla p + \nabla \cdot \mathbf{T} + \mathbf{f}, \tag{3.3}$$

where the viscous stress tensor is given by

$$\mathbf{T} = \mu[\nabla \mathbf{U} + (\nabla \mathbf{U})^T] - \frac{2}{3}\mu \mathbf{I}(\nabla \cdot \mathbf{U}), \tag{3.4}$$

with the identity tensor $\mathbf{I} \equiv \delta_{ij}$. The last term on the r.h.s. if Eq. (3.3) takes into account body forces, that generally include gravity as $\rho \mathbf{g}$. The indicator function γ is commonly defined in space as

$$\gamma = \begin{cases} 0, & \text{for points belonging to one phase;} \\ 0 < \gamma < 1, & \text{for points at the phase-interface;} \\ 1, & \text{for points belonging to another phase.} \end{cases} \tag{3.5}$$

Physically, the indicator function can be interpreted as the volume fraction or phase fraction of one phase (usually liquid) and may be defined as

$$\gamma = \frac{\int_{V \to \partial x^3} \gamma_l \mathrm{d}V}{\int_{V \to \partial x^3} (\gamma_l + \gamma_g) \mathrm{d}V}, \tag{3.6}$$

where the subscripts l and g denote liquid and gas, and the integration is performed over a small volume ∂x^3 around a point in space and $\gamma_l + \gamma_g = 1$.

Two immiscible fluids are considered as one effective fluid throughout the domain, the physical properties of which are calculated as weighted averages based on the distribution of the liquid phase fraction, being equal to the properties of each fluid in the regions they occupy and varying only across the interface

$$\rho = \gamma\rho_l + (1-\gamma)\rho_g \quad \text{and} \quad \mu = \gamma\mu_l + (1-\gamma)\mu_g. \tag{3.7}$$

The critical issue in numerical simulations of free-surface flows using the VOF model is the sharp resolution of the interface while preserving the boundedness and conservation of the phase fraction. The interface region between the phases is typically smeared over a few mesh cells and is therefore highly sensitive to mesh resolution. In flows with high density ratios small errors in phase fraction may lead to significant errors in calculations of physical properties. Accurate calculation of the phase fraction distribution is crucial for a proper evaluation of surface curvature, which is required for the determination of the surface tension force across the free surface.

Since the interface is artificially smeared due to the numerical diffusion, the proper discretization of the convective term is here of outmost importance. Various attempts have been made in order to overcome these difficulties, as outlined in Section 1.3.1. In the present study the approach according to Weller [128] is utilized. In this approach the smearing of steep gradients is suppressed by introducing an additional convective term in the phase fraction equation, Eq. (3.2), acting against the numerical diffusion, in the form

$$\frac{\partial\gamma}{\partial t} + \nabla\cdot(\mathbf{U}\gamma) + \nabla\cdot[\mathbf{U}_c\gamma(1-\gamma)] = 0. \tag{3.8}$$

In fact, the additional convective term (the third term on the l.h.s. of Eq. (3.8)) has the same form as the scalar flux closure for the counter-gradient transport in complex combustion models incorporating the relative velocity between the burnt and unburnt gases (Veynante et al. [120]). This relative velocity appearing in the term is replaced with the interface-compression equivalent $\mathbf{U}_c$, which ensures the shrinking of the interface, while the term guaranties both conservation and boundedness of phase fraction (Weller [128]).

It is interesting to note that Eq. (3.8) can be derived relying on a two-fluid Eulerian formulation, where phase fraction equations are solved separately for each individual phase

$$\frac{\partial\gamma}{\partial t} + \nabla\cdot(\mathbf{U}_l\gamma) = 0, \tag{3.9}$$

$$\frac{\partial(1-\gamma)}{\partial t} + \nabla\cdot[\mathbf{U}_g(1-\gamma)] = 0. \tag{3.10}$$

Defining the velocity of the effective fluid as a weighted average (Weller [127])

$$\mathbf{U} = \gamma\mathbf{U}_l + (1-\gamma)\mathbf{U}_g, \tag{3.11}$$

Eq. (3.9) can be rearranged to obtain exactly the same form as Eq. (3.8), used as the evolution equation for the liquid phase fraction

$$\frac{\partial \gamma}{\partial t} + \nabla \cdot (\mathbf{U}\gamma) + \nabla \cdot [\mathbf{U}_r \gamma(1-\gamma)] = 0, \tag{3.12}$$

where $\mathbf{U}_r = \mathbf{U}_l - \mathbf{U}_g$ is the vector of liquid-gas relative velocity, modeled as the compression velocity $\mathbf{U}_c$ in Eq. (3.8). The term *compression* comes from the role to shrink the phase-interphase towards a sharper one, representing just a denotation and does not relate to compressible flow.

The compression term must not bias the solution in any way and should only introduce the flow of γ in the direction normal to the interface. In order to ensure this, several possibilities are offered in Weller [128] to model the compression velocity, the most general form being

$$\mathbf{U}_c = \min\left[C_\gamma |\mathbf{U}|, \max(|\mathbf{U}|)\right] \frac{\nabla \gamma}{|\nabla \gamma|}, \tag{3.13}$$

where the compression velocity is based on the maximum velocity in the interface region. In fact, $\mathbf{U}_c$ must be somehow limited, which is achieved using the largest value of the velocity in the domain as the worst possible case (Weller [128]). The intensity of the interface compression is controlled by the constant C_γ, which yields no contribution if set to zero, a conservative compression if the value is one and an enhanced compression for values greater than one (OpenCFD Ltd [70]).

It should be noted that the compression term appears as an artificial contribution to the convection of the phase fraction. Its proper discretization contributes significantly to a higher interface resolution, thus avoiding the need to devise special compressive schemes (such as CICSAM or HRIC). The additional term is similar to the volume-averaged VOF model in Wörner et al. [131]. Although the above outlined approach is numerically motivated to suppress the numerical diffusion, it is emphasized that, due to its form, the additional compression term is active only in the numerically integrated form of the phase fraction equation within the interface region and vanishes at both limits of the phase fraction. Therefore it does not affect the solution outside this region. Moreover in the theoretical sense of a well defined macroscopic free surface having an infinitesimally small thickness, the relative velocity $\mathbf{U}_r$ vanishes recovering the standard phase fraction equation, Eq. (3.2).

The momentum equation, Eq. (3.3), is extended in order to account for the effects of surface tension. The surface tension at the liquid-gas interface generates an additional pressure gradient resulting in a force, which is evaluated per unit volume using the CSF model of Brackbill et al. [10]

$$\mathbf{f}_\sigma = \sigma \kappa \nabla \gamma f(\mathbf{x}), \tag{3.14}$$

where the mean curvature of the free surface is determined from the expression

$$\kappa = -\nabla \cdot \left(\frac{\nabla \gamma}{|\nabla \gamma|} \right). \tag{3.15}$$

The CSF model is suitable for fixed Eulerian meshes and applies a volumetric force in those cells of the mesh containing the transitional interface region as an approximation to the discontinuous surface tension force. Thus, the surface tension force is spread across the interface over several cells containing the free surface. In this manner the CSF model actually eliminates the need to explicitly reconstruct the interface during the computation. Equation (3.14) is valid for the cases with constant surface tension, whereas in the case of variable surface tension, e.g. due to non-uniformly distributed temperature, surface tension gradients are encountered, generating an additional shear stress at the interface, which should be taken into account. Brackbill et al. [10] suggested that the indicator function (phase fraction) can be smoothed before calculating the interface normal and that the function $f(\mathbf{x})$ in Eq. (3.14) is calculated as $f(\mathbf{x}) = \rho/\langle\rho\rangle$, where $\langle\rho\rangle = (\rho_l + \rho_g)/2$ is the average density of the two phases. Such approach should not influence the total magnitude of the force, but it weights the force toward regions of higher density fluid. Optionally, the function can be formulated in another way to bias the applied force more to either the center of the interface region, or to the points of the maximum phase fraction gradient. However, the numerical experiments of Lafaurie et al. [52] have shown no noticeable difference in applying this corrections compared to the case without them. In the present study the surface tension force is calculated from Eq. (3.14) using the phase fraction gradients without smoothing, i.e. $f(\mathbf{x}) = 1$.

Both fluids are considered to be Newtonian and incompressible ($\nabla\cdot\mathbf{U} = 0$), and the rate of strain tensor is linearly related to the stress tensor, which is decomposed into a more convenient form for discretization

$$\begin{aligned} \nabla\cdot\mathbf{T} &= \nabla\cdot\{\mu[\nabla\mathbf{U} + (\nabla\mathbf{U})^T]\} \\ &= \nabla\cdot(\mu\nabla\mathbf{U}) + (\nabla\mathbf{U})\cdot\nabla\mu. \end{aligned} \tag{3.16}$$

In a single pressure system, such as in the VOF method, the normal component of the pressure gradient at a stationary non-vertical solid wall with no-slip condition for the velocity, must be different for each phase due to the hydrostatic contribution when the phases are separated at the wall, i.e. if a contact line exists. In order to simplify the definition of boundary conditions, it is common to define the modified pressure as

$$p_d = p - \rho\mathbf{g}\cdot\mathbf{x}. \tag{3.17}$$

The negative gradient of the modified pressure p_d consists of the static pressure gradient, the body force due to gravity and an additional contribution originating from the density gradient

$$-\nabla p_d = -\nabla p + \rho\mathbf{g} + \mathbf{g}\cdot\mathbf{x}\nabla\rho, \tag{3.18}$$

and, in order to satisfy the momentum equation, the negative pressure gradient is expressed using Eq. (3.18) whereas the momentum equation is rearranged by introducing the term $-\mathbf{g}\cdot\mathbf{x}\nabla\rho$ (Rusche [100]).

Summing up, the set of equations governing the incompressible two-phase flow with free surface is given by

$$\nabla \cdot \mathbf{U} = 0, \tag{3.19}$$

$$\frac{\partial \gamma}{\partial t} + \nabla \cdot (\mathbf{U}\gamma) + \nabla \cdot [\mathbf{U}_c \gamma(1-\gamma)] = 0, \tag{3.20}$$

$$\begin{aligned} \frac{\partial(\rho \mathbf{U})}{\partial t} &+ \nabla \cdot (\rho \mathbf{U}\mathbf{U}) \\ &= -\nabla p_d - \mathbf{g} \cdot \mathbf{x} \nabla \rho + \nabla \cdot (\mu \nabla \mathbf{U}) + (\nabla \mathbf{U}) \cdot \nabla \mu + \sigma \kappa \nabla \gamma. \end{aligned} \tag{3.21}$$

where body forces due to pressure gradient and gravity are implicitly accounted for by the first two terms on the r.h.s. of the Eq. (3.21).

For the discretization of the compression term in Eq. (3.20), the magnitude of the volumetric compression flux at cell-faces is determined from

$$(\mathbf{U}_{c,f} \cdot \mathbf{S}_f) = n_f \min \left[C_\gamma \frac{|\mathbf{U}_f \cdot \mathbf{S}_f|}{|\mathbf{S}_f|}, \max \left(\frac{|\mathbf{U}_f \cdot \mathbf{S}_f|}{|\mathbf{S}_f|} \right) \right], \tag{3.22}$$

where the unit normal flux at cell-faces in the interface region is calculated using the phase fraction gradient interpolated to cell-faces

$$n_f = \frac{(\nabla \gamma)_f}{|(\nabla \gamma)_f| + \delta} \cdot \mathbf{S}_f, \tag{3.23}$$

and the stabilization factor is used in the normalization of the phase fraction gradient in Eq. (3.23) (and likewise in the discretized form of Eq. (3.15)), accounting for the nonuniformity of the mesh, according to

$$\delta = \frac{\varepsilon}{\left(\frac{\sum_N V_i}{N} \right)^{1/3}}, \tag{3.24}$$

with the small parameter set to $\varepsilon = 10^{-8}$ in the present study and the summation in the denominator is performed over all computational cells N. It should be noted that the cell-face volumetric flux $(\mathbf{U}_f \cdot \mathbf{S}_f)$ in Eq. (3.22) is not evaluated using the interpolated velocity, but is determined as a conservative volumetric flux resulting from the pressure-velocity coupling algorithm outlined in Section 2.4.1.

According to Weller [128] the discretization of the compressive term in Eq. (3.20) requires the compressive flux $(\mathbf{U}_{c,f} \cdot \mathbf{S}_f)$ in Eq. (3.22) to be used to interpolate γ and the negatively signed flux $-(\mathbf{U}_{c,f} \cdot \mathbf{S}_f)$ in the interpolation of $(1-\gamma)$ to the cell-faces. It is indicated that this scheme is similar to using the combined upwind/downwind differencing of the HRIC scheme (e.g. if upwind differencing is used for both the interpolation of γ and $(1-\gamma)$ with the change of the sign of the fluxes), except that the interface compression is applied here normal to the free surface instead of in the flow direction and that the compression intensity may be controlled independently of the flow. The procedure was successfully applied by Rusche [100] in the simulation of free rising bubbles and is also utilized in the present study. The values of γ

and $(1-\gamma)$ themselves are interpolated to the cell-faces by blending the CD with the UD scheme (Section 2.2.2.2) using the flux limiter due to Weller [128]

$$\psi = \min\{\max[1 - \max((1 - 4\gamma_P(1-\gamma_P))^2, (1 - 4\gamma_N(1-\gamma_N))^2), 0], 1\}, \quad (3.25)$$

which reduces to the UD scheme when the phase fraction approaches its limiting values $\gamma \to 0$ or $\gamma \to 1$.

The transient solution procedure is incorporated within the time iteration loop. At the beginning the new time step is adjusted and the phase fraction equation is solved. The fluid properties are updated, followed by the PISO loop for the momentum-pressure coupling. First, the momentum equation is solved and new volumetric fluxes are obtained from the first approximation of the new velocities. Using these the pressure equation is constructed and solved, followed by correcting the fluxes and explicitly reconstructing the new velocities, based on the obtained new pressure.

3.3 Validation of the Algorithm

The computational algorithm is validated using several test cases commonly found in the available literature. These include the transport of a hollow square in an oblique velocity field, rotation of a slotted circle, stretching of a circle in an imposed shear flow and droplet shape evolution due to surface tension.

Hollow Square in an Oblique Velocity Field

The configuration represents the scalar field advection by the fluid flow with uniform density and uniform viscosity. The phase fraction field is initialized as the hollow square aligned with the coordinate axes in the lower left corner, with the side lengths of outer and inner interfaces of the square having 40 and 20 cells, respectively. The square is exposed to the oblique unidirectional velocity field $\mathbf{U}(1.44, 1.44)$ on the uniform two-dimensional 100×100 mesh, and allowed to be advected to the upper right corner across a diagonal distance corresponding to 72×72 cells. Fig. 3.1 shows the initial and the final shapes after the advection indicated using the phase fraction contours $\gamma = 0.1; 0.5$ and 0.9. The simulation was performed with three limiting values for the Courant number and the number of time steps until the final position is reached was 480 for Co = 0.2, 310 for Co = 0.5 and 281 for Co = 1. The final shape of a square was preserved only for the smallest Courant number, whereas the shape deformed at its outer corners for higher Courant numbers.

Slotted Circle Rotation

In this configuration the shape of a circle with a slot is exposed to a circular velocity field $\mathbf{U}(-y, x)$. The two-dimensional mesh is uniform with 100×100 cells, the rotation axis is at the center of the computational domain $(0, 0)$ and the phase fraction is initialized as the slotted circle placed with its center at the position $(0, 10)$. The diameter of the circle is 50 cells, the slot has the width of 6 cells and

the length 30 cells. The Courant number is Co = 0.2 and the slotted circle was rotated through one revolution with the total number of time steps of 3153. The initial and final shapes obtained after one revolution are shown in Fig. 3.2 with the $\gamma = 0.1; 0.5$ and 0.9 contours. The overall shape is preserved except that the sharp initialized corners of the slot became rounded due to the insufficient mesh resolution.

Circle Stretching in a Shear Flow

In the previous simple advection and rotation tests, the deformation of the free surface is not present, since the velocity field satisfies not only $\nabla \cdot \mathbf{U} = 0$ but also $\partial U_x/\partial x = \partial U_y/\partial y = 0$. A more realistic problem includes the change of the free-surface topology by introducing the shear effects in the flow field. Such configuration is given by the circle placed in a single vortex in which the velocity field is defined as $\mathbf{U}[\sin(x)\cos(y), -\cos(x)\sin(y)]$. The computational mesh is two-dimensional and uniform with dimensions of edges equal to π, divided into 100×100 cells. The phase fraction is initialized as the circle with radius of $\pi/5$ placed at the position $(\pi/2, \pi/4)$. The simulation was performed for 1000 time steps of a fixed size followed by additional 1000 time steps with the reversed sign of the velocity field. The Courant number is set to Co = 0.25. Ideally the initialized shape of a circle should be recovered after the simulation in the reversed direction. Fig. 3.3 shows the final interface shapes, represented as the $\gamma = 0.1; 0.5$ and 0.9 contours, obtained after the forward integration, and after the forward followed by the backward integration. The final obtained shape is slightly deformed, because in the forward integration the interface becomes highly deformed, forming the tail of small thickness comparable with the cell size. Therefore, the tail could not be accurately resolved using the given mesh and the initial shape of a circle could not be completely recovered in the reversed motion.

Droplet Shape Evolution in Zero Gravity

In this configuration the liquid is initialized as having a shape of a cylindrical section (slice) in two dimensions and the evolution of the liquid/gas interface is tracked in time. The mesh is a two-dimensional axisymmetric slice having 100×100 uniformly distributed cells and one cell in the azimuthal direction. The properties of the liquid and the background fluid correspond to those of isopropanol and air, yielding the density and dynamic viscosity ratios of $\rho_l/\rho_g = 682$ and $\mu_l/\mu_g = 126$, respectively, and the surface tension coefficient is $\sigma = 0.0236$ N/m. The computational domain has dimensions of 1×1 mm^2 and the initialized radius and height of the cylindrical section are $R_{cyl} = 0.3$ mm and $H_{cyl} = 0.6$ mm, respectively. The body force due to gravity is absent and, at equilibrium, the surface tension force should be balanced by the pressure force resulting in a pressure jump at the interface from zero outside the droplet to the value in the droplet given by the Laplace equation $\Delta p = 2\sigma/R_{sph}$. The droplet radius at equilibrium results from equality of volumes of the cylinder and the sphere $R_{cyl}^2 \pi \; H_{cyl} = (4/3) R_{sph}^3 \; \pi$ yielding $R_{sph} = 0.343$ mm and the accompanying pressure jump $\Delta p = 137.5$ N/m^2. This theoretical value is compared

with the computed mean pressure inside the droplet determined from the expression

$$p = \frac{\sum_{i=1}^{N} p_i \Delta V_i}{\sum_{i=1}^{N} \Delta V_i}, \tag{3.26}$$

where the summation is performed over the number of cells N where at least 99 % liquid is present, according to the criterion $\gamma \geq 0.99$. Ideally, the pressure inside the droplet should be equal to the Laplace pressure at equilibrium and any existing velocity field represents a numerical artifact, known as the parasitic currents.

In the previous test cases small values for the compression coefficient up to 0.2 were used to obtain the relatively sharp interface regions so that the additional compression term is employed to a small extent. In this test case, the simulation was performed using four different values of the interface compression coefficients and the final obtained shapes of the droplet are shown in Fig. 3.4. The final resolution of the droplet was 35 cells per radius. The effects of the interface compression are illustrated in the droplet shapes in the four quarters corresponding to four simulation results. The sharper interface resolution can be observed for the higher values of C_γ used. The shapes of the interface at several times until reaching the equilibrium are shown in Fig. 3.5 for the two extreme cases, corresponding to $C_\gamma = 0$ and $C_\gamma = 1$. The interface between the phases is represented by five phase fraction contours from $\gamma = 0.1$ to $\gamma = 0.9$. It is seen that the interface region is resolved more sharply in the case where interface compression is invoked.

The droplet radius is tracked in time along the diagonal of the droplet. The representative point at the interface is found as the first point satisfying the criterion $\gamma \geq 0.5$ and the results for the droplet radius normalized with the theoretical value are shown in Fig. 3.6. Small oscillations of the radius are observed indicating the existence of the parasitic currents even in the quasi-equilibrium state. The greatest difference in droplet diameter compared to the theoretical value is less than 1%.

Numerical methods for interface capturing are known to generate artificial velocities instead of keeping steady, velocity-free spherical droplets. Following the work of Lafaurie et al. [52], the expression based on dimensional reasons is defined as the measure of the order of magnitude of the parasitic velocities

$$U_p = K_p \frac{\sigma}{\mu}, \tag{3.27}$$

with the dimensionless number K_p similar to the capillary number, which serves as the measure of the quality of the numerical modeling of surface tension forces. Ideally, the value of K_p should be zero, but the typical reported values are between $K_p \sim 10^{-2}$ in Lafaurie et al. [52] and $5 \cdot 10^{-5} < K_p < 7 \cdot 10^{-7}$ in Vincent and Caltagirone [121]. In the present study the scaling in Eq. (3.27) yielded $K_p \sim 10^{-4}$, as shown in Fig. 3.7, which is in accordance with the previous findings, indicating that the interface compression does not introduce additional artificial velocities. The generated parasitic currents are distributed more smoothly along the interface region in the case where the interface compression is invoked, as can be seen in Fig. 3.8, where the velocity vectors for the models without and with the interface

compression are plotted using the same scaling factor at the time instant when the quasi-equilibrium was reached.

The predicted pressure rise along the droplet's diagonal and the temporal pressure development in the droplet, both normalized with the theoretical value, are shown in Fig. 3.9. After initial oscillations during the formation of the droplet's shape, the mean pressure inside the droplet remains constant. The predicted pressure rise across the interface is more sharp in the case with interface compression, but the mean pressure in the droplet is somewhat lower compared to the theoretical value. This confirms the previous findings of the CSF model being better suitable for more smeared interfaces, which is the reason why in some interface-capturing models the interface region is first artificially smoothed before calculating the surface curvature. Nevertheless, the error in the calculated pressure is within 5% in all cases, being in accordance with the previous findings of Brackbill et al. [10] and Ubbink [116].

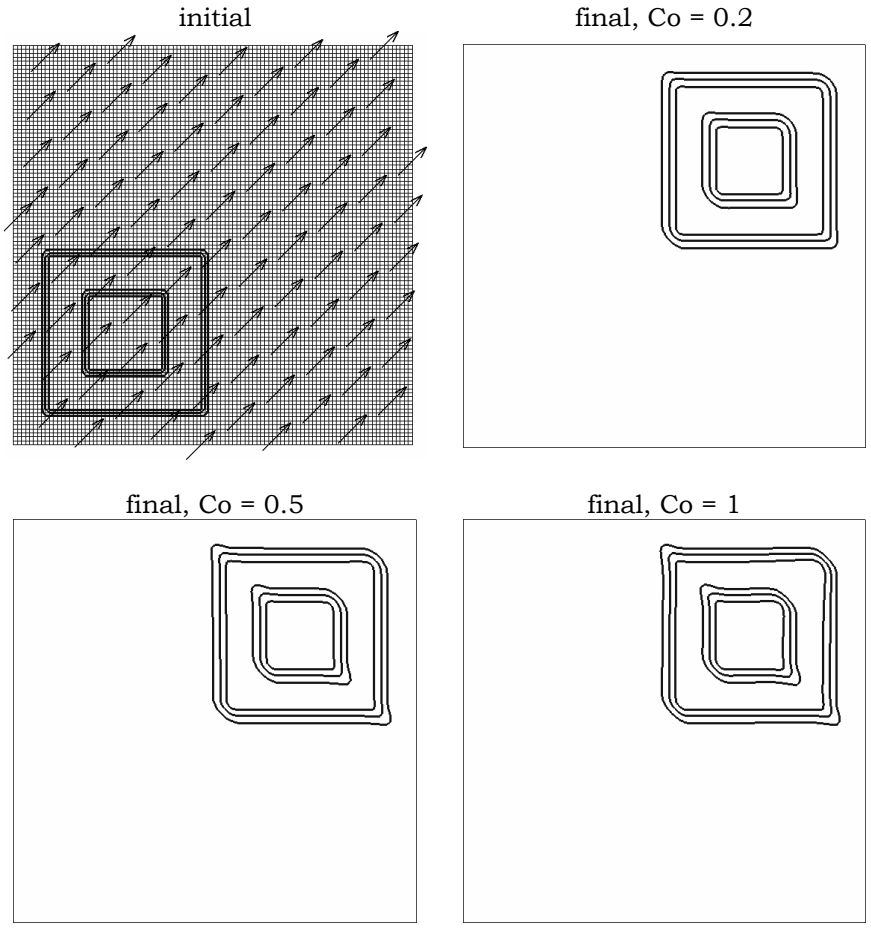

Figure 3.1: Advection of a hollow square in an oblique unidirectional velocity field.

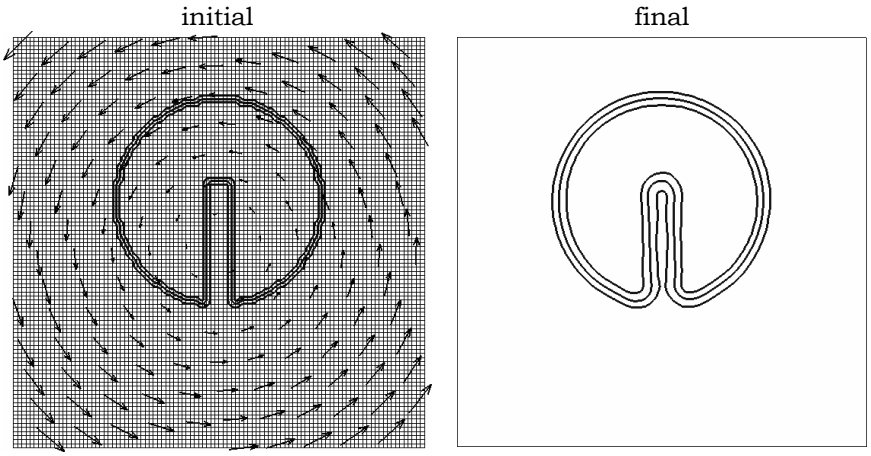

Figure 3.2: Rotation of a slotted circle.

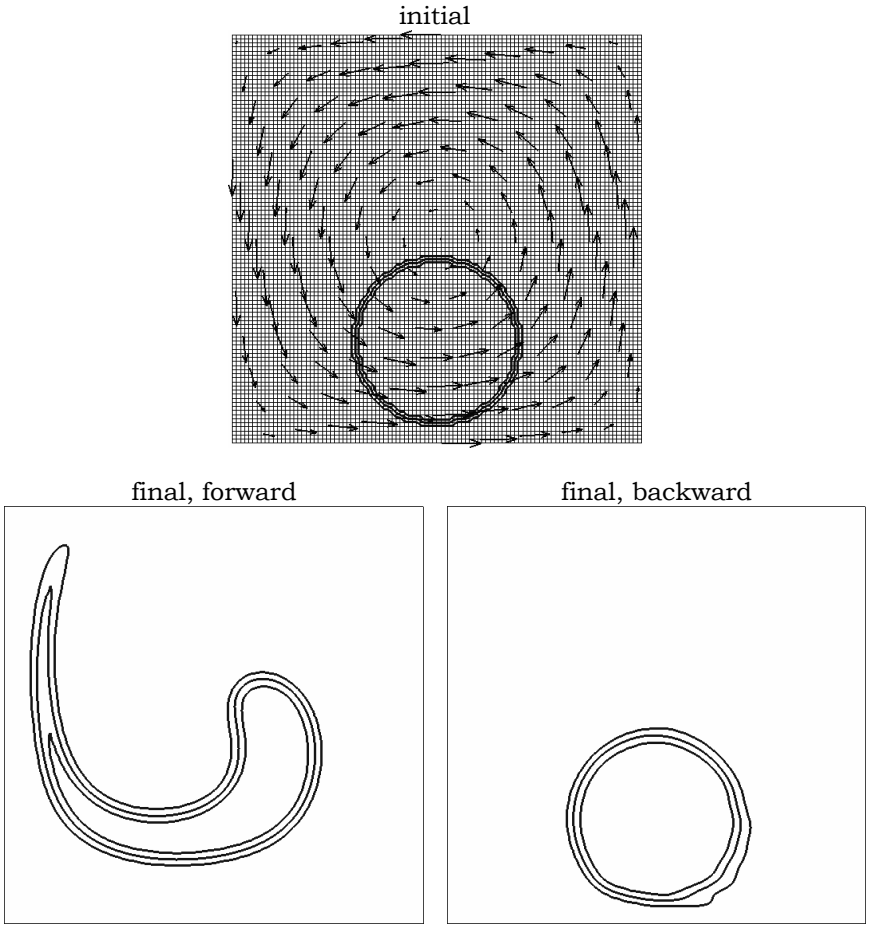

Figure 3.3: Stretching of a circle in shear flow.

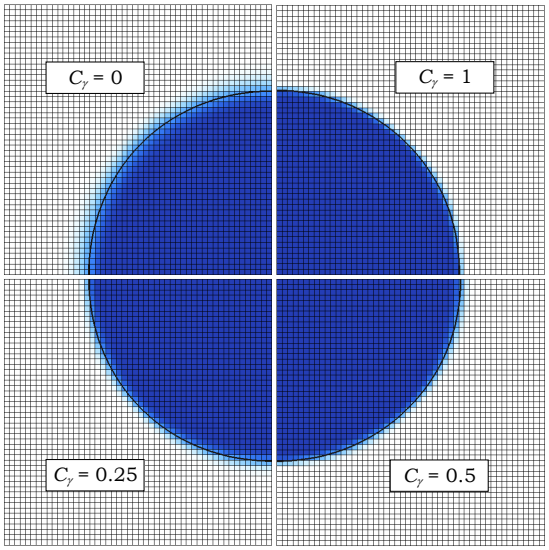

Figure 3.4: Final droplet shapes.

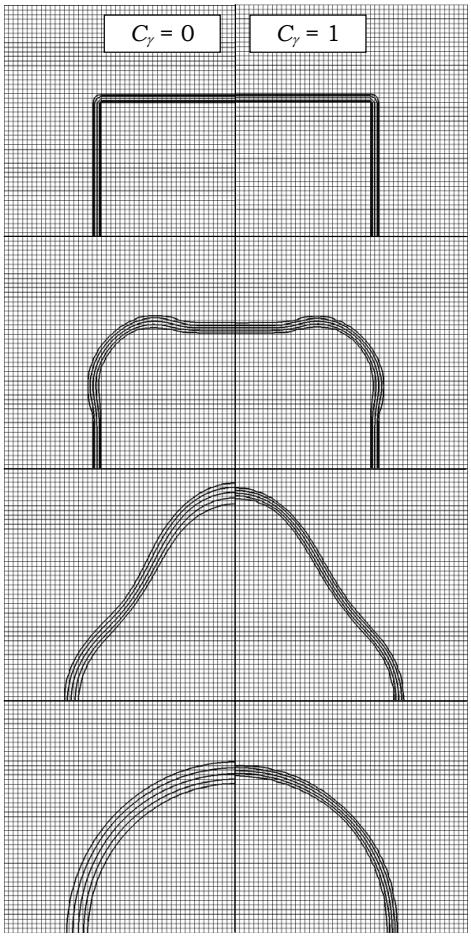

Figure 3.5: Temporal interface shape evolution.

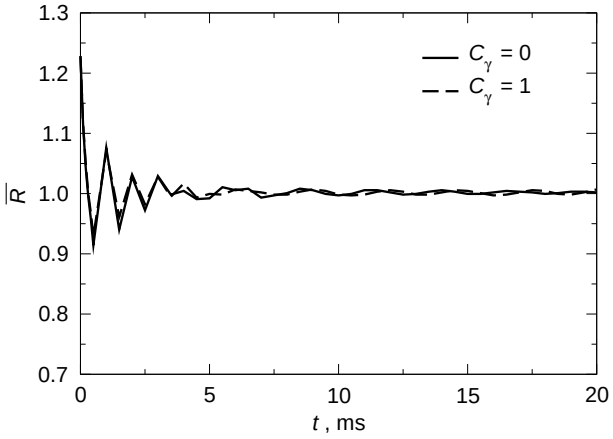

Figure 3.6: Temporal evolution of the droplet radius.

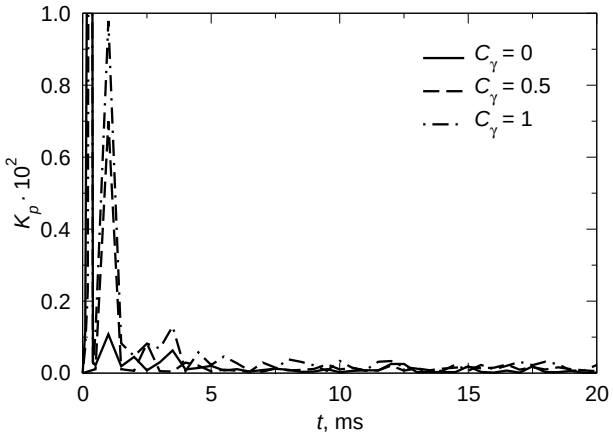

Figure 3.7: Scaled parasitic currents at the interface.

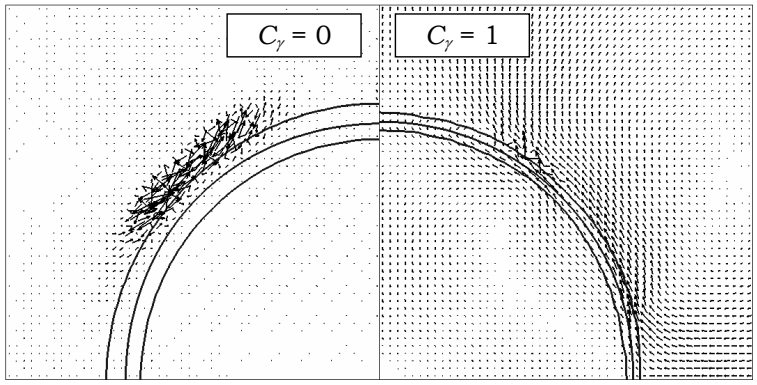

Figure 3.8: Velocity distributions after reaching the quasi-equilibrium state.

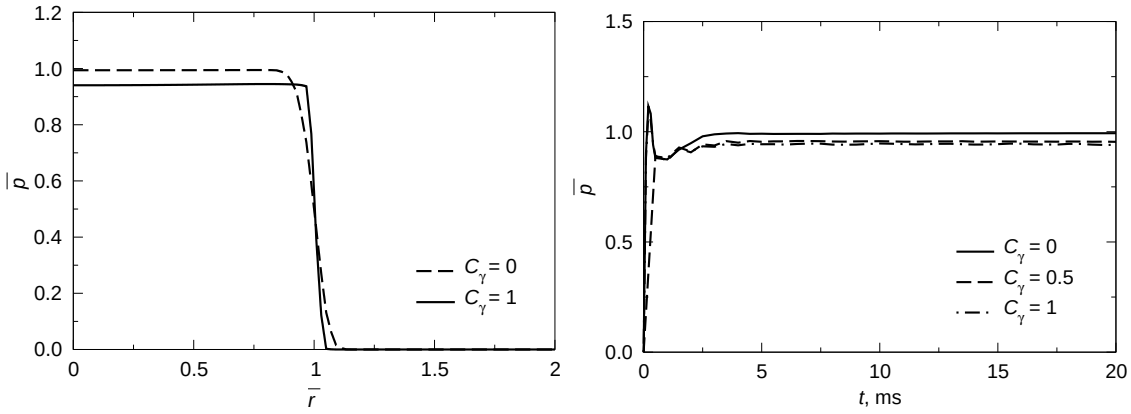

Figure 3.9: Pressure rise across the interface after reaching the quasi-equilibrium state (left) and temporal development of the mean pressure in the droplet (right).

3.4 Drop Collision with a Shallow Liquid Layer

The phenomena involved in drop collisions with various surfaces were the subject of experimental, numerical and also theoretical studies, a comprehensive review of which can be found in Rein [85]. The sequence of events which occurs during the impact of single drops onto films or pools of various depths has been described in Yarin [132]. Much research has been conducted in relation to the crown formation, splashing, the Worthington jet height and bubble entrainment during single drop impact onto thin and deep liquid pools. Less attention, however, has been paid to the phenomena taking place below the surface, in particular the evolution of the crater formed in shallow pools (Shin and McMahon [106], Fedorchenko and Wang [24]), which is important for spray cooling.

An interesting phenomenon, which appears at almost every drop collision with a shallow or deep pool, is the formation of a capillary wave after impact. This concentric capillary ripple travels along the crater sidewall and changes the shape of the crater from hemispherical for deep pools or from oblate for shallow pools to a conical shape. In Oğuz and Prosperetti [68] and Morton et al. [59] the origin of this traveling capillary wave was related to the strong surface disturbance immediately after the initial contact of the impacting drop with the undisturbed liquid surface. For deep pools, several authors found that when this capillary wave reaches the bottom of the crater at a certain time instant, its crest closes concentrically to trap an air bubble (Morton et al. [59], Deng et al. [19]). The inertia dominated capillary waves on a nearly planar, radially expanding liquid lamella resulting from drop impact are well understood. The analysis of such waves can be found in Yarin and Weiss [135] and some other capillary waves resulting from drop impact on liquid layers were reported in Weiss and Yarin [126], which lead to the ejection of a jet.

In this Section the numerical and theoretical investigations of a normal drop collision with a liquid layer of a finite thickness are presented. The formation and evolution of the crater formed within the layer upon the impact are investigated for

various layer thicknesses, drop impact velocities and using the properties of three different liquids. The study focuses on the description of the crater penetration, expansion, formation of the residual film on the substrate, as well as on the emergence and propagation of a sharp-edged axisymmetric capillary wave.

3.4.1 Theoretical Model for the Penetration Depth

In most of the existing theoretical studies of drop impact onto a deep pool the crater penetration is described using the energy balance approach, where the shape of the crater is approximated by an expanding sphere (Prosperetti and Oğuz [79], Fedorchenko and Wang [24]). Such approximation is based on the assumption that the crater expands equally in all directions.

A theoretical model for the crater penetration in a semi-infinity liquid is derived based on the balance of the linear momentum of the liquid around the crater (Berberović et al. [8]). Penetration of the crater is shown schematically in Fig. 3.10 in a spherical coordinate system with the origin fixed at the point of impact at the initial level of the liquid layer. The penetration depth of the crater is denoted z_{cr} and the penetration speed is $U_{cr} = \mathrm{d}z_{cr}/\mathrm{d}t$.

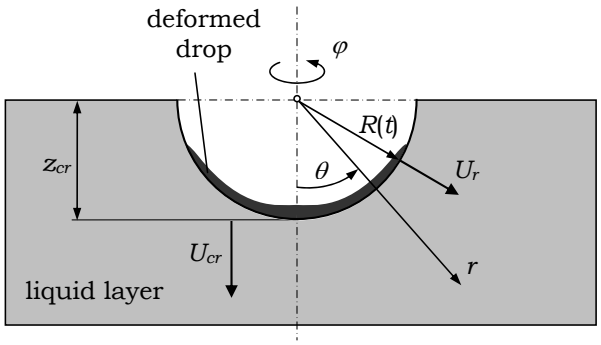

Figure 3.10: Sketch of the penetrating crater.

Since the impacting drop deforms during penetration, the penetration depth is roughly approximated by the position of the drop/layer interface at the impact axis. The penetration depth initially increases with almost constant velocity, which is approximately half of the impact velocity and depends only weakly on the surface tension, viscosity or layer thickness. The velocity of high-speed jet penetration whose density equals the density of the target, $U_{cr} \approx 0.5U_0$, is well-known in penetration mechanics (for example the penetration of an eroding metal projectile into an elastic-plastic target, Yarin et al. [134]). The corresponding penetration depth is $z_{cr} \approx U_0 t/2$ and the duration of this stage is finite, $t = 2D_0/U_0$, determined by the rate of the drop erosion, which is proportional to $U - U_{cr}$.

At the times $t > 2D_0/U_0$ the crater propagates only due to the inertia of the flow in the liquid layer and decelerates. At this stage the shape of the crater is approximated as a spherical crater with the center coinciding with the origin of the coordinate system fixed at the point of impact. The flow in the layer is similar

to the flow induced by a single spherical bubble changing in size, produced by an underwater explosion (Batchelor [6]). If the penetration depth is much smaller than the initial layer thickness, the flow around the crater can be approximated by a potential velocity field in the semi-infinite space. The velocity field in the liquid layer and the corresponding velocity potential in that case are given by Batchelor [6]

$$U_r = \frac{R^2}{r^2}\frac{\mathrm{d}R}{\mathrm{d}t}, \quad U_\theta = U_\varphi = 0, \tag{3.28}$$

$$\Psi = -\frac{R^2}{r}\frac{\mathrm{d}R}{\mathrm{d}t} \tag{3.29}$$

where $\mathrm{d}R/\mathrm{d}t$ is the radial velocity of propagation of the crater surface.

If the Froude number is much higher than unity the effect of gravity at the initial stage of crater expansion is negligibly small. If, in addition, the penetration depth is much smaller than the capillary length $\sqrt{\sigma/(\rho g)}$, the deviation of the crater shape from the spherical can also be neglected. The expression for the pressure field in the liquid can be obtained from the Bernoulli equation in the following form

$$\frac{\partial \Psi}{\partial t} + \frac{1}{2}U_r^2 + \frac{p}{\rho} = f(t), \tag{3.30}$$

where $f(t)$ is a function of time only. It can be shown that $f(t) = 0$ since the liquid velocity vanishes at $r \to \infty$. Substituting in Eq. (3.30) the expressions for the liquid velocity, Eq. (3.28), and velocity potential, Eq. (3.29), yields the following expression for the pressure distribution at the crater surface ($r = R$)

$$p_{cr} = \rho\frac{\mathrm{d}^2R}{\mathrm{d}t^2}R + \frac{3}{2}\rho\left(\frac{\mathrm{d}R}{\mathrm{d}t}\right)^2. \tag{3.31}$$

It should be noted that this pressure field is valid even if the viscosity of the liquid is significant. The viscous part of the radial component of the stress tensor at the crater surface is of order $4\mu(\mathrm{d}R/\mathrm{d}t)/R$, the pressure jump associated with the surface tension is $2\sigma/R$ and the hydrostatic pressure is $\rho g R$. These terms are negligibly small in comparison with the inertial stresses in Eq. (3.31) if the Reynolds, Weber and Froude numbers are much higher than the unity. In this case the equation of the crater penetration and expansion can be obtained from the condition that the pressure in the liquid vanishes at the crater surface. Moreover, in this model the penetration depth z_{cr} of the crater is equal to the crater radius R, as seen in Fig. 3.10. The asymptotic equation for the crater penetration is written with the help of Eq. (3.31) in the following dimensionless form, similar to the equation of rising of a spherical-cap bubble in Batchelor [6]

$$\frac{\mathrm{d}^2\overline{z}_{cr}}{\mathrm{d}\overline{t}^2} = -\frac{3}{2\overline{z}_{cr}}\left(\frac{\mathrm{d}\overline{z}_{cr}}{\mathrm{d}\overline{t}}\right)^2. \tag{3.32}$$

It is emphasized that Eq. (3.32) for the crater penetration is valid only for the initial stage of crater penetration when the deformation of the shape of the spherical

crater due to the gravity and capillary effects is negligibly small. The corresponding analytical solution of Eq. (3.32) for the crater depth is

$$\overline{z}_{cr} = 2^{-4/5}\left(5\overline{t} - 6\right)^{2/5}, \quad \overline{t} > 2. \tag{3.33}$$

In Fig. 3.11 the experimental data from Engel [23] and Elmore [22] for the penetration depth of the crater is compared with the theoretical predictions obtained using Eq. (3.33). In the case of high impact Weber and Froude numbers the asymptotic formula agrees very well with the experiments. In the case of relatively smaller impact velocity the influence of the gravity, viscosity and surface tension become significant leading to some deviation from the asymptotic solution and even to the damping of the penetration by gravity and capillary forces which are not accounted for in the obtained approximate solution, Eq. (3.33).

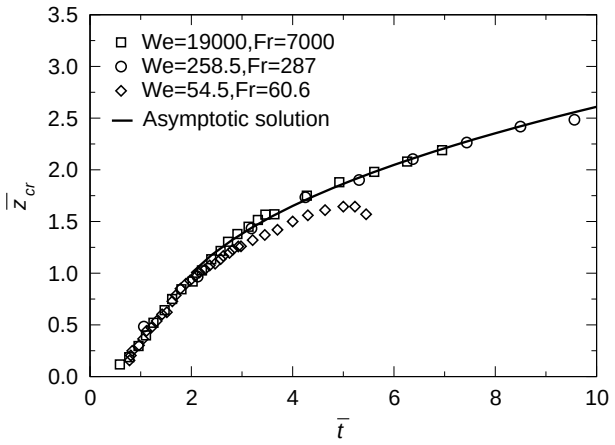

Figure 3.11: Drop impact onto a deep pool: comparison of the asymptotic solution, Eq. (3.33), for the penetration depth of the crater with the experimental data from Engel [23] and Elmore [22] (symbols).

The receding of the crater diameter can differ significantly from the receding of the crater in the axial direction, leading to a decrease of the crater penetration length. In this stage the shape of the crater changes significantly due to occurrence of capillary waves. Moreover, in some cases when the crater diameter recedes while the tip continues to penetrate, the impact leads to the formation of bubble entrainment (Elmore et al. [22]). The crater form at this stage cannot be approximated by the simple shape of a sphere and therefore, the theory is not valid for the receding phase of the crater motion. The asymptotic solution given by Eq. (3.33) for the penetration depth agrees well with the experimental data at the initial stage of penetration if the Reynolds and Weber numbers are high.

The experimental data from van Hinsberg [118] for the crater penetration length for various impact parameters and initial layer thicknesses is shown in Fig. 3.12 in comparison with the theoretical predictions. The deviation from Eq. (3.33) is determined by the initial layer thickness, or more precisely, by the vicinity of the crater tip to the rigid substrate. For example, the case with We = 315 corresponds

to $\overline{H} = 2$ whereas the case with We = 328 corresponds to $\overline{H} = 1$ leading to earlier deviation from the theory developed for deep pool. These results also demonstrate that wall effects may be significant already at the initial stages of drop impact. The most reliable way to predict such phenomena is using the numerical simulations of the flow.

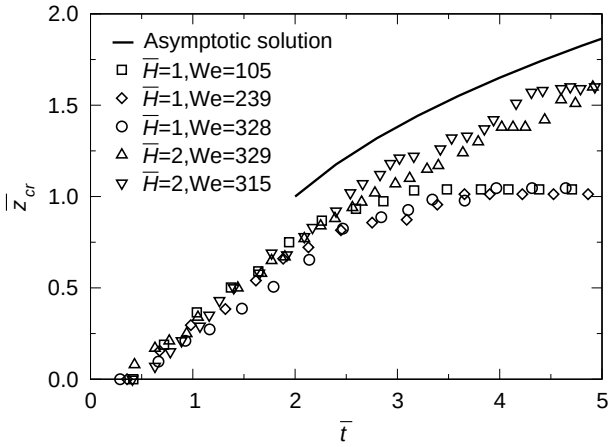

Figure 3.12: Drop impact onto a liquid layer of finite thickness: experimentally obtained penetration depth of the crater from van Hinsberg [118] (symbols) as a function of time for various layer thicknesses compared to the asymptotic solution, Eq. (3.33).

3.4.2 Numerical Simulations

The computational domain has the form of an axisymmetric slice with the mesh having one cell in the azimuthal direction, Fig. 3.13. The symmetry in azimuthal direction is presumed in accordance with the experimental observations. The dimensions of the solution domain in the vertical plane are $15D_0 \times 15D_0$ for distilled water, $21D_0 \times 21D_0$ for isopropanol and $17D_0 \times 17D_0$ for glycerin/water mixture, based on the drop initial diameter. The mesh is adaptively refined in the region of the crater development, having in total ≈ 70000 cells.

It could be observed in experiments, as well as in calculations with coarser meshes, that the liquid layer was not significantly affected at radial distances greater than approximately one third of the radial length of the solution domain, since the process of drop impact occurs very fast. Therefore the mesh was appropriately refined only in this region of the solution domain, where the process of drop impact takes place.

At the initial time, the distribution of phase fraction is prescribed in the cells of the mesh, defining the position and the shape of the interface at the beginning of the calculation. The shape of the drop in experiments just before the impact deviated negligibly from that of a sphere. Therefore, the drop in simulations is placed at a

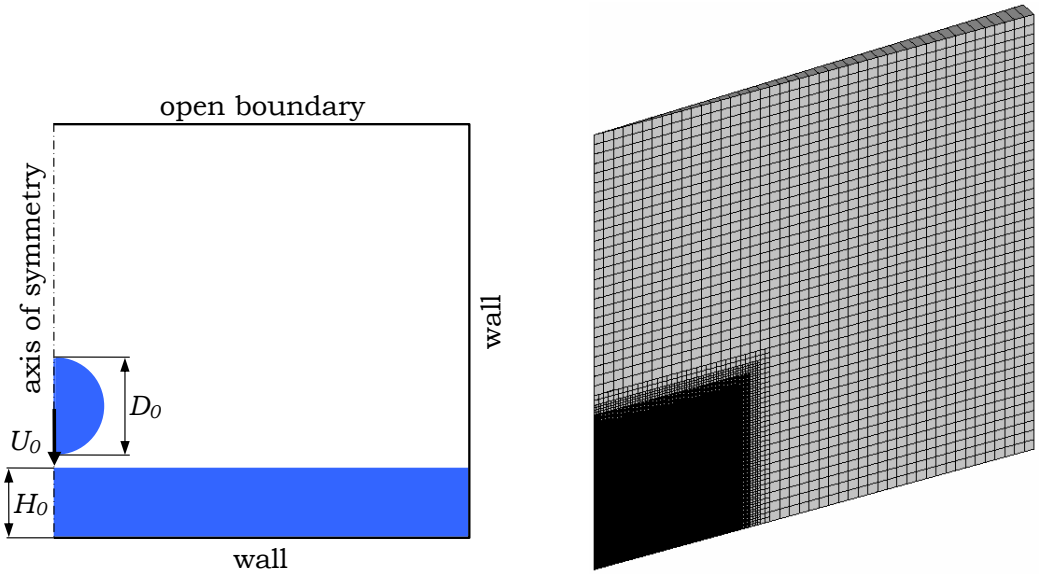

Figure 3.13: Initial case configuration (left) and computational mesh (right).

small initial distance from the liquid layer surface corresponding to a dimensionless time of $\bar{t} = 0.2$, thus allowing several time steps to be computed and the flow to develop before the first contact of the drop with the surface. Since the distance is very small the velocity change due to gravity and drag is negligibly small and the initial drop velocity is thus set equal to the drop impact velocity from experiments.

In addition to the axial symmetry, the bottom and the right side boundaries are set as walls with the no-slip condition prescribed. The top boundary is open with prescribed total pressure consisting of static and dynamic pressure, thus allowing the static pressure to be adjusted according to the calculated velocity field. At the walls the zero gradient is set for the modified pressure in accordance with its definition. Since the contact region of the crater with the bottom of the dish could not clearly be observed in the experiments, it was not possible to discern whether the bottom surface remained wetted or became completely or partially dry. Therefore, wall adhesion was not taken into account and correspondingly the zero-gradient condition for the phase fraction equation is set.

Experimental results are provided by van Hinsberg [118] where three liquids were used: distilled water, isopropanol and a glycerin/water mixture consisting of 70% glycerin and 30% water. The fluid of the drop and the layer was the same in all experiments. The initial drop diameter D_0 was 2.9 mm for distilled water, 2.14 mm for isopropanol and 2.67 mm for glycerin/water mixture. The drop impact velocity U_0 (velocity just before the drop reaches the surface) was varied from 1.68 m/s to 2.91 m/s for distilled water, from 1.7 m/s to 2.83 m/s for isopropanol and from 1.81 m/s to 3.25 m/s for glycerin/water mixture. The liquid layer thickness was varied for all liquids yielding three different dimensionless layer thickness which were used in the experiments, namely $\overline{H} = 0.5; 1; 2$. The reported errors in holding a constant thickness of the liquid layer in the experiments were 3–7% for distilled water, 2–10% for isopropanol and 1–5% for glycerin/water mixture. Comparison

of different cases is enabled by the use of the dimensionless numbers governing the impact process, the covered range of which is listed in Table 3.1 along with the physical properties.

Table 3.1: Physical properties of liquids and ranges of dimensionless numbers used in the numerical simulations.

	distilled water	isopropanol	glycerin/water
density ρ, kg/m^3	999	805	1179
viscosity μ, Ns/m^2	$9.9{\cdot}10^{-4}$	$2.3{\cdot}10^{-3}$	$18.57{\cdot}10^{-3}$
surface tension σ, N/m	$7.27{\cdot}10^{-2}$	$2.36{\cdot}10^{-2}$	$6.68{\cdot}10^{-2}$
Ohnesorge number	0.0021	0.0112	0.0409
Weber number	113 - 312	189 - 644	151 - 505
Reynolds number	4744 - 8587	1200 - 2010	299 - 561
K parameter	1331 - 3675	1101 - 3883	524 - 1814

3.4.3 Results and Discussion

3.4.3.1 Assessment of the Interface-compression Algorithm

In order to illustrate the effects of the interface-compression algorithm, simulations of a selected drop impact case were performed using the formulations with and then without the interface-compression term. The case in question corresponds to the glycerin/water mixture and impact parameters $\overline{H} = 1$, We = 329 and Re = 428. The results obtained in the simulations using both approaches are contrasted in Fig. 3.14. The interface is represented as the region situated between black lines corresponding to the values of phase fraction $\gamma = 0.1$ and $\gamma = 0.9$ and indicating the region of the free surface.

All details describing the case considered with respect to the computational mesh, initial and boundary conditions, dimensionless numbers and physical properties are equal in both simulations. It can be seen that the interface region captured using the model with interface compression exhibits much higher resolution during all stages after impact. This can be observed even at the time corresponding to the first contact between drop and the layer, where the interface already appears more smeared in the case without interface compression. The solution at later stages becomes non-physical, as can be seen for instance at $\bar{t} = 28.67$. On the other hand the introduction of the compression term leads to a physically plausible solution and the sharpness of the interface is preserved. Accordingly, all computational results displayed in the reminder of the study have been obtained using the algorithm with the included interface compression term.

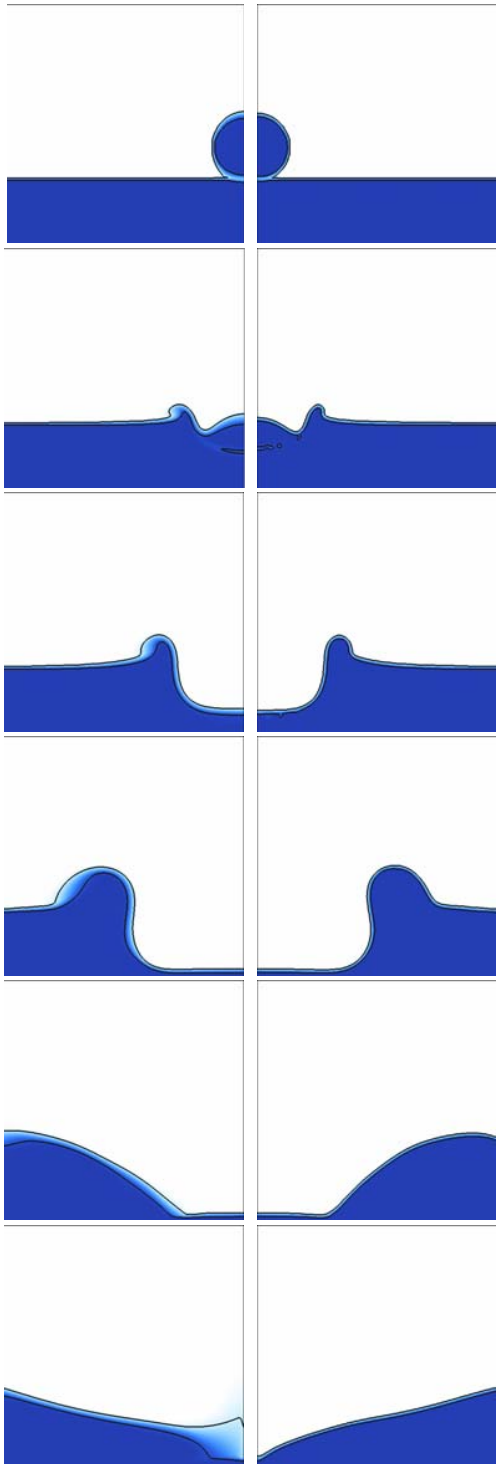

Figure 3.14: Time evolution of the crater shape for the impact of a glycerin/water mixture drop, $\overline{H} = 1$, We = 329, Re = 428, K = 1182: results obtained without (left) and with interface compression (right). Time instants from top to bottom are $\bar{t} = 0, 0.99, 2.47, 9.89, 19.76, 28.67$.

3.4.3.2 Penetration and Expansion of the Crater

First comparison between experiments and simulations relates to the time evolution of the crater shape. Fig. 3.15 and Fig. 3.16 show the crater shape at different time instants for the flow configuration corresponding to $\overline{H} = 2$ for isopropanol and distilled water, respectively. Immediately upon impact, a small circumferential free liquid jet is ejected upward. The geometry of this free jet (its height, shape and width) depends on the drop impact velocity, liquid properties and liquid layer thickness. Inside the liquid layer the drop impact leads to the formation of the crater, which penetrates into the layer and simultaneously expands radially. During the spreading period inertial forces are dominant over viscous and capillary forces since the Reynolds and Weber numbers are much higher than unity.

After reaching the maximum diameter, the crater begins a receding motion driven by capillary forces. It can be seen that the crater shape changes from a spherical form in the advancing motion to a conical one during the receding phase. The results of simulations indicate also that during the early stages of the impact the crater has a concave surface in its upper part. Afterwards, the crater is fully formed until its bottom becomes convex. This could not be observed in experiments due to capillary rise of the liquid layer meniscus at the side walls of the dish where it was placed and because of the ejected liquid sheet. Consequently, for the purpose of comparison, the measured crater depth is related to the lowest point at the surface of the crater obtained in the simulations.

The present axisymmetric simulations are not capable of describing precisely the three-dimensional nature of the flow in the uprising jet leading to the rim instability and in some cases to splash. For capturing such effects, a full three-dimensional computational model would be required, accompanied by additional considerations of physical perturbations leading to instability. Moreover, the exact shape of this jet cannot be easily compared with the experiments since the camera is focused on the crater, which is the main subject of the present study. Nevertheless, the influence of the three-dimensional effects on the dynamics of the crater propagation is regarded to be small in the considered range of the drop impact parameters. This assumption is further confirmed by correctly capturing the generation and propagation of the capillary wave at the crater sidewall.

For the purpose of a quantitative analysis, crater depth and diameter are made dimensionless through division by the initial drop diameter, and the measured values are compared to predicted ones. In the experiments the depth is measured at the lowest point of the crater observed in photographs, and the diameter is determined at a half layer thickness, $\overline{z} = 0.5$, whereas in the simulations the corresponding depth and the diameter are determined using computational cells where the value of the phase fraction becomes $\gamma \geq 0.5$.

Plots of dimensionless crater diameter and depth against dimensionless time are shown in Fig. 3.17 for isopropanol, distilled water and glycerin/water mixture, in graphs in the top, middle and bottom row, respectively. The agreement between

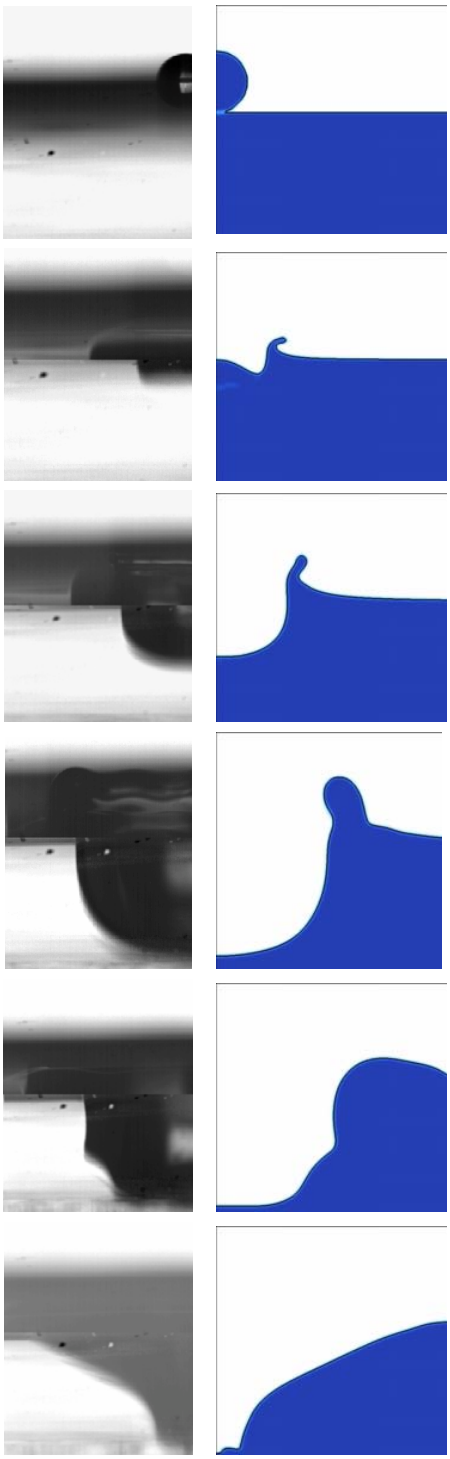

Figure 3.15: Time evolution of the crater shape for the impact of an isopropanol drop, $\overline{H} = 2$, We = 392, Re = 1730, K = 2364: experiment (left) and simulation (right). Time instants from top to bottom are $\bar{t} = 0, 1.08, 2.71, 10.84, 21.68, 31.44$

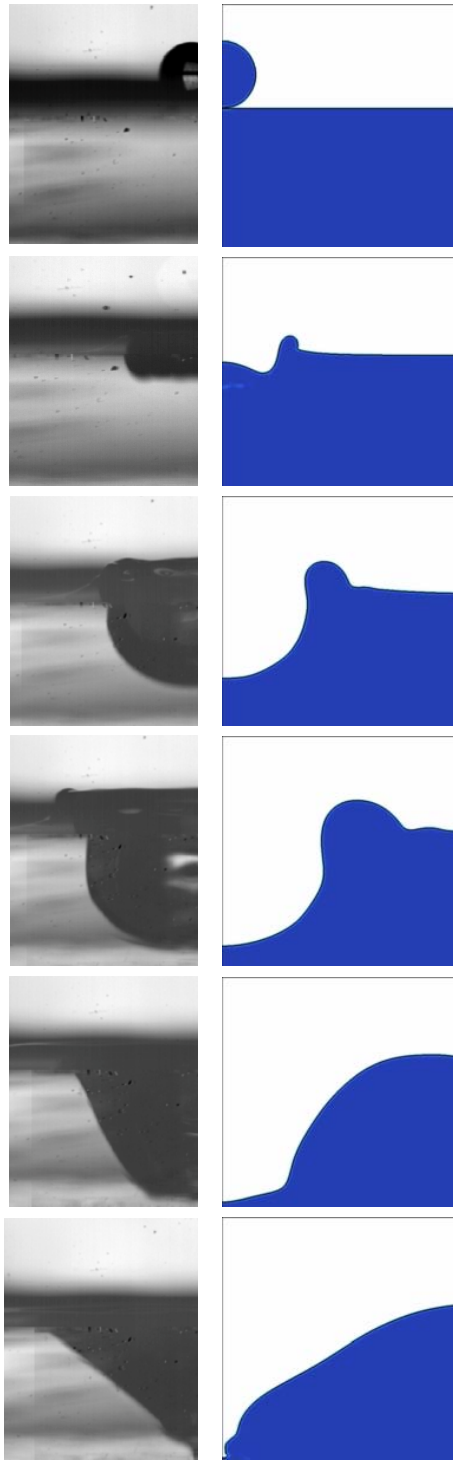

Figure 3.16: Time evolution of the crater shape for the impact of a distilled water drop, $\overline{H} = 2$, We = 215, Re = 6750, K = 2533: experiment (left) and simulation (right). Time instants from top to bottom are $\bar{t} = 0, 1.21, 4.03, 8.06, 16.13, 20.97$

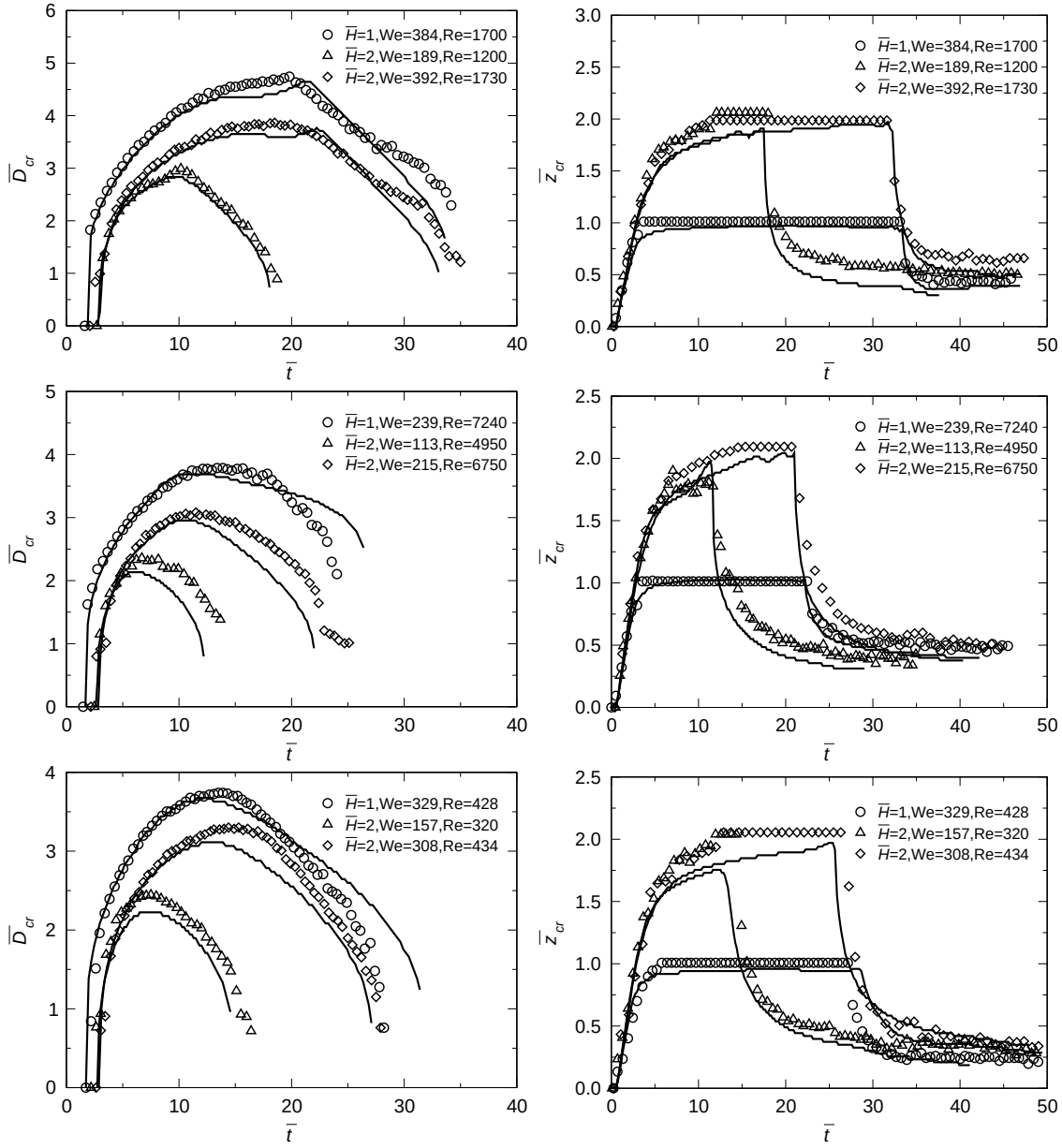

Figure 3.17: Computationally obtained dimensionless crater diameter (left) and crater depth (right) compared to the experimental data from van Hinsberg [118] for the impact of an isopropanol drop (top row), a distilled water drop (middle row) and a glycerin/water mixture drop (bottom row).

the numerical predictions (lines) and the experimental data from van Hinsberg [118] (symbols) is very good during the spreading phase, showing some deviations in the receding phase of the crater motion.

3.4.3.3 Residual Thickness of the Film between the Crater and the Bottom

When the crater approaches the bottom the penetration velocity decreases due to the wall effects. When the inertia of the liquid flow is strong enough, the thickness of the film below the crater follows the remote asymptotic solution of Yarin and Weiss [135] and decreases as the inverse of the time squared. At some time instant the film thickness becomes comparable with the thickness of the viscous boundary layer. The flow in the film is damped by viscosity. The remaining thin film thickness is much smaller than the initial thickness of the liquid layer. This phase corresponds to the *plateau* region in graphs showing the crater depths in Fig. 3.17.

The value of the residual film thickness is rather important for the modeling of heat transfer associated with drop or spray impact and prediction of the film breakup. However, since the residual film thickness is much smaller than the initial drop diameter and the initial thickness of the liquid layer, its experimental evaluation is very difficult. In the present study this value is determined from the numerical simulations. The predicted values of the residual film thickness $\overline{h}_{res} = h_{res}/D_0$ are given in Table 3.2 for various impact parameters.

Table 3.2: Residual film thickness predicted using the numerical simulations.

liquid	We	Re	K	$\overline{H}$	$\overline{h}_{res}$
isopropanol	384	1700	2238	1	0.01631
isopropanol	189	1200	1101	2	0.05650
isopropanol	392	1730	2364	2	0.04425
distilled water	239	7240	2815	1	0.00449
distilled water	113	4950	1331	2	0.02802
distilled water	215	6750	2533	2	0.01796
glycerin/water	329	428	1182	1	0.01534
glycerin/water	157	320	564	2	0.09206
glycerin/water	308	434	1106	2	0.08193

The dimensionless time $\overline{t}_b$ at which the crater almost reaches the bottom lies within the interval $12 < \overline{t}_b < 14$ for $\overline{H} = 2$ and $3 < \overline{t}_b < 5$ for $\overline{H} = 1$. The thickness of the boundary layer at this time instant is approximately $\overline{h}_{bl} \sim \sqrt{\overline{t}_b/\mathrm{Re}}$. When the crater approaches the bottom, the film thickness follows the remote asymptotic solution of Yarin and Weiss [135]. At larger times after impact the final thickness and the penetration velocity can be written in the simplified form as

$$\overline{h}_{cr} = \overline{H} - \overline{z}_{cr} \sim \overline{t}^{-2}, \tag{3.34}$$

$$\overline{U}_{cr} = \frac{\mathrm{d}\overline{h}_{cr}}{\mathrm{d}t} \sim \overline{t}^{-3}. \tag{3.35}$$

Therefore, the time instant at which the boundary layer reaches the free surface of the crater is $\overline{t}_{bl} \sim \mathrm{Re}^{1/5}$ and the crater velocity at this instant is $\overline{U}_{cr} \sim \mathrm{Re}^{-3/5}$. The film thickness $\overline{h}_{bl}$ corresponding to the time instant $\overline{t}_{bl}$ can be easily estimated from Eq. (3.34) as $\overline{h}_{bl} \sim \mathrm{Re}^{-2/5}$.

The residual film thickness is smaller than $\overline{h}_{bl}$ since the inertia of the fluid at the time instant $\overline{t} = \overline{t}_{bl}$ is still significant. The value of the residual film thickness is estimated assuming the creeping flow in the film from Bakshi et al. [4] in the following form

$$\overline{h}_{res} = \frac{\overline{h}_{bl}^{9/14}}{\left(\frac{1}{\overline{h}_{bl}} + \frac{14\mathrm{Re}\overline{U}_{cr}}{15}\right)^{5/14}}. \tag{3.36}$$

The scaling analysis leads to the following relation between the residual film thickness and the Reynolds number

$$\overline{h}_{res} = A\mathrm{Re}^{-2/5}. \tag{3.37}$$

The coefficient A depends on the dimensionless initial film thickness, Weber and Froude numbers. However, the dependency on the Weber and Froude numbers is weak if they are much larger than unity. Fig. 3.18 displays the comparison of the numerically predicted residual film thickness in terms of the impact Reynolds number. The scaling relation, Eq. (3.37), describes well the tendency of the obtained results.

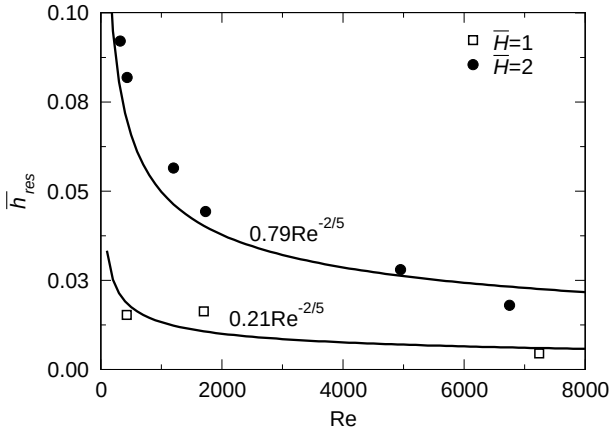

Figure 3.18: Computationally obtained residual film thickness under the crater as a function of the impact Reynolds number.

After some period of time the capillary forces become significant and the crater starts to contract, leading to the emergence of a central jet. The crater contraction starts earlier at impact parameters corresponding to smaller Weber numbers, for which the influence of the surface tension is more significant. The evolution of the diameter of the crater first follows the square-root dependence obtained from the remote asymptotic solution of Yarin and Weiss [135]. At longer times its propagation is governed by surface tension and gravity (Roisman et al. [98]). The maximum crater diameter and the corresponding duration of the crater expansion and merging are mainly determined by the impact Weber number.

3.4.3.4 Pressure and Velocity Fields

Computationally obtained pressure and velocity fields for impact of isopropanol drop at $\overline{H} = 2$, We = 392 and Re = 1730 are shown in Fig. 3.19 and Fig. 3.20, respectively, at several stages after the collision including the time instant when the drop first hits the surface of the liquid layer. For the sake of clarity, the velocity vectors are plotted using randomly spaced tracers.

The experimental data for these fields cannot be easily collected. On the other hand the knowledge about the pressure magnitudes in the flow is rather important for the modeling of the substrate erosion, splash, spray cleaning, drop impact onto a porous or elastic target, etc. A detailed description of the velocity field in the liquid layer initiated by drop impact is necessary for the reliable modeling of hydrodynamics of spray coating and spray cooling.

The pressure distribution at various instants of time is shown in Fig. 3.19. It can be seen that at the moment when the drop touches the liquid layer, a high pressure is formed in the region of contact. As a consequence of this, the liquid is ejected in a radially upward direction. As the drop penetrates into the layer, the liquid sheet straightens, driven by the local velocity field and a small deviation of the inner part of the sheet surface is observed. A relatively high pressure region can be identified at the edge of the uprising sheet. This region with the relatively high curvature corresponds to the formation of a rim (Taylor [111]). The velocity of the rim differs from the velocity of the sheet since its dynamics is determined mainly by the capillary forces. The pressure in the rim is not uniform due to the change of the curvature of the rim surface. The pressure gradient inside the rim is caused by its acceleration in the downward direction. It is interesting to note that the pressure in the rim does not change significantly even at the later stages of the sheet motion when the radius of the rim cross-section is relatively high.

The velocity field confined to the region occupied by the liquid at various time instants is shown in Fig. 3.20. At the moment when the drop hits the liquid layer the air velocities near the free surfaces are also shown, indicating a high speed flow of the air escaping from the space between the falling drop and the liquid layer. The vector plots and velocity magnitudes at the initial stages upon the impact show a radially outward oriented velocity distributions, with respect to the origin coinciding with the point of impact, thereby resembling closely the theoretically assumed potential flow in the liquid near the crater surface. According o these results, the evolution of the free surface is mainly caused by the velocity of the liquid in the region near the free surface with negligible influence of the surrounding air motion. Furthermore, the reduction of the velocity magnitude in time can be observed as the crater is decelerating. At later stages the velocity distribution becomes more complex, including some vortex-like motions, and cannot be approximated using a simple velocity potential.

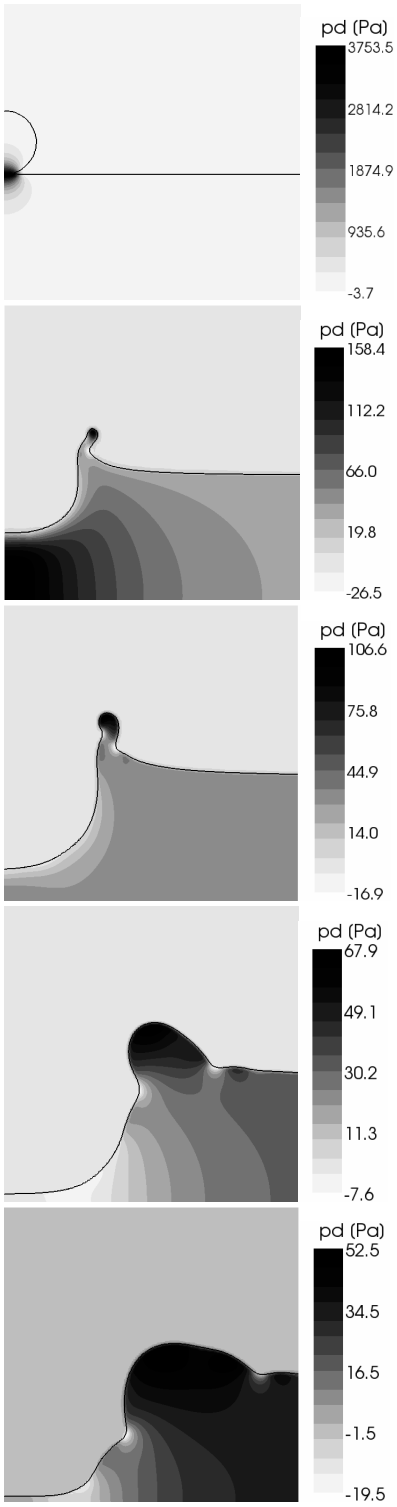

Figure 3.19: Predicted iso-contours of the pressure field for the impact of an iso-propanol drop: $\overline{H} = 2$, We $= 392$, Re $= 1730$, K $= 2364$. Time instants from top to bottom are $\bar{t} = 0, 2.71, 5.42, 16.26, 21.68$.

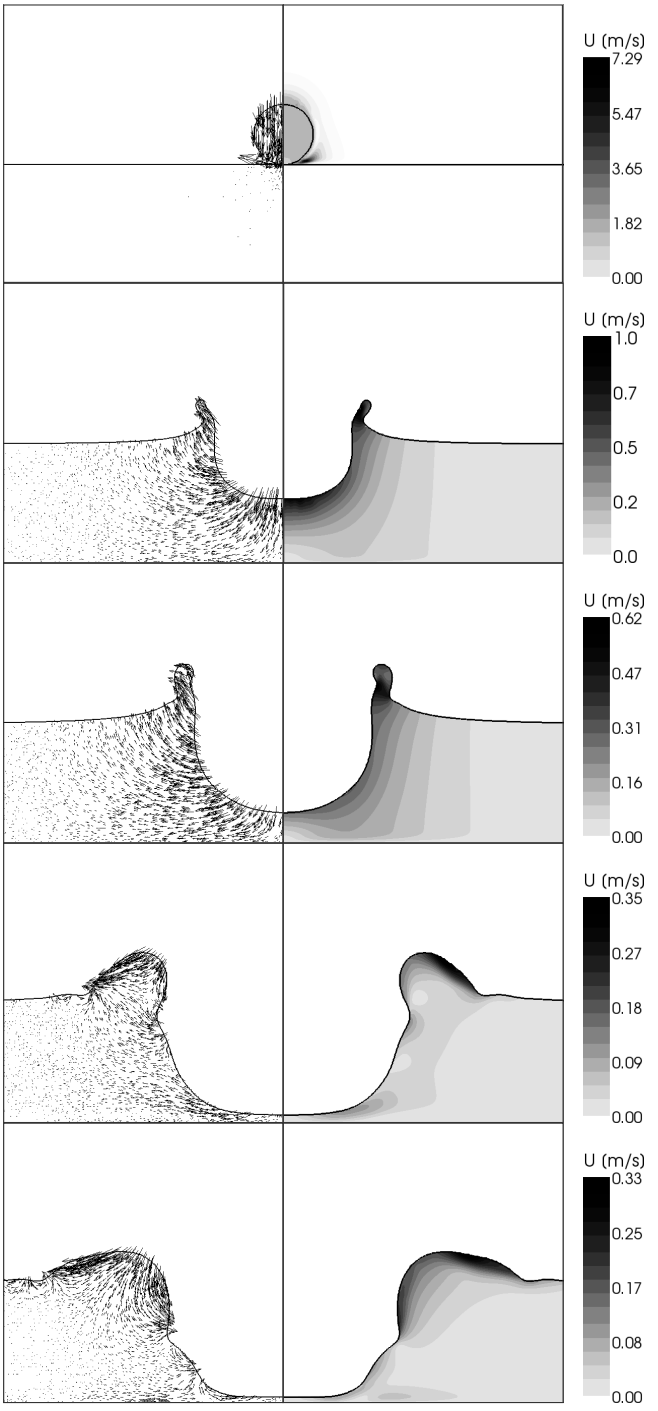

Figure 3.20: Predicted velocity vectors (left) and iso-contours of velocity magnitude (right) for the impact of an isopropanol drop: $\overline{H} = 2$, We $= 392$, Re $=$ 1730, K $= 2364$. The time instants from top to bottom correspond to $\bar{t} = 0, 2.71, 5.42, 16.26, 21.68$.

3.4.3.5 Initiation of the Capillary Wave

One of the most spectacular phenomena related to drop collision with the liquid layer is the generation of a rather sharp capillary wave on the surface of the crater. It is interesting that once the wave is created, its outer corner is rather sharp, indicating a strong local pressure drop. The wave propagates along the crater surface downwards, merging at the bottom of the crater and finally leads to the creation of a central jet (Zhang and Thoroddsen [136]). Similar waves have been observed in many experiments on drop impact onto a liquid layer or liquid pool (Morton et al. [59], Deng et al. [19]). The mechanism of the formation of these capillary axisymmetric waves and their propagation is not immediately clear.

Such a capillary wave is observed at the surface of the crater in Fig. 3.15. It is created inside the uprising sheet and travels downwards along the crater surface. This behavior is clearly resolved in the simulations. The capillary wave is observed here only when isopropanol is used, whereas it could not clearly be seen in impacts of distilled water and glycerin/water mixture. This is explained by the much lower surface tension of isopropanol.

In the case shown in Fig. 3.19, the moment at which the capillary wave can first clearly be seen corresponds to a dimensionless time $\bar{t} \approx 5.42$. At this instant the rim formed at the edge of the uprising sheet merges with the liquid layer. The pressure inside the rim is elevated and corresponds to the curvature of the rim cross-section and its acceleration. The flow in the rim is directed downwards. The capillary wave separates the high pressure region above and the relatively lower pressure region below the wave. The high pressure region above leads to the deformation of the shape of the crater behind the wave. Moreover, the pressure difference ahead and behind the wave leads to the liquid acceleration and enhances the wave propagation.

3.5 Binary Drop Collision

Binary drop collision presents an elementary process in dense sprays, which can affect the sizes and velocities of droplets thereby influencing the properties of the spray such as mass and momentum exchange between the spray and the underlaying liquid film. In contrast to an extensive knowledge about the geometry of drop spreading on a dry wall, available even at very early times after impact (Rioboo et al. [92]) much less data is collected for binary drop collisions. The reason is in the relatively small, sub-millimeter diameter of the drops which are commonly generated in such experiments. The experimental data for the temporal evolution of the diameter of the liquid mass formed after drop binary collision is available only for the relatively late stages after impact (Willis and Orme [130]). On the other hand, the phenomena related to axisymmetric binary drop collision can be much easier to model than drop impact onto a dry substrate since complicating wall effects are not present. Most of the efforts in the study of binary drop collisions are concentrated on the investigation of various modes of deformation and breakup: coalescence, bouncing, stretching separation and reflective separation (Qian and Law [82]).

The phenomena of a normal drop collision with a dry substrate and a double-

symmetric drop binary collision are very similar. Collision of two equal drops can be represented as a drop impact onto a symmetry plane as in Fig. 3.21. It is obvious that the modeling approaches to these two kindred problems should also be similar.

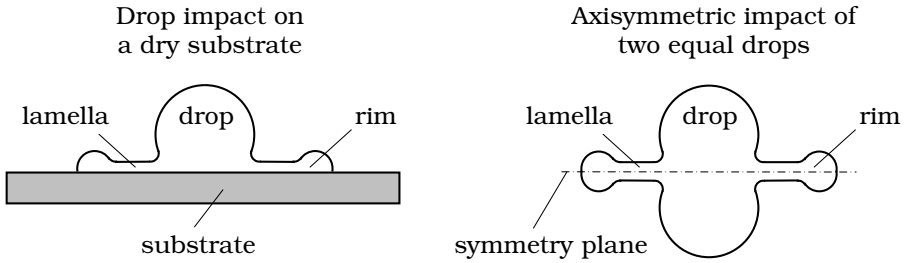

Figure 3.21: Sketch of the normal drop impact onto a dry substrate and the axisymmetric binary collision of two equal drops.

One of the important steps in the theoretical or semi-empirical modeling of the flow associated with the drop collision phenomena is the assumption of the approximate velocity field and typical problem geometry. In many cases, theories are developed assuming that the drop shape can be approximated as a disk, the characteristic thickness of which depends on Weber and Reynolds numbers, and within which the flow can be described using the energy balance of the entire deforming drop. In almost all existing theoretical models the drop shape at the time instant corresponding to the maximum spreading is approximated by a disc of diameter $D_{\max}$ and thickness h, estimated from the mass balance in dimensionless form as

$$\overline{h} = \frac{2}{3\overline{D}_{\max}^2}, \tag{3.38}$$

or in a similar form (Roisman [95]).

The real thickness of the lamella generated by drop impact onto a flat substrate often cannot be determined from experiments since the camera view is obscured by the rim. However, numerical simulations of drop impact can be used to estimate the real geometry of the spreading drop. To examine the validity of the Eq. (3.38) the predicted thickness of the lamella and the instantaneous drop spreading diameter from the numerical simulations from Šikalo et al. [107] are compared in Fig. 3.22. The agreement is poor over the entire time of drop spreading and receding. Similar results are obtained for many other impact parameters. It should be noted that in these numerical simulations the agreement between the predictions of the drop spreading diameter and the experimental data was rather good, which implicitly indicates that the numerics was capable of satisfactory predicting also the thickness of the lamella.

Therefore, Eq. (3.38) cannot be used as the relation between the lamella thickness and the drop diameter. The reason for this discrepancy is in the formation of the rim at the edge of the lamella. The volume of the rim is not negligible small in

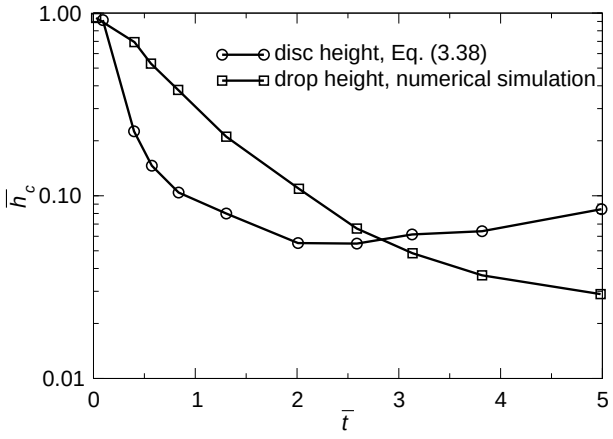

Figure 3.22: Comparison of the dimensionless drop height at the symmetry axis with the estimations by Eq. (3.38) as a function of the dimensionless time. The drop height and the drop spreading diameter, which is used in Eq. (3.38) for the estimation of the disc shape, are taken from the numerical simulations from Šikalo et al. [107]. The impact parameters are Re = 4010, We = 90.

comparison with the total volume of the drop. Another reason for the disagreement is the fact that the lamella is not flat, even at the dimensionless time instant $\overline{t} = 1$.

In this Section the theoretical and numerical investigation of the flow generated by double-symmetric collision of a drop with another drop are presented. The dynamics of the expansion of the lamella is described by the theory applicable to the relatively thin lamella thickness and thus valid for the later stages of drop spreading. The early stage of drop initial deformation and spreading are calculated numerically. The existing experimental data and the results of numerical simulations of the initial phase of axisymmetric drop collision with a rigid wall or with a symmetry plane are presented. It is discovered that the shape of the lamella in the central part of the spreading drop follows a universal law which almost does not depend on the impact conditions if the impact Reynolds and Weber numbers are high. This demonstrates that the energy balance approach is not able to describe well the flow in the spreading drop since it usually does not properly consider the flow and the energy losses at the drop edges.

3.5.1 Axisymmetric Spreading of a Free Thin Liquid Sheet

The flow in a thin spreading liquid sheet was described and the evolution equation for the film thickness was obtained by Roisman et al. [93], by considering the mass and momentum balance of the element of the sheet schematically shown in Fig. 3.23. The motion of the sheet is determined by the averaged through the sheet cross-section velocity $U_r(r,t)$ in the radial spreading direction. The mass balance accounts for volume change of the sheet element due to the flux gradient in the radial direction, whereas the momentum balance takes into account the internal stresses

applied to the element cross-section and the capillary pressure applied to the free surface of the liquid element. In the case of high Reynolds and Weber numbers, the momentum balance equation is linearized accounting for the smallness of the value of the gradient of the film thickness.

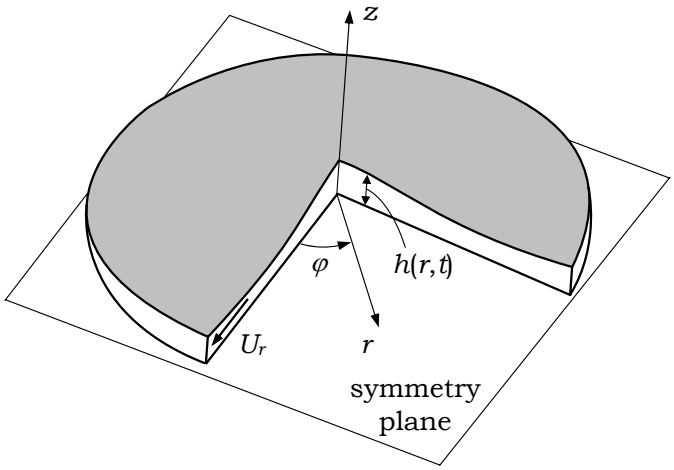

Figure 3.23: Axisymmetric spreading of a thin liquid sheet.

The incompressible axisymmetric flow in the thin spreading liquid sheet is described by the mass and the momentum balance

$$\frac{\partial \overline{U}_r}{\partial \overline{t}} + \overline{U}_r \frac{\partial \overline{U}_r}{\partial \overline{r}} \approx \frac{4}{\mathrm{Re}} \frac{\partial}{\partial \overline{r}} \left[\frac{1}{\overline{r}} \frac{\partial (\overline{r} \overline{U}_r)}{\partial \overline{r}} \right], \tag{3.39}$$

$$\frac{\partial \overline{r} \overline{U}_z}{\partial \overline{z}} + \frac{\partial \overline{r} \overline{U}_r}{\partial \overline{r}} = 0. \tag{3.40}$$

where Eq. (3.39) has the form similar to the Navier-Stokes equation in the radial direction with 4/Re being the effective dimensionless viscosity in the spreading sheet. A trivial solution to Eqs. (3.39–3.40) corresponds to a uniform stretching of the sheet

$$\overline{U}_r = \frac{\overline{r}}{\overline{t} + \tau}, \quad \overline{U}_z = -\frac{2\overline{z}}{\overline{t} + \tau}, \tag{3.41}$$

with τ being a constant. The solution given by Eqs. (3.41) has the same form as the remote inviscid asymptotic solution of Yarin and Weiss [135] and is relevant only in the central part of the sheet far from the sheet edge where the capillary effects and the surface curvature are not negligibly small and have to be taken into account.

For the predictions of the lamella thickness at large times after the impact the inviscid remote asymptotic solution of Yarin and Weiss [135] can be used

$$\overline{h} = \frac{\eta}{(\overline{t} + \tau)^2}, \tag{3.42}$$

with η being a constant to be determined from the analysis of the initial phase of drop deformation. Although the evolution of the thickness of the lamella is simply

described by the Eq. (3.42), it should be noted that it is valid only for long times after collision. Accounting for the fact that dimensionless time corresponding to the maximum drop spreading on a dry substrate in most of the experiments from Rioboo et al. [92] is usually in the range $2 < \overline{t} < 5$, the use of Eq. (3.42) has to be more justified. In fact, the film thickness at the initial stage of drop deformation is not uniform.

The general expression for the distribution of the film thickness, obtained by Roisman et al. [93], has the following form

$$\overline{h}(\xi, \overline{t}) = \overline{h}_0(\xi) \frac{\tau^2}{(\overline{t} + \tau)^2}, \tag{3.43}$$

where the parameter ξ is defined as

$$\xi = \frac{\overline{r}\tau}{\overline{t} + \tau}. \tag{3.44}$$

The initial shape of the radially spreading lamella $\overline{h}_0$ is approximated by the Gaussian distribution function in $\overline{r}$. This form was chosen for convenience since it approximates well the numerically predicted and experimentally observed drop shapes. The dimensionless shape of the lamella at the initial time instant $\overline{t} = 0$ is defined by the expression

$$\overline{h}_0 = A \exp(-\overline{r}^2/B). \tag{3.45}$$

The value of the coefficient B is estimated from the mass balance of the spreading drop

$$\frac{\pi}{6} = \int_0^\infty 2\pi \overline{r} \overline{h}_0 \, \mathrm{d}\overline{r}, \tag{3.46}$$

and the value $B = 1/(6A)$ is obtained. The shape of the lamella at an arbitrary time instant is evaluated from Eq. (3.43) and the obtained form is a Gaussian distribution function

$$\overline{h}_L = \frac{\eta}{\left(\overline{t} + \tau\right)^2} \exp\left[-\frac{6\eta\overline{r}^2}{\left(\overline{t} + \tau\right)^2}\right], \quad \eta = A\,\tau^2. \tag{3.47}$$

This result makes the Gaussian distribution function a convenient form for the approximation of the lamella thickness. The thickness of the lamella at the impact axis $\overline{h}_C = \overline{h}_{L(\overline{r}=0)}$ follows the remote asymptotic relation, Eq. (3.42), even at the early times of spreading.

3.5.2 Numerical Simulations

The analysis of the motion of the spreading lamella in Section 3.5.1 is applicable to the description of the film flow at long times after impact when the film surface can be described by a smooth function $\overline{z} = \overline{h}(\overline{r})$ with $\partial\overline{h}/\partial\overline{r} \ll 1$. The analysis is not relevant to the description at the early times of the drop deformation. In the present study the flow in the drop at these early times is computed numerically.

The computational domain is a two-dimensional axisymetric slice with dimensions in the vertical plane of $5D_0 \times 5D_0$, based on the drop initial diameter, and one cell in the azimuthal direction. The mesh is fixed in space and adaptively refined in the region where the motion of the liquid develops, having in total ≈ 120000 cells, Fig. 3.24.

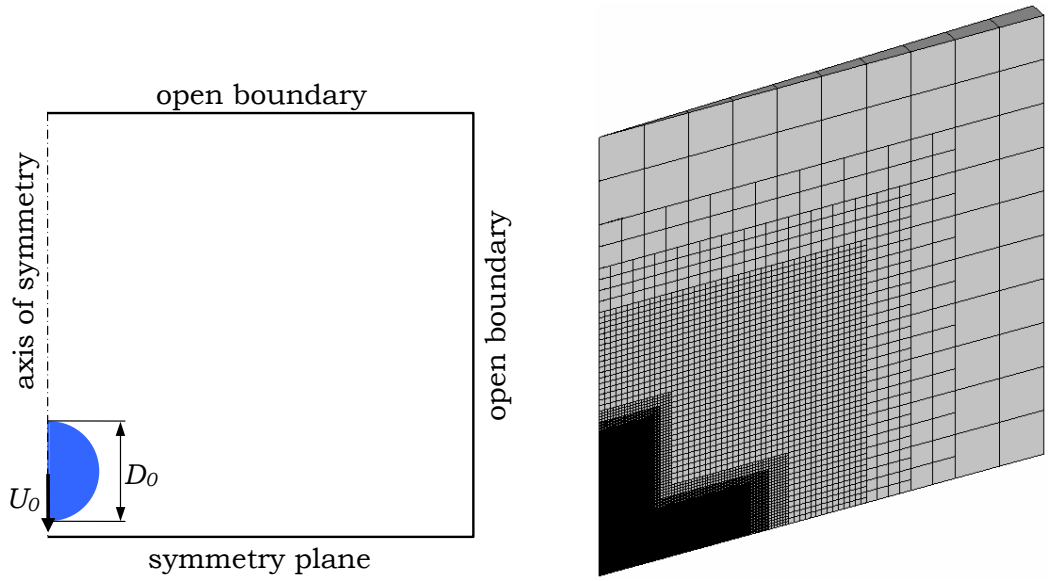

Figure 3.24: Initial case configuration (left) and computational mesh (right).

The simulation is initialized by prescribing the distribution of phase fraction defining one drops' shape and setting the drop initial velocity equal to impact velocity. Similar as done in the previous case, the drop is initialized at a distance from the symmetry plane corresponding to a dimensionless time of $\bar{t} = 0.2$, allowing several time steps to be computed before the first contact of the drop with the symmetry plane. The top and the right side boundaries are open with the prescribed total pressure and the combined inlet-outlet conditions for velocity. At the bottom, the symmetry plane boundary condition is set, thereby rendering the simulations of the collision of one drop with the symmetry plane as the axisymmetric drop binary collision.

Table 3.3: Dimensionless numbers used in the numerical simulations.

parameter	values					
Weber number	2.75	17	68	397	761	1165
Reynolds number	5	12.5	25	61	83	104

Simulations are performed for the impact conditions corresponding to the experiments of Willis and Orme [130], extended by a set of lower impact parameters. The applied impact conditions are summarized in Table 3.3. The listed values define

the collision of a drop with a symmetry plane and the corresponding values for the binary collision are by definition $We_r = 4We$, $Re_r = 2Re$, based on the relative velocity of two drops.

3.5.3 Results and Discussion

3.5.3.1 Liquid Shapes During the Collision

In the theoretical model of Roisman [95] the collision is subdivided into several phases shown schematically in Fig. 3.25. The first phase is termed the initial drops deformation, during which a radially expanding free lamella is generated. The second phase is the radial expansion of the lamella bounded by a rim formed by capillary forces. At a later time instant the third phase of the rim merging develops with the formation of the stretching finger-like jet. The fourth stage of the flow upon the drop collision corresponds to the axial expansion of the jet, accompanied by the formation of two small globules by capillary forces. The two globules move apart and then approach each other and merge again leading to the coalescence. The stretching jet is unstable and may lead to the droplets separation. The same flow pattern was observed by Willis and Orme [130] (Fig. 1.3) in the experiments with binary drop collisions in a vacuum environment.

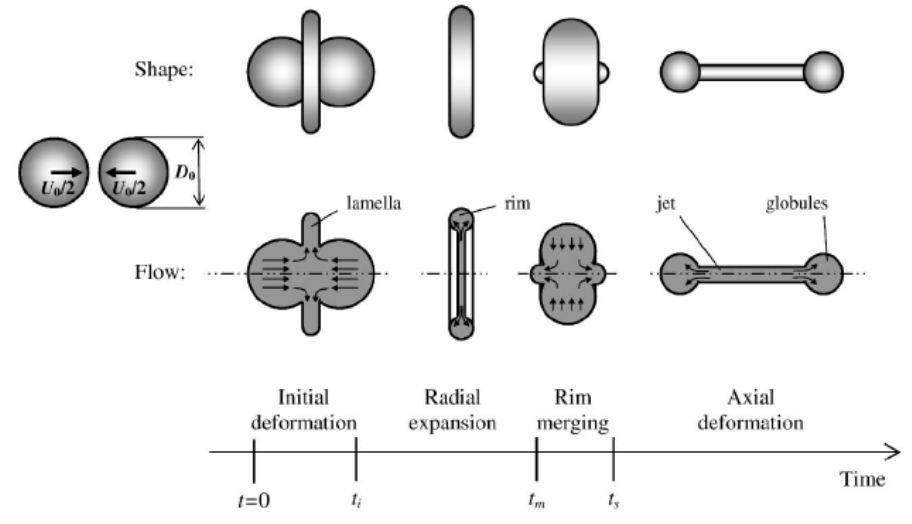

Figure 3.25: Different phases of droplet binary collision, from Roisman [95].

Fig. 3.26 shows the numerically predicted time evolution of the liquid upon the collision of two equally sized drops. The impact conditions correspond to $We_r = 1586$ and $Re_r = 121$ from Willis and Orme [130]. The two-dimensional axisymmetric computational model was used in the simulation and the snapshots shown in Fig. 3.26 are obtained by rotational extrusion of the liquid shapes.

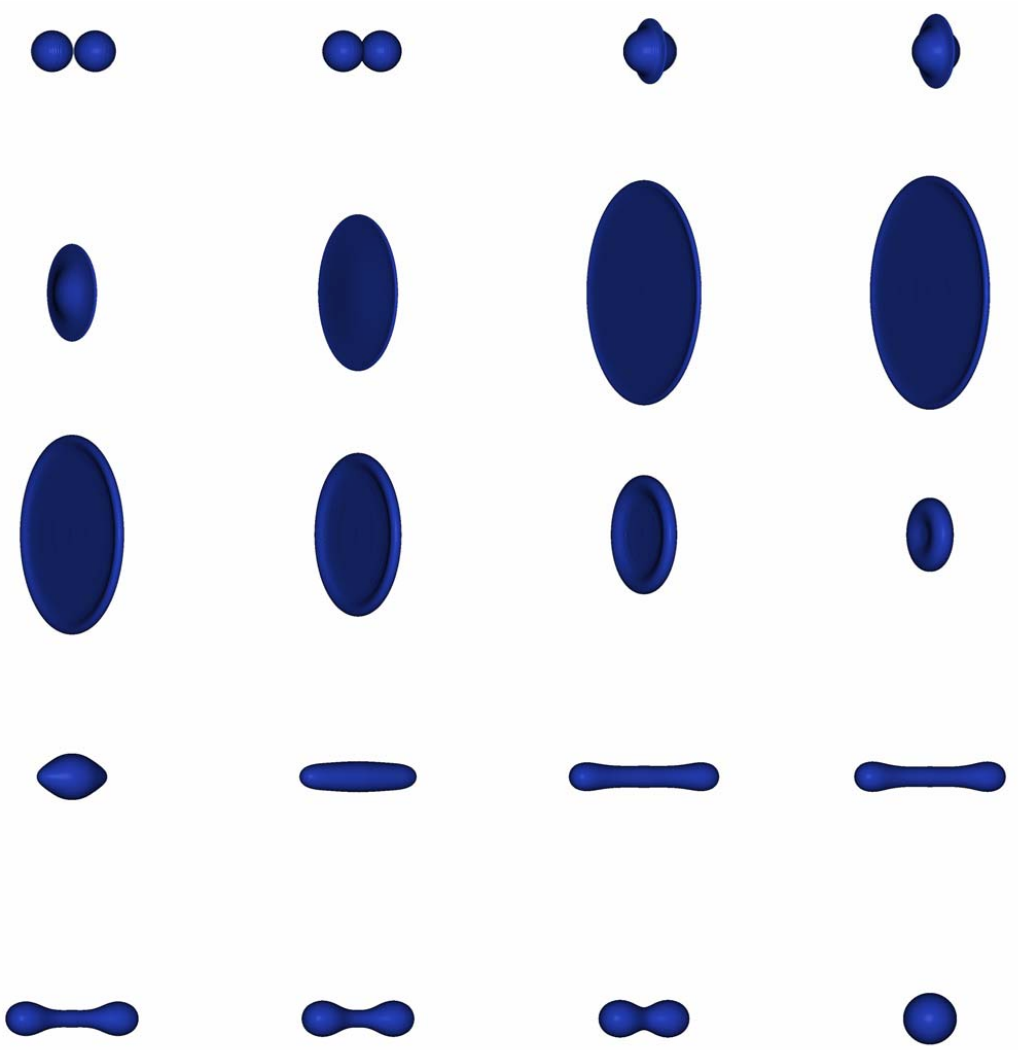

Figure 3.26: Computationally obtained liquid shape evolution during the binary drop collision. Time series is from left to right and top to bottom, impact parameters are $We_r = 1586$ and $Re_r = 121$.

It can be seen that the flow sequences corresponding to the oblate and the prolate flow regimes, as observed by Willis and Orme [130], are qualitatively well captured. In the prolate regime the liquid jet formed between the globules appears to be thicker compared to the experimentally observed. This is attributed to the fact that the experiments were conducted in a vacuum, whereas the computations were performed by taking into account the presence of the ambient air.

Fig. 3.27 shows the computationally predicted characteristic dimensions during the oblate and the prolate flow regime in comparison with the experimentally obtained values by Willis and Orme [130]. The two dimensions are measured as the longest distances between the opposite edges of the rim in the oblate regime (the equatorial dimension D_e) and between the edges of the globules in the prolate regime (the polar dimension D_p). As can be seen the evolution of the liquid is captured

very well in the initial oblate flow regime, but the results disagree after the lamella merges and the prolate regime develops. The thickness of the jet slightly increases in the simulation and the computed polar dimension representing the distance between the formed globules is lower than that in the experiments. This could be explained by the fact that the impact Reynolds and Weber numbers are relatively high and the flow is governed mainly by inertia at initial stages upon the collision. This stage corresponds to the oblate regime, where the effects of the surrounding air in the simulation are negligible. At later stages when the lamella starts to retract, the flow is much slower, driven by surface tension, and viscous effects become stronger. In this stage the flow of the liquid is affected by the drag of the surrounding air in the simulation acting as an outer resistance. These aerodynamical effects are not present in the experiments in vacuum environment and therefore the jet is allowed to stretch more yielding the greater polar dimension in Fig. 3.27.

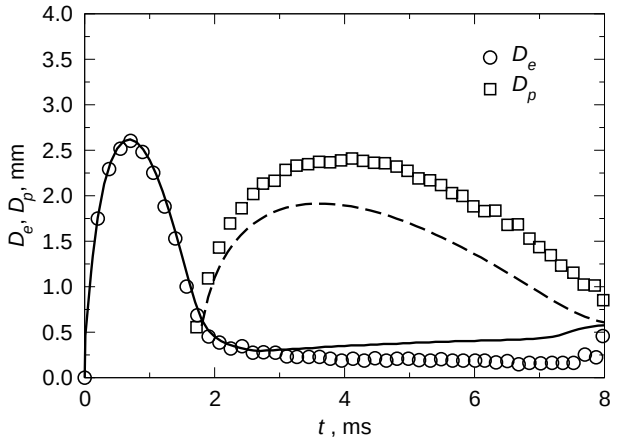

Figure 3.27: Comparison of the computationally obtained characteristic dimensions (lines) with experimental results from Willis and Orme [130] (symbols) at $\mathrm{We}_r = 1586$ and $\mathrm{Re}_r = 121$.

According to these results the numerical simulations are able to accurately predict the flow generated by the collision of two drops during the initial, inertia-dominated stage of the motion. The results of the simulations are used to describe the flow and for its theoretical modeling at the early times, as described in the following Sections.

3.5.3.2 Height of the Deforming Drop at the Symmetry Axis

If the impact Weber and Reynolds numbers are high, the flow far from the wall is determined mainly by inertia. Therefore, the dimensionless velocity of the lamella and its dimensionless shape in the central region of the deforming drop should not depend on the impact conditions. The recent study of Bakshi et al. [4] on the axisymmetric drop impact onto a dry spherical target confirms this assumption. The convex shape of the target geometry in this study allows one to observe the development of the lamella during the entire drop spreading process. Besides the other

parameters, the height of the deforming drop at the symmetry axis is measured. It was shown that in the initial phase of drop deformation the drop height first reduces with an almost constant velocity and the rear part of the drop moves almost as a rigid body. Then, at the time instant $\bar{t} \approx 1/2$ the process of drop deformation switches to a new regime and the drop height follows the inverse square dependence of time predicted by the remote asymptotic solution given in Eqs. (3.41–3.42). The evolution of the drop height depends neither on the impact Weber nor Reynolds number but is determined only by the ratio of the drop and target radii. Finally, when $\overline{h}$ is small enough, the viscous stresses govern the flow in the lamella. These viscous stresses, which become significant at time $\bar{t} = \bar{t}_{visc}$, lead to a damping of the flow. The residual film thickness is therefore a function of the Reynolds number only.

There is no reason to believe that drop impact onto a flat rigid substrate behaves differently. In the left graph in Fig. 3.28 the experimental data of Bakshi et al. [4] and the results of numerical predictions from Fukai et al. [28], Šikalo et al. [107] and Mukherjee and Abraham [60] for the evolution of the drop height $\overline{h}_C$ at the symmetry axis are shown as a function of time for various impact parameters. The corresponding results of the present numerical simulations of drop impact onto a symmetry plane are shown in the right graph in Fig. 3.28.

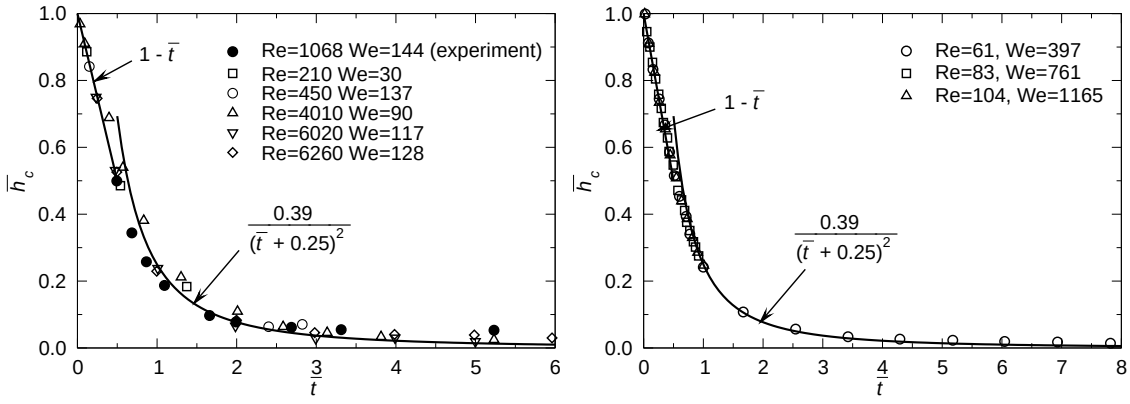

Figure 3.28: Drop impact onto a dry substrate (left): the experimental data from Bakshi et al. [4] and the results of existing numerical predictions from Fukai et al. [28], Šikalo et al. [107] and Mukherjee and Abraham [60] for the evolution of the lamella thickness at the impact axis as a function of dimensionless time. Drop impact onto a symmetry plane (right): the results of the present numerical predictions for the evolution of the lamella thickness at the impact axis as a function of dimensionless time.

During the first two regimes all the results lie approximately on a single curve for all the impact parameters. In the first and second non-viscous regimes, the height

of the drop at the symmetry axis can be approximated by the following expressions

$$\overline{h}_C \approx 1 - \bar{t}, \quad \text{at} \quad \bar{t} < 0.4, \tag{3.48}$$

$$\overline{h}_C \approx \frac{0.39}{(\bar{t} + 0.25)^2}, \quad \text{at} \quad 0.7 < \bar{t} < \bar{t}_{visc}, \tag{3.49}$$

which are also plotted in graphs in Fig. 3.28. Equation (3.48) is chosen from the assumption that the rear part of the drop moves initially almost as a rigid body, while Eq. (3.49) is taken in the form of the remote solution, Eq. (3.42). Equations (3.49–3.42) represent universal expressions for the thickness of the lamella generated by drop impact onto a dry flat substrate and onto a symmetry plane valid for all the impact parameters when both the Reynolds number and the Weber number are much larger than the unity.

In the left graph in Fig. 3.28 an indication of the third, viscous regime of the flow in the lamella at times $\bar{t} \geq \bar{t}_{visc}$ can be observed, since the Eq. (3.49) underestimates slightly the numerically predicted values. However, the precise estimation of the residual film thickness and the time instant $\bar{t}_{visc}$ is difficult, since in the results of Fukai et al. [28] the lamella thickness at the latest stages of drop impact is comparable to the thickness of a line plotted in the graph. From the obtained results shown in the right graph in Fig. 3.28 it is obvious that the development of the near-wall boundary layer is not relevant in the case for drop impact onto a symmetry plane and therefore $\bar{t}_{visc} \to \infty$ in this case.

3.5.3.3 Flow in the Lamella at Later Times

Since the height $\overline{h}_C$ of the lamella can be described well by Eq. (3.49), it can be concluded that the velocity in the close proximity of the drop axis can be approximated by the asymptotic solution, Eqs. (3.41).

In Fig. 3.29 the results of the numerical simulations of the average radial velocity and the velocity gradient at $\bar{t} = 1$ in the lamella generated by drop impact onto a symmetry plane are shown as a function of the radius for various impact conditions. Surprisingly, the velocity is linear over a relatively wide range of the radius. Moreover, the velocity distribution almost does not depend on the impact parameters except at the edge region, where the lamella is compressed due to the viscous and capillary forces. Far from the edge the velocity gradient is nearly uniform $\partial \overline{U}_r / \partial \overline{r} \approx 0.8$ at $\bar{t} = 1$ which agrees well with the remote asymptotic solution of Eqs. (3.41) with $\tau = 0.25$. This value of τ is used in Eq. (3.49) to fit the data for the lamella thickness $\overline{h}_C$ at the impact axis.

Fig. 3.30 shows the shape of the central part of the spreading lamella. It is seen that also the lamella shape almost does not depend on the impact conditions except for the edge region associated with the rim formation. Therefore, the thickness of the lamella and its velocity distribution at very high Weber and Reynolds numbers are self-similar.

The exact shape of the lamella is not modeled analytically, but it is determined using the numerical simulations during the initial stage of drop deformation. The

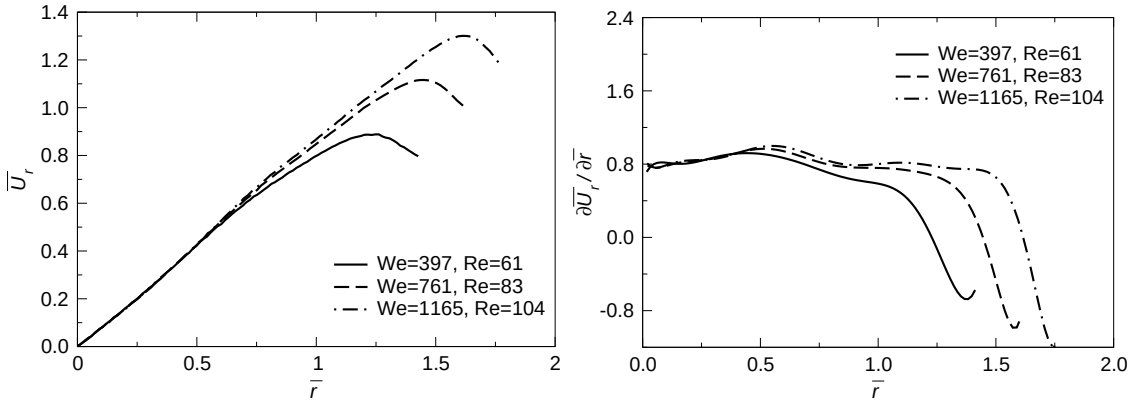

Figure 3.29: Drop impact onto a symmetry plane: the results of numerical predictions of the dimensionless average radial velocity (left) and the dimensionless gradient of the radial velocity (right) at the time instant $\overline{t} = 1$ as a function of the dimensionless radius.

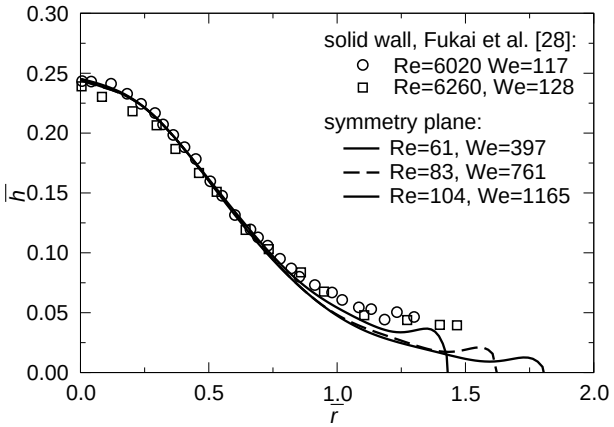

Figure 3.30: Drop impact onto a symmetry plane: the results of numerical predictions for the dimensionless lamella thickness at the time instant $\overline{t} = 1$ as a function of the dimensionless radius (lines) compared with the numerical simulations of drop impact onto a flat rigid substrate from Fukai et al. [28] (symbols).

lamella thickness distribution is approximated by the Gaussian function in Eq. (3.47) using $\tau = 0.25$ determined from the numerical simulations of drop impact onto a symmetry plane. The corresponding function satisfying the condition $\overline{h}_L = \overline{h}_C$ at $\overline{r} = 0$ has the following form

$$\overline{h}_L = \frac{0.39}{(\overline{t}+0.25)^2} \exp\left[-\frac{2.34\overline{r}^2}{\left(\overline{t}+0.25\right)^2}\right]. \tag{3.50}$$

In Fig. 3.31 the approximate shape determined by Eq. (3.50) is compared with the numerical simulations of Fukai et al. [28] of drop impact with Re = 1565 and

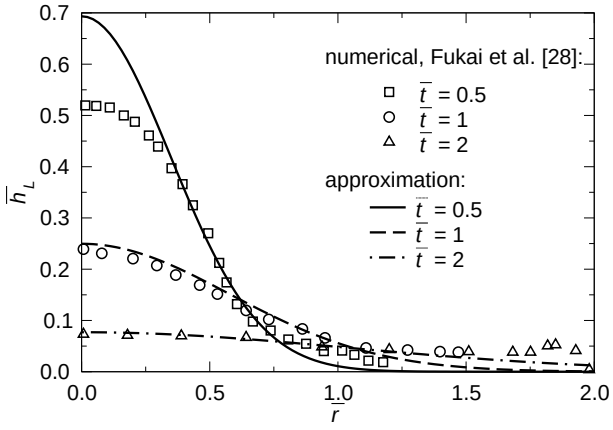

Figure 3.31: Drop impact onto a dry substrate at Re = 1565 and We = 32: numerical predictions from Fukai et al. [28] of the lamella shape at various time instants compared with the approximate shape, Eq. (3.50).

We = 32. At $\overline{t} = 1$ and $\overline{t} = 2$ the agreement is rather good far from the lamella edge where the lamella is thicker than predicted (indicating that the velocity gradient here is smaller then near the axis $\overline{r} = 0$) and where the rim formation becomes visible. This agreement indicates that the inviscid remote asymptotic solution of Yarin and Weiss [135] given by Eqs. (3.41) can predict well the velocity field in the central part of the deforming drop far enough from the rim. At $\overline{t} = 0.5$ the approximated solution overpredicts the results of numerical simulations. At this relatively early stage of spreading the velocity field is still two-dimensional and cannot be described by the remote asymptotic solution.

3.5.3.4 Pressure Distribution at the Symmetry Plane

One of the features of the self-similar flow in the deforming drop is the universal pressure field far from the edge of the spreading lamella. Pressure distribution at the substrate during drop spreading is one of the important elements which can help to better understand drop impact onto elastic, structured or porous targets.

Similar to drop impact on a dry wall, numerical calculation of the pressure distribution at the symmetry plane is a difficult task due to the appearance of entrapped small-size air bubbles. This is a known issue in the interface capturing computations using the VOF method. The discussion on whether the appearance of such bubbles is a numerical artifact or it has a physical base cannot be given without a clear experimental evidence. In the present numerical simulations the pressure is evaluated above the bubbles, at the dimensionless height $\overline{z} = 3 \times 10^{-3}$ above the symmetry plane. Accounting for the fact that the pressure gradient in the axial $\overline{z}$ direction vanishes at $\overline{z} = 0$, it is assumed that this represents a good prediction for the pressure distribution at the symmetry plane.

In the left graph in Fig. 3.32 the distribution of the dimensionless pressure $\overline{p}$ (scaled by $\rho_l U_0^2$), predicted by the numerical simulations of drop impact onto a symmetry plane, is shown for various time instants and different impact conditions. The

curves corresponding to different impact parameters but to the same time instant practically coincide over the most of the wetted part of the substrate except a short edge region of the lamella. Some scatter in the results is attributed to the influence of the computationally predicted small bubbles at the symmetry plane.

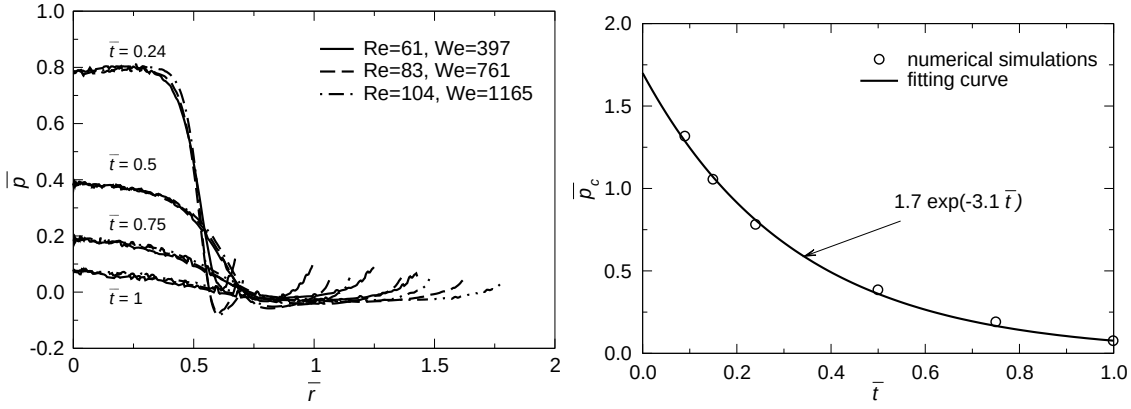

Figure 3.32: Drop impact onto a symmetry plane: numerical predictions of the dimensionless, universal pressure distribution near the symmetry plane $\overline{z} = 0$ as a function of the radius at various time instants (left) and numerical predictions of the dimensionless pressure $\overline{p}_C$ at the impact point $(\overline{r} = 0, \overline{z} = 0)$ as a function of the dimensionless time (right).

The results of the numerical predictions of the pressure $\overline{p}_C$ at the impact point $(\overline{r} = 0, \overline{z} = 0)$ are shown in the right graph in Fig. 3.32. The pressure $\overline{p}_C$ decays nearly exponentially in time. The best fit of the data is given by the expression

$$p_C = 1.7 \exp(-3.1t). \tag{3.51}$$

It should be noted that the results shown in Fig. 3.32 are applicable to the prediction of the pressure distribution at the wall also in the case of drop spreading on a smooth rigid substrate if the Weber and Reynolds numbers are high, since the pressure drop through a thin viscous boundary layer near the substrate is negligibly small.

3.5.3.5 Conditions for the Universal Flow in the Lamella

The universal flow in the lamella generated by drop collision corresponds to high Reynolds and Weber numbers. If the impact parameters are small the deformation of the drop is governed, besides the inertial forces, by the viscous stresses, surface tension and forces associated with wettability (Roisman et al. [94]).

The range of the impact parameters corresponding to the universal flow in the lamella was estimated by Roisman et al. [93] using Eq. (3.50) for the lamella thickness and Eqs. (3.41) for the velocity field with $\tau = 0.25$. Substituting these expressions in the linearized momentum balance equation the validity range of the universal solution is found to be determined by $\mathrm{Re} \gg 14$ and $\mathrm{We} \gg 2.5$. Another condition determining the range of impact parameters corresponding to the universal

flow in the lamella is the smallness of the viscous boundary layer $\overline{h}_{bl} \sim \sqrt{\overline{t}/\mathrm{Re}}$ in comparison with the lamella thickness and at the time instant $\overline{t} = 1$ this condition yields $\mathrm{Re} \gg 17$.

It is obvious that these estimations provide only the order of magnitude of the parameters corresponding to the universal flow in the lamella. In order to determine more precisely the range of validity of the universal solution, numerical simulations of drop impact on the symmetry plane were performed for various Reynolds and Weber numbers. In Fig. 3.33 the numerical predictions for the dimensionless drop height $\overline{h}_C$ at the axis of symmetry at the dimensionless time instant $\overline{t} = 1$ are shown for various impact conditions. At Reynolds numbers $\mathrm{Re} \geq 25$ the characteristic drop height at $\overline{t} = 1$ reaches a constant value of $\overline{h}_C = 0.245$. In this range of Reynolds numbers the universal solution is applicable to the description of the flow in the lamella regardless of the Weber number.

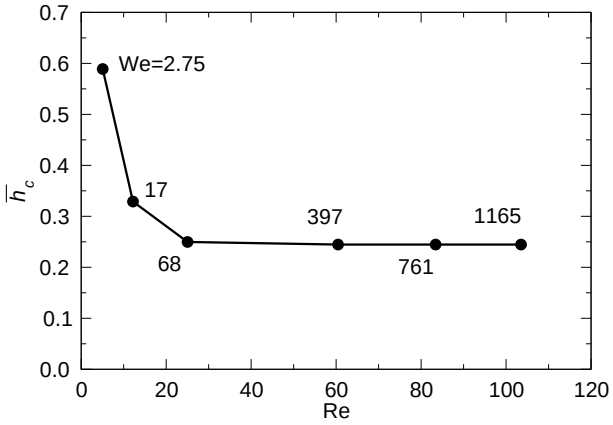

Figure 3.33: The dimensionless drop height $\overline{h}_C$ at the time instant $\overline{t} = 1$ as a function of the impact Reynolds number, obtained by numerical simulations of drop impact onto a symmetry plane.

In Fig. 3.34 the shapes of the deforming drop at the dimensionless time $\overline{t} = 1$ obtained by numerical simulations of drop impact onto a symmetry plane are compared with the approximate thickness distribution, Eq. (3.50), corresponding to the high-Reynolds impact collisions. As expected, the deviations from the universal shape is significant at relatively small impact Reynolds numbers since the effect of viscous forces is not negligibly small. It should be noted that in the case of drop impact onto a rigid substrate the wall effects can be significant at the later stages of drop spreading when the thickness of the boundary layer is comparable to the thickness of the lamella. At this stage the viscous effects are not negligibly small, as they lead to the flow deceleration and creation of a residual film (Bakshi et al. [4]).

The hypothesis on the self-similar flow in the lamella generated by drop collision contradicts numerous theoretical models of these phenomena, in particular models based on the consideration of the energy balance of the colliding drop. Following the derivations of these previous models, the velocity distribution in the lamella and

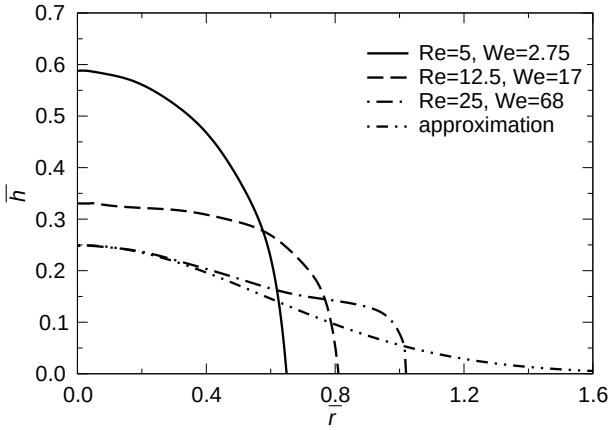

Figure 3.34: The dimensionless radial distribution of the drop height at the time instant $\overline{t} = 1$ at relatively small Reynolds numbers obtained by numerical simulations of drop impact onto a symmetry plane, compared with Eq. (3.50).

its thickness have to depend on the impact parameters. The energy lost due to the viscous dissipation and the increasing surface energy of the spreading lamella lead to a decrease of the kinetic energy and at some time instant even to its disappearance. This kinetic energy should therefore depend on the viscosity and surface tension of the liquid. The kinetic energy in the lamella is determined by the velocity distribution and its thickness. Therefore both the lamella thickness and the velocity distribution in the lamella should depend on the impact parameters. In order to explain this contradiction Roisman et al. [93] have proved that the energy balance approach can be applied to the description of the dynamics of drop spreading only if the edge effects corresponding to the rim formation are considered accurately. The universal flow in the lamella satisfies the energy balance despite the fact that this flow does not depend on the Reynolds and Weber numbers.

3.6 Drop Collision with a Dry Wall

Phenomenon of drop impingement onto a dry, rigid, flat and smooth substrate, besides occurring in a wide range of industrial applications, is an ideal system for investigation of inertia dominated capillary flow. Experimental investigations usually do not require a sophisticated setup. It is based mainly on observations using a high-speed video system of a millimeter sized falling drop. The spherical geometry of the impacting drop and thin spreading lamella resulting from drop impact enable the simplification of the governing equations and thus development of appropriate theoretical models of the flow. A comprehensive review on the modeling approaches is provided by Yarin [132]. Drop collision with a dry substrate is a frequently investigated phenomenon in fluid mechanics and various outcomes of drop impact, like splash, deposition or rebound (Rioboo et al. [91]) are determined by the impact parameters and substrate properties. Among them are the substrate roughness

(Range and Feuillebois [84]), shape (Bakshi et al. [4]), elasticity (Pepper et al. [77]), porosity (Kellay [48]) or local wettability (Šikalo et al. [107]). These phenomena can be modeled and understood when the main mechanisms involved in drop spreading are identified and well described.

Among the parameters predicted by the models are the maximum spreading drop diameter and the splashing threshold. Such models, among other parameters, require an appropriate scale for the thickness of the spreading lamella. Two main approaches can be distinguished. One approach is based on the energy balance of the entire drop, which is focused on the estimation of the surface and kinetic energies, and the energy lost due to viscous dissipation. It was shown in Section 3.5 that such an approach includes internal contradictions and is not applicable to the description of drop spreading. Moreover, the dimensionless thickness of the lamella at the initial stage is universal, it does not depend on the impact parameters, the Reynolds and Weber numbers. Another approach is based on a scaling analysis. In particular the thickness of the lamella is scaled by the thickness of the viscous boundary layer developed near the substrate surface, leading to the hypothesis that the film thickness is described well by $\overline{h} \sim \mathrm{Re}^{-1/2}$. Such an assumption has also been recently disproved by experiments of de Ruiter et al. [20]. It is evident that if the film thickness is comparable with the thickness of the viscous boundary layer, the boundary-layer approximation is no longer valid, since the outer flow is absent and the solution has to have a completely different form. Although much research has been conducted it is evident that the existing modeling of the lamella thickness requires fundamental changes.

In this Section the numerical investigations of a normal drop collision with a dry substrate are presented. Roisman [96] derived recently an analytical self-similar solution of the full Navier-Stokes equations, based on the remote asymptotic solution of Yarin and Weiss [135]. The theoretical model, valid at large times after the impact $t \gg D_0/U_0$, successfully predicts the evolution of the lamella thickness and its residual value. Moreover, this flow can be used for the description of heat transfer associated with drop impact, including near-wall phase transition (Roisman [97]). Good agreement with the experimental data serves, however, only as an implicit confirmation of the theory and a question still remains whether the similarity solution correctly approximates the real solution.

3.6.1 Solution for the Flow in the Lamella at Large Times

The analytical self-similar solution of the full Navier-Stokes equations obtained by Roisman [96] for the flow in the lamella at long times $t \gg D_0/U_0$, is based on the Stokes first problem for the two-dimensional case, but it considers the remote asymptotic solution of Yarin and Weiss [135]. The velocity field in the spreading lamella was obtained in the form

$$U_r = f'(\xi)\,\frac{r}{t}, \quad U_z = -2f(\xi)\,\frac{\sqrt{\nu}}{\sqrt{t}}, \tag{3.52}$$

where $\xi \equiv z/\sqrt{\nu t}$ was used as the self-similar variable. The stream function f was obtained from the ordinary differential equation

$$f''' + 2ff'' + \frac{1}{2}\xi f'' + f' - f'^2 = 0. \tag{3.53}$$

The numerical solution of Eq. (3.53) yielded $f''(0) \approx 1.04$. Moreover, the thickness of the viscous boundary layer was estimated in the form $h_{bl} \approx 1.88\sqrt{\nu t}$. In the case that the spreading liquid lamella is thicker than the viscous boundary layer the evolution of the film thickness was estimated as

$$\overline{h} = \overline{h}_{inv} + \overline{h}_{visc}, \text{ with} \tag{3.54}$$

$$\overline{h}_{inv} = \overline{t}^{-2}\eta\left(\frac{\overline{r}}{\overline{t}}\right), \quad \overline{h}_{visc} = \frac{4A}{5}\frac{\sqrt{\overline{t}}}{\sqrt{\mathrm{Re}}}, \tag{3.55}$$

consisting of the *inviscid* part $\overline{h}_{inv}$ in the form of the remote asymptotic solution of Yarin and Weiss [135] and the *viscous increment* $\overline{h}_{visc}$. Function η describes the limiting lamella profile corresponding to an inviscid drop impact and the constant $A \approx 0.6$ was obtained from the numerical solution of Eq. (3.53) (Roisman [96]). The viscous thickness increment $\overline{h}_{visc}$ becomes significant for small film thicknesses at large times.

3.6.2 Numerical Simulations

The simulation is performed on the two-dimensional axisymetric numerical mesh, with one cell in the azimuthal direction, adaptively refined in the region of liquid motion with ≈ 160000 cells in total.

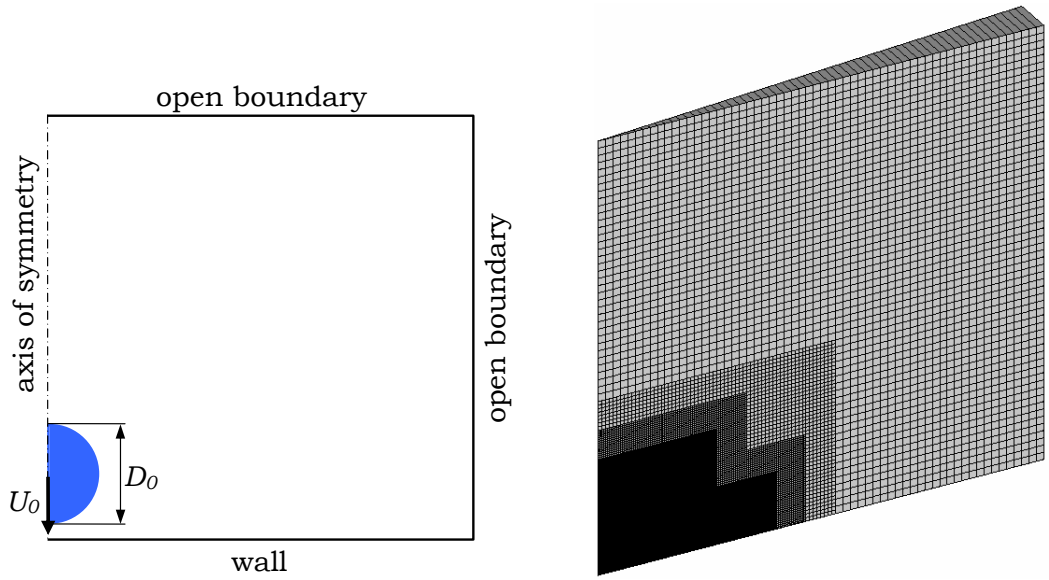

Figure 3.35: Initial case configuration (left) and computational mesh (right).

The dimensions of the computational domain in the vertical plane are $7D_0 \times 7D_0$ based on the drop initial diameter, Fig. 3.35.

Numerical simulations of drop impact are used to estimate the time evolution of the spreading drop. The simulation is initialized by prescribing the distribution of phase fraction corresponding to one drops' shape and setting the drop initial velocity equal to impact velocity. As in previous cases, in order to allow the fluid flow to develop before the drop hits the wall, the drop is initialized at a distance from the impacting surface corresponding to a dimensionless time of $\bar{t} = 0.2$. The top and the right side boundaries are open with the prescribed total pressure and the combined inlet-outlet boundary conditions for velocity. At the impacting surface at the bottom the no-slip boundary condition is set. Since no experimental data for the contact angle is provided, capillarity at the wall is not accounted for and the zero gradient condition is set for the phase fraction.

The impact conditions from de Ruiter et al. [20] are used in the simulation of drop collision with the dry wall and two additional simulations of drop collision with a symmetry plane are performed with $\mathrm{Re}_r = 3980$ and $\mathrm{Re}_r = 4720$. The applied impact conditions are summarized in Table 3.4.

Table 3.4: Dimensionless numbers used in the numerical simulations.

parameter	values			
Weber number	132	132	132	185
Reynolds number	500	1000	1990	2360

3.6.3 Results and Discussion

3.6.3.1 Shapes of the Spreading Drop

The results of comparison between the computationally obtained drop shapes with the experimental data from de Ruiter et al. [20] are shown in Fig. 3.36. The dashed lines represent drop shapes from different experimental runs with the same impact conditions, where the small differences are due to slightly different obtained impact velocities. The agreement is very good even at the early stages of drop deformation, which shows that the computational model predicts correctly the flow inside the spreading drop. The only noticeable disagreement is in the region of the rim, where the wettability at the wall is not accounted for in the simulations and the zero gradient condition is used for the phase fraction at the impacting surface.

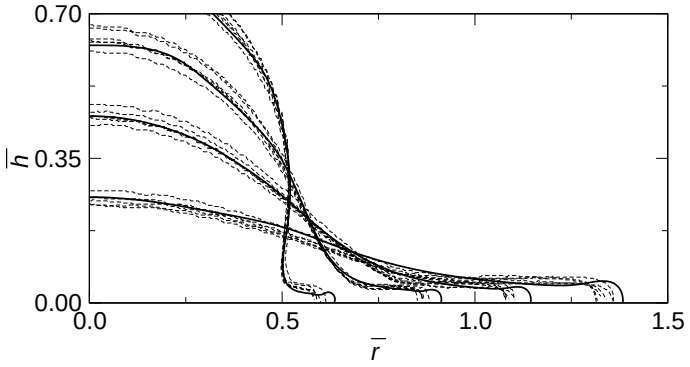

Figure 3.36: Comparison of computationally obtained drop shapes with the experimental data from de Ruiter et al. [20] for $\mathrm{Re} = 1990, \mathrm{We} = 132$. The dimensionless time instants are $\overline{t} = 0.2; 0.4; 0.63; 1.0$.

3.6.3.2 Vorticity at the Wall

In order to identify the region where the effect of the liquid viscosity is significant, in the present study the vorticity of the velocity field in the spreading lamella is estimated using Eqs. (3.52) as

$$\omega \equiv \frac{\partial U_r}{\partial z} - \frac{\partial U_z}{\partial r} = \frac{r f''(\xi)}{\nu^{1/2} t^{3/2}}. \tag{3.56}$$

The vorticity at the wall ($\xi = 0$) can be now estimated as

$$\omega_w \approx \frac{1.04 r}{\nu^{1/2} t^{3/2}}. \tag{3.57}$$

The vorticity is expressed in the dimensionless form $\overline{\omega}_w = \omega/\Omega$ by choosing an appropriate scale Ω. For convenience, in the present study the following expression is used as the scale for vorticity

$$\Omega = \frac{D_0}{\nu^{1/2} t^{3/2}}. \tag{3.58}$$

In Fig. 3.37 the contour plots of the scaled vorticity are shown for different time instants. As expected the region of the high vorticity is associated with the expansion of the near-wall viscous boundary layer. In addition, a small air bubble is entrapped in the simulations at the impact region, which is not shown in Fig. 3.36 for the sake of clarity. The entrapment of a small air bubble at the impact point could be a numerical artifact, but in absence of the experimental evidence this can not be unequivocally stated. However, it is noted that its appearance does not affect the solution for the drop shapes. The vorticity level monotonically increases in the radial direction, which is in agreement with the theoretical predictions of Eq. (3.57).

In Fig. 3.38 the numerically predicted scaled vorticity in the liquid flow at the wall is shown as a function of the dimensionless radial coordinate at various time instants and compared with the theoretical predictions of Eq. (3.57). In each case

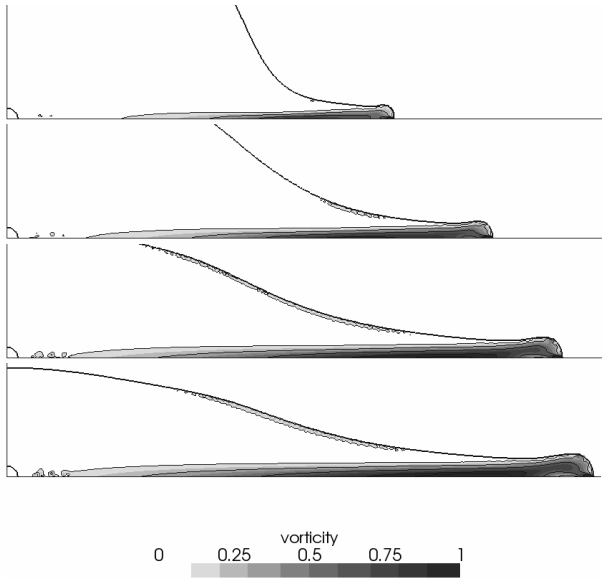

Figure 3.37: Contour plot of the dimensionless vorticity $\overline{\omega}_w$ in the spreading drop at various time instants, predicted by the numerical simulations for $\mathrm{Re} = 1990, \mathrm{We} = 132$. The dimensionless time instants are $\overline{t} = 0.4; 0.63; 0.87; 1.0$.

the vorticity monotonically increases with the radius and then quickly decreases in the rim region. This result demonstrates that the vorticity in the drop quickly approaches the theoretically predicted asymptote. This is an important result which confirms that the self-similar solution of Roisman [96] is valid and can be used for modeling the drop impact.

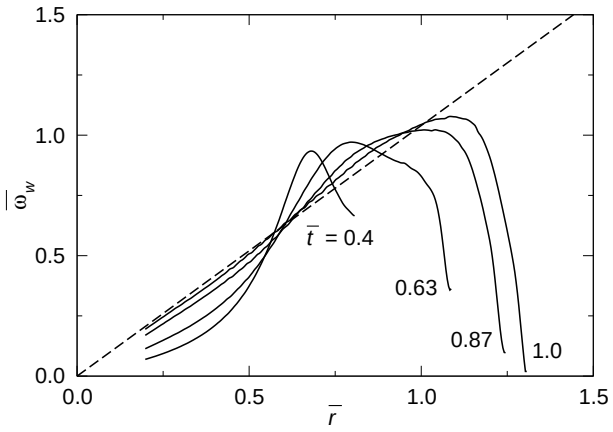

Figure 3.38: Dimensionless vorticity at the wall at various time instants as a function of the dimensionless radial coordinate. Dashed straight line corresponds to the theoretical prediction, Eq. (3.57), and impact parameters are $\mathrm{Re} = 1990$ and $\mathrm{We} = 132$.

It should be noted that only one case with the impact parameters Re = 1990 and We = 132 is shown in Fig. 3.38. However, it is found that the predicted levels of the dimensionless vorticity at the wall are only very slightly influenced by the impact parameters. In the lamella region outside the rim they are practically indistinguishable on the graph.

In Fig. 3.39 the dimensionless vorticity at the wall for different Reynolds numbers is shown for one time instant $\bar{t} = 0.4$. It is expectable that the linear dependence of vorticity, predicted for large times after the impact is not yet valid at this relatively early stage of drop deformation. It is surprising, however, that even at this relatively early time instant the scaled vorticities corresponding to different impact parameters practically coincide, excluding the rim region. The scaling developed for large times is applicable even at these early stages.

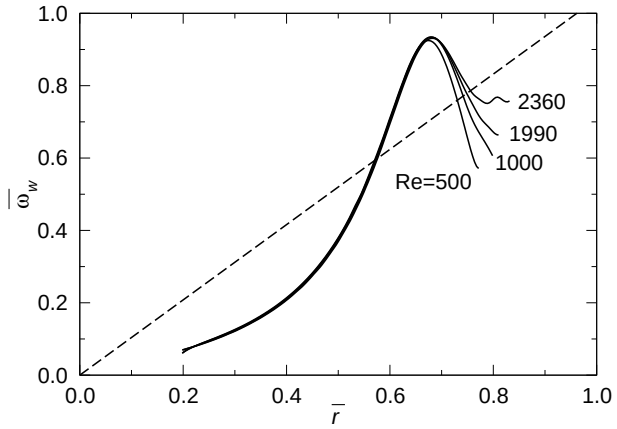

Figure 3.39: Dimensionless vorticity at the wall at $\bar{t} = 0.4$ as a function of the dimensionless radial coordinate for various impact parameters. Dashed straight line corresponds to the theoretical prediction, Eq. (3.57). The impact parameters are $\mathrm{Re} = 500, \mathrm{We} = 132; \mathrm{Re} = 1000, \mathrm{We} = 132; \mathrm{Re} = 1990, \mathrm{We} = 132$ and $\mathrm{Re} = 2360, \mathrm{We} = 185$.

3.6.3.3 The Thickness of the Spreading Lamella

The evolution of the lamella thickness is determined mainly by the inviscid flow in the outer region and by the flow generated by the expansion of the viscous boundary layer. The inviscid part of the lamella thickness, $\overline{h}_{inv}$, can be estimated by subtracting the theoretically predicted viscous increment, $\overline{h}_{visc}$, determined in Eqs. (3.55), from the computationally obtained lamella thickness. Since the scaling for the vorticity at the wall holds even at the relatively early times of drop deformation, the long-time prediction according to Eqs. (3.55) for the value of $\overline{h}_{visc}$ is assumed to be a good approximation for this stage.

In Fig. 3.40 the predicted values of $\overline{h}_{inv} = \overline{h} - \overline{h}_{visc}$ obtained using the numerical calculations of the drop height are shown as a function of the dimensionless radius for

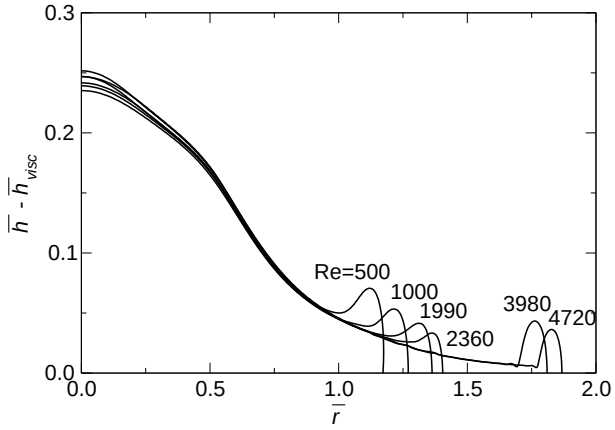

Figure 3.40: Dimensionless shape $\overline{h} - \overline{h}_{visc}$, scaled by the initial drop diameter, representing the inviscid part of the lamella thickness as a function of the dimensionless radial coordinate at $\overline{t} = 1$. The impact parameters are $\mathrm{Re} = 500, \mathrm{We} = 132; \mathrm{Re} = 1000, \mathrm{We} = 132; \mathrm{Re} = 1990, \mathrm{We} = 132; \mathrm{Re} = 2360, \mathrm{We} = 185$ for impact onto a wall (solid curves), and $\mathrm{Re}_r = 3980, \mathrm{We}_r = 528; \mathrm{Re}_r = 4720, \mathrm{We}_r = 740$ for impact onto a symmetry plane (dashed curves).

the time instant $\overline{t} = 1$. The numerical simulations for drop impact onto a solid wall are performed in a rather wide range of impact parameters, from $\mathrm{Re} = 500$ to $\mathrm{Re} = 2360$. In addition, two numerical simulations with drop impact onto planes in which the no-slip boundary condition is replaced by the symmetry plane condition are performed, and the results are included in Fig. 3.40. These two cases are associated with the double-symmetric binary drop collision. Since the inviscid flow in these cases can satisfy all the boundary conditions, the viscous boundary layer does not appear. This is confirmed by the numerical calculations of the vorticity levels which is found to be negligibly small in comparison with the corresponding case of drop impact onto a solid wall (except the rim region where the vorticities are of the same order of magnitude). The shapes of the drops impacting onto a symmetry plane shown in Fig. 3.40 correspond to $\mathrm{Re}_r = 3980$ and $\mathrm{Re}_r = 4720$. The predicted shapes of the inviscid lamella coincide for all the considered cases, excepting the short rim region.

4 Drop Impact on a Heated Wall

4.1 Introduction

The phenomenon of drop impingement on a hot surface represents a complex physical problem governed by various interacting parameters, some of which are drop size and velocity, surface temperature and roughness, angle of impact, liquid properties including surface tension and possibly the liquid wall film present in the case of a spray impact. The problem becomes even more difficult if phase change occurs and theoretical approaches require proper assumptions for simplifying the analysis.

The process of nonisothermal droplet collisions has received considerable attention among researchers in the past two decades. One of the motivations is the enhanced heat removal from solid surfaces by spraying them with liquid drops. A complete understanding of nonisothermal drop impact phenomenon still remains nontrivial and challenging due to its high unsteadiness and extremely small scales involved inhibiting direct experimental access to these phenomena.

The outcome of a flow generated by drop impact onto a dry target (splash, spread, rebound) generally depends on the energy of the impacting drop. In drop impacts on hot surfaces at a given impact energy of the drop, the surface temperature can affect the impact dynamics. For temperatures above the boiling point the drop starts to evaporate already when approaching the target. The vapor generated in the region between the drop and the surface is further compressed and at temperatures above the Leidenfrost the evaporation rate and vapor compression are fast enough to provide high enough pressure in the vapor layer that prevents a direct drop-surface contact. The liquid is said to be in the pool boiling regime and the impact dynamics can be different compared to lower temperatures (Chandra and Avedisian [14]). Such impacts incorporating phase change are not treated in the present work.

In this Chapter the computational model for conjugate heat transfer within the framework of the VOF-based method for free-surface capturing is formulated and validated. A series of configurations is computed including single water drop impact onto a heated solid surface with different thermophysical properties – stainless steel, aluminium and glass – in a range of Reynolds and Weber numbers and water-solid temperature differences.

The cases without phase change used for the validation of the computational model were investigated experimentally by Pasandideh-Fard et al. [74] and numerically by Healy et al. [39]. In addition, the present computational results are analyzed along with the corresponding analytical solution proposed by Roisman [97]. Contrary to previous studies, the presence of ambient air is accounted for, enabling air bubble entrapment under the impacting drop to be resolved. Accordingly, the results obtained represent a more realistic outcome, associated also with spray impact

where air entrainment in the wall film can easily arise. The dimensionless parameters governing the flow and heat transfer in the lamella spreading on the wall are the impact Reynolds, Weber and Prandtl numbers.

4.2 Governing Equations and Computational Details

A review of the published literature has revealed that there is a lack of available experimental results obtained under the conditions being such to allow only the liquid flow and heat transfer to be computed along with a constant heat flux at the solid boundary of the solution domain. This is due to difficulties in controlling the heat flux (or the wall temperature in the case of the isothermal wall), i.e. holding it constant during the entire duration of the experiment. Therefore the combined fluid flow and heat transfer model has to account for the simultaneous heat transfer in the solid substrate as well. The mathematical formulation of the free surface flow includes the interface capturing methodology described in Chapter 3. The model is extended here to include the conjugate heat transfer.

The transport equations governing the fluid flow and heat transfer in the drop impact process are the conservation of mass, phase fraction, momentum and energy

$$\nabla \cdot \mathbf{U} = 0, \tag{4.1}$$

$$\frac{\partial \gamma}{\partial t} + \nabla \cdot (\mathbf{U}\gamma) + \nabla \cdot [\mathbf{U}_c \gamma(1-\gamma)] = 0, \tag{4.2}$$

$$\frac{\partial(\rho \mathbf{U})}{\partial t} + \nabla \cdot (\rho \mathbf{U}\mathbf{U}) = -\nabla p_d - \mathbf{g} \cdot \mathbf{x} \nabla \rho + \nabla \cdot \mathbf{T} + \sigma \kappa \nabla \gamma, \tag{4.3}$$

$$\frac{\partial(\rho c_p T)}{\partial t} + \nabla \cdot (\rho c_p \mathbf{U} T) = \nabla \cdot [\nabla (kT)]. \tag{4.4}$$

Forces resulting from spatial variation of surface tension are neglected in the momentum equation, since the flow under consideration here includes low to moderate temperature variations. Chandra and Avedisian [14] observed a rather specific pattern consisting of circular and radial ridges forming cells of recirculating liquid on the surface of the liquid film spreading on a hot surface upon drop impact. The ridges could be observed only at elevated temperatures, very close to and above the liquid boiling temperature and are created by the action of surface tension gradients induced by temperature gradients. However since such effects are only seen at temperatures higher than the boiling point, the gradients of surface tension due to temperature gradients are neglected in the present study. The transport equation for energy is formulated in the form of the temperature equation. The heat source term originating from the viscous dissipation is neglected due to small Eckert number ($\mathrm{Eck} \ll 1$) in inertia dominated flows (Hase and Weigand [38]).

Equations (4.1–4.4) are extended to account for the energy transport due to transient heat conduction within the solid substrate

$$\frac{\partial(\rho_s c_{p,s} T_s)}{\partial t} = \nabla \cdot [\nabla (k_s T_s)], \tag{4.5}$$

where the subscript s denotes the solid substrate.

Density and specific heat vary only slightly within the temperature ranges used and can therefore be neglected. The temperature dependence of the thermophysical properties of air is also neglected, since flow and energy balances are determined predominantly by properties of liquid and solid substrate, the latter being assumed constant in this study. Again the effective fluid is treated as a homogeneous mixture, the thermophysical properties of which are evaluated as weighted averages based on the phase fraction distribution, similar as in Eqs.(3.7)

$$\rho c_p = \gamma \rho_l c_{p,l} + (1-\gamma)\rho_g c_{p,g} \quad \text{and} \quad k = \gamma k_l + (1-\gamma)k_g. \tag{4.6}$$

In order to enable analysis at higher temperatures (but still under the boiling point), temperature-dependent thermophysical properties of the liquid are used. A regression performed on the basis of the available property data from Batchelor [6] and Incropera and de Witt [42] yielded the following relations for the viscosity, thermal conductivity and surface tension of water

$$\nu_l = -2,61 \cdot 10^{-12} T^3 + 5.82 \cdot 10^{-10} T^2 - 4.68 \cdot 10^{-8} T^1 + 1.74, \tag{4.7}$$

$$k_l = -9,74 \cdot 10^{-6} T^2 + 2,12 \cdot 10^{-3} T + 5,58 \cdot 10^{-1}, \tag{4.8}$$

$$\sigma = -1,68 \cdot 10^{-4} T + 7,60 \cdot 10^{-2}. \tag{4.9}$$

The discretization of the temperature equation follows the finite-volume procedure outlined in Chapter 2. An important issue is however the cell-face interpolation of the conductivity in the diffusion term. As was shown by Patankar [76], the conductivity at the cell-face will have an improper value if it is interpolated linearly from the cell-centers. According to the heat flux balance at the cell-face between cells containing materials with different conductivities, the cell-face value of the conductivity must be evaluated using harmonic interpolation. Thus, the cell-face interpolation of the conductivity is performed according to the expression, with respect to Fig. 2.1

$$k_f = \left(\frac{1-f_{\mathbf{d}}}{k_P} + \frac{f_{\mathbf{d}}}{k_N} \right)^{-1}. \tag{4.10}$$

Due to the temperature dependence of the thermophysical properties of the liquid, the fluid flow equations cannot be solved decoupled from the energy equation. In addition, the proper coupling of the two temperature equations, Eq. (4.4) and Eq. (4.5) must be provided. The temperature must be continuous across the solid surface since no thermal contact resistance exists at the solid-fluid interface (as it would be the case of two solids pressed together, Çengel [13]). An additional requirement is that heat fluxes must be conserved across the solid surface. This means that there will be a discontinuity of temperature gradients in the direction normal to the surface and the following condition must hold at the fluid-solid interface

$$-k(\nabla T)|_\perp = -k_s(\nabla T_s)|_\perp, \tag{4.11}$$

where the surface-normal temperature gradients are evaluated separately at the fluid and the solid sides.

The solution procedure starts with adjusting the new time step and is performed within an outer iteration loop for every time step, consisting of iteratively solving the fluid motion in the region above the solid surface followed by solving the energy equation in a coupled manner for both regions simultaneously. To this end the two meshes are combined into one and the discretization matrix obtained from the energy transport equation on the fluid mesh is extended to include the coefficients' contributions from the entire solid mesh as well. In this manner the procedure enables the heat fluxes across the fluid-solid interface to be internally conserved and there is no need for explicit transferring the fluxes between the shared boundaries of the two regions in the course of the computation. At the beginning of every outer iteration the thermophysical properties are updated according to the current temperature and the phase fraction distribution. Although the Peclet number is much higher than unity in inertia-dominated flows indicating a weak coupling, the momentum and energy equations are solved in a coupled fashion.

4.3 Validation of the Algorithm

The computational algorithm for the nonisothermal two-phase flow with interface capturing is validated using the case of a liquid jet impinging on a heated surface, by comparing the computed results with the empirical results of Liu et al. [55], the numerical results of Fujimoto et al. [27] and Tong [112], and the experimental results of Stevens [108] reprinted in the latter two references. The coupling at the solid-fluid interface in the case of conjugate heat transfer is validated using a simple case of one-dimensional transient heat transfer.

Liquid Jet Impinging on a Heated Surface

The sketch of the flow configuration is shown in Fig. 4.1. The liquid jet enters the computational domain through the nozzle and impinges onto the heated plate. After the impingement, the thin liquid sheet is formed flowing over the wall surface and removing heat from it. When the steady state is reached, distributions of the temperature and the heat flux at the wall are established, being characterized by the Nusselt number at the wall. The computational mesh has the shape of a two-dimensional axisymmetric slice, adaptively refined in the regions comprising the falling jet and the liquid film spreading on the solid surface. The properties of liquid and gas are constant and correspond to those of water and air at ambient conditions. The geometrical parameters are the jet diameter $D_0 = 4.06$ mm, the plate diameter equal to $12D_0$ and the height representing the distance from the nozzle outlet to the plate of $3.7D_0$, with the characteristic Reynolds number $\mathrm{Re} = 10600$ based on mean liquid velocity at the nozzle exit. At the wall surface the constant heat flux $\dot{q}_w = 1.49 \cdot 10^5$ W/m^2 is applied. As in the aforementioned studies, the flow is assumed to be laminar. Although turbulent flow should be expected at the nozzle exit, its effects were neglected since the radial velocity of the thin liquid sheet spreading over the heated surface is relatively small and therefore it is assumed that the flow relaminarizes and stays laminar after the impingement.

For the constant applied heat flux at the wall surface, the conservation of energy requires the fluxes due to heat conduction and convection to be equal (Incropera and de Witt [42])

$$\dot{q}_w = h(T_w - T_{ref}) = -k_w(\nabla T)_w|_\perp, \tag{4.12}$$

where the subscript ref denotes the reference temperature of the undisturbed flow (in the particular case of jet impingement it is the liquid temperature at the nozzle outlet) and the symbol $\perp$ indicates the gradient component normal to the wall.

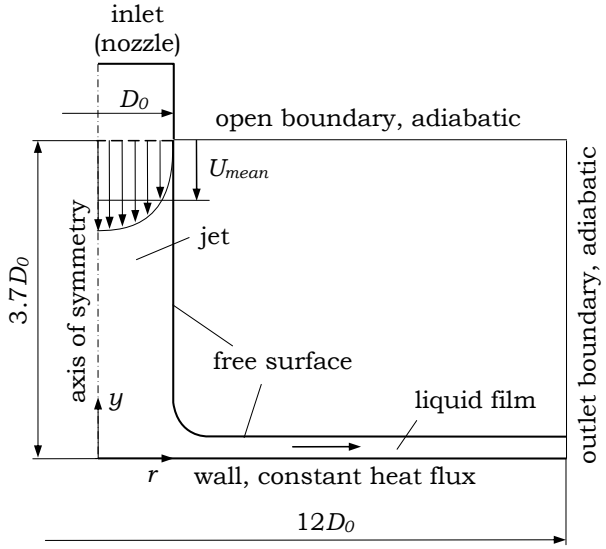

Figure 4.1: The configuration for the case of liquid jet impinging on a heated surface.

The discretization of the convective term in Eq. (4.4) requires the value for the temperature at all boundary cell-faces to be supplied. This is done by first calculating the surface-normal temperature gradient from the prescribed wall heat flux

$$|(\nabla T)_w|_\perp = \frac{\dot{q}_w}{k_w}, \tag{4.13}$$

and the temperature at the wall boundary is then obtained by interpolating the cell-center value using the calculated temperature gradient

$$T_b = T_P + \mathbf{d} \cdot (\nabla T)_w = T_P + |\mathbf{d}||(\nabla T)_w|_\perp. \tag{4.14}$$

Taking the nozzle diameter as the characteristic length, the Nusselt number characterizing the heat transfer from the wall surface is by definition (Incropera and de Witt [42])

$$\mathrm{Nu} = \frac{hD_0}{k}, \tag{4.15}$$

and substituting the overall heat transfer coefficient h from Eq. (4.12), the distribution of the Nusselt number at the wall is obtained from the expression

$$\mathrm{Nu}_w = \frac{D_0}{k_w}\frac{\dot{q}_w}{T_w - T_{ref}}. \tag{4.16}$$

The simulation was performed using two different velocity profiles at the nozzle outlet, namely the uniform velocity with $U_y = -U_{mean}$ and the 1/7 power-law profile given by the expression $U_y = -U_{\max}(1 - r/R_0)^{1/7}$ with $U_{\max} = U_{mean}/0.817$ and $R_0 = D_0/2$. The computationally obtained distributions of the Nusselt number for the two cases are shown in Fig. 4.2 versus the normalized radial coordinate ($\overline{r} = r/D_0$) and compared to the aforementioned experimental, theoretical and numerical results. As expected and in accordance with the previous findings the best agreement with the experimental results was obtained in the case of the uniform velocity profile. Additionally, in both cases small waves are resolved at the free surface of the spreading liquid film, being more pronounced in the case of the applied power-law velocity profile, which is why the Nusselt number distribution shows small oscillations along the radial coordinate.

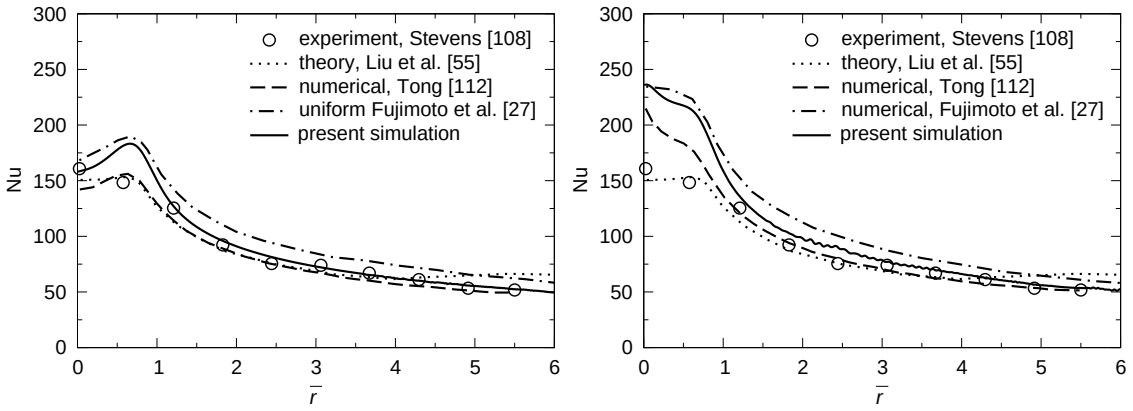

Figure 4.2: The distribution of the Nusselt number at the wall for the uniform (left) and the power-law (right) inlet velocity profile at Re = 10600.

Transient Conjugate Heat Transfer

In order to verify the coupling at the solid-fluid interface, the transient heat transfer in the fluid with the accompanying heat conduction in the wall is computed. The computational domain is one-dimensional consisting of three layers placed above each other, namely the solid wall, the liquid layer placed on the solid surface and the gas layer above the liquid surface. As depicted in Fig. 4.3 all three layers have equal heights of 5 mm, the fluids are at rest, the properties of the wall are that of stainless steel, and those of the fluids correspond to water and air. The domain is divided into 100 and 50 cells in the fluid and the solid region, respectively, and in order to obtain better resolution, both the fluid and the solid mesh are graded, with the smallest cells near the solid-fluid interface. The bottom surface of the wall and the top surface of the air are kept at constant temperatures of $T_1 = 100°\mathrm{C}$ and $T_2 = 25°\mathrm{C}$, respectively, and heat is conducted from the wall through the liquid to the air across the free surface.

The simulation was performed using constant liquid properties evaluated at 25°C, as well as using variable properties according to Eqs. (4.7–4.8). The theoretical

heat flux at the steady state and constant thermophysical properties of the materials is determined from the expression

$$\dot{q} = -\frac{T_2 - T_1}{\sum_{i=1}^{3} \frac{\Delta y_i}{k_i}}, \tag{4.17}$$

which for the given geometry equals $\dot{q} = 369.1$ W/m^2. This exact value is compared to the numerically obtained heat flux.

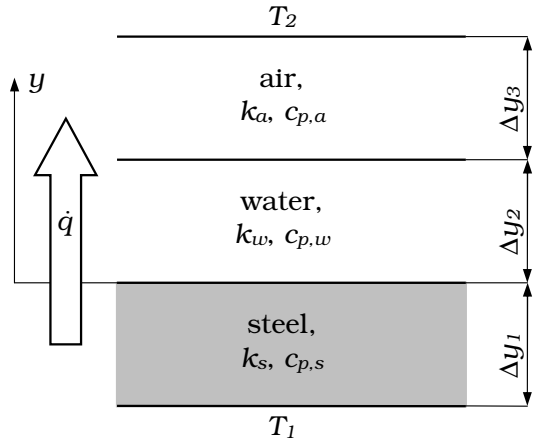

Figure 4.3: Initial configuration for the case of one-dimensional transient conjugate heat transfer.

The computed temporal distributions and the steady-state solutions of the temperature and the heat flux, the latter normalized by the theoretical value, are shown in Fig. 4.4.

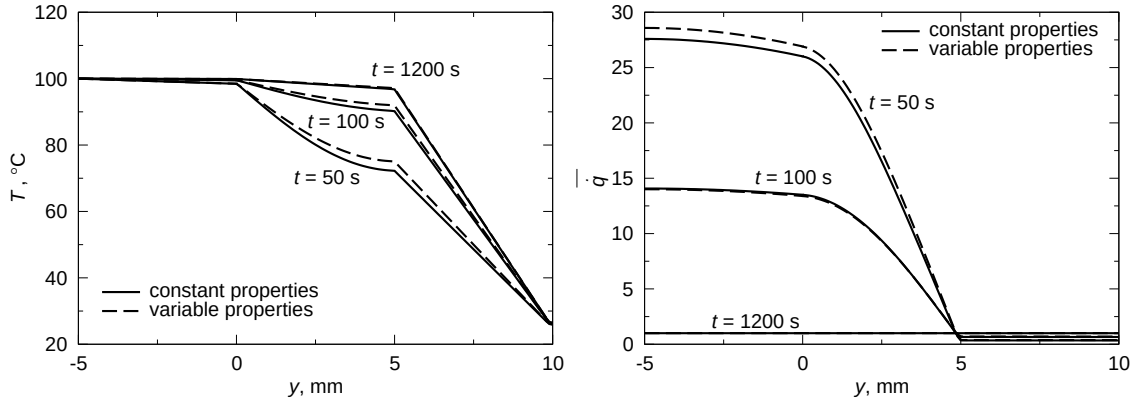

Figure 4.4: Temporal temperature profiles and heat flux distributions for the case of one-dimensional transient conjugate heat transfer.

The results show smooth obtained profiles of both temperature and heat flux at the fluid-solid and liquid-gas interfaces without discontinuities. The steady-state

temperature profile is linear in all three layers in the absence of heat sources. The relative error in the numerically obtained heat flux in the case of constant liquid properties is less than 0.1%. As expected, in the case of variable properties, the steady-state heat flux is slightly higher due to the increase of the liquid thermal conductivity with temperature.

4.4 Numerical Simulations

The computational domain, shown in Fig. 4.5, is a two-dimensional axisymetric slice with one cell in the azimuthal direction. The meshes for the fluid and the solid regions have dimensions in the vertical plane of $5D_0 \times 5D_0$ and $2.5D_0 \times 5D_0$, respectively, based on the drop initial diameter. The geometric mesh grading is utilized to obtain the best resolution in the region close to the solid surface. The combined mesh has $\approx$ 70000 cells in total, 40000 of that belonging to the fluid and the rest to the solid region.

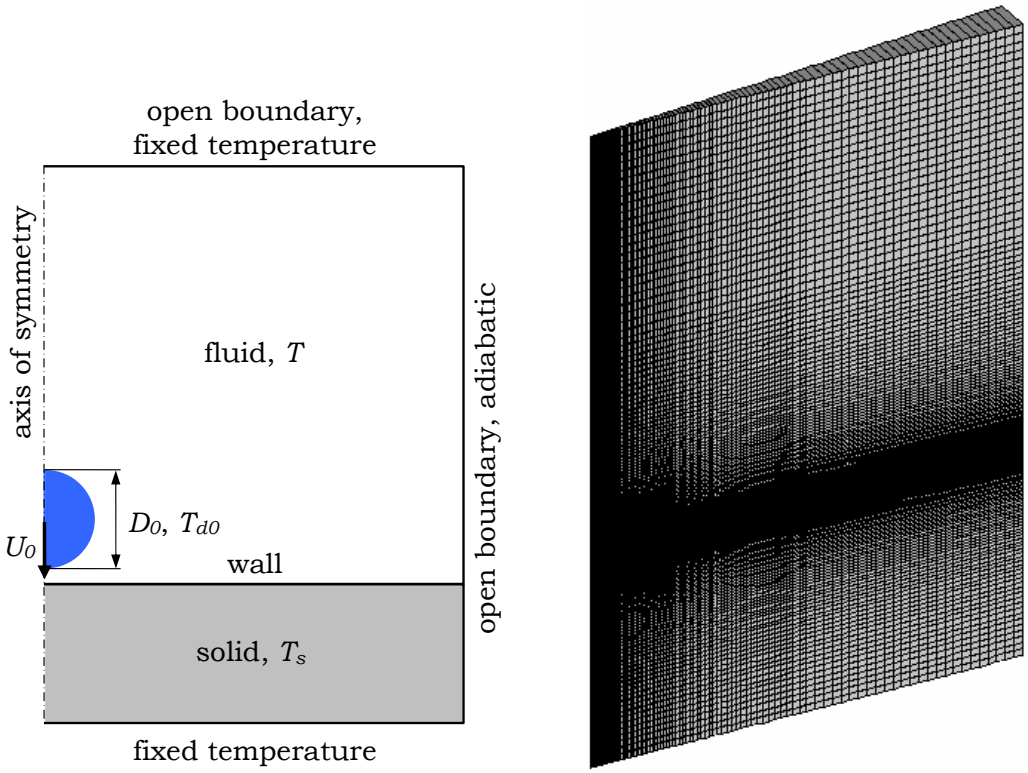

Figure 4.5: Initial case configuration (left) and computational mesh (right, every second line shown).

The simulation is initialized by prescribing the phase fraction distribution corresponding to one drop's shape and setting in those cells the initial velocity equal to the impact velocity. Furthermore, uniform temperature distributions in the solid substrate and throughout the fluid are prescribed at the initial time instant. The

boundary conditions for the fluid flow consist of a no-slip wall boundary at the fluid-solid interface and open boundaries at the top and to the right side with the prescribed total pressure and a combination of inlet and outlet conditions for velocity. For the temperature, fixed values are set at the top of the fluid and the bottom of the solid region, corresponding to their initial values and an adiabatic boundary to the right side with the zero gradient condition for temperature.

The wettability effects at the wall surface are taken into account according to Eq. (2.35) by using two approaches, namely the quasi-dynamic and the dynamic contact angle. In the first approach the quasi-dynamic contact angle is used by prescribing two different constant values for the contact angle, one for the advancing and the other for the receding phase of motion. In the second approach, the dynamic contact angle is evaluated from the expression of Kistler [49]

$$\theta_{dyn} = f_{Hoff}[\mathrm{Ca} + f_{Hoff}^{-1}(\theta_{eq})], \tag{4.18}$$

where the Hoffman's function f_{Hoff} is defined as

$$f_{Hoff} = \cos^{-1}\left\{1 - 2\tanh\left[5.16\left(\frac{\mathrm{Ca}}{1 + 1.31\mathrm{Ca}^{0.99}}\right)^{0.706}\right]\right\}. \tag{4.19}$$

In the above expressions the static advancing or receding contact angle is set for θ_{eq}, for the advancing and receding phase od motion, respectively. The capillary number is estimated based on the contact-line velocity as

$$\mathrm{Ca} = \frac{\mu|U_{cl}|}{\sigma}, \tag{4.20}$$

where the velocity of the contact line is roughly approximated by using the velocity at the interface in the first computational point above the wall, i.e. the velocity component normal to the contact line and tangential to the wall (Fig. 2.4)

$$U_{cl} = \left[\frac{\mathbf{n}_w - (\mathbf{n}_n \cdot \mathbf{n}_w)\mathbf{n}_n}{|\mathbf{n}_w - (\mathbf{n}_n \cdot \mathbf{n}_w)\mathbf{n}_n|}\right] \cdot \left[\mathbf{U}_P - (\mathbf{n}_n \cdot \mathbf{U}_P)\mathbf{n}_n\right]. \tag{4.21}$$

The inverse of f_{Hoff} appearing in Eq. (4.18) is determined using Eq. (4.19) from the following expression

$$(f_{Hoff}^{-1})^{0.706} - [1 + 1.31(f_{Hoff}^{-1})^{0.99}]^{0.706}\frac{1}{5.16}\tanh^{-1}\left(\frac{1 - \cos\theta_{eq}}{2}\right) = 0, \tag{4.22}$$

and is calculated numerically using the regula-falsi root-finding algorithm.

For the analysis of the nonisothermal flow generated by drop impact onto a heated wall accompanied by the conjugate heat transfer, the available published results (experimental and numerical) from Pasandideh-Fard et al. [74] and numerical from Healy et al. [39] are used. Initial thermophysical properties of liquid (water) and solids used in the simulations are listed in Table 4.1. The initial drop and solid temperatures $(T_s - T_d)_0$ and the corresponding characteristic dimensionless

numbers for the studied cases are given in Table 4.2, where the computed cases are denoted by letters A–F for simplicity. Prandtl numbers are evaluated at the analytically determined contact temperature T_c from Roisman [97]. In Table 4.2 the cases A and B correspond to the experimental and computational investigations from Pasandideh-Fard et al. [74] where variable viscosity is taken into account, and the cases C through F to the simulations performed by Healy et al. [39] where additionally the variable surface tension is accounted for.

Table 4.1: Thermophysical properties of water and solid surfaces used in the numerical simulations.

	water	steel	aluminium	glass
density ρ, kg/m^3	997.1 – 998.2	7900	2702	2500
viscosity μ, Ns/m^2	$(0.894 – 1.004)\cdot10^{-3}$	–	–	–
surface tension σ, N/m	0.072 – 0.0728	–	–	–
heat conductivity k, W/(mK)	0.59 – 0.6	16.6	237	1.4
specific heat c_p, J/(kgK)	4182 – 4179	515	915	750

Table 4.2: Characteristic dimensionless numbers and initial temperatures for the computed cases.

case	Re	We	Pr	Pe	Eck	substrate	T_c,° C	$(T_s - T_d)_0$,° C
A	2908	47	1.81	5263	$4.3 \cdot 10^{-6}$	stainless steel	98.6	120 – 25
B	4474	111	1.81	8098	$1 \cdot 10^{-5}$	stainless steel	98.6	120 – 25
C	2000	27	1.9	3800	$3 \cdot 10^{-6}$	aluminium	92.9	100 – 20
D	4000	110	1.9	7600	$1.2 \cdot 10^{-5}$	aluminium	92.9	100 – 20
E	2000	27	1.9	3800	$3 \cdot 10^{-6}$	glass	52.6	100 – 20
F	4000	110	1.9	7600	$1.2 \cdot 10^{-5}$	glass	52.6	100 – 20

4.5 Results and Discussion

An interesting phenomenon worth investigating is heat transfer during the initial spreading stage of the drop upon the impact. It was stated that in modeling of spray cooling the problem is split into two separate stages, i.e. an adiabatic initial drop spreading, which is followed by the heat transfer but only after the drop has spread into a film shape, thereby neglecting the heat transfer which may be significant already at the initial stage of spreading (Healy [39], di Marco et al. [21]).

4.5.1 Time Evolution of the Spreading Drop Diameter

Comparison of the present predictions with available experimental and numerical results for spreading ratio is presented in Fig. 4.6. The agreement is very good

in the initial spreading phase. The overprediction in the receding phase may be attributed to assumed values of receding contact angles and to possible differences in the evaluated thermophysical properties. In the mentioned references, the exact values of the thermophysical properties, the functional forms of their temperature dependence and receding contact angles are not provided. For the present purposes, the contact angle is implemented as quasi-dynamic, taking the value of 110° for the advancing phase, as stated in Pasandideh-Fard et al. [74], and 40° for the receding phase, taken from Pasandideh-Fard et al. [75]. The advancing contact angle of 70°, as used in Healy et al. [39], was applied in the corresponding cases. It can be seen that the simulation predicts a smaller spreading diameter in the case of constant properties. This is due to a decrease of liquid viscosity at higher temperatures, in accordance with the previous findings.

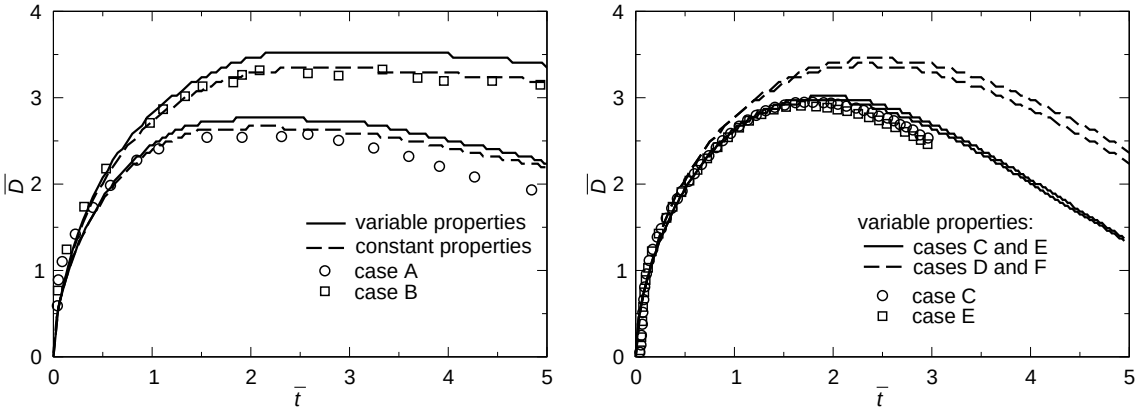

Figure 4.6: Comparison of the present numerical predictions for the spreading ratio (lines) with the experimental and numerical results (symbols) from Pasandideh-Fard et al. [74] (left) and Healy et al. [39] (right).

4.5.2 Temperature Fields in the Spreading Drop and in the Wall

The computed drop spreading pattern and the associated temperature distribution within both the fluid and the substrate at several time instants are displayed in Fig. 4.7 for drop impact onto a stainless steel with Re = 2908 and We = 47. The temperature is normalized by using the initial temperatures of the drop and the solid surface given as

$$\overline{T} = \frac{T - T_{d,0}}{T_{s,0} - T_{d,0}}. \tag{4.23}$$

The distributions are similar to those computed in Pasandideh-Fard et al. [74] and in Healy et al. [39], except for the impact region where the entrapped bubble can be presently observed. This phenomenon is responsible for the correspondingly higher temperature development in the region of impact. Very similar temperature fields were obtained in the other computed cases from Table 4.2 and are not presented here to avoid replication. It is seen that the entrapped air bubbles contribute to

a significant temperature rise in the fluid above the surface and the temperature in the substrate is also affected. Some small regions with higher temperatures are noted within the rim formed at the edge of the spreading lamella. Those are due to heat advection from the surface at higher temperature beneath the rim by the vortical velocity field in the rim.

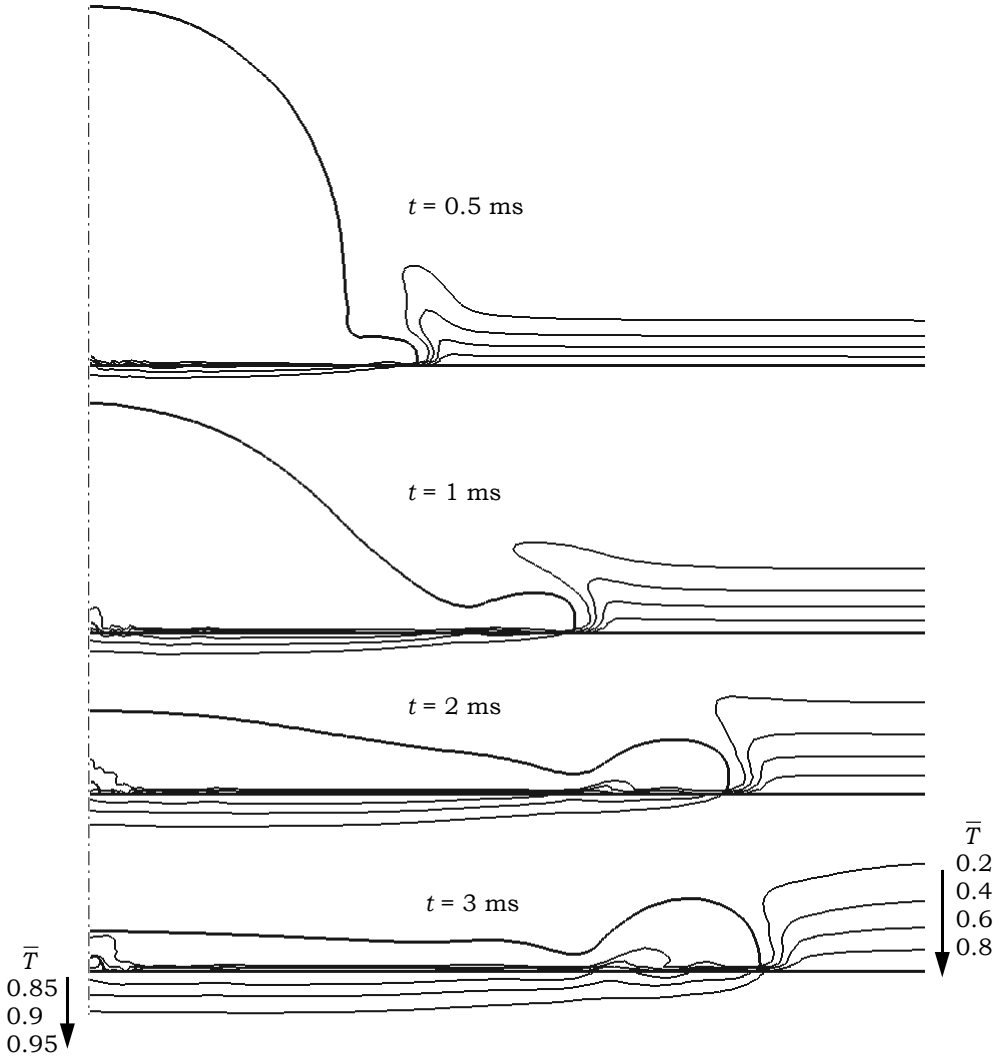

Figure 4.7: Spreading drop pattern and corresponding temperature distributions at different time instants for the case A.

As already mentioned, one of the interesting phenomena characteristic in the computations of free-surface flows with the VOF-related methods represent tiny air bubbles entrapped in the local region of the impact point. Although this issue might sometimes be regarded as a numerical artifact, there is an extensive experimental evidence of bubble entrainment upon impacts of drops on a solid surface (Chandra and Avedisian [14], Qiao and Chandra [83], Bartolo et al. [5]), as well as on a liquid layer (Prosperetti and Oğuz [80], Elmore et al. [22], Oğuz and Pros-

peretti [67]). In the numerical simulations of the interface dynamics during impacts of drops on liquid surfaces, Oğuz and Prosperetti [67] suggested that for a certain range of impact parameters a bubble is entrapped because the crater bottom has a larger downward momentum than its sides and the buoyancy may not reverse the motion of the bottom before the crater sidewall collapses. The computational model of Pasandideh-Fard et al. [74] neglects the presence of air and flow equations are solved for liquid only. Such models are not capable of reproducing entrapped air bubbles. Drop impact onto a solid surface with similar impact parameters and using the same liquid (water) and substrate material (stainless steel) was investigated experimentally and numerically in the study of Mehdi-Nejad et al. [58], where small air bubbles could be observed and numerically captured. It was shown that when the drop approaches the surface, the increased air pressure below the drop is greatest at the impact point and depresses the drop's surface while the surrounding liquid in the drop can still approach the surface. This depression in the surface of the drop allows a thin air film to be developed out of which a small bubble at the symmetry axis and an axisymmetric air ring are formed. The ring collapses and joins at the impact point creating the air bubble which stays entrapped. Entrapped air films and a subsequent creation of a bubble were resolved recently by Nikolopoulos et al. [63] in the VOF-method-based numerical simulations of central droplet collisions. In the recent simulations in Roisman et al. [93] and Berberović et al. [7] such bubbles were also captured.

4.5.3 Temperature at the Impact Point

Comparison of the present numerical predictions with available experimental results for the impact point temperature is shown in Fig. 4.8. The overprediction of the experiment by the simulation is clearly due to the presence of the predicted air bubble in the region of the impact.

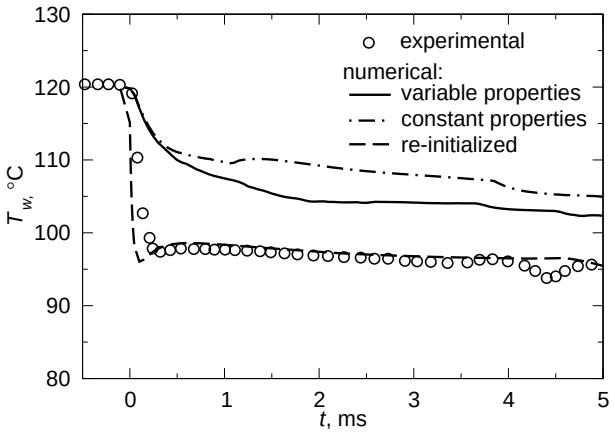

Figure 4.8: Comparison of the present numerical predictions (lines) with experimental results for the temporal evolution of the impact point temperature for the case A from Pasandideh-Fard et al. [74] (symbols).

In order to further analyze the reasons for such an outcome a hypothetical case was computed using the same impact parameters by re-initializing the distribution of the phase fraction field. The simulation was stopped at the moment of impact and values of the phase fraction $\gamma = 1$ were prescribed in those cells occupied by the entrapped bubble. Afterwards the simulation was continued. The impact point temperature agrees very well with experiments in the latter case. However, a small bubble was subsequently entrapped at some distance from the symmetry axis even in this case, following exactly the same mechanism as described by Mehdi-Nejad et al. [58]. Therefore, this is only a hypothetical case used to examine the performance of the computational model and this result is not considered as relevant for the overall analysis of heat transfer. The reason for resolving the bubble in numerics could be explained by observations reported by Elmore et al. [22]. It was indicated that the drop shape at the instant of impact, being either more prolate or oblate, influences the final outcome after the impact by either allowing or preventing an air bubble to be entrapped. Even in a single experiment with the same parameters, the bubble may appear in one run, but not in the second. In the present simulations, the drop is always initialized as perfectly spherical and although the afore-mentioned observations were made in the case of the drop impacts on a shallow pool, similar mechanisms could be responsible for air bubble entrapment in impacts on a solid target as well.

Similar computational results of the impact point temperature were recently obtained by Strotos et al. [109], where drop impact and heat transfer were computed for the same impact parameters as those used in Pasandideh-Fard et al. [74], but including phase change. The small bubble at the impact region was resolved in simulations in the receding phase, after the lamella collapses around the axis of symmetry. Traces of a small bubble are visible also in the results for the initial spreading phase upon the impact (c.f. Fig. 8 in Strotos et al. [109]), however this was not explicitly reported and therefore cannot be commented. The predicted mean drop temperatures were lower compared to those obtained in the present work (shown in Fig. 4.14), which is the consequence of taking the phase change due to evaporation into consideration. However, the computed impact point temperatures were still higher than in experiments from Pasandideh-Fard et al. [74], which seems to be contradictory. Strotos et al. [109] used three different estimations for the thermal conductivity in cells containing both fluids, namely the mass-averaged, the volume-averaged and the harmonic volume-averaged. The mass-averaged thermal conductivity showed the lowest disagreement with the experimental results, tending to indicate that this model should be the most accurate for the thermal conductivity. However, the computed temperature at the impact point represents actually the temperature of the contact between the entrapped air bubble and the solid surface, as in the present study, and thus it should not approach the measured values, if the bubbles were not observed in the experiments. It can be shown that the reason for a better agreement obtained using the mass-averaged thermal conductivity lies in the fact that the mass-averaged thermal conductivity value contains much more contribution of the liquid fraction due to the much larger liquid density, even in the case of small liquid phase fraction values in cells containing the bubble. Therefore, the

common phase fraction-based weighting used in the present work for the evaluation of the physical properties is considered to be more physical, yielding more accurate results.

The predicted temporal evolutions of the impact point temperature are shown in Fig. 4.9 for all simulated cases. As expected, the impact point temperature exhibits higher values than the theoretically predicted ones, given in Table 4.2, the outcome representing the consequence of the air bubble entrapment. Furthermore, very similar behavior is observed in all cases except in the case F representing the impact onto a glass substrate, being characterized by two peaks followed by sudden temperature changes.

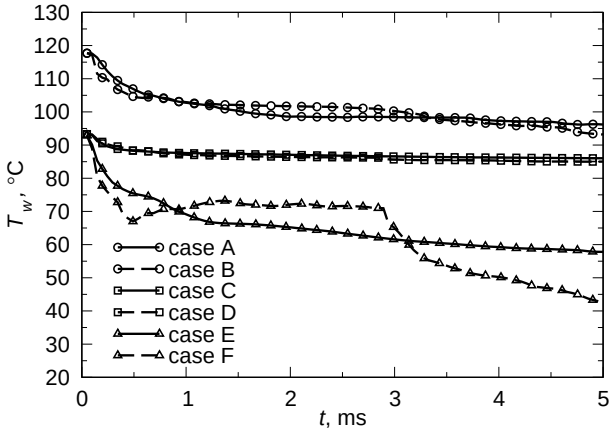

Figure 4.9: Computationally obtained temporal evolution of the impact point temperatures for the cases A-F.

The latter changes are to be explained with help of Fig. 4.10, where the lamella shape and the entrapped bubble are shown at several time instances, plotted as the $\gamma = 0.5$ contours. It can be seen that, after entrapment, the bubble starts to oscillate. Although similar bubble oscillations were also encountered in other simulated cases, the amplitudes of the oscillations were much larger in this case. At the time instant $\bar{t} = 0.5$ ms the bubble has a lower height compared to the previous time instant, leading to the temperature rise in the bubble and at the underlying solid surface, represented by the minimum at the temperature curve in Fig. 4.9 for the case F. At the time $\bar{t} = 2.85$ ms the lamella becomes very thin and comparable to the bubble size. When the top surface of the lamella at a later time reaches the bubble, it breaks and the temperature adjusts accordingly showing the local decrease in that region due to a sudden heat release from the solid substrate. This explains the sudden temperature drop at $\bar{t} = 2.95$ ms in Fig. 4.9. Afterwards, approximately at the time when the lamella starts to retract, the sides of the formed circumferential ring collapse, leaving only a tiny bubble entrapped. A clear physical mechanism for the oscillation of the bubble may not be recognized from these results. However, since this study is mainly devoted to the formulation and validation of the computational

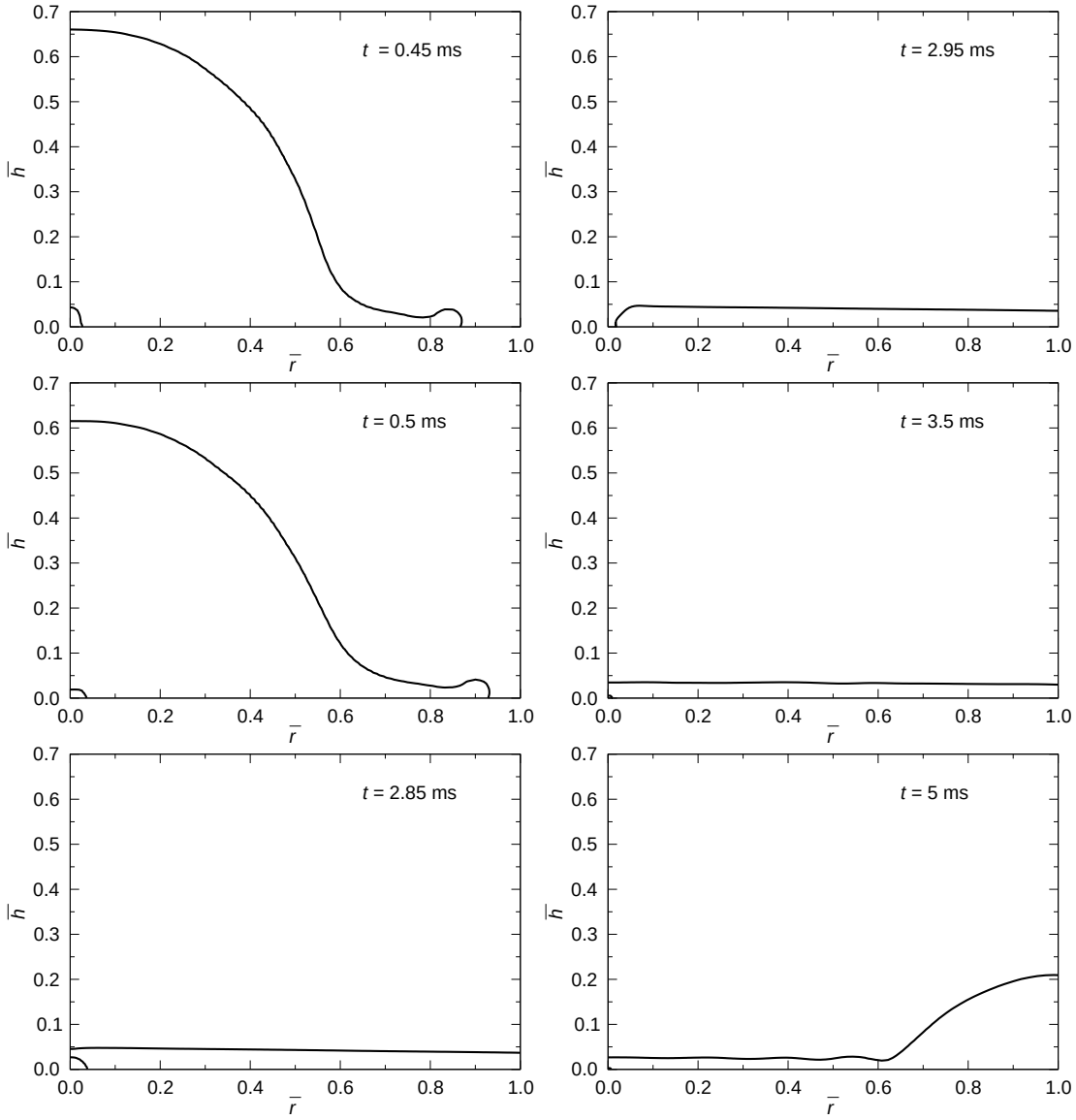

Figure 4.10: Free surface morphology variation illustrating the entrapped bubble oscillation and its consequent breakup in the case F.

model for combined simulations of free-surface flow and conjugate heat transfer, the hydrodynamics of the oscillating bubble is out of scope and is not further analyzed.

4.5.4 Distributions of Temperature and Heat Flux at the Wall Surface

Comparison of the present numerical predictions with available numerical results for the radial distributions of temperature and heat flux at the solid surface is presented in Fig. 4.11. The agreement is fairly good except in the vicinity of the impact region, where higher temperatures and considerably smaller heat fluxes are encountered. Small peaks appearing at the radial distance of $r \approx 0.5$ mm are due to

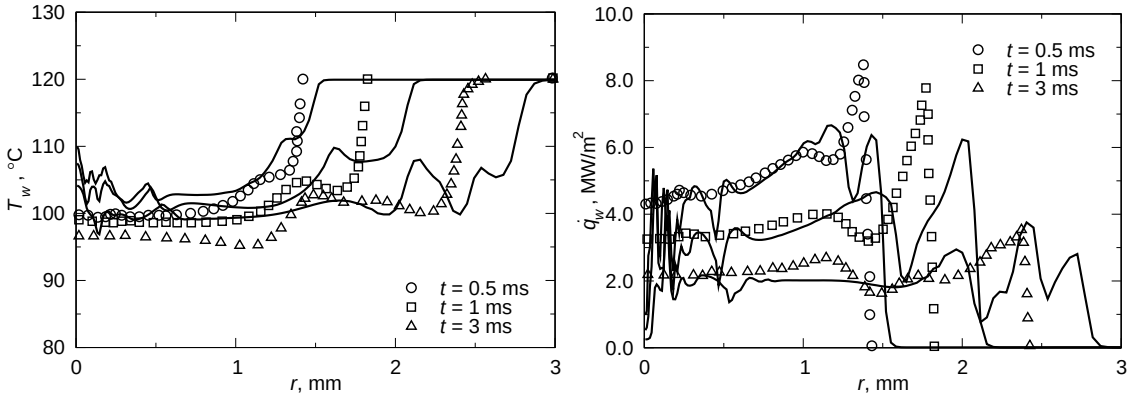

Figure 4.11: Comparison of the present predictions for the radial distribution of temperature (left) and heat flux (right) at the solid surface (lines) with numerical results from Pasandideh-Fard et al. [74] (symbols).

the presence of the afore-mentioned air ring (Mehdi-Nejad et al. [58]), where higher temperature and correspondingly lower heat flux are computed, before the ring joins and collapses at the axis of symmetry. The temperature and heat flux distributions are rather smooth underneath the lamella in the reminder of the observed area up to the rim region, within which, domains of higher and lower temperatures are created due to the complex local flow field.

The theoretical solution for the hydrodynamics and heat transfer in drop impact onto a solid substrate was obtained by Roisman [97]. In this study a similarity solution for the Navier-Stokes and energy equations is found for the case of a nonisothermal flow configuration, including the phenomena of near-wall phase transition. For the particular case of drop impact without phase change and constant thermophysical properties of the fluid and the wall, the theoretically predicted wall heat flux is expressed in the form

$$\dot{q}_{w,theor} = \frac{e_l e_s (T_{s,0} - T_{d,0})}{[e_l + e_s \mathcal{I}(\mathrm{Pr}, 0, \infty)]\sqrt{\pi}\sqrt{t}} \quad \text{at} \quad \bar{t} > 1. \tag{4.24}$$

where e_l and e_s are the thermal effusivities of liquid and solid substrate materials and $\mathcal{I}(\mathrm{Pr}, 0, \infty)$ is a dimensionless function of the Prandtl number, the numerical values of which are provided by Roisman [97]. The theoretically predicted contact temperature is constant and uniform

$$T_c = \frac{e_l T_{d,0} + e_s \mathcal{I}(\mathrm{Pr}, 0, \infty) T_{s,0}}{e_l + e_s \mathcal{I}(\mathrm{Pr}, 0, \infty)}. \tag{4.25}$$

Comparison of the present numerical predictions for the averaged heat flux at the solid surface with the analytical result is given in Fig. 4.12. In the simulations, the heat fluxes, averaged over the wall surface in one time step, are determined from the following expression

$$\dot{q}_w = \frac{\int_{S_w} (\dot{\mathbf{q}}_s \cdot \mathrm{d}\mathbf{S}_s)}{\int_{S_w} |\mathrm{d}\mathbf{S}_s|} \approx \frac{\sum_{i=1}^{N} [-k_{w,i} (\nabla T_{w,i})|_\perp |\mathbf{S}_{f,i}|]}{\sum_{i=1}^{N} |\mathbf{S}_{f,i}|}, \tag{4.26}$$

where the summation is performed over all cell-faces N at the solid-fluid interface. Although heat transfer in the air is accounted for in simulations, it is much smaller compared to heat removed from the substrate by the liquid. Therefore, only those cell-faces belonging to cells filled with liquid are taken into account.

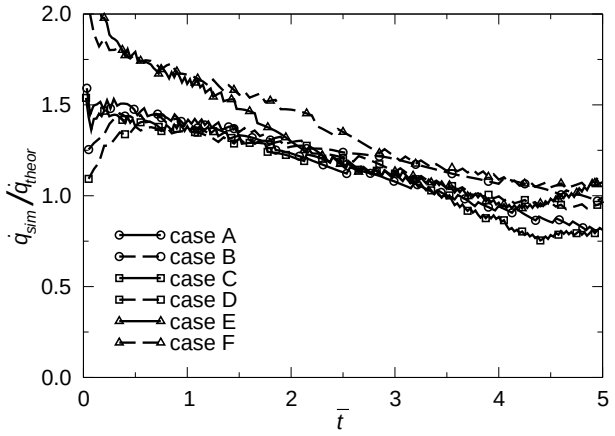

Figure 4.12: Comparison of the present numerical predictions for the averaged heat flux at the solid surface with the analytical result from Roisman [97].

According to the results shown in Fig. 4.12, the theory and the numerics quickly converge at the dimensionless time $\bar{t} = 1$. At the earlier times, not considered theoretically, the average heat flux is influenced by the edge effects in the neighborhood of the contact line. The predicted average heat fluxes are slightly smaller for higher impact parameters in the short time during the initial spreading phase up to $\bar{t} \approx 1$, as can be seen in Fig. 4.12. This is found to be in accordance with the results from Pasandideh-Fard et al. [74], where similar behavior was obtained indicating that the drop's cooling effectiveness is independent of the impact velocity only for large Weber numbers, $\mathrm{We} \gg \mathrm{Re}^{0.5}$.

In the present study the Weber numbers are much lower compared to this criterion resulting in the more pronounced dependence of the heat transfer rates on the impact velocity. This can be seen in Fig. 4.13, where the computed overall heat transfer versus time is shown. The averaged overall heat transfer from the wall surface to the drop is evaluated during the computations at every time instant from the expression

$$Q = \int_0^t \left[\int_{S_w} (\dot{\mathbf{q}}_{s,j} \cdot \mathrm{d}\mathbf{S}_s) \right] \mathrm{d}t \approx \sum_{j=1}^{n} \left[\dot{q}_{w,j} S_w \right] \Delta t_j, \tag{4.27}$$

where the term in the brackets represents the heat transfer rate corresponding to the time step Δt_j and the summation is performed over all time steps n. The wall heat flux $\dot{q}_{w,j}$ on the r.h.s. of Eq. (4.27) corresponding to the time step Δt_j is calculated from Eq. (4.26) by assuming that the obtained value prevails during the time step. Thus, the amount of heat transferred from the wall surface is obtained by accumulating the heat fluxes from all time steps up to the given time t_j. Since the

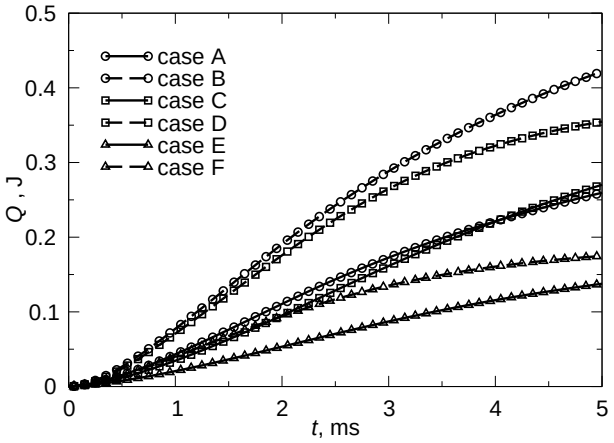

Figure 4.13: Predicted averaged heat transfer at the solid surface.

mesh is a two-dimensional slice, representing a part of the cylinder with an angle of 5° in the azimuthal direction, the total heat transfer from the substrate to the drop is evaluated by multiplying the values obtained from Eq. (4.27) by $360/5 = 72$ and these values are plotted in Fig. 4.13. It can be seen that the amount of heat transferred from the substrate to the spreading drop increases with increasing the impact velocity in all cases in the spreading phase, tending to decay in the receding phase due to lower velocities.

4.5.5 Mean Temperature in the Spreading Drop

In addition to the distributions of the temperature and the heat flux at the wall surface, it is interesting to examine the rise of the mean temperature in the spreading drop. The flow in the spreading lamella is fast, inertia-dominated, and it takes only a few milliseconds for the lamella to start receding. However, it is found that even in the relatively small temperature ranges considered here, the temperature in the spreading drop may increase significantly. The mean droplet temperature is determined in the simulation from the expression similar to Eq. (3.26)

$$T_{mean} = \frac{\sum_{i=1}^{N} T_i \Delta V_i}{\sum_{i=1}^{N} \Delta V_i}, \tag{4.28}$$

and the rise in the mean drop temperature over time is given in Fig. 4.14. It can be observed that the mean temperature within the spreading drop may rise up to $\approx 50\%$ of the initial temperature difference even during this very short initial spreading phase. This supports the observation that heat transfer may be significant already at the initial stage of spreading.

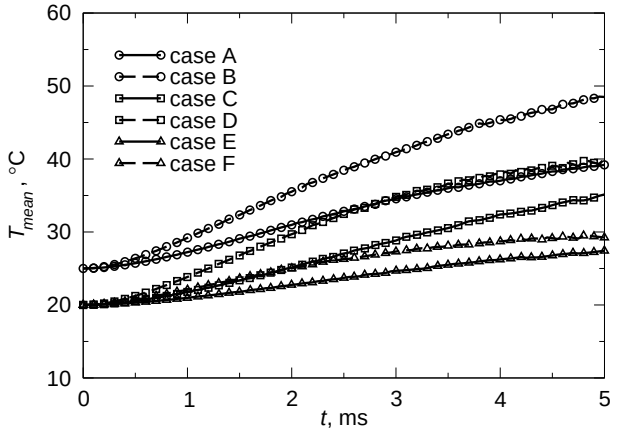

Figure 4.14: Predicted time variation of the mean drop temperature.

4.5.6 Comparison with the Case of the Isothermal Wall

In order to examine the effect of the theoretical assumption of the uniform temperature distribution at the solid surface as being equal to the impact point temperature, on the overall heat transfer, additional numerical simulations of flow and heat transfer in the fluid region only were performed. The solid surface was treated as an isothermal boundary by setting the fixed boundary value for temperature equal to the theoretically predicted one. The simulations were performed for the cases A and B, with $T_c = 98.6°\text{C}$ prescribed as the boundary condition for the temperature at the wall surface. The computed heat transfer for these two cases is shown in Fig. 4.15 and compared to the corresponding simulation results incorporating the conjugate heat transfer within the solid substrate.

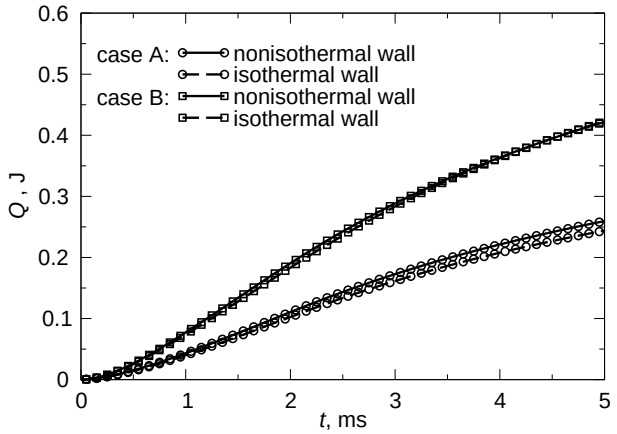

Figure 4.15: Comparison of the predicted averaged heat transfer at the solid surface for the cases A and B, using the assumption of an isothermal wall at $T_c = 98.6°\text{C}$ with the results incorporating the conjugate heat transfer within the solid substrate.

As expected, the heat extracted from the wall is slightly smaller if isothermal

wall is assumed and the difference between the cases with and without isothermal wall is more pronounced for the lower values of the impact parameters, corresponding to the lower impact velocity. For the impact at the higher velocity this difference is very small, which is also expected, due to the much larger Peclet and Eckert numbers for this case. These results suggest only a weak dependence of the overall heat removed from the solid surface on the temperature distribution at the fluid-solid interface.

4.5.7 Effects of the Wettability at the Wall

In all the cases the wettability at the wall is approximately accounted for by the quasi-dynamic contact angle at the contact line, by using two constant values for the contact angle at the advancing and the receding phase of drop spreading, respectively. In order to examine the effects of the contact angle on the heat transfer in the spreading drop, additional simulations were performed with the dynamic contact angle at the wall set according to Eq. (4.18) and the contact-line velocity evaluated from Eq. (4.21). The previously used values of 110° and 40° are used as limiting values for θ_{eq} in Eq. (4.18). The obtained results for the spreading ratio and the overall heat transfer at the wall in cases A and B are shown in Fig. 4.16 and compared to the same cases computed with the quasi-dynamic contact angle.

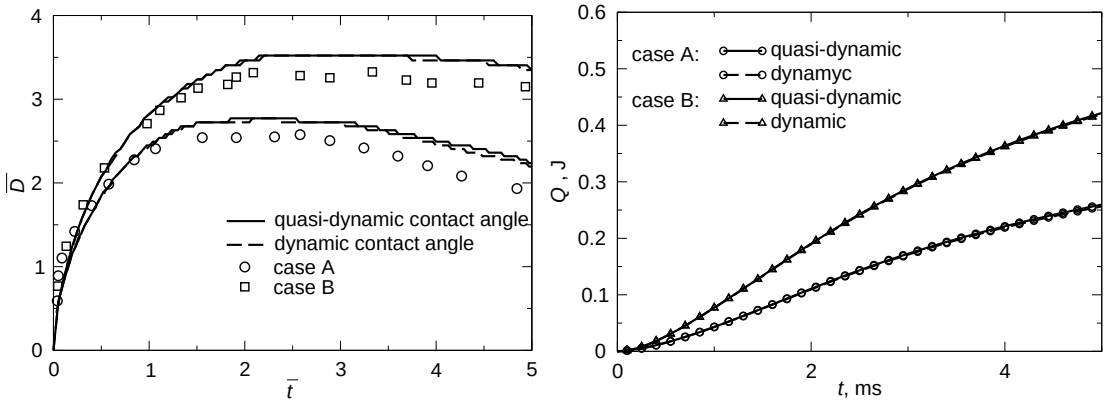

Figure 4.16: Influence of the dynamic contact angle on the spreading ratio (left) and on the overall heat transfer (right). The symbols on the left graph correspond to experiments from Pasandideh-Fard et al. [74].

In the particular cases it is found that the deviation from the results obtained using the quasi-dynamic contact angle is negligible during the initial spreading phase and becomes noticeable only at later stages when the lamella starts to recede. This can be explained by the fact that Eq. (4.21), although applicable to a general three-dimensional case, is only a rough approximation for the contact-line velocity. However, modeling the motion of the contact line is out of scope of the present study and is not considered further. Due to the small deviation of the spreading ratio, the results for the overall heat transfer show no noticeable difference.

5 Drop Impact on a Porous Substrate

5.1 Introduction

Drop impact onto a porous surface is a phenomenon encountered in everyday life and in various engineering applications. It is common in ink-jet printing, where the impacting droplets of ink are absorbed by the paper upon impact. Another example is composite processing, where the air in the fibrous network of a porous medium is displaced by a polymeric fluid. The wetting characteristics of the polymeric liquid within the porous network are of utmost importance for an efficient processing operation. Recent developments in medicine in the field of the needle-free vaccine delivery support the importance of studying the process of liquid penetrating into the porous medium. The methods for drug delivery without the needle and a syringe include impact and penetration of thin liquid medication jets through nozzles under high pressure into human skin (Giudice and Campbell [32]).

The flow includes simultaneous spreading and absorption of liquid into the porous substrate. In addition to the impact conditions, spreading and absorption of the liquid drop in fibrous substrates depends on the wettability of the porous surface and porosity and permeability of the porous material, which are related to the orientation of fibers in the network, number and size of the pores, etc. Due to the complexity of the porous network, theoretical solutions provide only limited information about the dynamics of the flow and experimental observations usually cannot reveal the behavior within the porous material. An additional difficulty arises from the fact that the impact with absorption of a drop into porous materials is governed by two different time scales, one for drop spreading and the other for the penetration into the porous medium (Golpaygan et al. [33]). The penetration time is usually several orders of magnitude larger than the characteristic time for the spreading, and the liquid drop may reach its equilibrium position after spreading on the porous surface much faster than a noticeable penetration even occurs.

In this Chapter the numerical procedure for interface capturing is applied to compute drop impact on a porous surface. The computational model is extended and the combined model is formulated including both the external flow for the spreading and the flow of the absorbed fluid in the porous substrate. In addition to this, drop spreading on the porous surface is numerically simulated by computing only the external flow induced by the drop impact and the presence of the porous surface is accounted for by formulating an appropriate boundary condition for the permeable wall. The two numerical models are validated by comparing the computational results with the existing experimental results from Chandra and Avedisian [15] and capabilities of both approaches are analyzed.

5.2 Governing Equations and Computational Details

5.2.1 The Combined Model

For the formulation of the combined model including the external flow and the flow in the porous substrate, the approach due to Reis et al. [86] is adopted. Two-phase flow through the porous material is assumed to be governed by the same flow equations as in the external nonporous region, Eqs. (3.19–3.21). The equations have to be solved at the extremely small scales, where the representative size of the mesh cells is very small in comparison to the pore dimensions. However, this is not possible, because of the complexity of the porous network, the large number of particles or fibers forming a porous material and very small pore sizes. Therefore the equations for the flow through the porous material are written at the macroscopic level, where the cell size is large compared to the pore dimensions and the effects of the porous network are treated as averaged quantities. The two parameters characterizing the porous substrate are its porosity and permeability. Porosity is used as a measure of the pore spaces in the material and is defined as the fraction of the volume of the pores over the total volume of the porous material

$$\varepsilon = \frac{V_\mathrm{p}}{V}. \tag{5.1}$$

Permeability is a property used to quantify the ability of the fluid to flow through the porous material. It is defined by Darcy's law for the flow in the porous material, which can be expressed as

$$\langle U \rangle = -\frac{K}{\mu}\frac{\Delta p}{L}, \tag{5.2}$$

where the symbol $\langle \quad \rangle$ denotes the averaged or superficial velocity. According to Eq. (5.2) the volumetric flow rate through a porous specimen is proportional to the mean pressure gradient across the specimen and inversely proportional to the fluid viscosity. The proportionality constant K is the permeability of the material and is generally a tensor in the case of an anisotropic porous medium.

The momentum equation for the flow inside the porous material is extended to include the viscous resistance from the Darcy-Forchheimer expression $(\mu/K)\langle \mathbf{U} \rangle$ (Reis et al. [86]). Replacing the velocity in Eq. (3.21) by the superficial velocity, which is by definition $\langle \mathbf{U} \rangle = \varepsilon \mathbf{U}$, and including the resistance term, the following set of equations is obtained for the flow in the porous region

$$\nabla \cdot \langle \mathbf{U} \rangle = 0, \tag{5.3}$$

$$\frac{\partial \gamma}{\partial t} + \nabla \cdot (\langle \mathbf{U} \rangle \gamma) + \nabla \cdot [\langle \mathbf{U}_c \rangle \gamma (1-\gamma)] = 0, \tag{5.4}$$

$$\frac{\partial (\rho \langle \mathbf{U} \rangle)}{\partial t} + \frac{1}{\varepsilon}\nabla \cdot (\rho \langle \mathbf{U} \rangle \, \langle \mathbf{U} \rangle) = -\nabla \langle p_d \rangle - \varepsilon \mathbf{g} \cdot \mathbf{x} \nabla \rho + \nabla \cdot \langle \mathbf{T} \rangle + \varepsilon \sigma \kappa \nabla \gamma - \frac{\varepsilon \mu}{K} \langle \mathbf{U} \rangle, \tag{5.5}$$

where $\langle p_d \rangle = \varepsilon p_d$ represents the averaged macroscopic modified pressure, the averaged stress tensor $\langle \mathbf{T} \rangle = \mu \nabla \left(\langle \mathbf{U} \rangle + \langle \mathbf{U} \rangle^T \right)$ corresponds to the definition of the averaged velocity and porosity and permeability are assumed to be constant.

The sets of equations governing the external flow and the flow through the porous region are similar, differing only in the additional resistance term and the appearance of the porosity. The two systems are combined into a single one, representative for the whole solution domain. The flow equations, Eqs. (5.3–5.5) are solved throughout the computational domain using the solution procedure outlined in Chapter 3. The additional resistance term and the terms containing the corrections with the porosity are added only in the mesh cells inside the region occupied by the porous material. The resistance term is treated implicitly, by adding the contribution to the diagonal matrix coefficients. The terms containing the porosity are handled by prescribing a field of porosity in all computational points, equal to unity in the external region and to the given constant porosity value in the porous material. Thus, the flow equations Eqs. (5.3–5.5) are solved for both regions simultaneously and the fluid velocity in the external region is preserved, while inside the porous material the velocity represents the macroscopic averaged velocity.

5.2.2 The Permeable-wall Model

Although the flow through porous media has been extensively studied, most attention was given to single-phase flows and estimations of the parameters characterizing the porous medium, namely the permeability and the porosity. In most studies the granular porous material is represented as a packed bed of randomly distributed spheres and less attention was given to fibrous materials. Theoretical expressions for the estimation of the permeability of fibrous materials are mostly obtained for simplified unidirectional flow along or perpendicular to long cylinders. The data is presented in the dimensionless form

$$\frac{K}{R_p^2} = f(\phi), \tag{5.6}$$

where $\phi = 1-\varepsilon$ is the solid volume fraction. An extensive overview of the estimations in the form of Eq. (5.6) covering a wide range of porous materials is provided by Jackson and James [44]. More recently a theoretical model for the permeability of a fibrous web with an orthogonal pattern of fibers was presented by Koponen et al. [50].

According to Yarin [133] the liquid flows in the fibrous porous material very slowly through the pores (the channels between the fibers) and can be approximated by the steady Stokes flow, the solution of which for the case of cylindrical pores is

$$U = \frac{1}{4\mu}\frac{\partial p}{\partial z}(r^2 - R^2), \tag{5.7}$$

with the corresponding mean velocity

$$\langle U \rangle = -\frac{R^2}{8\mu}\frac{\partial p}{\partial z}. \tag{5.8}$$

Comparing Eq. (5.8) and Eq. (5.2), the permeability of the fibrous material corresponds exactly to

$$K = \frac{R_p^2}{8}. \tag{5.9}$$

In the permeable-wall model, only the external flow is solved using the interface-capturing model given by Eqs. (3.19–3.21) and the solution procedure outlined in Chapter 3. The existence of the underlying porous substrate is accounted for by defining an appropriate boundary condition at the impacting surface. According to Yarin [133], the normal-to-the-surface velocity component is expressed from Eq. (5.8) and use is made of the fact that the velocity is continuous in the thin region identified in the vicinity of the plane where the porous surface begins, Fig. 5.1, yielding

$$U|_{\perp} = -\frac{K_{\text{down}}}{\mu_{\text{down}}}\nabla p_{\text{down}}|_{\perp} = -\frac{K_{\text{up}}}{\mu_{\text{up}}}\nabla p_{\text{up}}|_{\perp}. \tag{5.10}$$

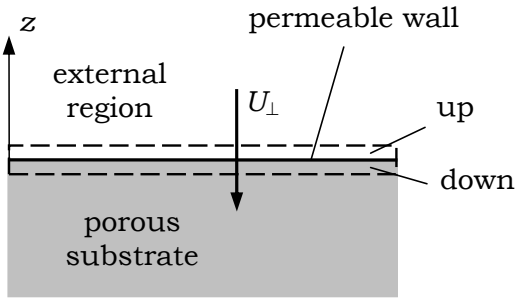

Figure 5.1: Definition of the permeable-wall boundary condition.

Although permeability (as well as porosity) may very in the porous medium, the variations are negligible in the intermediate vicinity of the porous surface and Eq. (5.10) is valid. The boundary condition for the velocity at the permeable wall then consists of the no-slip condition for the tangential component and the normal component is set using the expression

$$U|_{\perp} = -\frac{K}{\mu}\nabla p|_{\perp}, \tag{5.11}$$

where the pressure gradient is evaluated at the impacting surface and permeability is estimated from Eq. (5.9) for the given pore radius.

5.3 Numerical Simulations

The computational domain for the combined model, shown in Fig. 5.2, is a two-dimensional axisymetric slice with one cell in the azimuthal direction including both the external and the porous region. The mesh is graded with dimensions in the vertical plane of $4D_0 \times 6D_0$ based on the drop initial diameter. The total number of cells is ≈ 48000 cells, of which 8000 belongs to the porous region.

In the case of the model with the permeable wall the flow in the porous region is not computed and the mesh is the same as the one for the external flow in the combined model, consisting of ≈ 40000 cells, Fig 5.3.

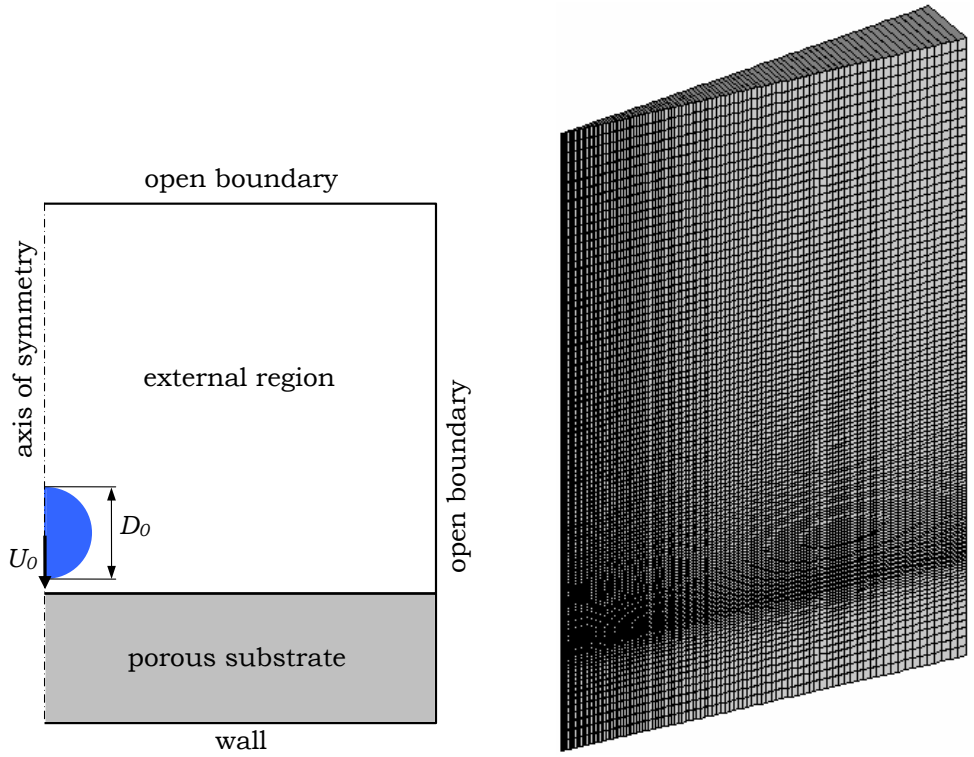

Figure 5.2: Initial case configuration (left) and computational mesh (right, every second line shown) for the combined model.

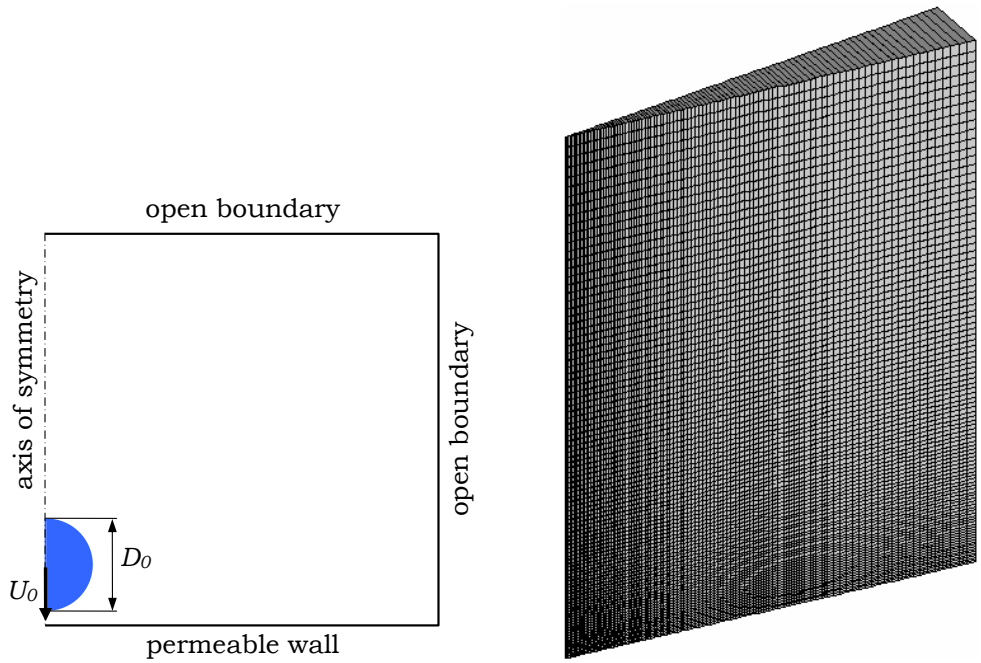

Figure 5.3: Initial case configuration (left) and computational mesh (right, every second line shown) for the model with the permeable wall.

Simulations are initialized by prescribing the phase fraction distribution defining the shape of the drop and setting the initial velocity equal to the impact velocity. The boundary conditions for the combined model include the no-slip wall boundary at the bottom and open boundaries at the top and to the right side with the prescribed total pressure and a combination of inlet and outlet conditions for velocity. For the permeable-wall model, Eq. (5.11) defines the boundary condition for the velocity at the bottom.

As previously mentioned, a review of the available literature has revealed that drop impact on fibrous media was not extensively studied. Most studies do not provide exact values for either the permeability or the fiber or pore radius. The porous substrate is commonly characterized by the value for porosity or the area density (density of the solid divided by the surface of the substrate's cross-section) and the thickness, thus yielding insufficient data required for the simulation (Arora et al. [2], Kumar and Deshpande [51], Clarke et al. [16]). Moreover, the experiments are mostly performed on sessile drops placed on the porous substrate where the evolution of the drop, the residual liquid volume above the surface and the spreading ratio are tracked in large time periods, ranging from several tens to several thousands of seconds. Such experiments are clearly not suitable for the simulation, where only the initial period upon the drop impact can be computed because of the high required computational efforts.

Therefore, the assessment of both computational models is performed using the experimental data for drop impact on the ceramic porous substrate from Chandra and Avedisian [15]. The liquid used in the simulation is n-heptane (C_7H_{16}) with the physical properties and the governing dimensionless numbers corresponding to the impact velocity $U_0 = 0.93$ m/s and the drop diameter and $D_0 = 1.5$ mm listed in Table 5.1.

Table 5.1: Physical properties of the liquid and the porous medium and dimensionless numbers used in the numerical simulations.

n-heptane/ceramic	
density ρ, kg/m^3	667.5
viscosity μ, Ns/m^2	$4.05{\cdot}10^{-4}$
surface tension σ, N/m	$2.01{\cdot}10^{-2}$
porosity ε	0.25
permeability K, m^2	$1.04{\cdot}10^{-12}$
pore radius R_p, μm	2.88
Weber number	43
Reynolds number	2300

The indicated value for the porosity is taken from Chandra and Avedisian [15]. Based on the provided value for the mean particle size in the range of 5–10 μm, Reis et al. [86] estimated the permeability, which, according to Eq. (5.9), yields the mean pore radius of $R_p = 2.88$ μm for the case of a fibrous medium. In the combined simulation the porosity and the estimated permeability from Table 5.1 are

prescribed, whereas for the permeable-wall model the mean pore radius is used for the boundary condition for the velocity at the permeable wall.

5.4 Results and Discussion

5.4.1 Drop Shapes

In Fig. 5.4 the numerically predicted drop shapes at several times during drop spreading on the porous substrate obtained by using the combined model and represented as $\gamma = 0.5$ contours are compared to the photographs from Chandra and Avedisian [15]. In order to assess the capabilities of the combined model with respect to the change of permeability of the porous region, an additional simulation is performed with an order of magnitude lower prescribed permeability. Fig. 5.5 shows the computationally obtained drop shapes at several times for two used permeabilities.

The combined model is able to capture the phenomenology of the flow in the external region and within the porous material only qualitatively and at very small times upon the impact. The suppression of the liquid penetration can be seen in Fig. 5.5, where almost no liquid penetrates into the substrate for the case in which the lower permeability is used. However, at times $\bar{t} \geq 1$ the lamella deforms taking the shape of a thin disk in the experiments, which is not properly resolved in the simulation, as can be seen in Fig. 5.4 and Fig. 5.5.

Although the combined model is relatively simple and analogous to the external flow, according to the obtained results its validity is restricted only to the initial stage of spreading for two main reasons. First, the wettability at the porous surface is not accounted for, since no boundary condition for the contact angle can be prescribed in the computational model at the surface which is internal to the mesh. Second, in the absence of a suitable model for the wettability within the substrate, there is no driving force for the penetration of the liquid into the porous material except inertia, leading to suppression of the penetration at the end of the inertia driven spreading stage of the drop. This can be seen in Fig. 5.4 and Fig. 5.5 at times $\bar{t} \geq 1$ where the liquid front hardly penetrates in the porous medium. Furthermore, the presence of the inertia term may not be physically justified in the momentum equation for the flow in the porous region, which should obey Darcy's expression, Eq. (5.2). The extension of the full momentum equation in the form of the viscous resistance term represents essentially the solution of the momentum equation for the steady creeping flow in the pores and the governing equation should therefore not include any inertial effects.

In the case of the permeable wall the porous surface represents the boundary of the computational domain allowing the wettability to be accounted for. Chandra and Avedisian [15] provided only the value of the measured apparent contact angle at the end of the drop spreading on the surface equal to $\theta = 47.5°$. However, Kumar and Deshpande [51] performed experiments with absorption of drops of silicon

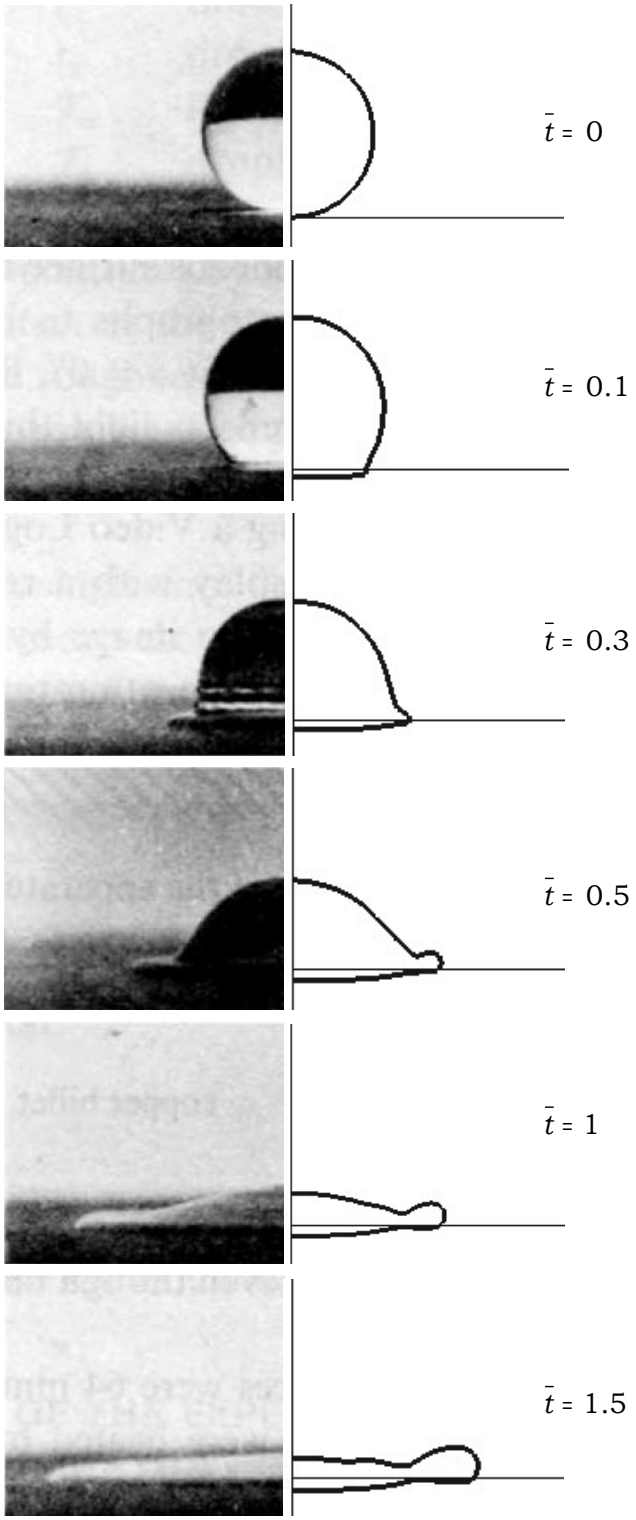

Figure 5.4: Comparison of the liquid shapes at the porous surface for Re = 2300, We = 43, $K = 1.04 \cdot 10^{-12}$ m^2: photographs from Chandra and Avedisian [15] (left) and prediction using the combined model (right).

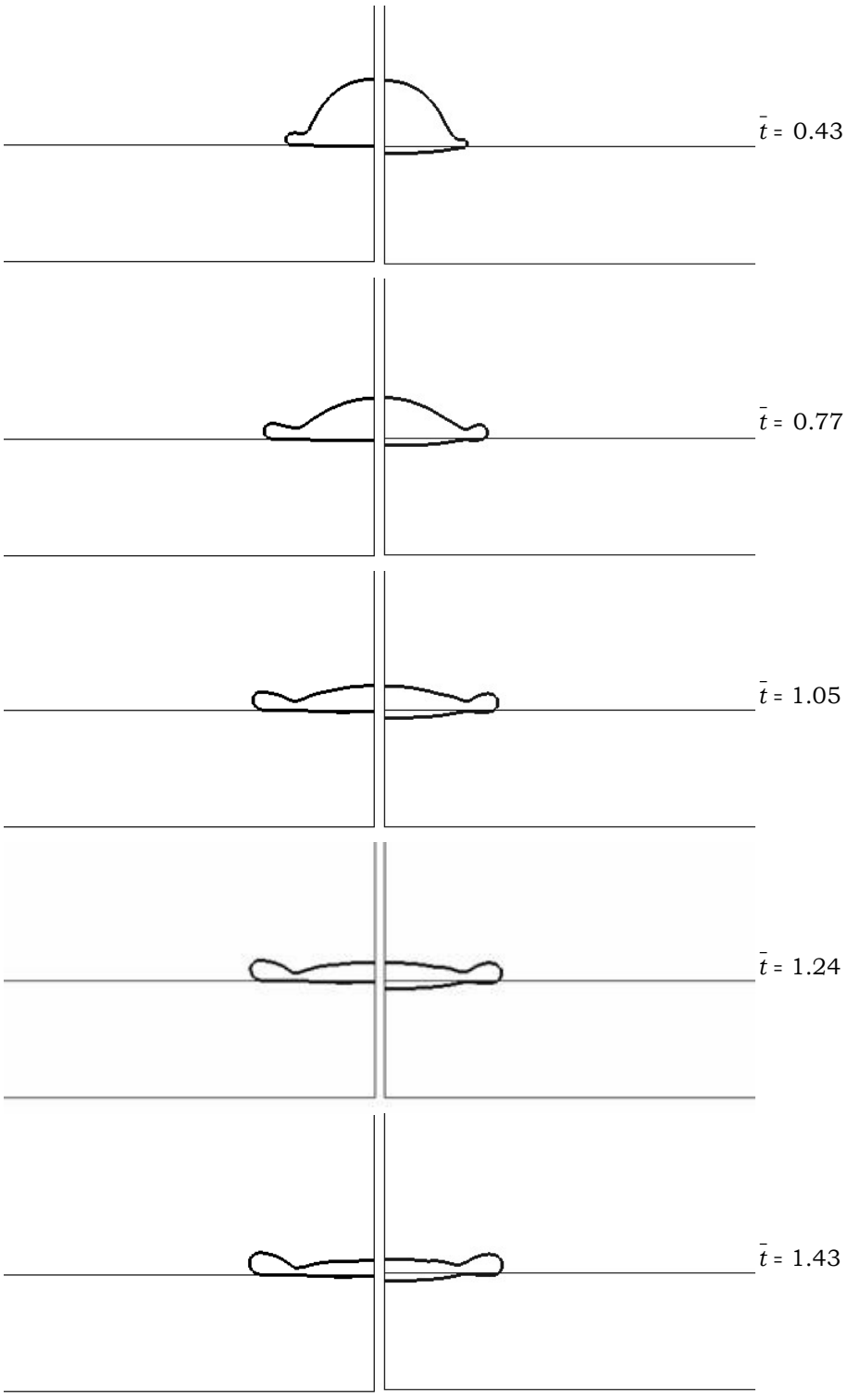

Figure 5.5: Liquid shapes at the porous surface for Re = 2300, We = 43, obtained using the combined model with the permeability $K = 1.04 \cdot 10^{-13}$ m^2 (left) and $K = 1.04 \cdot 10^{-12}$ m^2 (right).

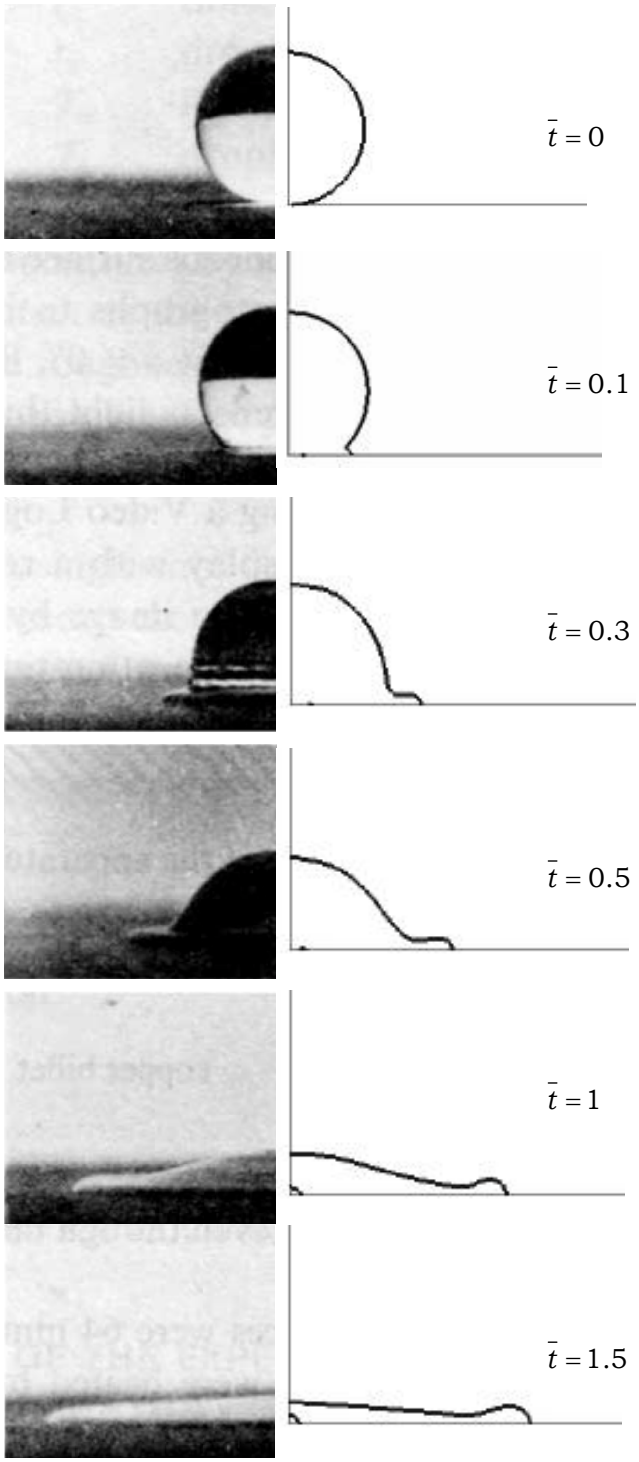

Figure 5.6: Comparison of the liquid shapes at the porous surface for Re = 2300, We = 43, $K = 1.04 \cdot 10^{-12}$ m^2: photographs from Chandra and Avedisian [15] (left) and prediction using the model with the permeable wall and time-dependent contact angle (right).

oil and a water/alcohol solution into glass fiber woven fabric and glass fiber unidirectional mats. They found that the contact angle at the porous surface is changing linearly in time during the initial period of spreading, beginning at $\theta \approx 90°$. In the absence of the exact values for the contact angle, in the present study numerical simulations are performed by prescribing three different contact angles at the porous surface: $\theta = 47.5°$, $\theta = 90°$ and a time dependent contact angle in the range $47.5° \leq \theta \leq 90°$, where the intermediate values are determined by linear interpolation in time. Computationally obtained drop shapes for the case of the permeable wall and the time-dependent contact angle are shown in Fig. 5.6.

It is seen that the shape of the liquid lamella is captured much more accurately in the simulation with the permeable wall. Even at longer times $\bar{t} \geq 1$ the lamella shape corresponds to the photographs from experiments, except at the edges, where the rim region is more pronounced in the simulation compared to the experiment. According to these results, the model including the permeable wall is able to qualitatively resolve the liquid spreading on the porous surface and the disagreement in the liquid shapes in the region of the rim is solely due to the imposed contact angle, which was not provided in the experimental data. As in the previous cases of drop collision with a dry wall and binary drop collision, a small entrapped bubble is resolved in the simulation in the region of the impact point.

5.4.2 Spreading Ratio, Lamella Height and Volume

In order to assess the predictive capabilities of both models in the quantitative sense, the computationally obtained spreading ratio and the change of the lamella height at the axis of symmetry in time are compared to the experimental results. In addition, the decrease of the lamella volume above the porous surface is computed, which determines the absorbed liquid volume. In order to determine the effects of the permeability of the porous substrate, an additional simulation using the permeable-wall model is performed with a greater pore radius of $R_p = 28\ \mu$m, which corresponds to a higher permeability of $K = 1.04 \cdot 10^{-10}$ m^2. Fig. 5.7 and Fig. 5.8 show the comparison of the computed spreading ratio and the change of the lamella height at the axis of symmetry in time with the experimental results from Chandra and Avedisian [15], and Fig. 5.9 shows the computed residual volume of the lamella over the porous substrate during spreading. The lamella height and volume are normalized by the drop initial diameter and volume.

As expected, the numerical results of the model with the permeable wall show closer agreement with the experimental data than the combined model. The disagreement of the computed spreading ratio with the experimental results is higher at the lower applied contact angle at the porous surface in Fig. 5.7. It is also seen in Fig. 5.7 and Fig. 5.8 that the permeability of the porous medium has negligible effects on the spreading ratio and the lamella height during the initial spreading phase, indicating the fact that the time scale for the liquid absorption is much larger than that for the spreading. The two results for the lamella height obtained using

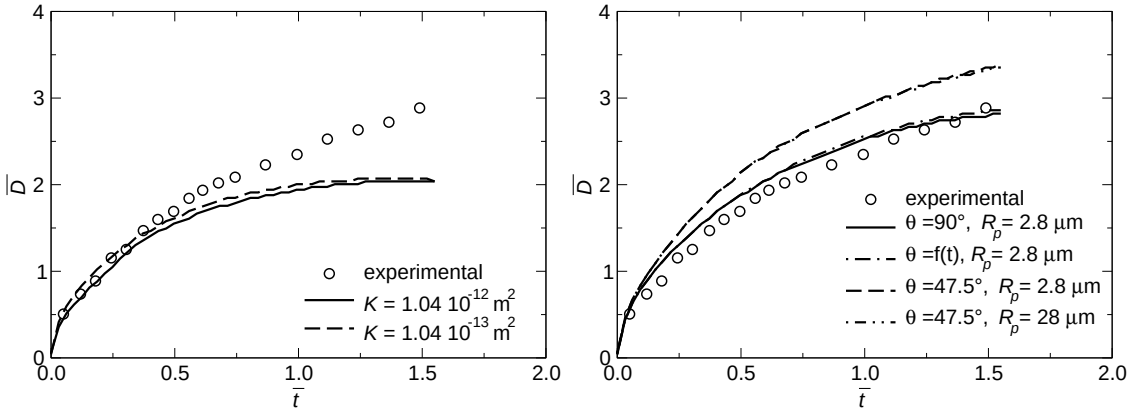

Figure 5.7: Spreading ratio for drop impact at Re = 2300, We = 43 obtained by using the combined model (left) and the permeable wall (right).

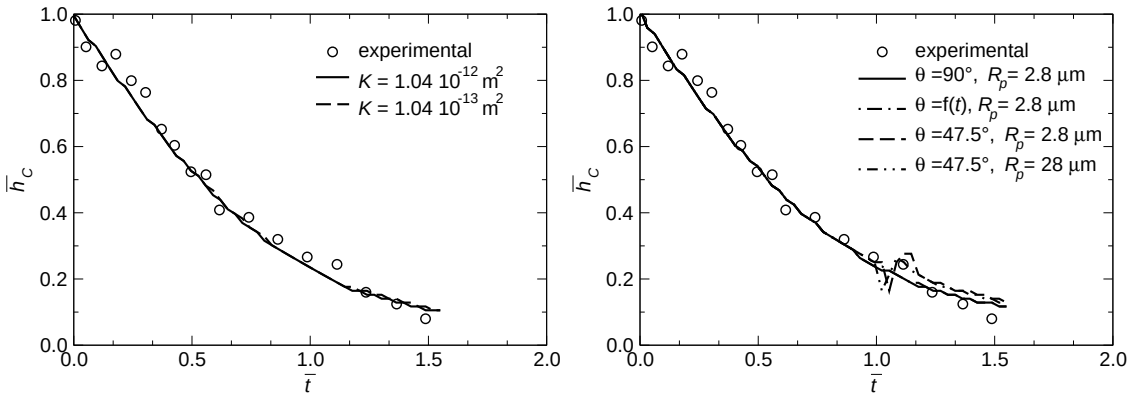

Figure 5.8: Dimensionless lamella height at the symmetry axis for drop impact at Re = 2300, We = 43 obtained by using the combined model (left) and the permeable wall (right).

the model with the permeable wall and the lower contact angle in Fig. 5.8 show a small peak at time $\bar{t} \approx 1.1$, which is caused by the entrapped air bubble at the region of impact. This air bubble moves upwards and escapes through the free surface of the lamella in these two cases causing the small peaks shown in the graph.

The computationally determined change of the residual liquid volume above the porous surface, plotted in Fig. 5.9, shows a non-linear dependence of the volume with time for both permeabilities used in the combined model, and for the higher permeability used in the model with the permeable wall. At lower permeability, the permeable-wall model yields a very small change of the volume which is linear with time. As expected, both models predict greater liquid volumes above the porous surface for substrates with lower permeabilities, corresponding to lower absorbed liquid volume. In the case of the permeable wall, a noticeable change in the liquid volume is present only for the higher permeability.

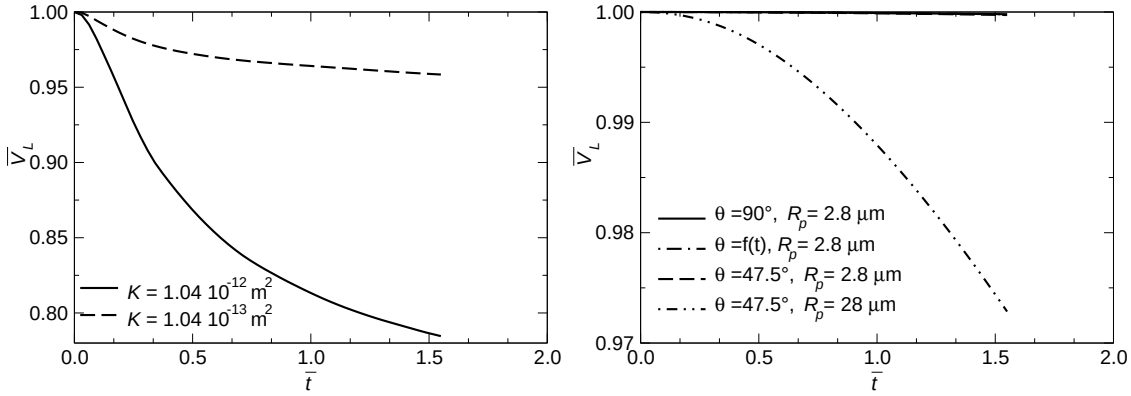

Figure 5.9: Dimensionless lamella volume above the porous surface for drop impact at Re = 2300, We = 43 obtained by using the combined model (left) and the permeable wall (right).

5.4.3 Conditions at the Porous Surface

Using the assumption of the incompressible fluid $\nabla \cdot \langle \mathbf{U} \rangle = 0$ in Eq. (5.8) the governing equation for the flow in the porous substrate reduces to

$$\nabla^2 p = 0, \tag{5.12}$$

which states that the pressure gradient in the porous region and the pressure gradient at which the liquid enters the porous substrate are constant. In order to prove Eq. (5.12), the mean pressure gradient and the normal velocity at the porous surface are computed in each time step using the expressions

$$\nabla p_w = \frac{\sum_{i=1}^{N} \nabla p_i|_\perp}{N}, \tag{5.13}$$

$$U_w = \frac{\sum_{i=1}^{N} U_i|_\perp}{N}, \tag{5.14}$$

where the summations are performed over the number of cell-faces N at the plane representing the porous surface. It should be noted that the above expressions represent the arithmetic mean values which are used for the comparison of the two models, rather than the true mean values, which would be obtained from expressions similar to Eq. (4.28) by using the cell-face surfaces instead of volumes, summing the products of $\nabla p_i|_\perp$ or $U_i|_\perp$ and the corresponding cell-face surfaces and dividing the sums by the surface of the permeable wall representing the porous surface.

Fig. 5.10 and Fig. 5.11 show the computed mean pressure gradient at the porous surface normalized by $\rho_l U_0^2/D_0$ and the mean velocity normalized by U_0 for both models, respectively. As expected the mean velocity and pressure gradient are not constant for the combined model. The mean velocity is decreasing because of the

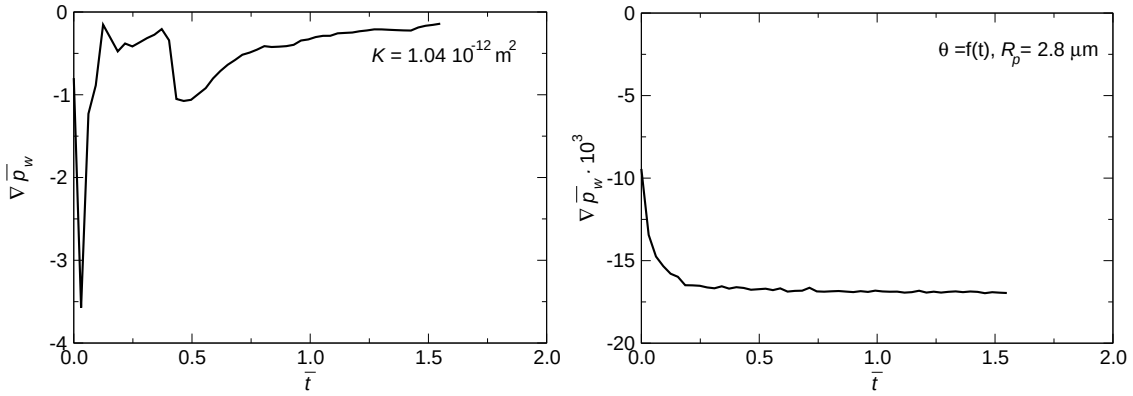

Figure 5.10: Dimensionless mean pressure gradient at the porous surface for Re = 2300, We = 43, $K = 1.04 \cdot 10^{-12}$ m^2 obtained by using the combined model (left) and the permeable wall (right).

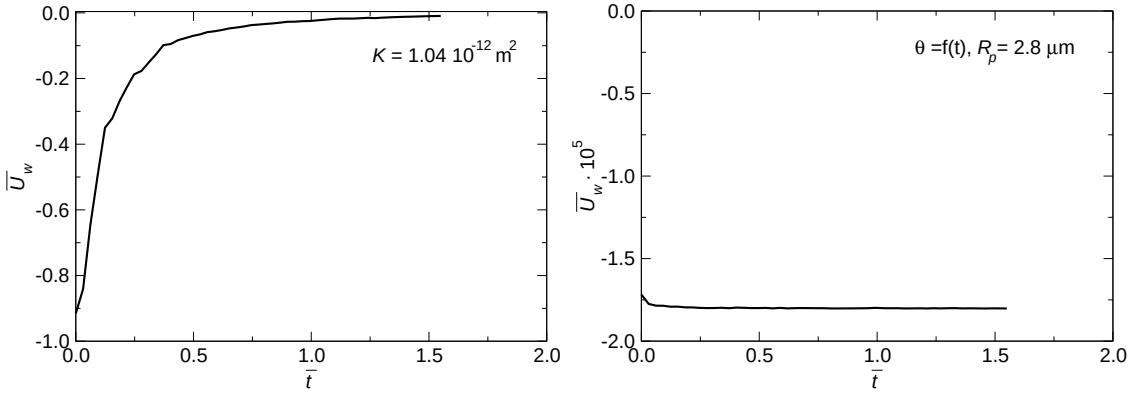

Figure 5.11: Dimensionless mean velocity at the porous surface for Re = 2300, We = 43, $K = 1.04 \cdot 10^{-12}$ m^2 obtained by using the combined model (left) and the permeable wall (right).

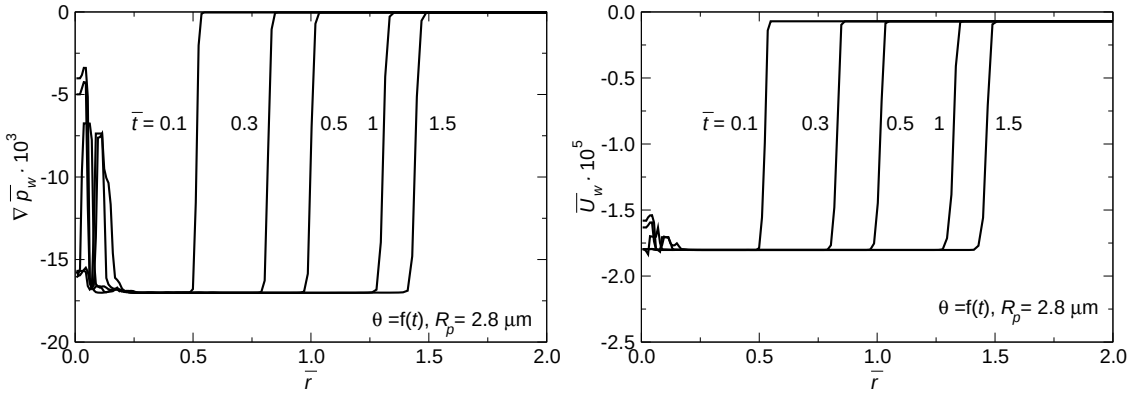

Figure 5.12: Distributions of the dimensionless pressure gradient (left) and velocity (right) at the permeable wall for drop impact at Re = 2300, We = 43, $K = 1.04 \cdot 10^{-12}$ m^2.

reasons stated in Section 5.4.1. Since there is no other driving force for the liquid absorption except inertia, the velocity of the penetration decreases in time. The pressure gradient shows no deterministic behavior. In the case of the model with the permeable wall, after a short initial time period the mean velocity as well as the mean pressure gradient become constant at the porous surface, which is in accordance with Eq. (5.12).

Instantaneous radial distributions of the normalized pressure gradient and velocity at the permeable wall are plotted in Fig. 5.12 at several time instants from left to right corresponding to those from Fig. 5.6. It is seen that both the pressure gradient and the velocity are constant over the porous surface, except in the region close to the impact point, where the profiles are disturbed by the presence of the entrapped air bubbles. As already stated, observation of such bubbles was reported in the experimental studies of drop impacts on dry and wet surfaces and they were resolved also in the other cases computed perviously in the present study. The existence and the evolution of these bubbles are out of scope and are not further analyzed.

5.4.4 Liquid Absorption at Longer Times

Kumar and Deshpande [51] found that the volume of the sessile drop absorbed in the porous material depends on both, the liquid used and the porous substrate. They obtained a square root dependence of the volume with time for silicon oil and a linear dependence for alcohol-water solution in drop spreading on woven and unidirectional fibrous mats. Furthermore, the absorbed volume was different for each fluid-substrate pair. The exact values of the permeability for the two substrates were not provided in the study, and the experimental results were obtained for very long times ranging to 50 s, which would consume extremely long computational time in the numerical simulation. In order to assess the capabilities of the model with the permeable wall at larger time scales, an additional numerical simulation of drop impact is performed with lower impact parameters than in the previous cases. The liquid has the properties of water and the corresponding impact parameters are $\mathrm{Re} = 1400$ and $\mathrm{We} = 27$. The spreading of the drop and the subsequential liquid absorption are computed up to the time $t = 0,2$ s corresponding to the dimensionless time of $\bar{t} = 280$, and the liquid is assumed to perfectly wet the porous surface by prescribing the constant contact angle equal to zero. The mean pore radius is set to $R_p = 5$ μm which yields the permeability of $K = 3.125 \cdot 10^{-12}$ m^2.

Computationally obtained liquid shapes are plotted in Fig. 5.13 at several time instants during spreading. Similar to the previous cases a small air bubble is entrapped in the region of impact in the initial phase of spreading. This bubble moves upwards and escapes through the lamella surface at $\bar{t} \approx 1.26$. The liquid continues to spread over the surface with no noticeable rim formation at the lamella edge, showing similar behavior to the flow regime termed the deposition by Rioboo et al. [91] in drop impact onto a rigid surface. At later times the lamella takes the shape of a flat disk with curved edges and slowly penetrates into the permeable wall.

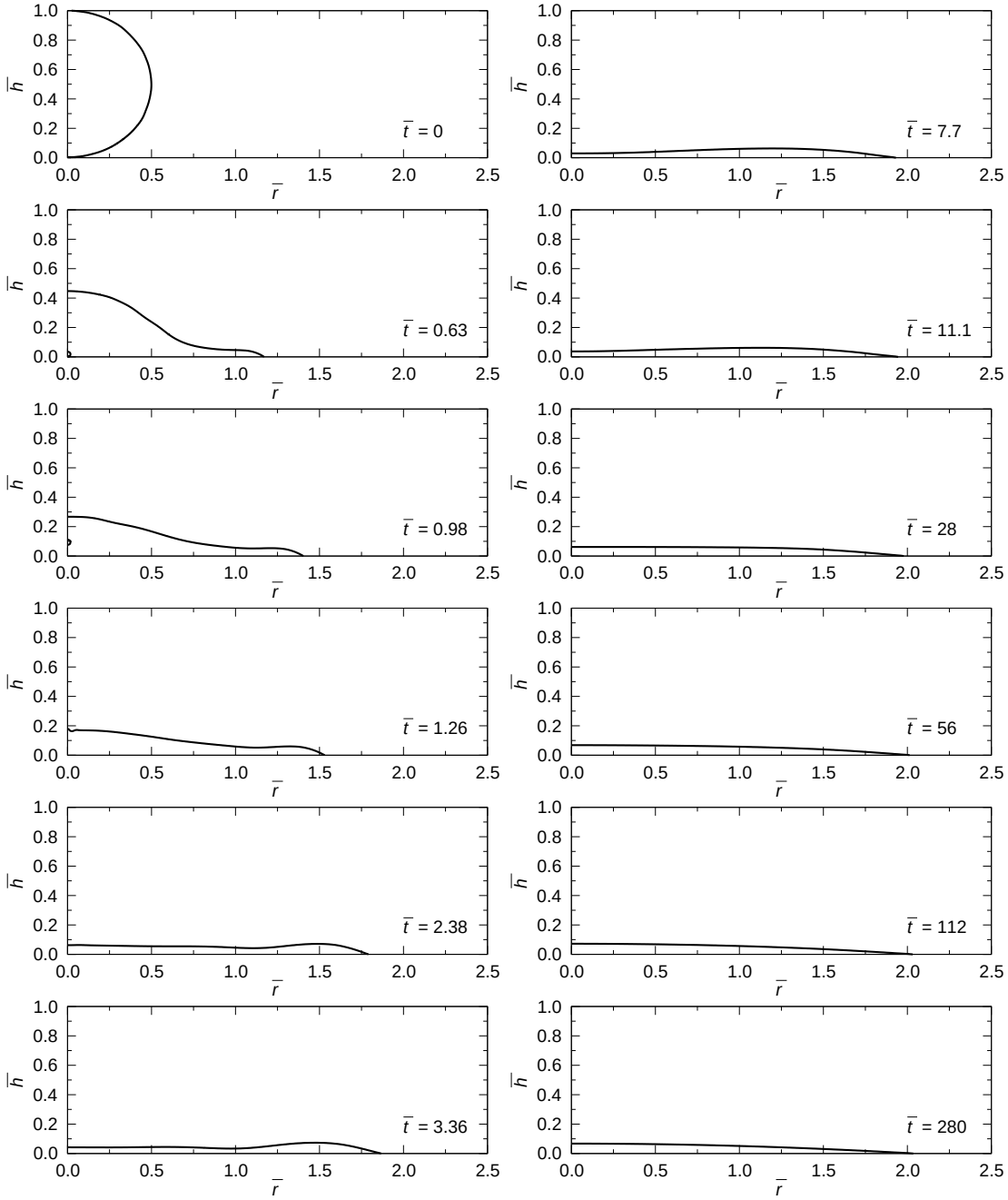

Figure 5.13: Liquid shapes for drop impact on the permeable wall at Re = 1400, We = 27, $K = 3.125 \cdot 10^{-12}$ m^2.

The computationally obtained spreading ratio is shown in Fig. 5.14 and the dimensionless lamella height at the axis of symmetry in Fig. 5.15. In order to show the details, the plots are divided in two graphs, the left graph corresponding to smaller times (up to $\bar{t} = 10$) and the right graph to longer times ($100 \leq \bar{t} \leq 280$). Due to the assumed perfect wetting the lamella spreads continuously over the permeable wall and reaches a diameter at $\bar{t} \approx 60$ which remains constant. The height of the

lamella at the axis of symmetry initially rapidly decreases after the drop hits the surface and slightly oscillates due to surface tension, starting to slowly decrease at $\overline{t} \approx 100$. The small peak appearing in the left graph in Fig. 5.15 corresponds to the time instant $\overline{t} \approx 1.26$ when the entrapped air bubble escapes through the upper lamella surface.

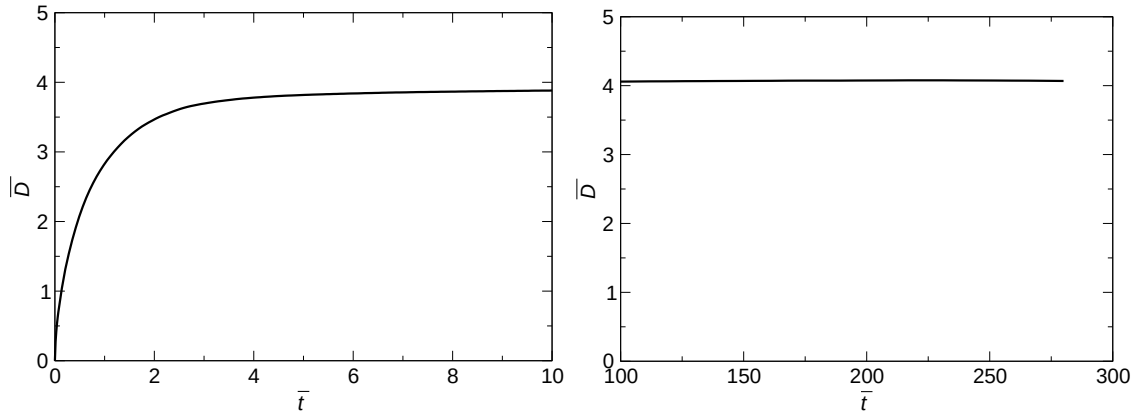

Figure 5.14: Spreading ratio for drop impact on the permeable wall at Re = 1400, We = 27, $K = 3.125 \cdot 10^{-12}$ m^2.

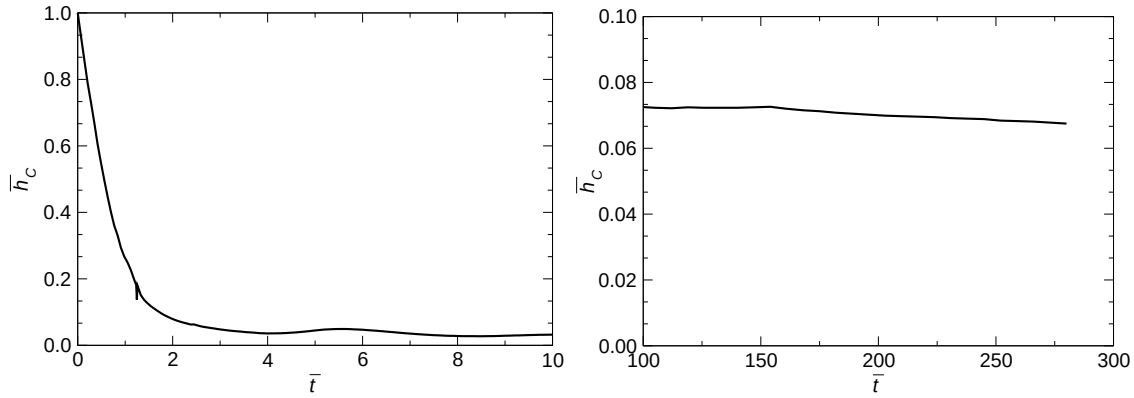

Figure 5.15: Dimensionless lamella height at the symmetry axis for drop impact on the permeable wall at Re = 1400, We = 27, $K = 3.125 \cdot 10^{-12}$ m^2.

Simultaneously the liquid flows through the permeable wall corresponding to the absorption of the liquid in the porous substrate. The height of the lamella is not constant over the surface and the decrease of the lamella height is more pronounced in the region farther from the edge, as can be seen in Fig. 5.16 in which the lamella shapes are plotted at times $\overline{t} = 112$ and $\overline{t} = 280$. The liquid penetration is very slow and, in order to show the difference in the lamella height, the plots are divided in two parts, showing the lamella shapes at radial distances $0 \leq \overline{r} \leq 0.6$ and $1.5 \leq \overline{r} \leq 2.1$, the former corresponding to the region closer to the axis of

symmetry and the latter to the region closer to the lamella edge, respectively. The reason why the spreading ratio remains constant lies in the competitive effects of the spreading of the lamella and the liquid penetration through the permeable wall. The liquid is assumed to completely wet the surface and the contact line tends to move outward. However, the liquid is also being absorbed and the lamella loses height in time and the results is that the contact line remains stationary. It is expected at very long times that the spreading ratio would slowly start to decrease after a greater amount of liquid was absorbed, but this was not simulated because of high computational costs.

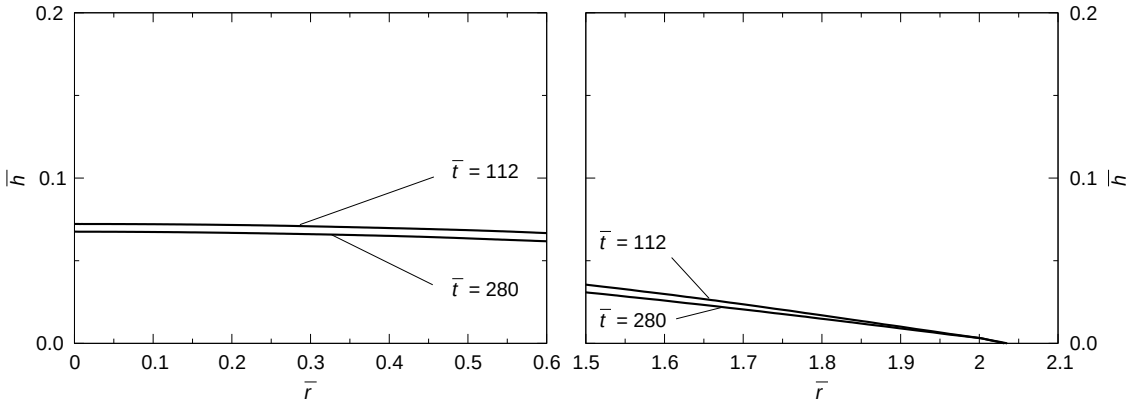

Figure 5.16: Lamella shapes close to the axis of symmetry (left) and to the lamella edge (right) for drop impact onto the permeable wall at Re = 1400, We = 27, $K = 3.125 \cdot 10^{-12}$ m^2.

The dimensionless residual volume of the lamella over the permeable wall is plotted in Fig. 5.17. The liquid volume remaining over the surface decreases linearly with time, which yields a linear increase of the absorbed liquid volume in time.

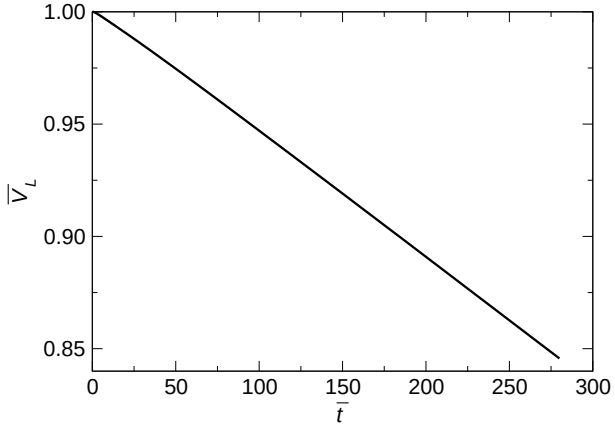

Figure 5.17: Dimensionless lamella volume above the permeable wall for drop impact at Re = 1400, We = 27, $K = 3.125 \cdot 10^{-12}$ m^2.

Instantaneous radial distributions of the dimensionless pressure gradient and velocity at the permeable wall are plotted in Fig. 5.18 at several time instants.

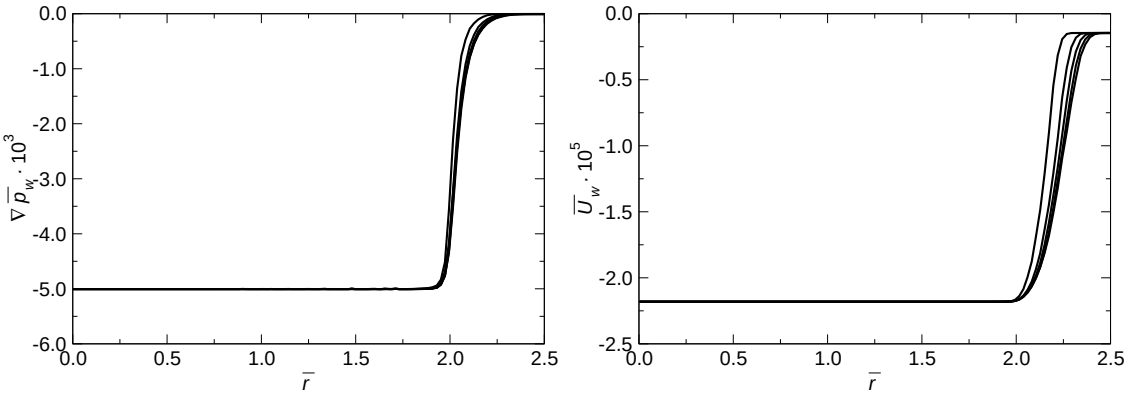

Figure 5.18: Distributions of the dimensionless pressure gradient (left) and velocity at the porous surface (right) obtained using the model with the permeable wall for Re = 1400, We = 27, $K = 3.125 \cdot 10^{-12}$ m^2. Time instants from left to right are $\overline{t} = 56; 84; 168; 224; 280$.

Again, both the pressure gradient and the velocity are constant over the surface of the permeable wall. Even in the region of the impact close to the axis of symmetry, the disturbances of the pressure gradient and velocity caused by the entrapped air bubble at small times diminished, since the air bubble escaped through the lamella surface short after the instant of the impact, and the profiles of the pressure gradient and velocity over the permeable wall at longer times are smooth.

6 Conclusions and Recommendations for Future Work

6.1 Conclusions

In this work, the numerical and theoretical investigations of flow generated by single-drop impacts were performed. In order to improve the overall understanding of the physical mechanisms in flows pertinent to spray impingement, the analyzed configurations include drop collisions, comprising collision with a shallow liquid layer, binary drop collision and collision with a dry wall, then drop impact onto a heated wall with the simultaneous heat transfer in the wall, and drop impact on a porous substrate.

The capabilities of the computational procedure for interface capturing based on the VOF-method were assessed. In this model an additional convective term is introduced into the transport equation for phase fraction, contributing decisively to a sharper interface resolution. The used numerical code was appropriately extended to account for the advancing and receding contact angles, the nonisothermal free-surface flow and simultaneous heat transfer in the solid and for the fluid penetration in the porous substrate. The results of numerical predictions eventually help to understand the flow in the liquid during the impact, since no detailed experimental data for the distributions of pressure and velocity is available.

In the case of drop collision with a liquid layer, focus was given to the evolution of the crater formed beneath the surface upon the impact. The shape of the crater, the formation and propagation of a capillary wave in the crater and the residual film thickness on the rigid wall were determined and analyzed. Numerical simulations yielded a very good agreement with experimental results. It was confirmed that increasing the impact velocity at a constant film thickness has little to no effect on the crater evolution in depth and on the time to reach maximum depth. The surface tension has a clear influence on the receding motion of the crater and the decrease in diameter, as for higher values of surface tension the decrease starts earlier and is somewhat steeper. Furthermore, an analytical model for the penetration depth of the crater was developed, where the shape of the crater was approximated by a spherical crater and the velocity field past the propagating crater by the potential flow. The equations of motion of the crater tip were obtained from the pressure balance at this point and the asymptotic solution was obtained by neglecting capillary, viscous and gravity effects. The model agrees well with the experiments at the early times of penetration far from the wall if the impact velocity is high. Finally, a scaling analysis of the residual film thickness on the wall was conducted demonstrating a good agreement with the numerical predictions. A scaling relation for the residual film thickness was proposed based on the description of the film evolution and devel-

opment of the viscous boundary layer, and can be valuable in the modeling of spray cooling. The scaling obtained in the form $\overline{h}_{res} = A\mathrm{Re}^{-2/5}$ was proved in a recent study of van Hinsberg et al. [117] to be also valid for very thin liquid films with dimensionless film thicknesses ranging down to $\overline{H} = 0.07$, as well as for a general case of a spreading viscous liquid film generated by drop collision (Roisman [96]). The numerical simulations demonstrate not only high level of the predictive capabilities of the interface-capturing model resolving the free surface, they also help to better understand the mechanisms of crater evolution. In particular the formation and propagation of the capillary wave along the crater surface could be explained using the results of the numerical predictions of the pressure field in the liquid.

In the case of binary drop collision, the existing experimental data were compared to existing and new numerical simulations for the shape of the lamella generated at the early times of drop impact for various impact conditions. The results show that if the impact Reynolds and Weber numbers are high enough, the flow in the lamella far from its edge is universal and the evolution of the lamella thickness almost does not depend on the viscosity and surface tension. Therefore these results completely change the understanding of the flow generated by drop collisions. Moreover, it was demonstrated that the theoretical models based on the approximation of the shape of the deforming drop by a disk and the models based on the energy balance approach are not correct. Universal dimensionless distributions for the lamella thickness, velocity and pressure were obtained from the numerical simulations of drop impact onto a symmetry plane, associated with the binary drop collisions. These universal distributions are valid at high impact Weber and Reynolds numbers. The results for the universal distribution of the thickness of the lamella, velocity distribution and pressure distribution obtained in this work can be useful for future modeling of the phenomena related to the inertia dominated drop collisions, including drop impact onto a rigid or elastic surfaces, impact of solidifying drops and binary drop collisions.

In the case of drop collision with a dry wall, it was confirmed that for high impact Reynolds and Weber numbers the lamella shape far enough from the rim is universal. The scaling obtained recently from the analytical self-similar solution for the viscous flow in the spreading lamella and satisfying the full Navier-Stokes equations was proved to be valid for a wide range of impact parameters and even at relatively small times. The characteristic thickness and the radial distribution of the viscous boundary layer developed near the wall were determined based on this analytical solution and confirmed using numerical simulations. The velocity field in the lamella quickly converges to the self-similar analytical solution of the Navier-Stokes equations. The evolution of the lamella thickness is determined by the competitive effects of the inviscid flow and viscosity. The theory can be used as a base for further modeling of drop spreading.

In the case of drop impact onto a heated wall, the computational model for the two-phase flow with interface capturing and simultaneous heat transfer was formulated. The potential of the computational model was illustrated by computing a series of the configurations including single drop impact onto solid surface with different thermophysical properties, in a range of impact conditions and liquid-solid

temperature differences. The model accounts for temperature-dependent fluid properties and the considered temperature range in the simulations does not account for the phase change, that is boiling and evaporation. The change in the drop morphology during the impact and consequent advancing process being quantified in terms of drop spreading diameter as function of time was returned in good agreement with the available experimental data. Somewhat higher values obtained presently compared to the experimental findings and analytical results were the consequence of the air bubble being entrapped in the impact region. Its artificial removal in the computational procedure led to the correct temperature values. The increase of the mean temperature of the spreading drop amounts up to the half of the initial temperature difference. The influence of the increasing impact velocity is, as expected, manifested through the increase in the amount of heat transferred from the substrate. Further simulations of the drop impacting the stainless steel surface accounting only for the fluid flow by prescribing the fixed surface temperature were performed in order to examine the effects of the homogeneous temperature distribution assumed in the recent theoretical derivation of the wall heat flux. The results obtained reveal a fairly weak dependency of heat removed from the solid surface on the temperature distribution at the fluid-solid interface. The aforementioned air bubble entrapment is a consequence of the air flow taken into account in the computational model. Accordingly, the present computational model enables a more realistic insight into the heat transfer process pertinent to spray cooling, where situations with air entrainment within the wall film may easily arise.

In the case of drop impact on a porous surface, the computational model for two-phase flow with interface capturing was extended and the combined model was formulated, which includes both the external flow above and the flow of the absorbed fluid in the porous substrate. In addition, an alternative approach was presented, by computing only the external flow in drop spreading over the porous surface, and the presence of the porous substrate was accounted for by formulating an appropriate boundary condition for the permeable wall. The two models were validated by comparing the computational results with the existing experimental results and capabilities of both approaches were analyzed. The model with the permeable wall yields more accurate results regarding the spreading ratio and the lamella height at the axis of symmetry. Moreover, this model predicts the constant values of the normal velocity and the pressure gradient at the permeable wall, in accordance with the assumed slow creeping flow in the porous material. The computed residual volume of the spreading liquid lamella over the permeable wall was found to be linearly changing in time, which yields a linear time dependence of the absorbed volume in the porous medium, in accordance with some previous experimental findings.

6.2 Recommendations for Future Work

Based on the results obtained in this work, suggestions for improvements and future work are proposed, as outlined below.

The greater disagreement for the computed spreading ratio in the receding

motion of the spreading lamella, or the crater diameter in the liquid layer, suggests that the CSF model does not calculate the surface tension force accurately enough. Parasitic currents, commonly encountered in VOF-based simulations, are attributed to the inaccurate determination of the mean surface curvature. However, this model is best suitable for interface capturing in the framework of the finite-volume method without explicit free-surface reconstruction. Possibilities for improvement of the modeling of the surface tension force should be further analyzed.

In flows dominated by capillary forces and wettability at the wall, the motion of the contact line plays an important role. Further investigations are required for the derivation of a proper and generally applicable model for the contact-line velocity in order to reduce the differences between the computed and experimentally determined results.

Entrapment of small air bubbles in drop impact on various surfaces is observed in experiments at certain impact conditions. Since the air flow is included in the computational model, the air bubbles were resolved in all simulations of drop collisions with dry surfaces. Although the described mechanism for the formation of such bubbles is physically justified, further analysis should be conducted regarding their existence and behavior.

The computational model for the two-phase flow with free surfaces and the simultaneous heat transfer should be further extended to include the effects of phase change. In particular, the processes of liquid evaporation or solidification are interesting to analyze due to their great industrial relevance.

In the liquid flow through a porous medium, the smallest length scale is the one over which the details of the pore morphology and topology are considered. On the other hand, Darcy's law is typically applied at macroscales, which are well above the pore scale. The flow through the porous material relies upon transport equations developed and applied at these macroscales in terms of averaged over the macroscale volume quantities. However, Darcy's law was defined based upon measurements of flow rate and pressure drop related as averaged properties of the entire system, which is as a much larger length scale than the above mentioned macroscale. Therefore, it is only this large length scale at which the averaged quantities will be well defined. Further investigations should be conducted in order to define a coupled model for the flow outside and inside the porous medium. Moreover, the transition from the external flow to the Darcy flow in the porous medium should be properly modeled, since averaging the velocity becomes inappropriate in the small transitional region at the boundary of the porous medium.

Bibliography

[1] Afkhami, S., Bussmann, M.: *Height functions for applying contact angles to 2D VOF simulations.* International Journal for Numerical Methods in Fluids, 57:453–472, 2008.

[2] Arora, D., Deshpande, A.P., Chakravarthy, S.R.: *Experimental investigation of fluid drop spreading on heterogeneous and anisotropic porous media.* Journal of Colloid and Interface Science, 293:496–499, 2006.

[3] Aulisa, E., Manservisi, S., Scardovelli, R,. Zaleski, S.: *Interface reconstruction with least-squares fit and split advection in three-dimensional Cartesian geometry.* Journal of Computational Physics, 225:2301–2319, 2007.

[4] Bakshi, S., Roisman, I. V., Tropea, C.: *Investigations on the impact of a drop onto a small spherical target.* Physics of Fluids, 19:032102, 2007.

[5] Bartolo, D., Josserand, C., Bonn, D.: *Singular jets and bubbles in drop impact.* Physical Review Letters, 96:124501, 2006.

[6] Batchelor, F.R.S.: *An Introduction to Fluid Mechanics.* Cambridge Universty Press, Cambridge, 1970.

[7] Berberović, E., Roisman, I.V., Jakirlić S., Tropea, C.: *Inertia dominated flow and heat transfer in liquid drop spreading on a hot substrate.* International Journal of Heat and Fluid Flow, 2010. submitted.

[8] Berberović, E., van Hinsberg, N.P., Jakirlić, S., Roisman, I.V., Tropea, C.: *Drop impact onto a liquid layer of finite thickness: Dynamics of the cavity evolution.* Physical Review E, 79:036306, 2009.

[9] Bhardwej, R., Attinger, D.: *Non-isothermal wetting during impact of milimeter-size water drop on a flat substrate: Numerical investigation and comparison with high-speed visualization experiments.* International Journal of Heat and Fluid Flow, 29:1422–1435, 2008.

[10] Brackbill, J.U., Kothe, D.B., Zemach, C.: *A continuum method for modeling surface tension.* Journal of Computational Physics, 100:335–354, 1992.

[11] Bussmann, M., Chandra, S., Mostaghimi, J.: *Modeling the splash of a droplet impacting a solid surface.* Physics of Fluids, 12:3121–3132, 2000.

[12] Bussmann, M., Mostaghimi, J., Chandra, S.: *On a three-dimensional volume tracking model of droplet impact.* Physics of Fluids, 11:1406–1417, 1999.

[13] Çengel, Y.A.: *Heat transfer: A practical approach.* McGraw-Hill Higher Education, 2003.

[14] Chandra, S., Avedisian, C.T.: *On the collision of a droplet with a solid surface.* Proceedings of the Royal Society London A, 423:13–41, 1991.

[15] Chandra, S., Avedisian, C.T.: *Observations of droplet impingement on a ceramic porous surface.* International Journal of Heat and Mass Transfer, 35:2377–2388, 1992.

[16] Clarke, A., Blake, T.D., Carruthers, K., Woodward, A.: *Spreading and imbibition of liquid droplets on porous surfaces.* Langmuir, 18:2980–2984, 2002.

[17] Cossali, G.E., Coghe, A., Marengo, M.: *The impact of a single drop on a wetted solid surface.* Experiments in Fluids, 22, 1997.

[18] Dai, M., Schmidt, D.P.: *Numerical simulation of head-on droplet collision: Effect of viscosity on maximum deformation.* Physics of Fluids, 17:041701, 2005.

[19] Deng, Q., Anilkumar, A.V., Wang, T.G.: *The role of viscosity and surface tension in bubble entrapment during drop impact onto a deep liquid pool.* Journal of Fluid Mechanics, 578:119–138, 2007.

[20] de Ruiter, J., Pepper, R.E., Stone, H.A.: *Thickness of the rim of an expanding lamella near the splash threshold.* Physics of Fluids, 22:022104, 2010.

[21] di Marco, M., Tartarini, P., Liao, Y., Evans, D., Baum, H.: *Evaporative cooling due to a gently deposited droplet.* International Journal of Heat and Mass Transfer, 36:4133–4139, 1993.

[22] Elmore, P.A., Chahine, G.L., Oğuz, H.N.: *Cavity and flow measurements of reproducible bubble entrainment following drop impacts.* Experiments in Fluids, 31:664–673, 2001.

[23] Engel, O.G.: *Initial pressure, initial flow velocity, and the time dependence of crater depth in fluid impacts.* Journal of Applied Physics, 38:3935–3940, 1967.

[24] Fedorchenko, A.I., Wang, A.B.: *On some common features of drop impact on liquid surfaces.* Physics of Fluids, 16:1349–1365, 2004.

[25] Ferziger, J.H. Perić, M.: *Computational methods for fluid dynamics.* Springer-Verlag, Berlin, 2002.

[26] Francois, M.M., Cummins, S.J., Dendy, E.D., Kothe, D.B., Sicilian, J.M., Williams, M.W.: *A balanced-force algorithm for continuous and sharp interfacial surface tension models within a volume tracking framework.* Journal of Computational Physics, 213:141–173, 2006.

[27] Fujimoto, H., Hatta, N., Viskanta, R.: *Numerical simulation of convective heat transfer to a radial free surface jet impinging on a hot solid.* Heat and Mass Transfer, 35:266–272, 1999.

[28] Fukai, J., Shiiba, Y., Yamamoto, T., Miyatake, O., Poulikakos, D., Megaridis, C.M., Zhao, Z.: *Wetting effects on the spreading of a liquid droplet colliding with a flat surface: Experiment and modeling.* Physics of Fluids, 7:236–247, 1995.

[29] Gaskell, P.H., Lau, K.C.: *Curvature-compensated convective transport: SMART, a new boundedness-preserving transport algorithm.* International Journal for Numerical Methods in Fluids, 8:617–641, 1988.

[30] Geldorp, W.I., Rioboo, R., Jakirlić, S., Muzaferija, S., Tropea, C.: *Numerical and experimental drop impact on solid dry surfaces.* In *Proc.* 8^{th} *International Conference on Atomization and Spray Systems*, Pasadena, CA, USA, July 2000.

[31] Gerlach, D., Tomar, G., Biswas, G., Durst, F.: *Comparison of volume-of-fluid methods for surface tension-dominant two-phase flows.* International Journal of Heat and Mass Transfer, 49:740–754, 2006.

[32] Giudice, E.L., Campbell, J.D.: *Needle-free vaccine delivery.* Advanced Drug Delivery Reviews, 58:68–89, 2006.

[33] Golpaygan, A., Hsu, N., Ashgriz, N.: *Numerical investigation of impact and penetration of a droplet onto a porous substrate.* Journal of Porous Media, 11:323–341, 2008.

[34] Gotaas, C., Havelka, P., Jakobsen, H.A., Svendsen, H.F., Hase, M., Roth, N., Weigand, B.: *Effects of viscosity on droplet-droplet collision outcome: Experimental study and numerical comparison.* Physics of Fluids, 19:102106, 2007.

[35] Gueyffier, D., Zaleski, S.: *Full Navier-Stokes simulations of droplet impact on thin liquid films.* In *Proc.* 3^{rd} *International Conference on Multiphase Flow*, Lyon, France, June 8 - 12 1998.

[36] Harlow, F.H. Welch, J.E.: *Numerical calculation of time-dependent viscous incompressible flow of fluid with free surface.* Physics of Fluids, 8:2182–2189, 1965.

[37] Harvie, D.J.E., Davidson, M.R., Rudman, M.: *An analysis of parasitic current generation in Volume of Fluid simulations.* Aplied Mathematical Modelling, 30:1065–1066, 2006.

[38] Hase, M., Weigand, B.: *Transient heat transfer of deforming droplets at high Reynolds numbers.* International Journal for Numerical Methods in Heat and Fluid Flow, 14:85–97, 2004.

[39] Healy, W.M., Hartley, J.G., Abdel-Khalik, S.I.: *On the validity of the adiabatic spreading assumption in droplet impact cooling.* International Journal of Heat and Mass Transfer, 44:3869–3881, 2001.

[40] Hirt, C.W., Nichols, B.D.: *Volume of fluid (VOF) method for the dynamics of free boundaries.* Journal of Computational Physics, 39:201–225, 1981.

[41] Hsu, N., Ashgriz, N.: *Nonlinear penetration of liquid drops into radial capillaries.* Journal of Colloid and Interface Science, 270:146–162, 2004.

[42] Incropera, F.P., de Witt, D.P.: *Fundamentals of heat and mass transfer.* John Wiley and Sons, 5^{th} edition, 2002.

[43] Issa, R.I.: *Solution of the implicitly discretised fluid flow equations by operator-splitting.* Journal of Computational Physics, 62:40–65, 1986.

[44] Jackson, G.W., James, D.F.: *The permeability of fibrous porous media.* The Canadian Journal of Chemical Engineering, 64:364–374, 1986.

[45] Jasak, H.: *Error analysis and estimation for the finite volume method with applications to fluid flows.* PhD thesis, Imperial College of Science, Technology and Medicine, London, 1996.

[46] Josserand, C., Zaleski, S.: *Droplet splashing on a thin liquid film.* Physics of Fluids, 15:1650–1657, 2003.

[47] Kärrholm, F.P.: *Numerical modelling of diesel spray injection, turbulence interaction and combustion.* PhD thesis, Chalmers University of Technology, Göteborg, Sweden, 2008.

[48] Kellay, H.: *Impact of drops on a water-covered sand bed: Erosion, entrainement and pattern formation.* Europhysics Letters, 71:400–406, 2005.

[49] Kistler, S.F.: *Wettability*, chapter Hydrodynamics of Wetting, pages 311–429. Marcel Dekker, Inc, 1993.

[50] Koponen, A., Kandhai, D., Hellén, E., Alava, M., Hoekstra, A., Kataja, M., Niskanen, K., Sloot, P., Timonen, J.: *Permeability of three-dimensional random fiber webs.* Physical Review Letters, 80:716, 1998.

[51] Kumar, S.M., Deshpande, A.P.: *Dynamics of drop spreading on fibrous porous media.* Colloids and Surfaces A: Psysicochemical Engineering Aspects, 277:157–163, 2006.

[52] Lafaurie, B., Nardone, C., Scardovelli, R., Zaleski, S., Zaneti, G.: *Modelling merging and fragmentation in multiphase flows with SURFER.* Journal of Computational Physics, 113:134–147, 1994.

[53] Leonard, B.P.: *Simple high-accuracy resolution program for convective modelling of discontinuities.* International Journal for Numerical Methods in Fluids, 8:1291–1318, 1988.

[54] Leonard, B.P.: *The ULTIMATE conservative difference scheme applied to unsteady one-dimensional advection.* Computer Methods in Applied Mechanics and Engineering, 88:17–74, 1991.

[55] Liu, X., Lienhard, J.H.V., Lombara, J.S.: *Convective heat transfer by impingement of circular liquid jets.* ASME Transactions, Journal of Heat Transfer, 113:571–582, 1991.

[56] López, J., Hernández, J., Gómez, P,. Faura, F.: *A volume of fluid method based on multidimensional advection and spline interface reconstruction.* Journal of Computational Physics, 195:718–742, 2004.

[57] Lunkad, S.F., Buwa, V.V., Nigam, K.D.P.: *Numerical simulations of drop impacts and spreading on horizontal and inclined surfaces.* Chemical Engineering Science, 62:7214–7224, 2007.

[58] Mehdi-Nejad, V., Mostaghimi, J., Chandra, S.: *Air bubble entrapment under an impacting droplet.* Physics of Fluids, 15:173–183, 2003.

[59] Morton, D., Rudman, M., Leng, L.J.: *An investigation of the flow regimes resulting from splashing drops.* Physics of Fluids, 12:747–763, 2000.

[60] Mukherjee, S., Abraham, J.: *Investigations of drop impact on dry walls with a lattice-Boltzmann model.* Journal of Colloid and Interface Science, 312:341, 2007.

[61] Mundo, C., Sommerfeld, M., Tropea, C.: *On the modeling of liquid sprays impinging on surfaces.* Atomisation and Sprays, 8:625–652, 1998.

[62] Muzaferija, S., Perić, M.: *Computation of free surface flows using interface-tracking and interface-capturing methods*, chapter 2 in Nonlinear Water Wave Interaction, pages 59–100. WIT Press, 1999.

[63] Nikolopoulos, N., Nikas, K.S.S., Bergeles, G.: *A numerical investigation of central binary collision of droplets.* Computers and Fluids, 38:1191–1202, 2009.

[64] Nikolopoulos, N., Theodorakakos, A., Bergeles, A.: *Three-dimensional numerical investigation of a droplet impinging normally onto a wall film.* Journal of Computational Physics, 225:322–341, 2007.

[65] Nikolopoulos, N., Theodorakakos, A., Bergeles, G.: *A numerical investigation of the evaporation process of a liquid droplet impinging onto a hot substrate.* Inernational Journal of Heat and Mass Transfer, 50:303–319, 2007.

[66] Nikolopoulos, N., Theodorakakos, A., Bergeles, G.: *Off-centre binary collision of droplets: A numerical investigation.* International Journal of Heat and Mass Transfer, 52:4160–4174, 2009.

[67] Oğuz, H.N., Prosperetti, A.: *Bubble entrainment by the impact of drops on liquid surfaces.* Journal of Fluid Mechanics, 219:143–179, 1990.

[68] Oğuz, H.N., Prosperetti, A.: *Numerical calculations of the underwater noise of rain.* Journal of Fluid Mechanics, 228:417–442, 1991.

[69] OpenCFD Ltd: *OpenFOAM, The Open Source CFD Toolbox, Programmer's Guide*, 2008.

[70] OpenCFD Ltd: *OpenFOAM, The Open Source CFD Toolbox, User Guide*, 2008.

[71] Osher, S., Sethian, J.A.: *Fronts propagating with curvature dependent speed: Algorithms based on Hamilton-Jacobi formulations.* Journal of Computational Physics, 79:12–49, 1988.

[72] Pan, K.L., Law, C.K., Zhou, B.: *Experimental and mechanistic description of merging and bouncing in head-on binary droplet collision.* Journal of Applied Physics, 103:064901, 2008.

[73] Pan, Y., Suga, K.: *Numerical simulation of binary liquid droplet collision.* Physics of Fluids, 17:082105, 2005.

[74] Pasandideh-Fard, M., Aziz, S.D. Chandra, S., Mostaghimi, J.: *Cooling effectivness of a water drop impinging on a hot surface.* International Journal of Heat and Fluid Flow, 22:201–210, 2001.

[75] Pasandideh-Fard, M., Qiao, Y.M., Chandra, S., Mostaghimi, J.: *Capillary effects during droplet impact on a solid surface.* Physics of Fluids, 8:650–659, 1996.

[76] Patankar, S.V.: *Numerical heat transfer and fluid flow.* Hemisphere Publishing Corporation, Washington, DC, 1980.

[77] Pepper, R.E., Laurent, C., Stone, H.A.: *Splashing on elastic membranes: The importance of early-time dynamics.* Physics of Fluids, 20:082103, 2008.

[78] Pillioid, J.E., Puckett, E.G.: *Second-order accurate volume-of-fluid algorithms for tracking material interfaces.* Journal of Computational Physics, 199:465–502, 2004.

[79] Prosperetti, A., Oğuz, H.N.: *The impact of drops on liquid surfaces and the underwater noise of rain.* Annual Review of Fluid Mechanics, 25:577–602, 1993.

[80] Prosperetti, A., Oğuz, H.N.: *Air entrainment upon liquid impact.* Philosophical Transactions of the Royal Society London A, 355:491–506, 1997.

[81] Pucket, E.G., Almgren, A.S., Bell, J.B., Marcus, D.L., Rider, W.J.: *A high-order projection method for tracking fluid interfaces in variable density incompressible flows.* Journal of Computational Physics, 130:269–282, 1997.

[82] Qian, J., Law, C.K.: *Regimes of coalescence and separation in droplet collision.* Journal of Fluid Mechanics, 331:59–80, 1997.

[83] Qiao, Y.M., Chandra, S.: *Experiments on adding a surfactant to water drop boiling on a hot surface.* Proceedings of the Royal Society London A, 453:673–689, 1997.

[84] Range, K., Feuillebois, F.: *Influence of surface roughness on liquid drop impact.* Journal of Colloid Interface Science, 203:16–30, 1998.

[85] Rein, M.: *Phenomena of liquid drop impact on solid and liquid surfaces.* Fluid Dynamics Research, 12:61–93, 1993.

[86] Reis, N.C., Griffiths, R.F., Santos, J.M.: *Numerical simulation of the impact of liquid droplets on porous surfaces.* Journal of Computational Physics, 198:747–770, 2004.

[87] Reis, N.C., Griffiths, R.F., Santos, J.M.: *Parametric study of liquid droplets impinging on porous surfaces.* Applied Mathematical Modelling, 32:341–361, 2008.

[88] Renardy, Y., Renardy, M.: *PROST: A parabolic reconstruction of surface tension for the volume-of-fluid method.* Journal of Computational Physics, 183:400–421, 2002.

[89] Rider, W.J., Kothe, D.B.: *Reconstructing volume tracking.* Journal of Computational Physics, 141:112–152, 1998.

[90] Rieber, M., Frohn, A.: *A numerical study on the mechanism of splashing.* International Journal of Heat and Fluid Flow, 20:455–461, 1999.

[91] Rioboo, R., Marengo, M., Tropea, C.: *Outcomes from a drop impact on solid surfaces.* Atomization and Sprays, 11:155–165, 2001.

[92] Rioboo, R., Marengo, M., Tropea, C.: *Time evolution of liquid drop impact onto solid, dry surfaces.* Experiments in Fluids, 33:112–124, 2002.

[93] Roisman, I.V., Berberović, E., Tropea, C.: *Inertia dominated drop collisions I. On the universal flow in the lamella.* Physics of Fluids, 79:052103, 2009.

[94] Roisman, I.V., Chandra, S., Mostaghimi, J., Opfer, L., Raessi, M., Tropea, C.: *Drop impact onto a dry surface: role of the dynamic contact angle.* Colloids and Surfaces A: Physicochemical Engineering Aspects, 322:183–191, 2008.

[95] Roisman, I.V.: *Dynamics of inertia dominated binary drop collisions.* Physics of Fluids, 16:3438–3449, 2004.

[96] Roisman, I.V.: *Inertia dominated drop collisions II. An analytical solution of the Navier-Stokes equations for a spreading viscous film.* Physics of Fluids, 21:052104, 2009.

[97] Roisman, I.V.: *Fast forced liquid film spreading on a substrate: flow, heat transfer and phase transition.* Journal of Fluid Mechanics, 656:189–204, 2010.

[98] Roisman, I.V., van Hinsberg, N.P., Tropea, C.: *Propagation of a kinematic instability in a liquid layer: Capillary and gravity effects.* Physical Review E, 77:046305, 2008.

[99] Rudman, M.: *Volume-tracking methods for interfacial flow calculations.* International Journal for Numerical Methods in Fluids, 24:671–691, 1997.

[100] Rusche, H.: *Computational fluid dynamics of dispersed two-phase flows at high phase fractions.* PhD thesis, Imperial College of Science, Technology and Medicine, London, 2002.

[101] Saad, Y.: *Iterative Methods for Sparse Linear Systems.* Society for Industrial and Applied Mathematics, Second edition, 2003.

[102] Scardovelli, R. Zaleski, S.: *Interface reconstruction with least-square fit and split Eulerian-Lagrangian advection.* International Journal for Numerical Methods in Fluids, 41:251–274, 2003.

[103] Scardovelli, R., Zaleski, S.: *Direct numerical simulation of free-surface and interfacial flow.* Annual Review of Fluid Mechanics, 31:567–603, 1999.

[104] Selvam, R.P., Lin, L., Ponnappan, R.: *Direct simulation of spray cooling: Effect of vapor bubble growth and liquid droplet impact on heat transfer.* International Journal of Heat and Mass Transfer, 49:4265–4278, 2006.

[105] Seveno, D., Ledauphin, V., Martic, G., Voué, M., DeConinck, J.: *Spreading drop dynamics on porous surfaces.* Langmuir, 18:7496–7502, 2002.

[106] Shin, J., McMahon, T.A.: *The tuning of a splash.* Physics of Fluids, 2(8):1312–1317, 1990.

[107] Šikalo, Š., Wilhelm, H.D., Roisman, I.V., Jakirlić S., Tropea, C.: *Dynamic contact angle of spreading droplets: Experiments and simulations.* Physics of Fluids, 17:62103, 2005.

[108] Stevens, J.: *Measurements of local heat transfer coefficients: Results for an axisymmetric, single-phase water jet impinging normally on a flat plate with uniform heat flux.* Master's thesis, Brigham Young University, Provo, Utah, 1988.

[109] Strotos, G., Gavaises, M., Theodorakakos, A., Bergeles, G.: *Numerical investigation of the cooling effectiveness of a droplet impinging on a heated surface.* International Journal of Heat and Mass Transfer, 51, 2008.

[110] Sweby, P.K.: *High resolution schemes using flux limiters for hyperbolic conservation laws.* SIAM Journal on Numerical Analysis, 21:995–1011, 1984.

[111] Taylor, G.: *The dynamics of Thin Sheets of Fluid. II. Waves on Fluid.* Proceedings of the Royal Society London A, 253:296–312, 1959.

[112] Tong, A.Y.: *A numerical study on the hydrodynamics and heat transfer of a circular liquid jet impinging onto a surface.* Numerical Heat Transfer A, 44:11–19, 2004.

[113] Tong, A.Y., Zhaoyuan, W.: *A numerical method for capillary-dominant free surface flows.* Journal of Computational Physics, 221:506–523, 2007.

[114] Tropea, C., Roisman, I.V.: *Modeling of spray impact on solid surfaces.* Atomisation and Sprays, 10:387–408, 2000.

[115] Ubbink, O., Issa, R.I.: *A method for capturing sharp fluid interfaces on arbitrary meshes.* Journal of Computational Physics, 153:26–50, 1999.

[116] Ubbink, O.: *Numerical rediction of two fluid systems with sharp interfaces.* PhD thesis, Imperial College of Science, Technology and Medicine, London, 1997.

[117] van Hinsberg, N.P., Budakli, M., Göhler, S., Berberović, E., Roisman, I.V., Gambaryan-Roisman, T., Tropea, C., Stephan, P.: *Dynamics of the cavity and the surface film for impingements of single drops on liquid films of various thicknesses.* Journal of Colloid and Interface Science, 350:336–343, 2010.

[118] van Hinsberg, N.P.: *Investigation of drop and spray impingement on a thin liquid layer accounting for the wall film topology.* PhD thesis, Technische Universität Darmstadt, 2009.

[119] van Leer, B.: *Towards the ultimate conservative difference scheme II. Monotonicity and conservation combined in a second order scheme.* Journal of Computational Physics, 14:361–370, 1974.

[120] Veynante, D., Trouvé, A., Bray, K.N.C., Mantel, T.: *Gradient and counter-gradient scalar transport in turbulent premixed flames.* Journal of Fluid Mechanics, 332:263–293, 1997.

[121] Vincent, S., Caltagirone, J.P.: *Test-case number 10: Parasitic currents induced by surface tension PC.* Multiphase Science and Technology, 16:69–74, 2004.

[122] Vu, H., Aguilar, G., Jepsen, R.: *Single droplet heat transfer through shallow liquid pools.* In *Proc. 11^{th} Triennial International Conference on Liquid Atomization and Spray Systems*, Vail, Colorado USA, July 2009.

[123] Waclawczyk, T., Koronowicz, T.: *Comparison of CICSAM and HRIC high-resolution schemes for interface capturing.* Journal of Theoretical and Applied Mechanics, 42:325–345, 2008.

[124] Watanabe, Y., Saruwatari, A., Ingram, D.M.: *Free-surface flows under impacting droplets.* Journal of Computational Physics, 227:2344–2365, 2008.

[125] Waterson, N.P., Deconinck, H.: *Design principles for bounded higher-order convection schemes – a unified approach.* Journal of Computational Physics, 224:182–207, 2007.

[126] Weiss, D.A., Yarin, A.L.: *Single drop impact onto liquid films: Neck distortion, jetting, tiny bubbles entrainment, and crown formation.* Journal of Fluid Mechanics, 385:229–254, 1999.

[127] Weller, H.G.: *Derivation, modelling and solution of the conditionally averaged two-phase flow equations.* Technical Report TR/HGW/02, OpenCFD Ltd., 2005.

[128] Weller, H.G.: *A new approach to VOF-based interface capturing methods for incompressible and compressible flow.* Technical Report TR/HGW/04, OpenCFD Ltd., 2008.

[129] Weller, H.G., Tabor, G., Jasak, H., Fureby, C.: *A tensorial approach to computational continuum mechanics using object-oriented techniques.* Computers in Physics, 12:620–631, 1998.

[130] Willis, K., Orme, M.: *Binary droplet collisions in a vacuum environment: an experimental investigation of the role of viscosity.* Experiments in Fluids, 34:28–41, 2003.

[131] Wörner, M., Sabisch, W, Grötzbach, G, Cacuci, D.G.: *Volume-averaged conservation equations for volume-of-fluid interface tracking.* In *Proc. 4^{th} International Conference on Multiphase Flow*, New Orleans, Louisiana, USA, May 27 - June 1 2001.

[132] Yarin, A.L.: *Drop impact dynamics: splashing, spreading, receding, bouncing...* Annual Review of Fluid Mechanics, 38:159–192, 2006.

[133] Yarin, A.L.: *private communication*, december 2009.

[134] Yarin, A.L., Rubin, M.B., Roisman, I.V.: *Penetration of a rigid projectile into an elastic-plastic target of finite thickness.* International Journal of Impact Engineering, 16:801–831, 1995.

[135] Yarin, A.L., Weiss, D.A.: *Impact of drops on solid surfaces: self-similar capillary waves, and splashing as a new type of kinematic discontinuity.* Journal of Fluid Mechanics, 283:141–173, 1995.

[136] Zhang, F.H., Thoroddsen, S.T.: *Satellite generation during bubble coalescence.* Physics of Fluids, 20:119–138, 2008.

Lebenslauf

Persönliche Daten

Name	Edin Berberović
Geburtsdatum	14.09.1974.
Geburtsort	Zenica, Bosnien und Herzegowina
Familienstand	verheiratet, 1 Kind

Hochschulbildung

2004 – 2006	Maschinenbaufakultät Sarajevo, Universität in Sarajevo Magister (M.Sc.) Maschinenbau, Energie- und Verfahrenstechnik
1996 – 2002	Maschinenbaufakultät Zenica, Universität in Sarajevo Diplomingenieur Maschinenbau, Konstruktions- und Produktionstechnik

Wehrdienst

2001	Militär der Föderation Bosnien und Herzegowina

Berufliche Tätigkeit

2007 – 2010	Technische Universität Darmstadt Fachgebiet Strömungslehre und Aerodynamik, externer Doktorand
seit 05/2003	Maschinenbaufakultät Zenica, Universität in Zenica wissenschaftlicher Mitarbeiter (Assistent), Fachgebiet Energie- und Verfahrenstechnik
03/2003 – 05/2003	UNIS Fagas, Sarajevo selbstständiger Ingenieur Gasdruckregulatoren
10/2002 – 03/2003	Narodno grijanje, Sarajevo Fertigungsingenieur Solarkollektoren

Stipendien DAAD

2007 – 2009	Technische Universität Darmstadt Fachgebiet Strömungslehre und Aerodynamik, Forschungsstipendium für Doktoranden und Nachwuchswissenschaftler, jeweils einmal im Jahr
10/2004 – 07/2005	Friedrich-Alexander Universität Erlangen-Nürnberg Institut für Prozessmaschinen und Anlagentechnik, Anfertigung der Masterarbeit
01/2002 – 04/2002	Technische Universität Darmstadt Fachgebiet Energie- und Kraftwerkstechnik, Anfertigung der Diplomarbeit